

Polymer Crystallization under Quiescent and Flow Conditions: Relationships between Molecular Dynamics, Morphology, and Rheology

Zur Erlangung des akademischen Grades eines

DOKTORS DER NATURWISSENSCHAFTEN

(Dr. rer. nat.)

der KIT-Fakultät für Chemie und Biowissenschaften

des Karlsruher Instituts für Technologie (KIT)

genehmigte

DISSERTATION

von

Dipl.-Chem. Volker A. Röntzsch

aus Bad Kreuznach

Dekan:	Prof. Dr. Reinhard Fischer
Referent:	Prof. Dr. Manfred Wilhelm
Koreferentin:	Prof. Dr. Gisela Guthausen
Tag der mündlichen Prüfung:	18. Juli 2018

Diese Arbeit wurde in der Zeit vom 1. Juni 2014 bis zum 30. April 2018 am Institut für Technische Chemie und Polymerchemie (ITCP) des Karlsruher Instituts für Technologie (KIT) unter Anleitung von Prof. Dr. Manfred Wilhelm durchgeführt.

Hiermit versichere ich, dass ich die von mir vorgelegte Arbeit selbstständig verfasst habe, dass ich die verwendeten Quellen und Hilfsmittel vollständig angegeben und die Stellen der Arbeit, die anderen Werken im Wortlaut oder dem Sinn nach entnommen sind, entsprechend kenntlich gemacht habe.

Volker Röntzsch

Karlsruhe, den 1. Juni 2018

“I would rather have questions that can’t be answered
than answers that can’t be questioned.”

— Richard Feynman

Kurzfassung

Die Kontrolle der Morphologie von teilkristallinen Kunststoffen auf der Nano-, Meso- und Makroebene ist ein zentraler Aspekt beim Design von Spritzgussteilen, Filmen und Fasern. Besonders im Bereich moderner Verarbeitungstechniken wie 3D-Druck, Mikroformen oder Elektrosponnen sind tiefe Kenntnisse des Materialverhaltens notwendig. Weiterhin hilft dieses Wissen bei der Entwicklung von Computer-Simulationen der Strukturbildung und resultierenden Materialeigenschaften von kristallisierenden Kunststoffen.

In der vorliegenden Arbeit wurden neuartige Charakterisierungsmethoden verwendet um das Kristallisationsverhalten synthetischer Kunststoffe unter ruhenden und fließinduzierten Bedingungen zu untersuchen. Zur Aufklärung der Zusammenhänge zwischen molekularer Dynamik, Morphologie und Fließverhalten kristallisierender Kunststoffe wurden kombinierte RheoNMR, RheoSAXS und optische RheoMikroskopie eingesetzt. Diese Aufbauten ermöglichten eine zweidimensionale Messung und die Beeinflussung der Kristallisation durch Scherprofile. Als wichtiges Teilprojekt wurde eine Methode der NMR-Relaxometrie zur Bestimmung der Kristallinität und der Kristallisationskinetik von kommerziell relevanten Kunststoffen erprobt und mit herkömmlichen Bestimmungsmethoden wie der Differenzkalorimetrie und Röntgenstreuung verglichen.

Die erhaltenen Ergebnisse bestätigten einen physikalischen Gelbildungsprozess bei der Kristallisation von Kunststoffen, der durch wachsende und interagierende Überstrukturen bei Raumfüllungen von ca. 10–15% verursacht wird. Die Analyse des Aushärtvorgangs mit Hilfe rheologischer Modelle zeigte einen stark nichtlinearen Zusammenhang zwischen Raumfüllung und Viskosität (Zunahme der relativen Viskosität von vier Dekaden im Vergleich zur Schmelze). Dieses Wissen kann helfen Zykluszeiten im Spritzguss zu verbessern und ist ein wichtiger Wissensgewinn für die erfolgreiche Verwendung teilkristalliner Kunststoffe in modernen Verarbeitungsmethoden. Aufgrund der beobachteten Abhängigkeiten der molekularen Dynamik und Morphologie von Temperatur, Additiven und Fließbedingungen ist der Mechanismus der Kristallisation sehr wahrscheinlich durch Keimbildung und Wachstum geprägt. Die Bildung reihennukleierter Strukturen bei der fließinduzierten Kristallisation wird vermutlich durch eine modifizierte Konformation der längsten Polymerketten unter dem Einfluss von Scherung verursacht. Die NMR-Methodik zur Bestimmung der Kristallinität ist ab erhöhten Temperaturen von der Glasübergangstemperatur $T_g + 100$ °C in guter Übereinstimmung mit der Differenzkalorimetrie und Röntgenstreuung im Rahmen der Unsicherheit von $\pm 10\%$ der jeweiligen Methoden. Somit kann die NMR-Relaxometrie in der Zukunft als weitere Standardtechnik in Qualitäts- und Prozesslaboren zur Bestimmung der Kristallinität von teilkristallinen

Kunststoffen eingesetzt werden. Zusammenfassend haben diese Arbeiten einen Beitrag zur Aufklärung des Kristallisationsmechanismus, der Bildung von anisotropen Strukturen und des Aushärteverhaltens unter ruhenden und fließinduzierten Bedingungen geliefert. Diese Ergebnisse haben zu einem besseren Verständnis der Beziehungen zwischen Kristallisationskinetik, Fließbedingungen und Additiven in Bezug auf die molekulare Dynamik, Morphologie und das Fließverhalten teilkristalliner Kunststoffe geführt.

Abstract

Controlling the morphology of semi-crystalline polymers on the nano-, meso-, and macro-scale is a crucial aspect in the design of injection-molded parts, films, and fibers. Especially when exploring advanced processing techniques such as 3D printing, micro-molding, or electrospinning, a detailed knowledge of the material behavior is required. Furthermore, this know-how will help to improve the computer simulation of structural buildup and resulting material properties during polymer crystallization.

In this thesis, new characterization techniques were employed to study the crystallization behavior of synthetic polymers under quiescent and flow conditions. Relationships between the molecular dynamics, morphology, and rheology of crystallizing polymers were investigated using custom-built hyphenated RheoNMR, RheoSAXS, and optical RheoMicroscopy techniques. These combined set-ups allowed for simultaneous two-dimensional measurements and the application of flow profiles during polymer crystallization. In an important subproject, a method to determine the crystallinity and crystallization kinetics via NMR relaxometry was evaluated for the most relevant semi-crystalline polymers, and compared to other characterization techniques such as differential scanning calorimetry and X-ray scattering.

The obtained results confirmed a physical gelation process during polymer crystallization mediated by the interaction of growing superstructures at volume fractions of approximately 10–15%. The analysis of the hardening behavior with the help of rheological models showed a strong nonlinear relationship between the degree of space filling and the viscosity (relative increase in viscosity by four orders of magnitude compared to the melt). This knowledge will help to optimize cycle times in injection molding and is an important cornerstone for the optimal use of semi-crystalline polymers in advanced processing technologies. Based on the experimental data obtained by hyphenated RheoNMR, RheoSAXS, and optical RheoMicroscopy, polymer crystallization from the melt most probably follows a nucleation and growth mechanism under the explored experimental conditions because of the dependencies on temperature, additives, and applied flow. The formation of row-nucleated structures during flow-induced crystallization is likely associated with the altered conformation of the longest polymer chains under the application of flow as described by a Weissenberg number larger than one. The NMR method to determine crystallinity and crystallization kinetics was found to deliver reasonable results for temperatures larger or equal to the glass transition temperature $T_g + 100$ °C compared to differential scanning calorimetry and X-ray scattering within an estimated relative error of $\pm 10\%$ for the respective methods. Consequently, NMR relaxometry could even be used in the future as a standard technique in quality control or processing labs. Overall, these

investigations helped to clarify the crystallization mechanism, the formation of row-nucleated structures, and the hardening behavior during quiescent and flow-induced crystallization. The results led to a better understanding of the relationships between the crystallization kinetics, flow conditions, and additives with respect to the molecular dynamics, morphology, and rheology of semi-crystalline polymers.

Contents

1	Introduction	1
2	Fundamentals of Synthetic Semi-Crystalline Polymers	7
2.1	Introduction	7
2.2	Types of semi-crystalline polymers	7
2.3	Polypropylene: synthesis, morphology, and properties	13
2.4	Selected materials for the study of polymer crystallization	19
3	Theory of Polymer Crystallization	20
3.1	Introduction	20
3.2	Equilibrium thermodynamics	20
3.3	Quiescent crystallization	25
3.3.1	General remarks	25
3.3.2	Classical nucleation theory	25
3.3.3	Hoffman and Lauritzen theory	27
3.3.4	Olmsted's spinodal decomposition model	32
3.3.5	Strobl's mesomorphic phase transition model	33
3.3.6	Kinetic analysis of crystallization data	35
3.4	Flow-induced crystallization	38
3.4.1	General remarks	38
3.4.2	Effects of flow on the morphology of crystallizing polymers	39
3.4.3	Modeling flow-induced crystallization	41
4	Theory of Characterization Techniques	44
4.1	Rheology	44
4.1.1	Fundamentals	44
4.1.2	Rotational and oscillatory shear rheometry	46
4.1.3	Nonlinear rheology	49
4.2	Nuclear magnetic resonance (NMR)	51
4.2.1	Fundamentals	51
4.2.2	Theory of NMR relaxation	55
4.2.3	NMR pulse sequences	58
4.3	X-ray scattering	61
4.3.1	Fundamentals	61
4.3.2	Theory of scattering	62

5	Molecular Dynamics of Semi-Crystalline Polymers Studied by NMR	66
5.1	Introduction	66
5.2	Experimental	69
5.3	Solid-state ^1H -NMR experiments at 400 MHz	70
5.3.1	Temperature-dependent static solid-state ^1H -NMR experiments	70
5.3.2	Magic angle spinning (MAS)-NMR experiments	75
5.4	Polymer crystallinity determined by low-field NMR relaxometry	77
5.4.1	Temperature-dependent experiments on various polymers	77
5.4.2	Comparison with DSC and XRD	81
5.5	Monitoring polymer crystallization using low-field NMR relaxometry	82
5.5.1	Experiments on common semi-crystalline polymers	84
5.5.2	Comparison with DSC	87
5.6	Development of a high-temperature LF-NMR probe and an active Q-switch	89
5.7	Concluding remarks	93
6	Interplay between Molecular Dynamics and Rheology in Polymer Crystallization: RheoNMR	95
6.1	Introduction	95
6.2	Experimental	96
6.3	Quiescent crystallization of isotactic polypropylene	98
6.3.1	Temperature-dependence of isothermal crystallization	102
6.3.2	Physical gelation – characteristics and modeling	103
6.3.3	Influence of the polymer grade, fillers, and nucleating agents	107
6.4	Flow-induced crystallization of isotactic polypropylene	116
6.4.1	Variations of strain rate, shear duration, and total strain	116
6.4.2	Physical gelation during flow-induced crystallization	121
6.5	Morphology investigations using scanning electron microscopy	124
6.6	Concluding remarks	131
7	Correlation between Nano-Scale Morphology and Rheology in Polymer Crystallization: RheoSAXS	132
7.1	Introduction	132
7.2	Experimental	133
7.3	Quiescent crystallization of isotactic polypropylene	134
7.3.1	Quantitative analysis of the 2D-SAXS and rheology data	134
7.3.2	Correlation of the SAXS invariants and the rheological parameters	137
7.3.3	Effect of regio defects on the morphology under quiescent conditions	138
7.4	Flow-induced crystallization of isotactic polypropylene	141
7.4.1	Quantitative analysis of the azimuthally integrated 2D-SAXS patterns	144
7.4.2	Effect of regio defects on the flow-induced semi-crystalline morphology	147
7.5	Morphology investigations using scanning electron microscopy	151
7.6	Concluding remarks	155

8 Relationship between Microstructure and Rheology in Polymer Crystallization: RheoMicroscopy	157
8.1 Introduction	157
8.2 Experimental	158
8.3 Quiescent crystallization experiments	159
8.3.1 Early stages of crystallization	159
8.3.2 The microstructure at the point of gelation	160
8.4 Flow-induced crystallization experiments	163
8.4.1 The point of gelation under flow conditions	166
8.4.2 Ex-situ polarized light microscopy	166
8.5 Concluding remarks	167
9 Conclusion and Outlook	169
Acknowledgements (Danksagung)	173
A Appendix	174
A.1 Additional experimental data	174
A.1.1 Solid-state ¹ H-NMR (400 MHz)	174
A.1.2 Liquid-state ¹³ C-NMR (400 MHz)	176
A.1.3 Differential scanning calorimetry (DSC)	177
A.1.4 X-ray diffraction (XRD)	179
A.1.5 RheoNMR	180
A.1.6 RheoSAXS	183
A.1.7 RheoMicroscopy	185
A.1.8 Scanning electron microscopy (SEM)	186
A.2 Photographs	188
Nomenclature	192
References	195

1 Introduction

Because of the enormous commercial relevance of synthetic semi-crystalline polymers, the variety of structure-property relationships, and the mechanistic complexity, the interest in understanding every detail of polymer crystallization is constantly high. In the following sections, a brief overview of the semi-crystalline polymer market, the applications, and the challenges in engineering and polymer science associated with semi-crystalline polymers are presented. Research questions are deduced and the project steps of this thesis are outlined.

Market and applications of synthetic semi-crystalline polymers

The overall world polymer production in 2015 was ~300 million tons with a market value of ~600 billion € and more than two thirds being semi-crystalline polymers (Plastics Europe Report 2016). In Central Europe the demand per person and year is at the moment ~80 kg/year. The market of polymers is exponentially growing since the 1950's with the beginning of large-scale industrial polymer production (see Figure 1.1).

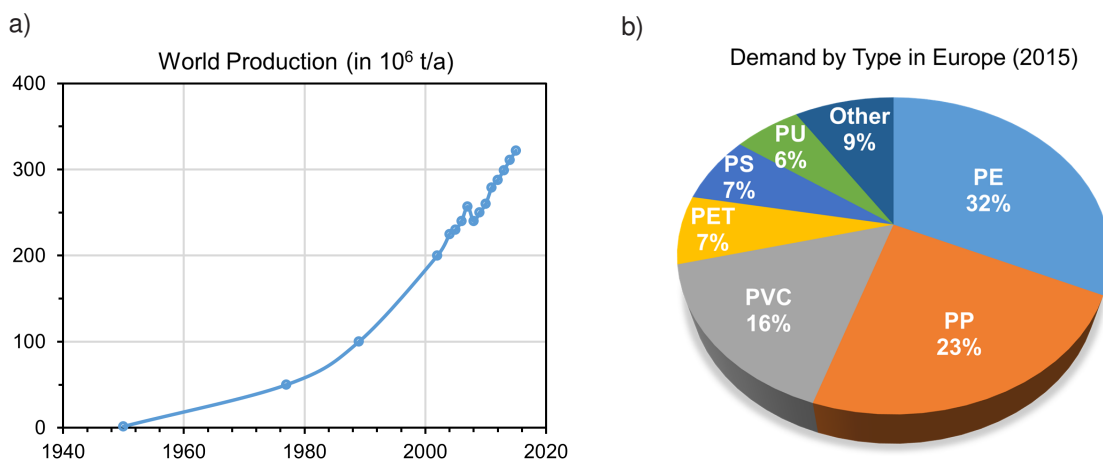


Figure 1.1: World production of polymers from 1950 – today (a) and the demand by polymer type in Europe from 2015 (b). An exponential growth is observed which is triggered by increased trade and development. PE: polyethylene, PP: polypropylene, PVC: polyvinyl chloride, PET: polyethylene terephthalate, PS: polystyrene, PU: polyurethane. Data taken from the Plastics Europe Report (2016).

Half of the produced polymers today are polyolefins, mainly high-density, low-density, and linear low-density polyethylene (HDPE, LDPE, LLDPE), isotactic polypropylene (i-PP), and polyolefin copolymers. The second largest group of semi-crystalline polymers are polyesters, mainly polyethylene terephthalate (PET), polybutylene terephthalate (PBT), polylactide (PLA), and polycaprolactone (PCL). The third group are polyamides, either aliphatic (e.g., PA-6, PA-66, Nylons) or aromatic (e.g., polyparaphenylene terephthalamide, Kevlar). Another group of important semi-crystalline polymers are fluoropolymers such as polytetrafluoroethylene

(PTFE, Teflon), polyvinylidene fluoride (PVDF, Kynar), or perfluorosulfonic acid (Nafion). The semi-crystalline nature of these polymers leads to outstanding toughness, tensile strength, impact resistance, and chemical robustness (Mark 2007; Van Krevelen and Te Nijenhuis 2009; Ward and Sweeney 2012; Elsner *et al.* 2012). Besides these engineering properties, also functionalities with respect to optical, electrical, or separation properties are oftentimes a direct consequence of the underlying order and crystallinity in materials such as conjugated polymers, dielectrics, or membranes, respectively (Skotheim and Reynolds 2006; O'Halloran *et al.* 2008; Pabby *et al.* 2008; Lalia *et al.* 2013). Because of their easy processability, cheap price, and low density, semi-crystalline polymers are used in numerous applications for packaging, construction, automotive parts, electronics, textiles, household appliances, sports, and agriculture. They come in forms of bulk parts, films, or fibers which can be tailored to the needs of specific applications (Crawford 1998; Chanda and Roy 2006).



Figure 1.2: Examples of applications for semi-crystalline polymers: molded parts (a), textiles (b), packaging (c). images: PxHere CC0 1.0 Universal (CC0 1.0) creative commons license.

Challenges in science and engineering of semi-crystalline polymers

Controlling the hierarchical structure of semi-crystalline polymers on the nano-, meso-, and macro-scale is a crucial aspect in the controlled design of material properties. In contrast to low molecular weight substances, the crystalline structure of polymers are determined not only by the molecular structure, but also by the actual crystallization conditions (Mandelkern 2002, 2004; Piorkowska and Rutledge 2013). The bulk crystallinity is very much affected by these factors as it is sensitive to the molecular weight distribution, chain topology, stereo- and regio-regularity, additives, thermal history, applied pressure, and flow conditions during processing (Reiter and Strobl 2007; Piorkowska and Rutledge 2013). The kinetics of polymer crystallization are also of high interest, i.e., an understanding of the pathway that often leads to a kinetically trapped state of the material. Polymer crystallization kinetics are comprised of the inherent polymer nucleation and growth rates, which together with the processing conditions (applied flow, temperature, pressure) and selected additives (nucleating agents, fillers, pigments), lead to systems of remarkable complexity (Somani, Yang, Zhu and Hsiao 2005; Pappageorgiou *et al.* 2005). In polymer processing steps such as injection molding, film blowing, or fiber spinning, polymer melts are crystallized under strong shear and elongational flows

which has a strong impact on the micro-structure (Ward and Sweeney 2012). From a polymer processing point of view, the molecular weight distribution, branching, and additives together with the applied temperature, deformation rates, and absolute deformations are the most critical parameters in obtaining certain morphologies and desired material properties. New processing techniques such as 3D printing, micro-molding, or electrospinning require a precise knowledge of the crystallization and hardening behavior of semi-crystalline polymers and of the interplay between the applied processing conditions and the resulting semi-crystalline morphologies.

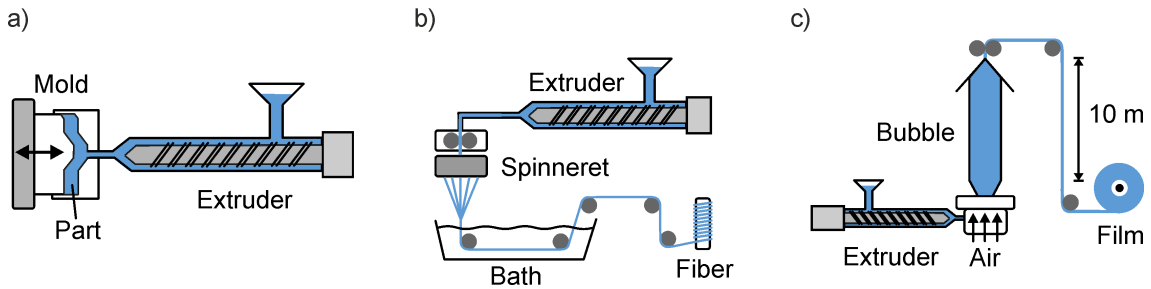


Figure 1.3: Processing techniques for semi-crystalline polymers: injection molding (a), fiber spinning (b), and film blowing (c). Adapted from Elsner *et al.* (2012).

In terms of polymer science, a conclusive picture of the mechanism behind polymer crystallization is still missing. Classical concepts based on nucleation and growth e.g., by Hoffman and Lauritzen (1961) were questioned during the past as they didn't explain all observed structure-property relationships and were not always in accordance with theoretical calculations. New models based on multiple stages (Strobl 2006) and spinodal decomposition (Olmsted *et al.* 1998) were proposed, however, with only little experimental evidence. Especially for material systems and crystallization conditions that are more complex (flow, pressure, blends, additives, etc.) a detailed understanding of the interplay between local molecular dynamics, the structural buildup at the meso-scale, and macroscopic material properties would be very important for clarifying the mechanism of polymer crystallization. In all of these aspects, new characterization techniques are needed to achieve better insight into structure-property relationships, the underlying mechanisms, and will ultimately lead to higher product qualities of new or recycled materials. In combination with computer simulations they will be key to proof or disproof the concepts under discussion, and they will help to find rules in the controlled design of semi-crystalline materials.

Hyphenated rheology techniques

In order to further understand the process of polymer crystallization, knowledge on the relationships between local molecular dynamics, structural buildup, and macroscopic material behavior under quiescent and flow conditions is required. For this task, hyphenated rheology techniques are promising analytical tools as they combine information on the macroscopic flow and deformation behavior of soft matter with insights into structural and dynamic features on different length and time scales. Furthermore, they can be used to change the state of the material, permitting the study of polymer crystallization under well-defined flow conditions. The

concept of *hyphenation* has the advantage of simultaneous measurements and the potential to identify correlations between two experimental techniques that are otherwise not accessible (Figure 1.4). The correlation from separate experiments is usually not possible due to the strong temperature dependence of polymer crystallization, leading to different experimental conditions depending on the sample size, shape, and experimental design. The correlated information obtained using hyphenated rheology techniques can be analyzed quantitatively, providing a substantial gain in knowledge that will help to elucidate the mechanism of polymer crystallization, the hardening behavior, and the interplay between molecular features and the buildup of semi-crystalline morphologies.

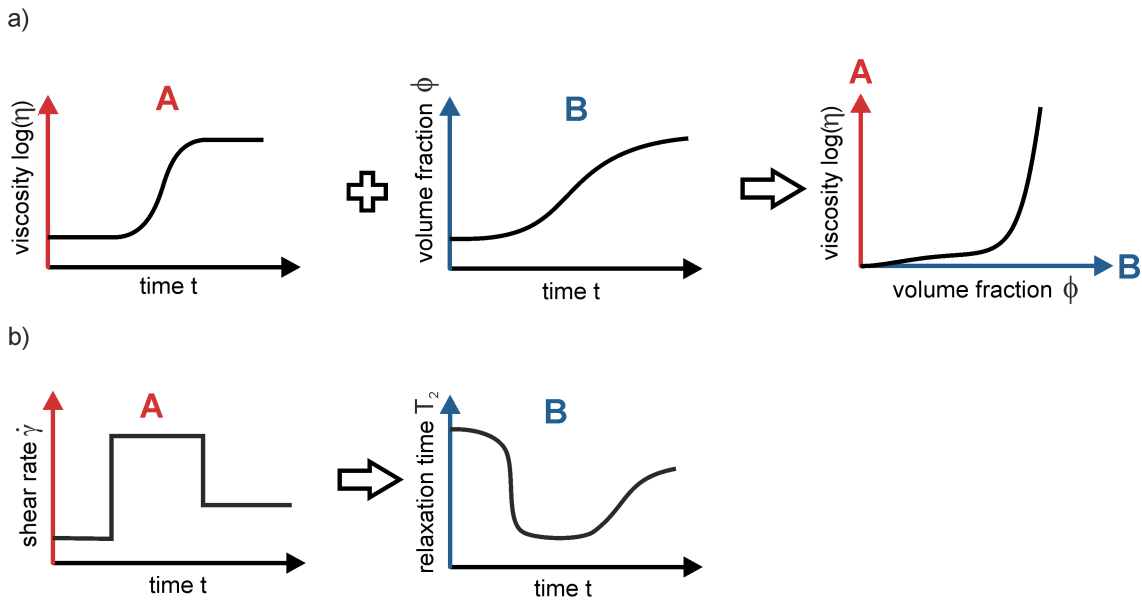


Figure 1.4: Two main types of hyphenated experiments: simultaneously acquired sets of data from techniques A and B can be correlated (a). The response of B on a parameter change in A can be determined and quantified (b).

Three main types of hyphenated rheology techniques can be distinguished that were designed to characterize a) sample morphology, b) chemical structure, or c) molecular dynamics while performing rheological experiments. The largest group are RheoOptics/Microscopy techniques, which were used for the study of suspensions (Champion *et al.* 1996; Paulin *et al.* 1997), liquid crystals (Berghausen *et al.* 1997; Onogi and Asada 1980; Walker *et al.* 1997), polymer solutions (Bossart and Oettinger 1995; Kume *et al.* 1997; Pathak and Hudson 2006), block copolymers (Chen and Kornfield 1998; Kannan and Kornfield 1994), and crystallization phenomena (Kumaraswamy *et al.* 1999; Mackley *et al.* 2000; Pogodina *et al.* 1999; Scelsi and Mackley 2008). Usually, only set-ups with visible light sources (potentially monochromatic and coherent) are referred to as RheoOptics. Closely related are tomography set-ups using nuclear magnetic resonance (NMR) (Callaghan 1999; Callaghan and Gil 2000; Kilfoil and Callaghan 2000; Callaghan 2006; Galvosas and Callaghan 2006; Callaghan 2008) as well as scattering techniques based on X-rays (Hamley *et al.* 1998; Somani *et al.* 2000; Castelletto *et al.* 2001, 2005; Polushkin *et al.* 2005; Meins *et al.* 2012; Stellamanns *et al.* 2013)

or neutrons (Maranzano and Wagner 2002; Egres *et al.* 2006; Liberatore *et al.* 2006; Eberle and Porcar 2012). Hyphenations of rheology and spectroscopy techniques were used to obtain *in-situ* information on the chemical structure of polymers, liquid crystals, or fats during chemical reactions, gelations, or crystallization while monitoring their rheological behavior. The employed set-ups were based on IR spectroscopy (Boulet-Audet *et al.* 2011; Auriemma *et al.* 2015; Mascia *et al.* 2015; Zuppari *et al.* 2017), Raman spectroscopy (Chai *et al.* 1995; Chevrel *et al.* 2012; Kotula *et al.* 2016), or NMR spectroscopy (Grabowski and Schmidt 1994; Lukaschek *et al.* 1995; Schmidt 2006; Ohgo *et al.* 2008; Medronho *et al.* 2010). Techniques that characterize molecular dynamics and consequently probe local molecular conformation were also combined with rheology. They can be used to investigate the origins of macroscopic flow behavior in e.g., polymer melts and the connections between applied flow and molecular conformation. Such set-ups were designed based on dielectric spectroscopy (Capaccioli *et al.* 2007; Höfl *et al.* 2006; Khastgir and Adachi 2000; Meins *et al.* 2012; Watanabe *et al.* 1998, 1999) and NMR relaxometry (Kahle *et al.* 2008; Meins *et al.* 2011; Rätzsch *et al.* 2017; Rätzsch *et al.* 2016). Further hyphenated rheology set-ups that do not belong to any of the three groups were built based on calorimetry (Block *et al.* 2013; Janssens *et al.* 2009, 2010; Kiewiet *et al.* 2008), dilatometry (Bruker and Lodge 1985; Bruker 1986; Yemelyanov 1990), or electrical conductivity (Helal *et al.* 2016). Some of the set-ups discussed above contain shear cells that allow for the application of flow, but do not provide rheology data.

Thesis Outline

In this thesis, new hyphenated characterization techniques were employed to study the crystallization behavior of synthetic polymers under quiescent and flow conditions. The experimental set-ups were based on commercial rheometers that allowed the correlation of rheological data with additionally obtained *in-situ* information on different length and time scales. Namely, three combinations of rheology *plus* nuclear magnetic resonance (NMR), small angle X-ray scattering (SAXS), and optical microscopy were selected to perform *in-situ* studies on the molecular dynamics, nano-scale morphology, and microstructure (Figure 1.5). In order to lay the proper groundwork, the temperature-dependence of molecular dynamics in semi-crystalline polymers was studied using standalone NMR and compared against other established characterization techniques.

The following main research questions were addressed:

- How do crystallizing polymer melts rigidify under quiescent and flow conditions?
- What is the temperature-dependence of molecular dynamics in semi-crystalline polymers, and can mobility provide a valuable measure of polymer crystallinity?
- How does shear flow during crystallization affect the nano-scale morphology and microstructure of semi-crystalline polymers?
- What is the mechanism of polymer crystallization, especially during the nucleation period and under shear flow?

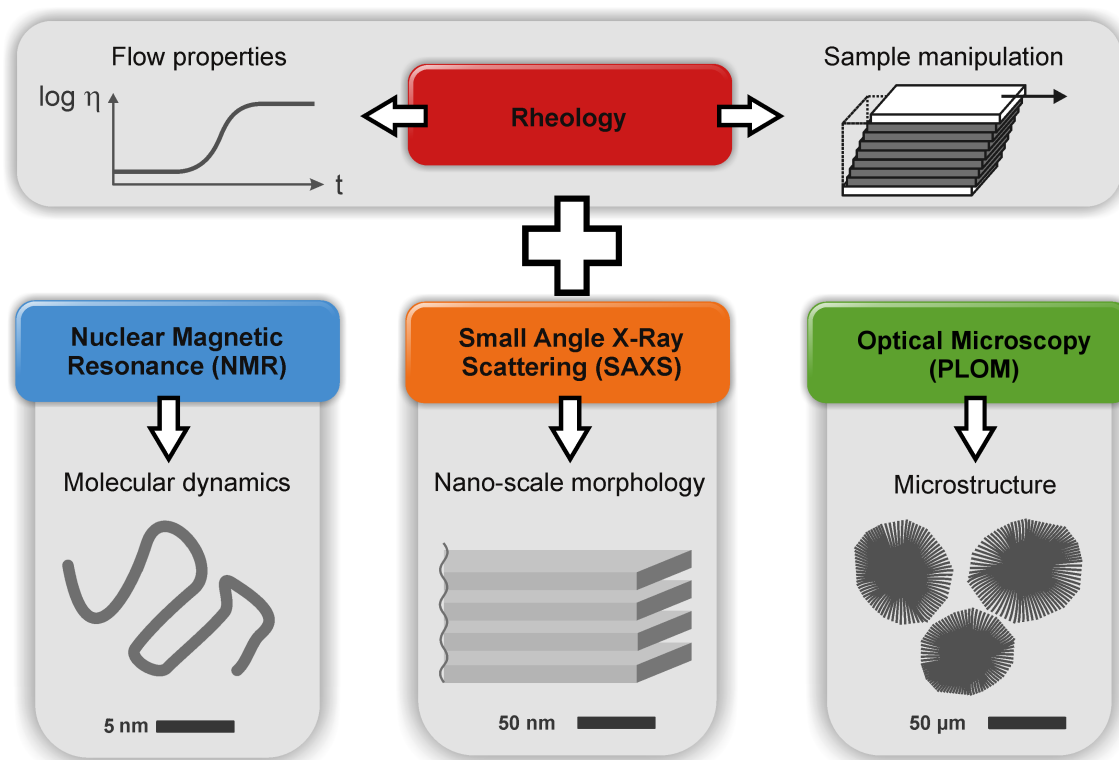


Figure 1.5: By combining rheology and nuclear magnetic resonance (NMR), small angle X-ray scattering (SAXS), and optical microscopy into hyphenated rheology set-ups, we could study *in-situ* molecular dynamics, nano-scale morphology, and microstructure during polymer crystallization. Furthermore, rheology can be used to change the sample state and measure the implications on the dynamics and morphology of the material as captured by the other experimental techniques.

Our research questions were tackled by...

- evaluating the temperature-dependent molecular dynamics of crystallizing polymers using NMR, and comparing the information on the degree of crystallinity and crystallization kinetics against X-ray diffraction (XRD) and differential scanning calorimetry (DSC);
- studying the interplay of the molecular dynamics and rheology during polymer crystallization using RheoNMR;
- investigating the buildup of nano-scale morphology during polymer crystallization and its correlation with the macroscopic flow behavior via RheoSAXS;
- identifying correlations between the microstructure and rheology during polymer crystallization using optical RheoMicroscopy;
- performing *ex-situ*-scanning electron microscopy (SEM) and optical microscopy on the recovered specimen to further obtain information on the relationship between applied flow and morphology of semi-crystalline polymers.

The obtained experimental results were compared against other works and discussed in the context of theoretical models in order to develop a comprehensive understanding of polymer crystallization under quiescent and flow conditions.

2 Fundamentals of Synthetic Semi-Crystalline Polymers

2.1 Introduction

In this chapter, a brief overview of the main types of synthetic semi-crystalline polymers, their synthesis, and their properties will be given based on books by Odian (2004); Mark (2007); Elsner *et al.* (2012); Ward and Sweeney (2012). For the main part of this thesis, isotactic polypropylene was chosen as the material of investigation. Consequently, its synthesis, morphology and properties will be discussed in more detail based on Karger-Kocsis (1994, 2012).

2.2 Types of semi-crystalline polymers

Semi-crystalline polymers can be divided into three groups: commodity, engineering, and high performance materials (Figure 2.1). The production volume is inversely proportional to the price: commodity plastics such as polyolefins are sold at 1 – 2 €/kg with an annual production volume of 150 million tons (2015), whereas high performance materials such as polyaryletherketones are sold at ~100 €/kg with an annual production of 5.000 tons (2015). The class of engineering polymers contains polyamides and polyesters that can be tailored precisely to the needs of the individual application, e.g., injection molding or fiber spinning. Furthermore, specialty polymers such as fluoropolymers and polyimides exhibit high chemical and thermal resistance together with desirable dielectric properties that make them valuable materials for applications in electronics and construction under demanding conditions.

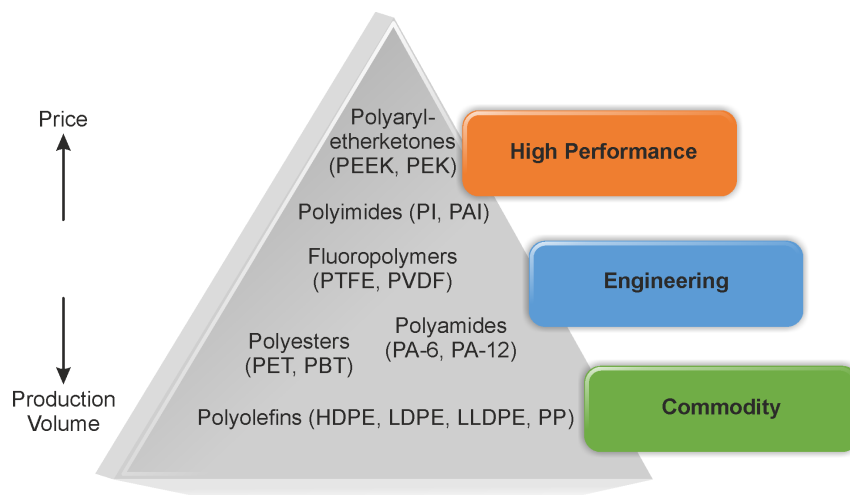


Figure 2.1: Classification of semi-crystalline polymers as commodity, engineering, and high performance materials. Prices range from 1 – 100 €/kg depending on the polymer type (Elsner *et al.* 2012).

For semi-crystalline polymers, solid properties are strongly connected to the way the material was processed. In Figure 2.2, mechanical properties of bulk samples and fibers are compared against other materials such as glass or steel. The tensile modulus increases by up to two orders of magnitude for e.g., ultra-high molecular weight polyethylene (UHMWPE) in the case of fibers compared to the bulk material, thereby exceeding the tensile modulus of steel. Similarly, the elongation at break values decrease substantially to below 10%. This enormous bandwidth of solid properties depending on the processing method is an important argument for the wide application of semi-crystalline polymers.

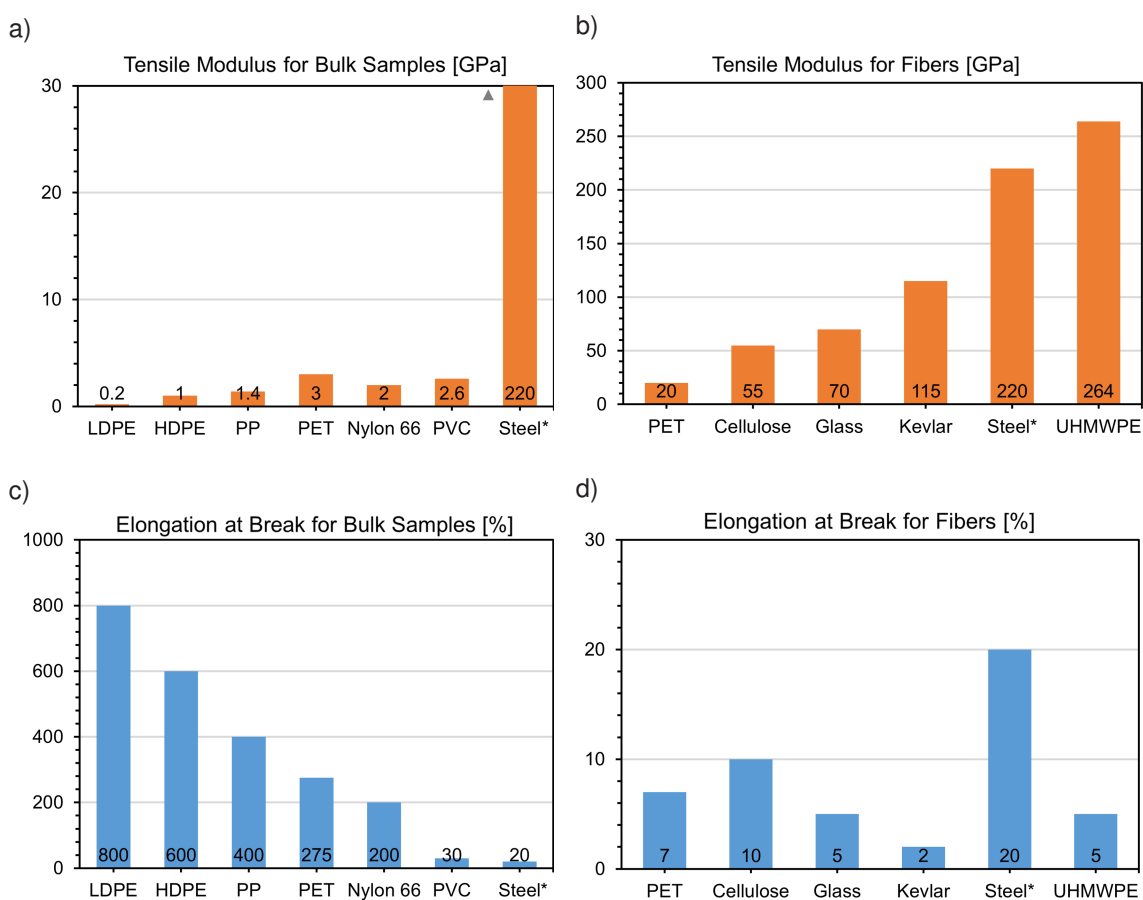


Figure 2.2: Mechanical properties of semi-crystalline polymers at room temperature compared against other materials (Van Krevelen and Te Nijenhuis 2009). Tensile and Young's modulus for bulk samples (a) and fibers (b). Elongation at break for bulk samples (c) and fibers (d). (*) Steel: X2CrTi12, always bulk sample.

Polyolefins

Semi-crystalline polymers synthesized from olefinic monomers such as ethylene or propylene are cheap, chemically inert, and easy to process. However, their synthesis requires either harsh conditions (high pressure, temperature) or more sophisticated synthesis methods such as coordination polymerization. In Figure 2.3, the main types of olefinic polymerizations are shown. The free radical polymerization of ethylene leads to a long-chain branched topology

with a relatively low degree of crystallinity of $\sim 40 - 50\%$ (low-density polyethylene, LDPE). Coordination polymerization using Ziegler-Natta catalysts is frequently used to obtain high-density polyethylene (HDPE) and isotactic polypropylene. The mechanism and alternatives to conventional ZN catalysts will be discussed in section 2.3.

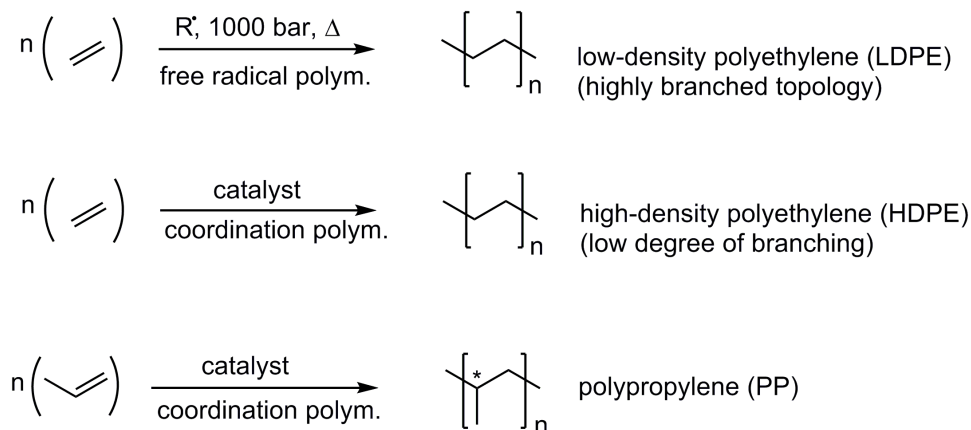


Figure 2.3: Synthesis of semi-crystalline polyolefins by radical and coordination polymerization.

Polyolefins are used in many relatively low-cost applications such as packaging, household appliances, housings, and construction. As the glass transition temperatures are well below room temperature, they show high impact resistance and toughness. Their chemical inertness leads to a long lifetime of molded parts, films or fibers. The downside is a low bio-degradability and persistence in nature, leading to a substantial issue for aquatic life (Andrady 2011).

Polyesters

Polyesters show high tensile strength when spun into fibers, and are frequently used in textile industry. As their glass transition temperature is usually above room temperature, they are less impact-resistant compared to polyolefins, but show a relatively high ductility due to their low crystallinity of $< 40\%$. The most important representative is polyethylene terephthalate (PET), which is synthesized by a polycondensation reaction from ethylene glycol and terephthalic acid following a step-growth mechanism (Figure 2.4a). Due to its high glass transition temperature of $+70^\circ\text{C}$, it can be quenched to room temperature without developing substantial crystallinity. A second derivative is polybutylene terephthalate (PBT), frequently selected for housings or fibers. A special polyester is polylactide (PLA), which is more and more used as a biodegradable alternative to polyolefins in injection molding and film blowing. Another application of PLA is 3D-printing as it shows low warping and fast crystallization. Its synthesis can either be carried out by direct condensation using lactic acid or by a ring-opening polymerization from the cyclic di-ester (Figure 2.4b).

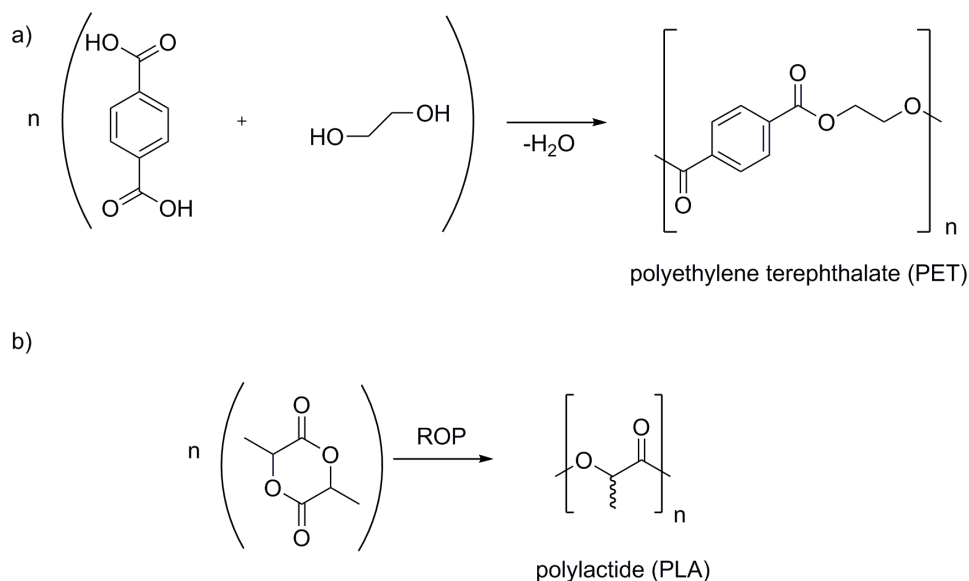


Figure 2.4: Synthesis of polyesters by polycondensation or ring-opening polymerization (ROP).

Polyamides

Similarly to polyesters, polyamides are mostly used for fibers in textile industry. Due to their structural versatility depending on the length of the respective amine and carboxylic acid blocks, material properties can be fine-tuned for each individual application. The most important representatives of polyamides (Nylons) are polyamide 6–6, polyamide 6, polyamide 6–10, and polyamide 6–12, which are synthesized either by polycondensation reactions from the respective amines and carboxylic acids or chlorides (Figure 2.5a), or by a ring-opening polymerization as in the case of PA-6 from ϵ -caprolactam (Figure 2.5b).

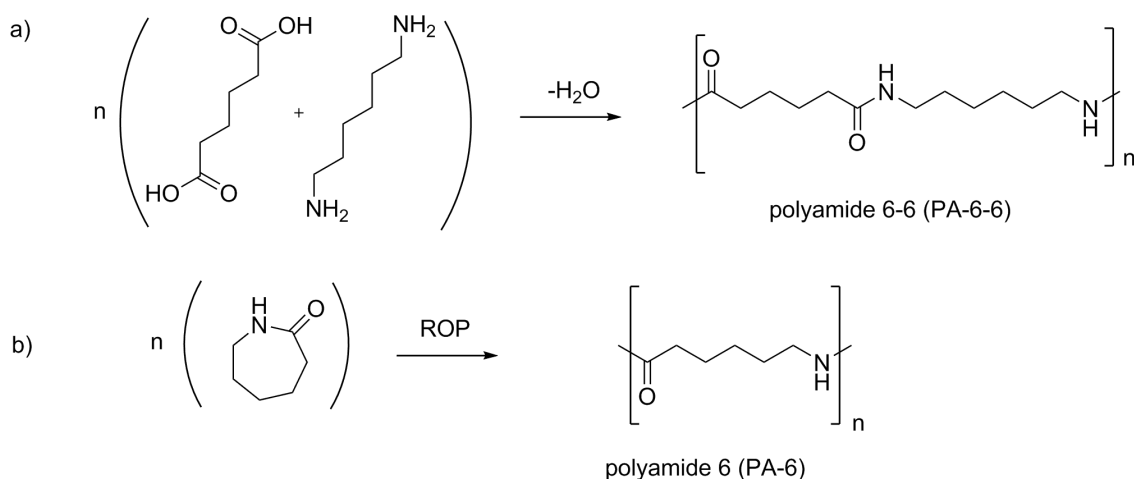


Figure 2.5: Synthesis of polyamides by polycondensation or ring-opening polymerization (ROP).

Besides aliphatic derivatives, also aromatic polyamides –so-called aramides– can be synthesized. The most important representative is sold under the trade name Kevlar (polypara-

phenylene terephthalamide) and has an extremely high tensile strength and melting point due to significant hydrogen bonding between multiple amide groups. Kevlar is used for body armor fabric, tires, and in reinforced composites.

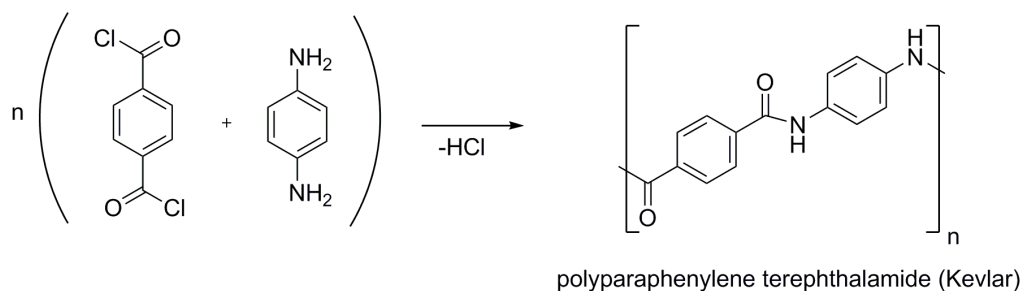


Figure 2.6: Synthesis of poly(paraphenylene terephthalamide) (Kevlar) by polycondensation.

Fluoropolymers

Fully or partially fluorinated olefins can be polymerized by free radical polymerization at relatively low pressures. The most important ones are polytetrafluoroethylene (PTFE, Teflon), polyvinylidene fluoride (PVDF, Kynar), polychlorotrifluoroethylene (PCTFE, Kel-F). In Figure 2.7, the synthesis of PTFE is shown. All fluoropolymers show extremely high chemical and thermal resistance. Therefore, they are used as containers, tubings, or sealings for hazardous materials. Furthermore, they are used as electrical insulators due to their low dielectric permittivity. PTFE is used frequently as a coating material for kitchen tools due to its non-stick properties. Expanded PTFE films (Gore-Tex) shows a high permeability for moisture and is used for weatherproof jackets.



Figure 2.7: Synthesis of polytetrafluoroethylene (PTFE, Teflon) by free radical polymerization.

The persistence of fluoropolymers together with potential CMR¹ decomposition products represent considerable environmental issues. Furthermore, the disposal of fluoropolymers is cumbersome as hazardous hydrofluoric acid might be produced during their decomposition.

Other synthetic semi-crystalline polymers

The class of polyimides contains aliphatic and aromatic derivatives. One of the most important representatives is poly(oxydiphenylene-pyromellitimide) (Kapton, Figure 2.8). Because of its high temperature resistance (short times >400 °C) it is used in high-temperature applications for electronics, spacecrafts, and airplanes. Additionally, Kapton is used in X-ray transmissive windows (see also chapter 7).

¹ CMR = carcinogenic, mutagenic, reprotoxic

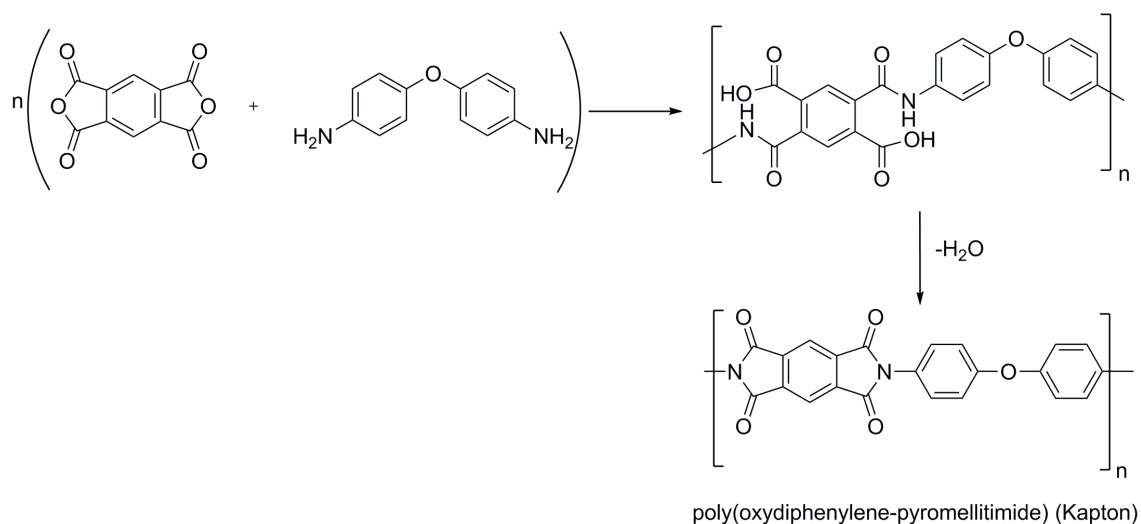


Figure 2.8: Synthesis of poly(oxydiphenylene-pyromellitimide) (Kapton) via a two-step reaction.

Polyaryletherketones such as polyetheretherketone (PEEK), polyetherketone (PEK), or polyetherketoneetherketoneketone (PEKEKK) with high melting points of $>300\text{ }^\circ\text{C}$ are another class of high-temperature thermoplastics. They are chemically robust, stiff, and excellently machinable. Applications of polyaryletherketones include bearings, piston parts, or valves.

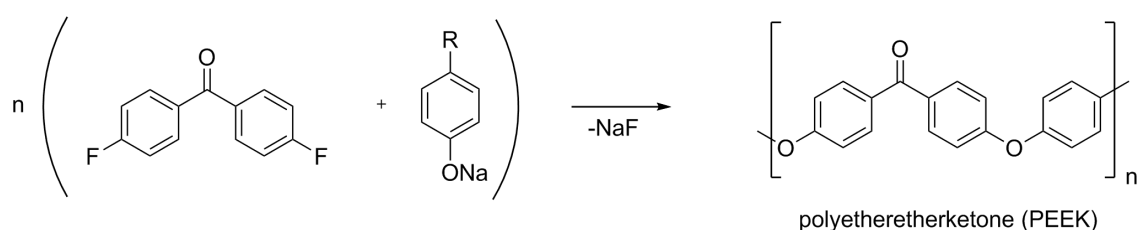


Figure 2.9: Synthesis of polyetheretherketone (PEEK) by polycondensation.

Another relevant synthetic semi-crystalline polymer is polyoxymethylene (POM, Delrin) and in its copolymers with other acetal components (Ultraform, Celcon). Its synthesis is based on ionic polymerization as shown in Figure 2.10. Due to its low friction coefficient and its resistance to creep, fatigue, and abrasion, it is used e.g., for gears, bearing and fittings.

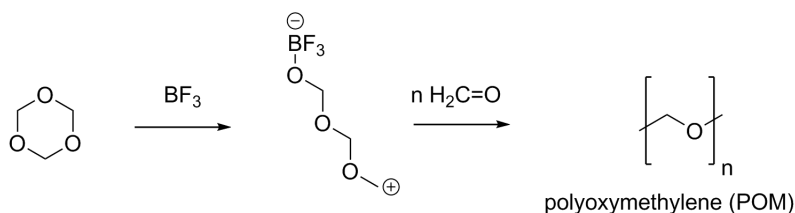


Figure 2.10: Synthesis of polyoxymethylene (POM) by cationic polymerization from (trioxane).

2.3 Polypropylene: synthesis, morphology, and properties

Polypropylene is the second most produced semi-crystalline polymer with a large variety of applications in injection molding and fiber spinning. Its impact-resistance, inertness, and recyclability make it an ideal polymer for packaging, construction, and textiles. It was selected as the main material of investigation in this thesis, because of its relevance, slow crystallization behavior, and well-defined chemical structure / topology. On the following pages, the synthesis of polypropylene, its morphological features, and properties will be discussed in more detail based on (Karger-Kocsis 2012; Baugh and Canich 2007; Kaminsky 2013a,b).

Synthesis

Polypropylene is chemically synthesized by a coordination polymerization of propylene using organometallic catalysts. Initial works were carried out by Ziegler *et al.* (1955) at the Max Planck Institute for Coal Research in Mülheim, Germany and by Natta *et al.* (1955) at the Politecnico di Milano, Italy, who both received the Nobel prize for their works in 1963. They discovered that a combination of titanium chloride and triethylaluminium can be used to effectively polymerize olefins at low pressures (Figure 2.11). K. Ziegler focused on the polymerization of ethylene, whereas G. Natta applied the catalytic system to different α -olefins and discovered its high stereo-selectivity.

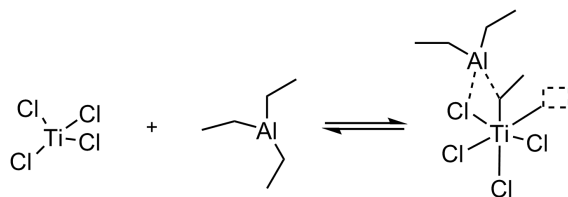


Figure 2.11: Ziegler-Natta catalyst: titanium chloride and triethylaluminium (Kaminsky 2013a).

The mechanism of coordination polymerization using Ziegler-Natta (ZN) catalysts was described in detail by Cossee (1964); Arlman (1964); Arlman and Cossee (1964). In Figure 2.12, the main mechanistic steps are shown for the polymerization of propylene.

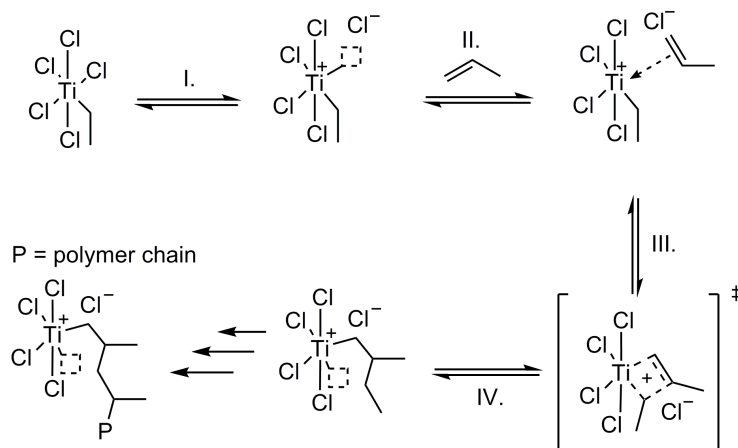


Figure 2.12: Mechanism of coordination polymerization using a ZN catalyst (Cossee 1964).

The steps are:

- I. Ion-pair formation;
- II. Addition of monomer;
- III. 4-membered ring transition state
- IV. Chain extension

Upon complete polymerization, the catalyst is hydrolyzed using alcohols. Ziegler-Natta catalysts are known to be regioselective, i.e., the insertion of α -olefins follows a strictly head-to-tail-sequence. The stereo-selectivity of Ziegler-Natta catalysts is mainly based on chain end control as the stereogenic carbon atom of the previously inserted propylene monomer directs the insertion of the next monomer. Despite the great success of the coordination polymerization at low pressures using ZN catalysts, industry demanded for homogeneous catalyst systems that would allow a simpler purification and removal of the catalyst. In the 1980's, the group of W. Kaminsky at the University of Hamburg, Germany developed metallocene-based homogeneous catalyst systems that showed equal catalytic activity as their heterogeneous counterparts (Kaminsky *et al.* 1985; Brintzinger *et al.* 1995; Kaminsky 2013b). In Figure 2.13, a frequently used catalyst is shown together with typical reaction conditions (Spaleck *et al.* 1994). The activation of the catalyst is carried out by adding methylaluminoxane (MAO), which is a partially hydrolyzed derivative of triethylaluminium.

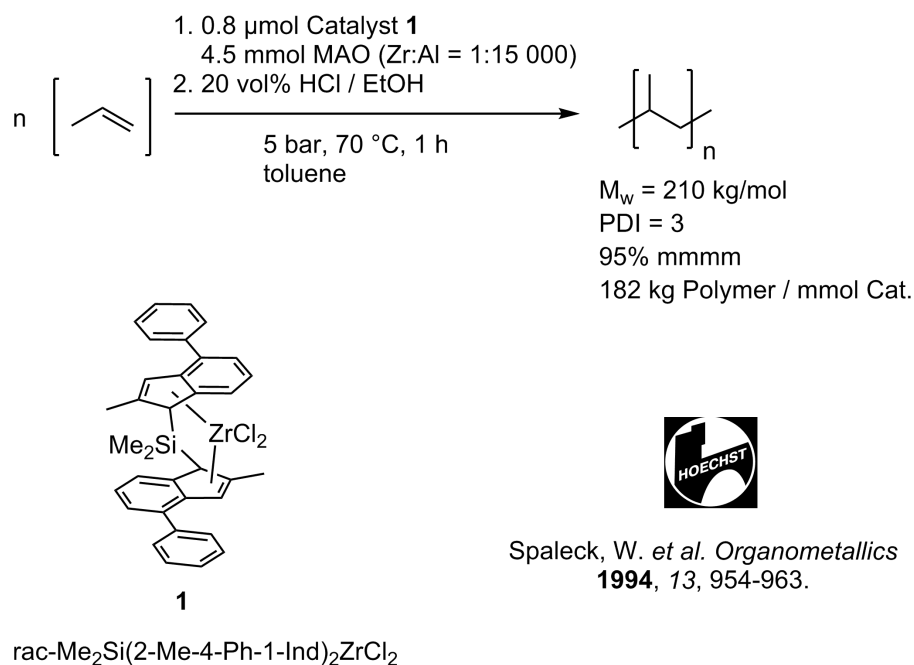


Figure 2.13: Example of a metallocene catalyst and reaction conditions for the polymerization of propylene (Spaleck *et al.* 1994).

The shared structural feature of many metallocene catalysts is the C2 symmetry generated by an *ansa*-bridging group (here: $-\text{Me}_2\text{Si}$). Different from the heterogeneous ZN catalysts, this

symmetry leads to enantiomorphic site control, i.e., stereo-selectivity is achieved by a preferential orientation of the monomer with respect to the stereogenic catalyst. The mechanism of metallocene-catalyzed olefin polymerizations is similar to that of the heterogeneous ZN catalysts (Figure 2.14).

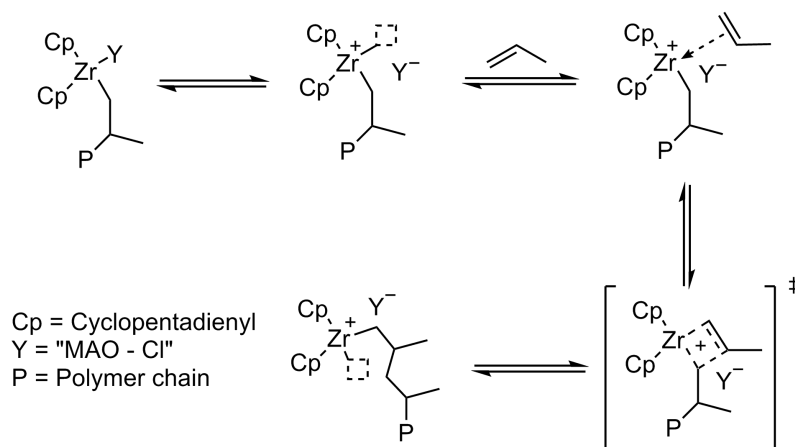


Figure 2.14: Mechanism of coordination polymerization using a metallocene catalyst.

Other than the heterogeneous ZN catalysts, metallocene catalysts tend to introduce regio defects (Resconi *et al.* 2000). The most frequently encountered defect is a 2,1-erythro insertion (see Figure 2.15), which can be determined and quantified by ^{13}C -NMR (Busico and Cipullo 2001). Such regio defects have strong implications on the crystallization behavior as they disturb the formation of the crystallographic lattice and lead to modified material properties (De Rosa *et al.* 2005; Meer *et al.* 2015).

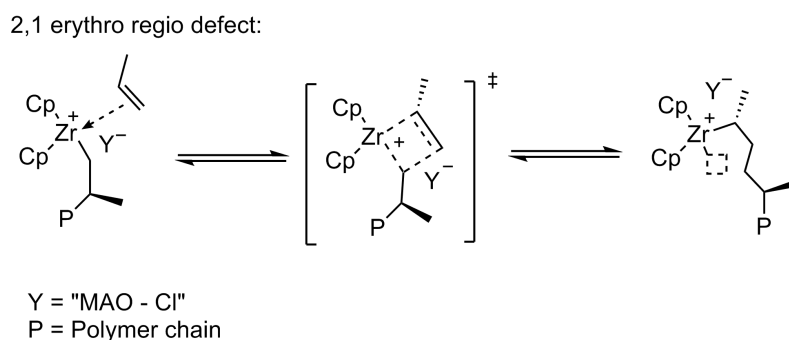


Figure 2.15: Creation of 2,1-erythro defects during a metallocene-catalyzed polymerization of propylene.

In recent years, so-called post-metallocene catalysts were developed that were based on large organometallic complexes of group 4 metals (Ti, Zr, Hf). The ligands contained aromatic heterocycles (e.g., pyridine) and were designed to control the stereo- and regio-selectivity. For a detailed discussion on the large number of catalysts for stereoselective olefin polymerization, see Baugh and Canich (2007).

Morphology: from the chain to unit cells, lamellae, and spherulites

The morphology of semi-crystalline polymers follows a highly hierarchical pattern: chain segments build up a crystallographic unit cell that is part of large extending sheets (lamellae), which themselves form superstructures such as so-called spherulites. For polypropylene the hierarchical morphology is shown in Figure 2.16.

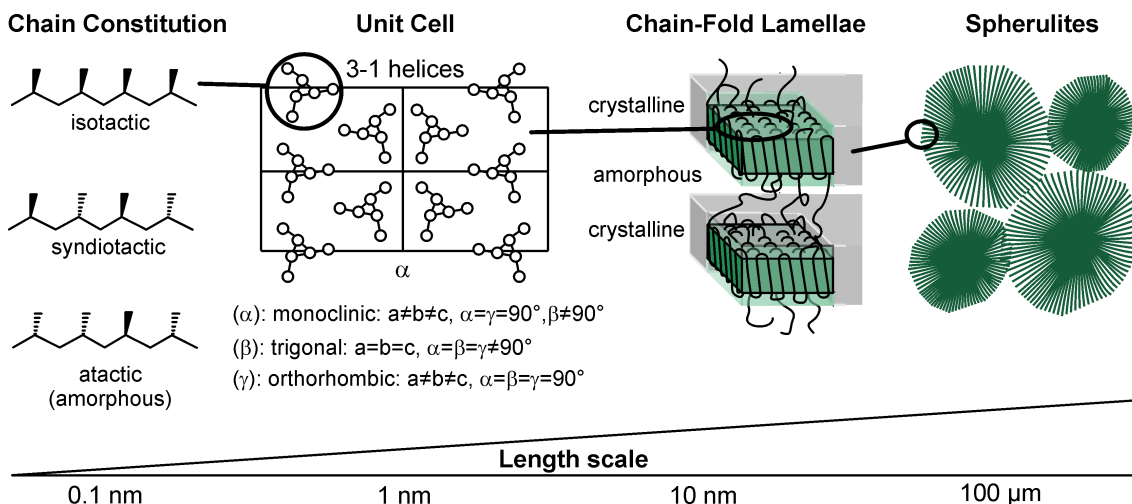


Figure 2.16: Hierarchical morphology of crystallized polypropylene: 3-1 helices build up a unit cell that is part of a chain-fold lamellae, which themselves form larger superstructures (spherulites).

Based on the two main chain constitutions of polypropylene (isotactic and syndiotactic) unit cells are formed by a conformational chain twist into 3-1 helices. The polymorphs of polypropylene are classified as α , β , and γ with α being the predominantly formed polymorph for ZN-catalyzed i-PP under quiescent conditions (Piorkowska and Rutledge 2013). The trigonal β -polymorph is obtained by incorporating specific nucleating agents or by the application of flow (Meille *et al.* 1994; Varga 2002; Kotek *et al.* 2002; Huo *et al.* 2004). The γ -form of isotactic polypropylene has an orthorhombic unit cell with non-parallel chain-packing (Meille and Brückner 1989) and is frequently found in metallocene-catalyzed regio-defective i-PP grades (Thomann *et al.* 1996).

On the second hierarchy level, the characteristic structural feature of chain-fold lamellae is found, which is an important difference to small molecules. The size of polymeric crystals is limited in one dimension to some tens of nanometers. However, the lateral lamellar dimensions can go up to several hundreds of microns, depending on the crystallization conditions. The incorporated chains are most probably tilted as recently discussed by Fritzsching *et al.* (2017) to decrease the density at the interface. Lamellae grow radially from a nucleation center and form the shown sphere-like superstructures. These spherulites are being classified as negative, positive, mixed, or ring-like depending on the orientation of the lamellae and their twist (Varga 1992). In Figure 2.17, a series of scanning electron micrographs is shown for a quiescently crystallized isotactic polypropylene. The sample was etched (oxidized) using an acidic permanganate solution to remove the amorphous fraction of polymer chains. The lamel-

lar substructure shows another feature of isotactic polypropylene – so-called cross-hatching. This phenomenon describes the splaying of lamellae orthogonal to the primary growth direction (daughter lamellae). This secondary crystallization process is thought to be induced by a nucleation of new lamellae from the methyl groups standing out from the 3-1 helices of parent lamellae (Piorkowska and Rutledge 2013).

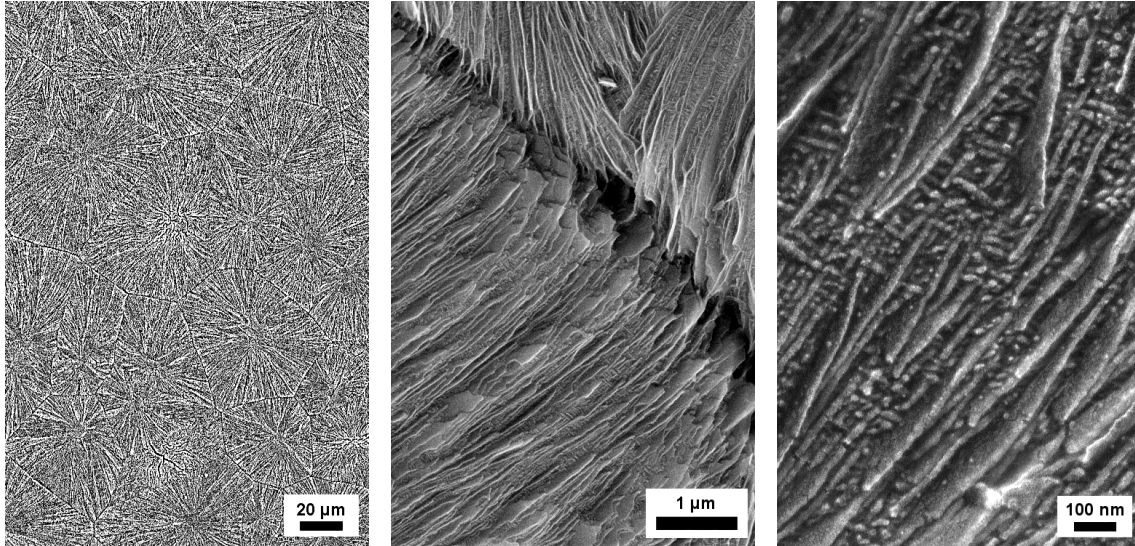


Figure 2.17: Scanning electron micrographs of etched isotactic polypropylene crystallized under quiescent conditions. The spherulitic superstructure consisted of lamellae and showed cross-hatching.

Properties

The properties of polypropylene are temperature- and molecular-weight-dependent and differ depending on the sample preparation. Some characteristic thermal, mechanical, and electrical properties of a standard isotactic polypropylene grade at room temperature are given in Table 2.1 based on data from Elsner *et al.* (2012). Usual molecular weights of Ziegler-Natta i-PP grades are on the order of $M_w = 200 - 300$ kg/mol (polydispersity $D = 3 - 4$).

Property	Unit	Value
Density	g/cm ³	0.91
Glass transition temperature	°C	-10
Melting range	°C	160 – 170 °C
Torsional stiffness	MPa	480
Hardness (Shore) D	–	74
Impact strength	mJ/mm ²	20
Thermal conductivity	W/mK	0.22
Dielectric permittivity	10 ⁶ Hz	2.25

Table 2.1: Properties of an i-PP homopolymer at room temperature based on Elsner *et al.* (2012).

In Figure 2.18, a stress-strain curve measured at room temperature and the temperature-dependence of the G modulus are shown again for a standard isotactic polypropylene grade. As at room temperature the material is above its glass transition, it starts to flow at relatively low strains and can be elongated to several hundred percent before the material ruptures. The temperature-dependence of the G modulus (see section 4.1) shows a plateau-like behavior up to the glass transition temperature of $-10\text{ }^{\circ}\text{C}$, then a linear decrease on a logarithmic scale, and finally a steep decrease at the nominal melting point of $\sim 165\text{ }^{\circ}\text{C}$.

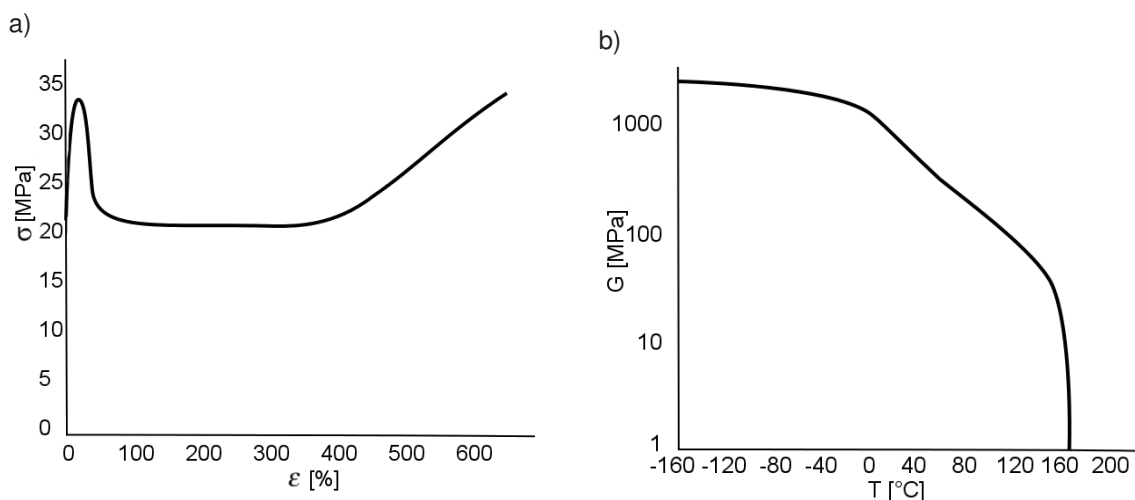


Figure 2.18: Stress-strain curve at room temperature (a) and temperature-dependence of the G modulus (b) for an i-PP homopolymer. Adapted from Elsner *et al.* (2012).

In many cases, polypropylene is mixed with fillers, nucleating agents, and processing additives to alter the properties and enhance processability. Nucleating agents play an important role in manufacturing of polypropylene parts as they decrease turbidity, generate impact-resistance, and raise the possible processing temperature for injection molding. There are two main groups of nucleating agents: non-polymer-soluble and polymer-soluble substances. The first group consists of inorganic and organic small molecules such as talc, sodium benzoate or phosphates which were empirically found to induce nucleation, but can lead to odor, yellowing and aging. Polymer-soluble nucleating agents are either sorbitol-based (e.g., Milliken Millad 3988 / DMDBS, Bernland *et al.* (2009); Kristiansen *et al.* (2003, 2005, 2009)) or 1,3,5-benzene tricarboxamides (e.g., BASF Irgaclear XT 386). 1,3,5-benzene tricarboxamides are very effective nucleating agents and were structurally optimized with regard to haze and clarity by modification of the alkyl groups (Bernland *et al.* 2016). The discotic structure permits a supramolecular organization into columnar structures / fibers, which are stabilized by hydrogen bonding. During cooling of a polypropylene melt, the nucleating agent precipitates and forms a 3D-network of fibers with a high surface area compared to insoluble bulk nucleating agents. Fillers such as silica or titania can have a similar nucleating effect when their surfaces are hydrophobically modified using chlorosilanes. For further information on the different types of materials that can be incorporated into the neat polypropylene matrix see Karger-Kocsis (2012).

2.4 Selected materials for the study of polymer crystallization

The main material of investigation in this thesis was a Ziegler-Natta polypropylene grade i-PP-1 (Repsol Isplen PP070G2M). Additional experiments were performed on a metallocene-catalyzed polypropylene grade i-PP-2 (LyondellBasell Metocene HM562P) in order to unravel the effect of regio-defects on the crystallization behavior. The potential of NMR relaxometry to determine polymer crystallinity and crystallization kinetics was studied using a broad range of commercially relevant polymers. In Table 2.2, molecular weights, polydispersities, glass transitions temperatures, and peak melting temperatures are shown for all materials. The samples contained standard anti-oxidants, but no nucleating agents. PA-6 and PET were dried at 70 °C under vacuum for 7 days to remove residual moisture. The tacticity of the polypropylenes was determined to be ~94% *mmm*, and sample i-PP-2 contained 1 mol% of 2,1-erythro regio defects (¹³C-NMR – Appendix A). The ZN grade i-PP-1 crystallizes in the α -form, whereas the metallocene-catalyzed i-PP-2 showed γ -form crystallization and a higher nucleation density (XRD and PLOM data in Appendix A). High-temperature gel permeation chromatography at 145 °C was done using tri-chloro-benzene as the eluent for i-PP, HDPE, and LDPE. Standard GPC at room temperature was performed using respective calibration standards for t-PI and PS in tetrahydrofuran, and for PET and PA-6 in hexafluoroisopropanol.

Sample Code	Polymer Grade	Supplier	M_w (\bar{D}) [kg/mol]	T_g [°C]	T_m [°C]
i-PP-1	Isplen PP070G2M (batch 1)	Repsol	246 (2.7)	-10	168
i-PP-1'	Isplen PP070G2M (batch 2)	Repsol	282 (3.4)	-10	168
i-PP-2	Metocene HM562P	LyondellBasell	202 (1.9)	-10	161
HDPE	N/A* (batch 1)	LyondellBasell	182 (11)	-120	135
HDPE'	N/A* (batch 2)	LyondellBasell	155 (15)	-120	134
LDPE	Lupolen 1840H	LyondellBasell	135 (11)	-120	112
PA-6	Ultramid B27E	BASF	61.8 (2.1)	+40	226
PET	Xpure V004	Invista	50.2 (2.0)	+70	261
t-PI	N/A (>99% trans)	Sigma Aldrich	129 (4.6)	-60	65
PS	N/A (amorph.)	Sigma Aldrich	209 (1.9)	+105	N/A
PBMA	N/A (amorph.)	Sigma Aldrich	205 (2.2)	+21	N/A

Table 2.2: Molecular weight distributions (GPC), glass transition temperatures (Mark 2007), and peak melting temperatures (DSC) for all polymers investigated. (*) Research grades.

The influence of nucleating agents on polymer crystallization was studied using compounds of i-PP-1' (batch 2) with 250, 500, 750, 1500 ppm of N, N', N''-tris(3-methylbutyl)-1,3,5-benzene tricarboxamide (DH677), which were prepared by our collaborators Dr. K. Kreger and D. Kremer in the group of Prof. H.W. Schmidt (University of Bayreuth, Germany) using a lab-scale twin-screw extruder. Furthermore, the effect of fillers on the crystallization behavior was analyzed using compounds of i-PP-1 with 1 – 5 wt% fumed silica (CAB-O-SIL TS-530, Cabot Corporation, Alpharetta, USA), which were compounded by Dr. J. Palacios in the group of Prof. A. Müller (Universidad del País Vasco, San Sebastián, Spain).

3 Theory of Polymer Crystallization

3.1 Introduction

Early works on the thermodynamics, kinetics, and underlying mechanism of polymer crystallization have been carried out by Hoffman and Lauritzen (1961); Hoffman and Weeks (1962); Hoffman *et al.* (1969), Mandelkern *et al.* (1954); Mandelkern (1964), Keith and Padden Jr (1963) and Keller and Mackley (1974). They made important theoretical contributions that helped to rationalize experimental data and could accurately describe phenomena such as lamellar thickening and the melting point depression in polymeric crystals. The spherulitic growth of chain-fold lamellae (Figure 3.1) was described in great detail by the groups of Hoffman and others. At the heart of classical nucleation and growth theories is a thermally activated two-step process of the formation of thermodynamically stable nuclei and their growth over time. However, classical nucleation theories are only partially applicable to polymer melts as the complex macromolecular nature with their long chain structure, entanglements, and their reptating motion is not sufficiently incorporated into these models. In recent years, new concepts were proposed, namely the spinodal decomposition model by Olmsted *et al.* (1998) and the mesomorphic phase transition model by Strobl (2000, 2006, 2009), which were triggered by experiments using improved characterization methods. Furthermore, molecular dynamics simulations (Muthukumar 2003, 2004; Milner 2011; Yi *et al.* 2013) delivered valuable information on the early stages of crystal nucleation. In the following chapters, the main theoretical concepts in the description of polymer crystallization are presented based on texts by Strickland-Constable (1968); Armitstead *et al.* (1992); Gedde (1999); Muthukumar (2004); Sperling (2005); Piorkowska and Rutledge (2013).

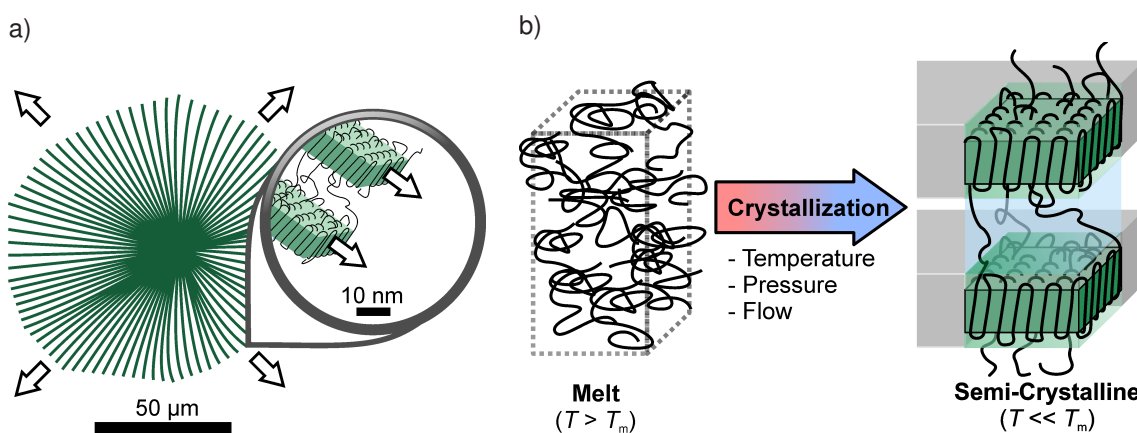


Figure 3.1: a) Spherulitic crystallization under quiescent conditions with radially growing chain-fold lamellae. b) Crystallization process for a volume element dV . The applied conditions (temperature, pressure, flow) determine the morphology, crystallinity, and crystallization kinetics.

3.2 Equilibrium thermodynamics

The starting point for most crystallization theories is the ideal case of thermodynamic equilibrium. In contrast to low molecular weight substances, polymers usually do not reach that state on experimentally relevant time scales. Because of their macromolecular structure, the mechanism of crystallization is complex with many kinetically controlled steps. Nevertheless, the fundamental thermodynamic aspects concerning stability are the basis for all further discussions and help to understand phenomena such as lamellar thickening or the melting point depression depending on the supercooling with respect to the equilibrium melting point.

Thermodynamic criteria for the stability of crystals in a liquid

Under a given conditions of temperature, pressure, and concentration, a thermodynamically most favored state with a minimum of the Gibbs free energy G is pursued (see Figure 3.2). When a liquid is supercooled below the melting point, it is crystallizing accompanied by a release of latent heat (expressed as a free enthalpy ΔH) overcompensating the loss in entropy ΔS . The net difference in the Gibbs free energy ΔG is given by:

$$\Delta G = \Delta H - T\Delta S \quad (3.1)$$

ΔG : Gibbs free energy, ΔH : free enthalpy, T : absolute temperature, ΔS : entropy.

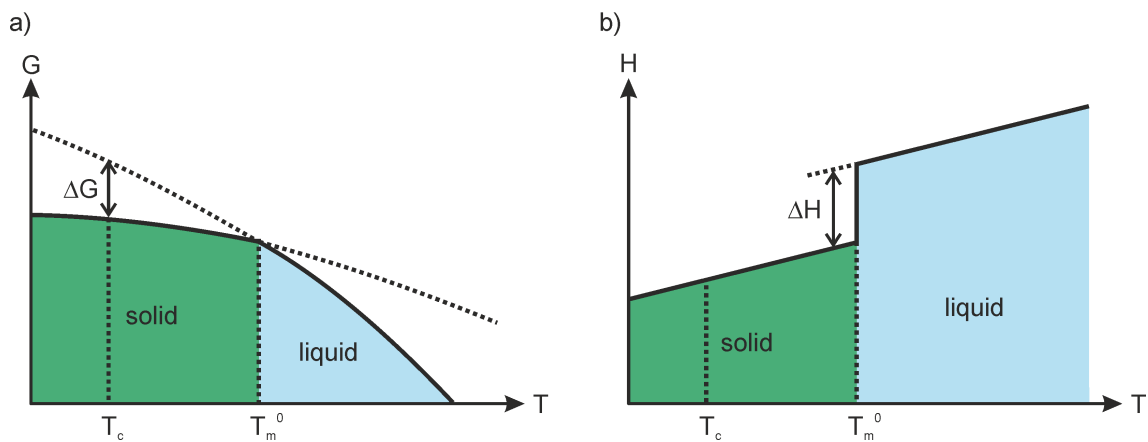


Figure 3.2: Gibbs free energy G (a) and free enthalpy H (b) as a function of temperature T . At a given crystallization temperature T_c below the melting point T_m^0 , the material crystallizes with $\Delta G < 0$ and $\Delta H < 0$.

A prerequisite for the formation of stable crystals are intermolecular forces that give rise to the release of heat compared to the disordered liquid state. The type of bonding can be of ionic, metallic, dipole-dipole, hydrogen bonding, or Van-der-Waals character. For polymers, the latter two are the most important ones (e.g., hydrogen bonding in polyesters and dispersion forces in polyolefins). The stability and dimensions of crystalline entities are strongly connected with the balance of surface stresses and the minimization of surface energies.

The Gibbs free energy ΔG of a two-phase system with n solid – liquid interfaces is given by:

$$\Delta G = \Delta G_0 + \Delta G_S = V \Delta g_0 + \sum_{i=1}^n A_i \sigma_i \quad (3.2)$$

ΔG : total Gibbs free energy, ΔG_0 : Gibbs free energy of fusion, ΔG_S : excess surface Gibbs free energy, V : volume of the solid, Δg_0 : specific Gibbs free energy of fusion, A_i : surface areas of the solid interfaces, σ_i : specific surface energies.

By assuming a cuboid solid shape with $V = L_1 L_2 L_3$ and corresponding surface energies σ_1 , σ_2 , and σ_3 (in J/m^2 or N/m – not to be confused with stresses in units of pressure (N/m^2)) contributing to ΔG_S , Equation 3.2 is modified to:

$$\begin{aligned} \Delta G &= V \cdot \Delta g_0 + 2L_1 L_2 \sigma_3 + 2L_1 L_3 \sigma_2 + 2L_2 L_3 \sigma_1 \\ &= V \cdot \Delta g_0 + \frac{2V}{L_3} \cdot \sigma_3 + 2L_1 L_3 \sigma_2 + \frac{2V}{L_1} \cdot \sigma_1 \end{aligned} \quad (3.3)$$

In order to find the minimum Gibbs free energy, the derivatives of ΔG with respect to L_1 , and L_3 are set to 0 and rearranged using $V = L_1 L_2 L_3$:

$$\frac{\partial (\Delta G)}{\partial L_1} = 2L_3 \sigma_2 - \frac{2V}{(L_1)^2} \cdot \sigma_1 \stackrel{!}{=} 0 \Rightarrow \frac{\sigma_1}{L_1} = \frac{\sigma_2}{L_2} \quad (3.4)$$

$$\frac{\partial (\Delta G)}{\partial L_3} = 2L_1 \sigma_2 - \frac{2V}{(L_3)^2} \cdot \sigma_1 \stackrel{!}{=} 0 \Rightarrow \frac{\sigma_2}{L_2} = \frac{\sigma_3}{L_3} \quad (3.5)$$

$$\Rightarrow \frac{\sigma_1}{L_1} = \frac{\sigma_2}{L_2} = \frac{\sigma_3}{L_3} \quad (3.6)$$

The dimensions L_1 , L_2 , and L_3 are thus in direct connection with the surface Gibbs free energies σ_i . In polymeric crystals, the specific surface energy of the fold surface σ_e is several times higher than the specific surface energy of the lateral surfaces σ_L . For polyethylene, $\sigma_e \approx 100 \text{ mJ/m}^2$ and $\sigma_L \approx 10 \text{ mJ/m}^2$, leading to an equilibrium ratio of $L_2 = 10L_1$ (Mark 2007). In experiments however, the lateral dimensions are found to be several orders of magnitude larger than the crystal thickness (e.g., $10 \mu\text{m}$ vs. 10 nm), indicating that the structures are usually far from thermodynamic equilibrium.

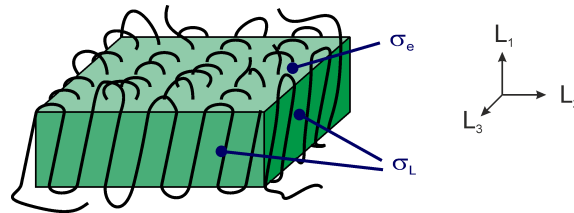


Figure 3.3: Schematic representation of a chain-folded crystal with the specific surface energies σ_L and σ_e of the lateral and the fold surface, respectively.

Relationship between polymer crystal thickness and temperature

The thickness L_c of polymeric crystals depends on the crystallization temperature, i.e., the supercooling with respect to the equilibrium melting point¹. The larger the supercooling – the thinner the crystallites, which is a consequence of the kinetic trapping during crystallization (Gedde 1999):

$$L_c = \frac{C}{T_m^0 - T_c} + \delta L \quad (3.7)$$

T_m^0 : equilibrium melting point, T_c : crystallization temperature, C : const., δL : const.

In Figure 3.4, data from Barham *et al.* (1985) on a low molecular weight polyethylene standard shows the linear relationship between L_c and $1/\Delta T = 1/(T_m^0 - T_c)$.

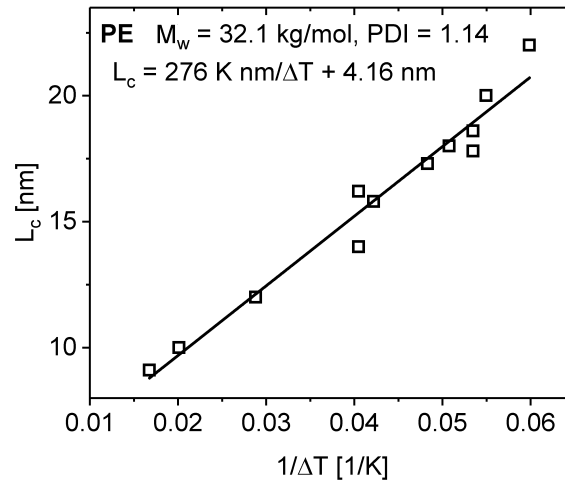


Figure 3.4: Lamellar thickness L_c vs. supercooling $1/\Delta T$ for a PE standard. A linear relationship is found that can be described by Equation 3.7. Data taken from Barham *et al.* (1985).

By annealing a polymeric crystal at temperatures close to its nominal melting point T_m , the thickness L_c is increased. An important consequence is that during non-isothermal heating experiments, thin crystals undergo thickening prior to melting.

Fusion of semi-crystalline polymers

The finite thickness of polymer crystals has major implications on their melting behavior, especially on the nominal melting temperature T_m . From a thermodynamics standpoint, crystal melting is a first order phase transition with $\Delta G = 0$ at the melting point:

$$\Delta G = \Delta G_0 + \sum_{i=1}^n A_i \sigma_i \stackrel{!}{=} 0 \quad (3.8)$$

¹ The equilibrium melting point T_m^0 is the theoretical melting point of infinitely thick crystals. It corresponds to the limiting theoretical case of a (polymeric) crystal in thermodynamic equilibrium.

Since the fold surface is usually several orders of magnitude larger than the lateral surfaces, and the surface energy σ_e is $\sim 10x$ higher than σ_L , ΔG_0 is approximated by:

$$\sum_{i=1}^n A_i \sigma_i \approx 2A\sigma_e \quad (3.9)$$

$$\Rightarrow \Delta G_0 \approx 2A\sigma_e \quad (3.10)$$

Equation 3.10 can also be expressed in specific quantities:

$$\Delta G_0 = \Delta g_0 \cdot AL_c = 2A\sigma_e \quad \Rightarrow \quad \Delta g_0 = \frac{2\sigma_e}{L_c} \quad (3.11)$$

ΔG_0 : Gibbs energy of fusion, Δg_0 : specific Gibbs energy of fusion, A : surface area of the crystal, L_c : crystal thickness.

Based on Equation 3.1, a relationship between the specific Gibbs energy of fusion and the temperature difference $\Delta T = T_m^0 - T_m$ is established:

$$\Delta g_0 = \Delta h_0 - T \Delta s_0 \stackrel{!}{=} 0 \quad \Rightarrow \quad \Delta h_0 = T \Delta s_0 \quad (3.12)$$

with $\frac{\Delta h_0}{T_m} \approx \frac{\Delta h_0}{T_m^0}$ and $T_m \Delta s_0 \approx T_m^0 \Delta s_0$ follows:

$$\Delta g_0 \approx \Delta h_0 - \frac{T_m \cdot \Delta h_0}{T_m^0} = \Delta h_0 \cdot \left(1 - \frac{T_m}{T_m^0}\right) = \Delta h_0 \left(\frac{\Delta T}{T_m^0}\right) \quad (3.13)$$

Combining Equation 3.11 and Equation 3.13 yields:

$$\Delta h_0 \left(\frac{\Delta T}{T_m^0}\right) = \frac{2\sigma_e}{L_c} \quad \Rightarrow \quad \Delta T = \frac{2\sigma_e T_m^0}{L_c \Delta h_0} \quad (3.14)$$

$$\Rightarrow \quad \boxed{T_m = T_m^0 \left(1 - \frac{2\sigma_e}{L_c \Delta h_0}\right)} \quad (\text{Gibbs - Thomson}) \quad (3.15)$$

T_m : nominal melting point, T_m^0 : equilibrium melting point, σ_e : fold surface energy, L_c : crystal thickness, Δh_0 : specific enthalpy of fusion.

Equation 3.15 is known as the Gibbs-Thomson equation and describes the melting point depression in terms of fundamental parameters: fold surface energy σ_e and crystal thickness L_c . Notably, the dependence on the surface area A cancels out, which implies that the nominal melting point only depends on crystal thickness and is independent of the lateral crystal dimensions.

3.3 Quiescent crystallization

3.3.1 General remarks

The process of polymer crystallization involves the formation of thermodynamically stable nuclei and their growth over time. In a classical treatment of nucleation and growth, the equilibrium concepts described in the previous section are combined with kinetic nucleation and growth rates. More recently, theories based on spinodal decomposition Olmsted *et al.* (1998) and mesomorphic phase transitions Strobl (2000, 2006) were developed that questioned the classical concept of nucleation and growth. In this section, the main aspects of the different crystallization theories will be outlined and discussed.

3.3.2 Classical nucleation theory

The nucleation of crystals, liquid drops, or gas bubbles can be treated using classical nucleation theory. Early works by Volmer and Weber (1926), Becker and Döring (1935), Frenkel (1946), and Turnbull and Fisher (1949) laid out the foundation and were adapted to different material systems. An important outcome of the theory is that a nucleus has to reach a critical cluster size by spontaneous fluctuations in order to survive the nucleation phase. Essentially, nucleation is treated as a growth process on a very small scale that is competing with the opposing separation process.

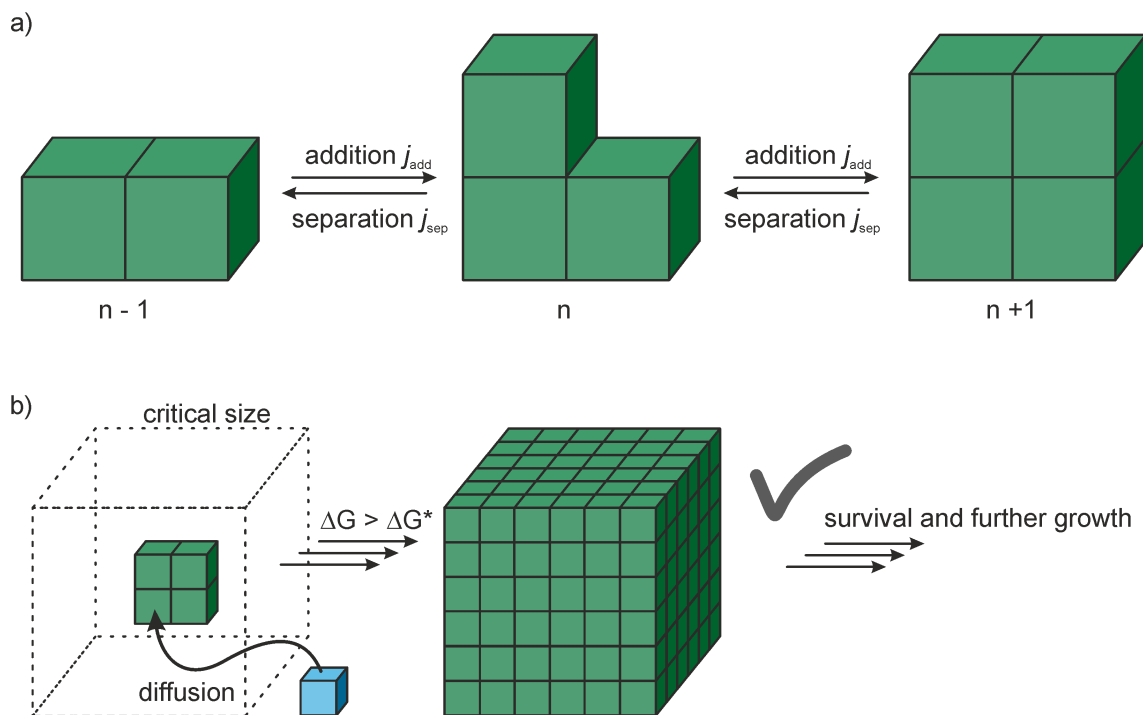


Figure 3.5: a) Schematic representation of the addition and separation equilibrium processes preceding the formation of a stable nucleus. b) A nucleus survives the formation process if the critical size is exceeded. The process is determined by the size of the activation barrier ΔG^* and the thermally activated diffusion of nucleus forming elements.

At any given time t , a nucleus (or cluster) consists of n elements and is in equilibrium with a cluster of $n - 1$ elements (separation) and a larger cluster of $n + 1$ elements (addition) (see Figure 3.5). For N clusters this can be expressed as:



N : number of clusters, n : number of elements per cluster, j : addition and separation rates

The nucleation rate I (number of clusters converted per unit time) is given by:

$$I = j_{\text{add}}N_{n-1} - j_{\text{sep}}N_n = j_{\text{add}}N_i - j_{\text{sep}}N_{n+1} \quad (3.17)$$

The temperature-dependence of the nucleation rate I can be described by an Arrhenius-type activation behavior (see Figure 3.6):

$$I = I_0 \cdot \exp\left(-\frac{\Delta G^*}{kT}\right) \quad (3.18)$$

I_0 : prefactor, ΔG^* : Gibbs free energy of activation, k : Boltzmann constant, T : temperature.

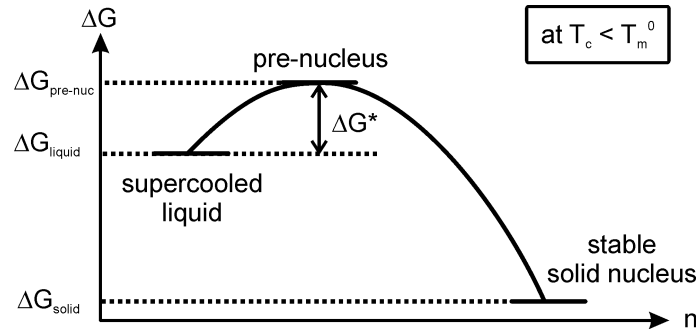


Figure 3.6: Activation energy chart for the formation of a stable nucleus at $T_c < T_m^0$. With an increasing number of elements n , the Gibbs free energy ΔG rises until the critical size is reached.

The prefactor I_0 in Equation 3.18 depends on the diffusion behavior of the individual elements:

$$I_0 = n \cdot \frac{kT}{h} \cdot \exp\left(-\frac{\Delta E_{\text{diff}}}{kT}\right) \quad (3.19)$$

n : number of elements, h : Planck constant, ΔE_{diff} : activation energy of diffusion per molecule.

Combining Equation 3.18 and Equation 3.19 leads to:

$$I = \frac{nkT}{h} \cdot \exp\left(-\frac{\Delta E_{\text{diff}} + \Delta G^*}{kT}\right) \quad (\text{Turnbull and Fisher 1949}) \quad (3.20)$$

The term ΔG^* depends on the geometry of the growing cluster, because of the different surface-to-volume ratios for e.g., spheres, cubes, or cylinders.

Equation 3.2 can be applied to describe the critical term ΔG^* :

$$\text{Spheres : } \Delta G_{\text{sph}}^* = \frac{4\pi(r^*)^3}{3} \cdot \Delta g_0 + 4\pi(r^*)^2 \sigma \quad (3.21)$$

$$\text{Cylinders : } \Delta G_{\text{cyl}}^* = \pi(r^*)^2 h^* \cdot \Delta g_0 + 2\pi r^* h^* \sigma_2 + 2\pi(r^*)^2 \sigma_1 \quad (3.22)$$

$$\text{Cuboids : } \Delta G_{\text{cub}}^* = L_1^* L_2^* L_3^* \cdot \Delta g_0 + 2L_1^* L_2^* \sigma_3^* + 2L_1^* L_3^* \sigma_2 + 2L_2^* L_3^* \sigma_1 \quad (3.23)$$

The specific Gibbs free energy Δg_0 is related to the enthalpy of fusion (Equation 3.13):

$$\Delta g_0 \approx \Delta h_0 \left(\frac{\Delta T}{T_m^0} \right)$$

Here, $\Delta T = T_m^0 - T_c$ describes the supercooling conditions (not the melting point depression as in the derivation of the Gibbs-Thomson relation). The respective critical terms ΔG^* can be expressed as a function of ΔT :

$$\text{Spheres : } \Delta G_{\text{sph}}^* = \frac{16\pi\sigma^3(T_m^0)^2}{3(\Delta h_0)^2(\Delta T)^2} \quad (3.24)$$

$$\text{Cylinders : } \Delta G_{\text{cyl}}^* = \frac{8\pi\sigma_2^2\sigma_1(T_m^0)^2}{(\Delta h_0)^2(\Delta T)^2} \quad (3.25)$$

$$\text{Cuboids : } \Delta G_{\text{cub}}^* = \frac{32\sigma_2^2\sigma_1(T_m^0)^2}{(\Delta h_0)^2(\Delta T)^2} \quad \text{for } \sigma_2 = \sigma_3 \quad (3.26)$$

Most importantly, the proportionality $\Delta G^* \sim 1/\Delta T^2$ leads to lower activation barriers for larger supercoolings ΔT and therefore higher tendencies of nucleation, which is experimentally observed. The result implies that the critical size of nuclei is smaller and more likely to be reached by spontaneous fluctuations for larger supercoolings.

3.3.3 Hoffman and Lauritzen theory

The concepts of the classical nucleation theory were adapted to polymer crystallization in the 1960's after the chain-fold lamellar structure of polymeric crystals was discovered (Keller 1957). A research group at the US National Bureau of Standards (today: National Institute of Standards and Technology – NIST) led by John D. Hoffman and John I. Lauritzen Jr. presented a theory that provided a profound description of the crystallization mechanism and its kinetics (commonly referred to as the HL or LH theory (Lauritzen and Hoffman 1960; Hoffman and Lauritzen 1961; Hoffman and Weeks 1962; Hoffman *et al.* 1969, 1976). Since then, the theory was constantly refined and checked against experiments. Its basis is the consideration of nucleation as a primary process that is followed by successive growth steps, which can be treated as secondary nucleation events.

Outline and fundamental assumptions

The HL theory assumes that lamellae grow radially from a nucleus with a constant growth rate \mathbf{G} that is proportional to the degree of supercooling $\Delta T = T_m^0 - T_c$ (note the bold face notation for the growth rate \mathbf{G} vs. the Gibbs free energy G). Primary nuclei are being formed by spontaneous fluctuations of stems that accidentally reach the critical cluster size governed by the thermodynamics described in subsection 3.3.2. The deposition of stems onto these nuclei (secondary nucleation) and their separation from it follow again the activation behavior described by classical nucleation theory and are divided into an initial and all subsequent events along the growth front. Of high importance is the competition between nucleation in the radial direction and perpendicular to it (Figure 3.7) leading to different growth regimes depending on the supercooling conditions. In the most simple version, all addition and separation processes are independent of the lateral dimensions and the chain length.

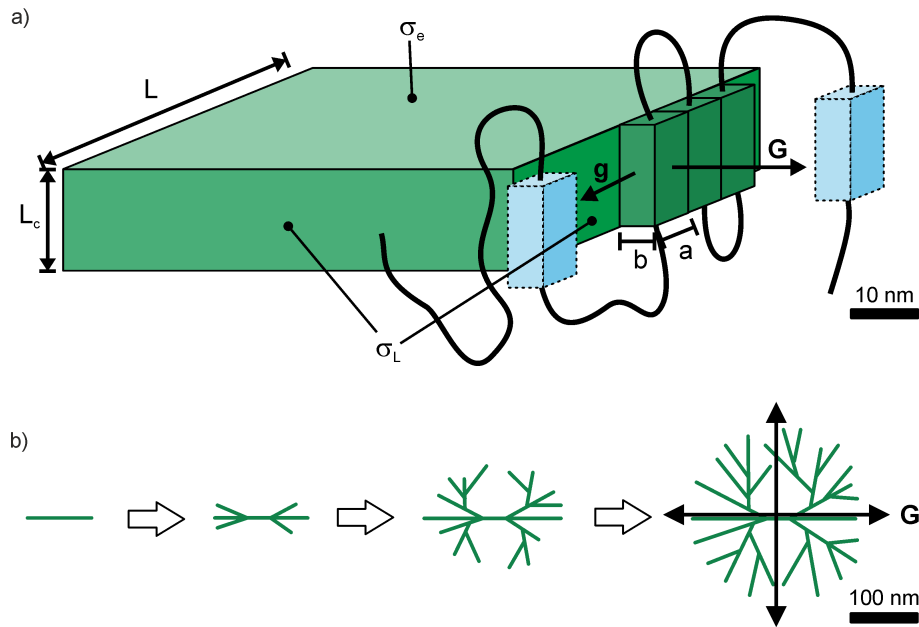


Figure 3.7: a) Lamella at the growth front of a spherulite. The growth process is modeled by the stepwise addition of chain segments (stems) with a lateral rate g . b) Lamellar splaying and ultimately radial growth with the rate \mathbf{G} that can be macroscopically determined by polarized light microscopy.

Homogeneous nucleation

The starting point for the HL theory is an Arrhenius-type thermal activation behavior of homogeneous nucleation as introduced by Turnbull and Fisher (1949) (Equation 3.18):

$$I = I_0 \cdot \exp\left(-\frac{\Delta G^*}{kT}\right)$$

For polymers, the prefactor I_0 (sometimes termed β) cannot be described by a simple thermally activated diffusion term because of the inherent more complex dynamics compared to small molecules. In early descriptions, a Williams Landel Ferry (WLF) activation behavior was assumed, and was later modified to include the reptation concept of de Gennes.

Assuming WLF activation behavior, the nucleation rate I per unit time is defined as:

$$I = \frac{nkT}{h} \cdot \exp\left[-\frac{E_a}{k \cdot (T - T_0)}\right] \cdot \exp\left[-\frac{\Delta G^*}{kT}\right] \quad (3.27)$$

A : addition rate, ΔG^* : Gibbs free energy of activation, k : Boltzmann constant, T : temperature, n : number of stems, h : Planck constant, E_a : activation energy per molecule, T_0 : reference temperature (e.g., the glass transition temperature).

The Gibbs free energy of activation ΔG^* is given by Equation 3.26 for a cuboid nucleus with $\sigma_1 = \sigma_e$ (the fold surface energy) and $\sigma_2 = \sigma_3 = \sigma_L$ (the lateral surface energies):

$$\Delta G_{\text{cub}}^* = \frac{32\sigma_L^2\sigma_e(T_m^0)^2}{(\Delta h_0)^2(\Delta T)^2} \quad (3.28)$$

In order to survive the nucleation process, a forming nucleus has to reach a critical cluster size for which the latent heat balances the excess surface energy terms (Equation 3.2). The critical size depends inversely on the supercooling $\Delta T = T_m^0 - T_c$, leading to a higher number of successful nucleation events per unit volume for larger supercoolings.

Growth from a pre-existing surface (secondary nucleation)

The growth process is defined as the addition of stems onto a pre-existing surface which was either formed by homogeneous nucleation or is part of a solid object (heterogeneous nucleation). It is important to note that there is no fundamental distinction between surfaces of polymeric nuclei or other solid materials in the HL theory, except from their possibly different surface energy and enthalpy terms. For the growth process, the net energy barrier is determined by the initial step of placing a stem onto a pre-existing surface, differing from the case of homogeneous nucleation (Figure 3.8a vs. Figure 3.6).

The competition of growth along the growth front and perpendicular to it gives rise to three regimes depending on the supercooling conditions (Figure 3.9a). The radial growth rates g for the different regimes were shown to be (Sanchez and DiMarzio 1971; Frank 1974):

$$G_I = biL \quad \text{for } g \gg i \quad (3.29)$$

$$G_{II} = b \cdot \sqrt{ig} \quad \text{for } g \approx i \quad (3.30)$$

$$G_{III} = biL \quad \text{for } g \ll i \quad (3.31)$$

G : radial growth rate, L : lamellar width (see Figure 3.7), b : stem width in the radial direction, i : secondary nucleation rate, g : lateral spreading rate (growth rate along the growth front).

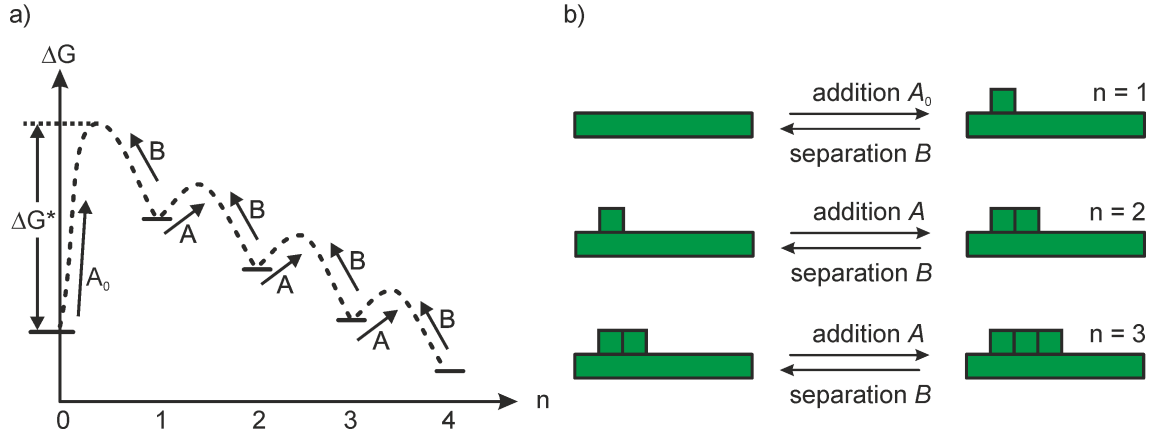


Figure 3.8: a) Activation energy chart for the growth process, i.e., secondary nucleation from a pre-existing surface. The initial step A_0 determines the net energy barrier. All succeeding addition steps along the growth front follow an activation behavior with lower energy barriers. b) Schematic representation of the individual addition and separation steps along the growth front.

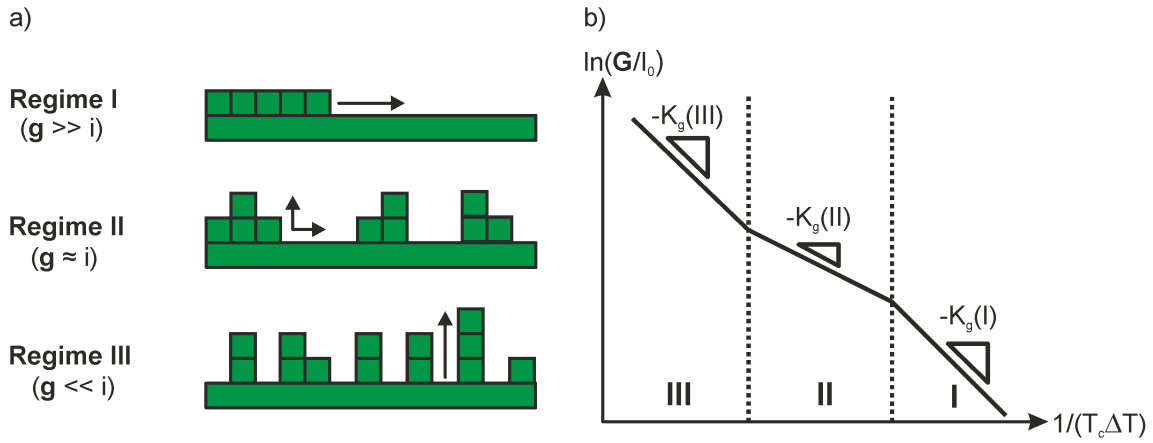


Figure 3.9: a) Different regimes of growth described by the Hoffman-Lauritzen model. The lateral spreading rate g competes with the secondary nucleation rate i which determines the overall growth rate G . b) Hoffman-Lauritzen plot of $\ln(G/I_0)$ vs. $1/(T_c\Delta T)$ to identify the different growth regimes and corresponding slopes. The HL theory predicts the slopes to be $K_g(I) = K_g(III) = 1/2 \cdot K_g(II)$.

The thermal activation behavior of G_I , G_{II} , and G_{III} is given by:

$$G_I = G_{I,0} \cdot \exp\left(-\frac{E_A}{k(T-T_0)}\right) \exp\left(-\frac{4 b \sigma_e \sigma_L T_m^0}{\Delta h'_0 (T_m^0 - T) k T}\right) \quad (3.32)$$

$$G_{II} = G_{II,0} \cdot \exp\left(-\frac{E_A}{k(T-T_0)}\right) \exp\left(-\frac{2 b \sigma_e \sigma_L T_m^0}{\Delta h'_0 (T_m^0 - T) k T}\right) \quad (3.33)$$

$$G_{III} = G_{III,0} \cdot \exp\left(-\frac{E_A}{k(T-T_0)}\right) \exp\left(-\frac{4 b \sigma_e \sigma_L T_m^0}{\Delta h'_0 (T_m^0 - T) k T}\right) \quad (3.34)$$

Similarly to primary nucleation (Equation 3.27, p. 29), the rates G_I , G_{II} , and G_{III} contain transport and energetic terms. For small degrees of supercooling $\Delta T = T_m^0 - T$, the Gibbs free

energy of activation ΔG^* dominates the growth rate, whereas for temperatures close to T_0 , diffusion controls the growth process.

Equation 3.32, Equation 3.33, and Equation 3.34 are of the form:

$$G = I_0 \cdot \exp\left(-\frac{K_g}{T\Delta T}\right) \quad (3.35)$$

By plotting $\ln(G/I_0)$ vs. $1/(T\Delta T)$ in a Hoffman-Lauritzen plot, the slope K_g can be determined that characterizes secondary nucleation in the respective regimes (see Figure 3.9b). Furthermore, the surface energy terms σ_e and σ_L can be extracted from the slopes K_g . For most high molecular weight polymers, only one or two regimes can be observed experimentally using standard methods such as optical microscopy or DSC. Tabulated K_g values for different polymers can be found in reference books (Mark 2007).

Discussion

The kinetic model developed by Hoffman and Lauritzen is based on the concepts of classical nucleation theory, and thus requires the formation of a critical nucleus and its subsequent growth over time by passing activation energy barriers of enthalpic character. In its original form, the model has shortcomings with respect to the dynamics of long-chain polymers, and the assumptions in terms of one-shot stem addition, fixed stem length, and strictly flat growth can be regarded as strong simplifications. Therefore, the HL theory does not generally lead to quantitatively correct predictions of surface energies, lamellar dimensions, and growth rates (Point and Dosiere 1989).

The main points of criticism are related to the:

- General mechanism: sequential stem deposition; uniform lamellar thickness throughout the growth; strictly adjacent chain re-entry;
- Thermodynamics: kinetic treatment; rate-determining step of enthalpic character;
- Oversimplifications: Disregard of polymer dynamics, molecular weight distribution, fractionation effects, cilia, side-chains, stereo-/regio-defects; phenomena such as lamellar twisting and curved growth fronts are not covered by the model;

There is a long list of modifications to the original HL model and alternative theories that have been developed to account for the mentioned aspects. Here are the most prominent ones (without claim for completeness):

- Modified HL model including polymer reptation (Hoffman and Miller 1988);
- Sliding diffusion model to account for a variation of stem thickness and two-dimensional growth (Hikosaka 1987, 1990);

- Multipath approach for the step-wise addition of individual segments to form a complete stem (Point 1979);
- Surface roughening model by (Sadler and Gilmer 1984; Sadler 1987) suggesting an entropic origin of the activation barrier;
- Model based on spinodal decomposition by Olmsted *et al.* (1998);
- Mesomorphic phase transition model by Strobl (2000, 2006, 2009);

The models by Olmsted and Strobl reflect approaches which do not rely on the concepts of classical nucleation theory and will therefore be presented briefly in the following sections.

3.3.4 Olmsted's spinodal decomposition model

In the late 1990's, multiple research groups reported that for certain polymers small-angle X-ray scattering (SAXS) patterns showed up earlier during polymer crystallizations compared to the corresponding wide-angle patterns, which was associated with density fluctuations prior to the crystallographic packing of chains (Imai *et al.* 1992, 1994, 1995; Ezquerra *et al.* 1996; Heeley *et al.* 2003; Kaji *et al.* 2005). The SAXS data was analyzed using a model initially developed by Cahn and Hilliard for the spinodal decomposition of binary mixtures, describing the data sufficiently well (Cahn and Hilliard 1959; Cahn 1961; Huston *et al.* 1966). The group of Peter D. Olmsted at the University of Leeds later proposed a theoretical model based on spinodal decomposition for crystallizing polymers that contradicted the concepts of thermally activated nucleation and growth (Olmsted *et al.* 1998). The main difference in the theory is that whereas in the kinetic treatment of nucleation an activation barrier has to be overcome, spinodal decomposition happens spontaneously.

Theoretical approach

The thermodynamics of spinodal decompositions have been extensively studied for binary mixtures, e.g., metal alloys (Binder and Fratzl 2005). Spontaneous demixing occurs when a constant loss in free energy is associated with the phase separation, which is the case when the curvature in a plot of the Gibbs free energy G vs. composition X is negative with $d^2G/dX^2 < 0$ (Figure 3.10a). For curve segments with $d^2G/dX^2 > 0$, demixing leads to a gain in free energy ΔG that is characteristic for a thermally activated nucleation and growth process. The binodal and spinodal lines represent phase boundaries between the respective unstable, metastable, and stable phases in a $T - X$ -plot (Figure 3.10b). The selected temperature T_{exp} and composition X determine whether spinodal decomposition or thermally activated nucleation and growth will take place. A generic phase diagram for semi-crystalline polymers was proposed by Olmsted *et al.* (1998) (Figure 3.10c), which is based on the scaled density $\rho \cdot w$ instead of the composition X as for binary mixtures. In order to account for all features of semi-crystalline polymers, co-existence, metastable, and unstable regimes are included.

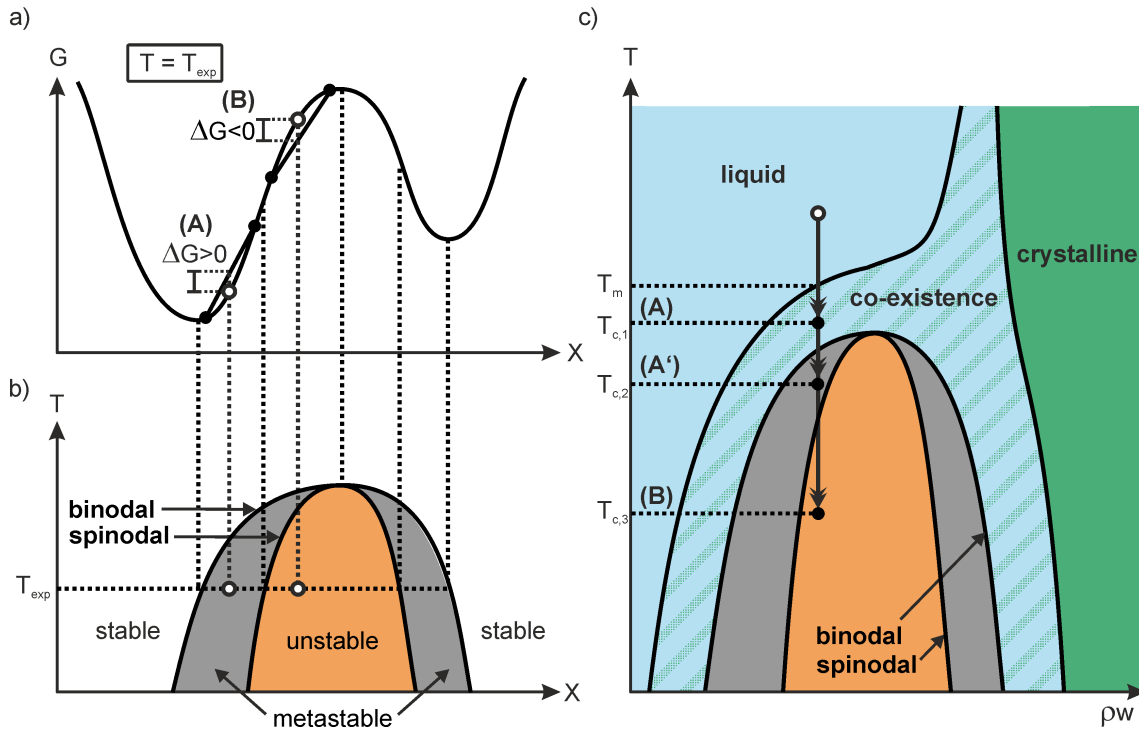


Figure 3.10: a) Gibbs free energy G vs. composition X for a binary mixture. For case A, the difference in Gibbs free energy ΔG for demixing is positive, corresponding to a thermally activated nucleation and growth process from a metastable state. For case B, the ΔG is negative, leading to spontaneous demixing (spinodal decomposition). b) Temperature T vs. composition X for the binary mixture of a). The binodal and spinodal lines represent phase boundaries for the respective unstable, metastable, and stable phases. c) Suggested phase diagram for a semi-crystalline polymer after Olmsted *et al.* (1998) (temperature vs. density ρ times the monomeric specific volume w). By quenching from a temperature $T > T_m$ to temperatures $T_c < T_m$ different scenarios can occur: for low supercooling, a nucleation and growth process directly from the melt is realized (A), for higher supercoolings, an ordered nematic precursor phase and an isotropic metastable phase are created through a nucleation and growth process (A'), for even higher supercoolings, a spontaneous demixing into an ordered isotropic phase takes place by a spinodal decomposition mechanism (B).

Discussion

The spinodal decomposition model focuses on the initial stages of homogeneous nucleation and does not represent a full theory for all stages of polymer crystallization. There have been discussions to whether the early appearance of SAXS patterns compared to WAXS reflexes during polymer crystallizations is indeed a real effect or caused by the different sensitivities of SAXS and WAXS detectors (Baert and Van Puyvelde 2008; Panine *et al.* 2008). Some researchers reported that by taking into account the different detection limits, the observed SAXS patterns would be reasonably well explained by the formation of anisotropic sheaf-like nuclei (Wang *et al.* 2000; Hikosaka *et al.* 2005). Furthermore, some groups observed a temperature-dependence of the SAXS intensities that was not in accordance with the theory of spinodal decomposition as discussed by Muthukumar (2004).

3.3.5 Strobl's mesomorphic phase transition model

The concept of pre-ordering preceding homogeneous nucleation was extended to the whole growth process in the early 2000's by Gert Strobl and co-workers at the University of Freiburg (Germany) (Strobl 2000, 2006; Strobl and Cho 2007; Strobl 2009). Their reasoning was that if density fluctuations occur during the very early stages of homogeneous nucleation, they should as well play an important role at the growth front later on during polymer crystallization. The model involves three basic steps: (1) formation of slightly ordered mesomorphic domains in the melt, (2) stabilization by crystallization into granular blocks, (3) merging of the granular blocks and surface re-ordering to form long extending lamellae (see Figure 3.11).

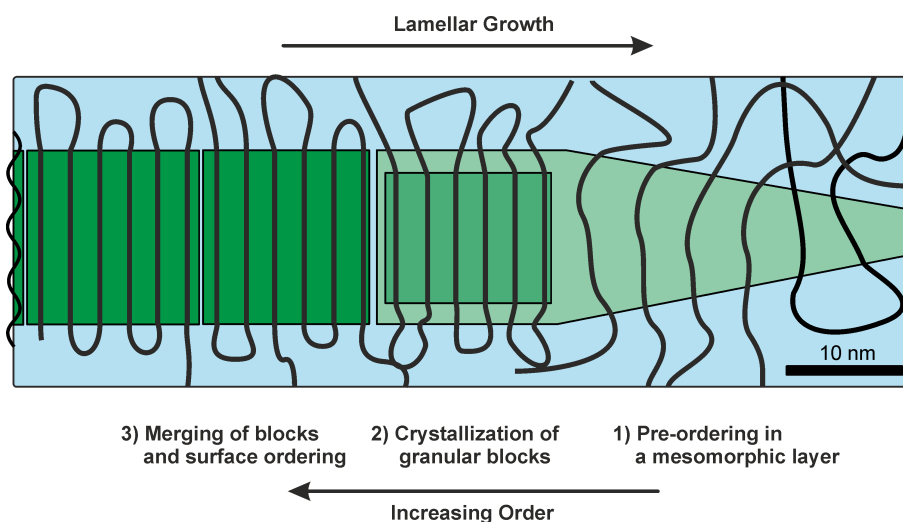


Figure 3.11: Mesomorphic phase transition model by Strobl (2000, 2006, 2009). Rather than a step-wise addition of individual stems as in the HL theory, the model consists of multiple stages starting with the formation of a slightly ordered mesophase that crystallizes into granular blocks, which are then merged to form long extending lamellae.

Experiments and reasoning behind the proposed multistage model

Strobl and co-workers analyzed a range of materials including polylactide (PLA), poly ϵ -caprolactone (PCL), syndiotactic polypropylene (s-PP), s-PP-co-octene and PE-co-octenes in terms of their temperature-dependent crystallization and melting behavior using small angle X-ray scattering (SAXS). They could determine the respective lamellar thicknesses for different experimental conditions and compared them in Gibbs-Thomson plots of melting and crystallization temperatures vs. $1/L_c$ (see Figure 3.12a). By linearly extrapolating the crystallization and melting temperatures to $1/L_c = 0$, they obtained melting and crystallization lines, and identified another equilibrium temperature T_c^0 that is higher than T_m^0 . They suggested to replace T_m^0 by T_c^0 in Equation 3.7, claiming that the lamellar thickness is controlled by the supercooling conditions with respect to T_c^0 . Furthermore, growth rate measurements were performed and a third temperature T_{zg} was identified as the one controlling lateral growth instead of T_m^0 with the overall order being $T_{zg} < T_m^0 < T_c^0$ (Strobl 2009).

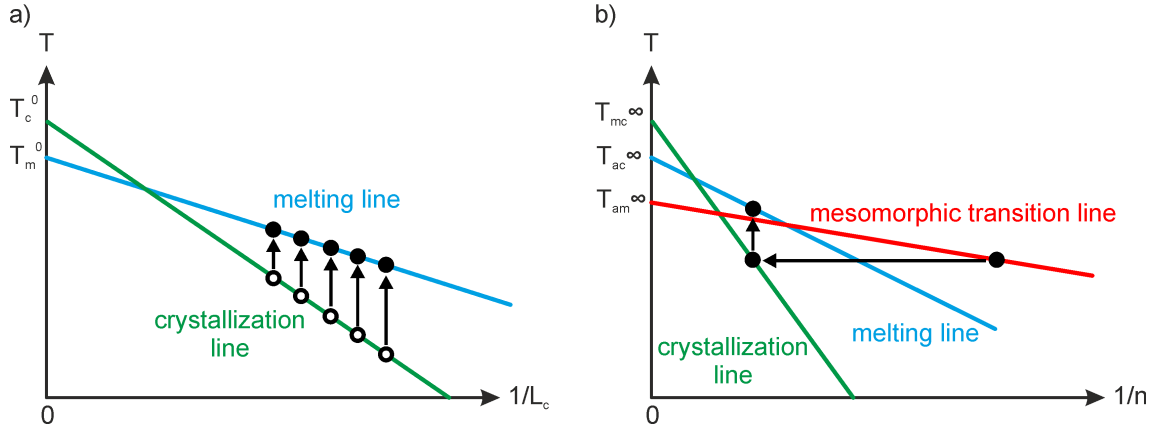


Figure 3.12: a) Gibbs-Thomson plot for different crystallization temperatures (open symbols) and corresponding melting points (solid symbols). The crystallization and melting lines are linear extrapolations and lead to the equilibrium temperatures T_m^0 and T_c^0 . b) Temperature vs. the inverse of the stem length for the multi-stage crystallization model with $T_{am}^\infty = T_{zg} < T_{ac}^\infty = T_m^0 < T_{mc}^\infty = T_c^0$ and three lines that describe melting, crystallization, and the mesomorphic phase transition.

As the observations of Strobl and co-workers could not be fully explained by the HL model with its single characteristic temperature T_m^0 , they proposed their model of multiple stages during crystallization. Their main reasoning was that, if crystallization and melting were controlled by different laws and characteristic temperatures, the processes are not exactly the inverse of each other, and thus involve different mechanisms. The experimental observations were discussed in the light of Ostwald's rule of stages, stating that nano-sized crystals will adopt a structure that is favorable at small length scales, but might change when the object grows (Keller *et al.* 1994). The initial pre-ordering was suggested to be governed by the mesomorphic phase transition line with the characteristic temperature T_{am}^∞ , which is identical with the macroscopically observed zero-growth rate temperature T_{zg} (Figure 3.12b).

Discussion

The mesomorphic phase transition model treats crystal growth as a multistage process, but doesn't provide an explanation for the very initial stages of homogeneous nucleation. It is based on a phenomenological analysis of crystallization and melting temperatures, which are only accessible over a relatively small temperature range. Under most real crystallization conditions, a distribution of lamellar thicknesses and respective melting points is observed, leading to less obvious trends in Gibbs-Thomson plots as the ones sketched in Figure 3.12a or even non-linear curves that might collapse onto one line for $1/L_c = 0$ (Xu *et al.* 2016). However, the concept of a pre-ordering step preceding polymer crystallization has been thoroughly investigated by different groups using molecular dynamics simulations, who discovered that very likely a pre-cursor phase is formed at the growth front (Sirota 2007; Sommer and Luo 2010; Milner 2011; Luo and Sommer 2011). In addition, atomic force microscopy (AFM) images of crystallized polymers revealed the proposed granular structure of lamellae in different materials (Magonov and Godovsky 1999; Hugel *et al.* 1999).

3.3.6 Kinetic analysis of crystallization data

Crystallization experiments are usually carried out by monitoring the buildup of crystallinity in time-dependent experiments using e.g., optical microscopy, differential scanning calorimetry, or X-ray scattering. By extracting kinetic parameters, crystallizations can be analyzed in terms of their time-dependent nucleation and growth behavior. These parameters can be compared for different polymers, experimental conditions, and additives, providing a way of reducing the large amounts of data acquired in crystallization experiments. There are two important types of experimental conditions: isothermal at constant temperature and non-isothermal at constant cooling rate. The former delivers information on the nucleation and growth characteristics for a chosen set of conditions in one single experiment, whereas the latter provides information on the entire growth rate distribution when multiple experiments are carried out.

The Avrami model

Under isothermal conditions, radial spherulitic growth as shown in Figure 3.13 is well described by a constant rate and a dimensionality parameter. In case of heterogeneous / athermal nucleation, the following derivation leads to an analytical expression that describes the crystallization kinetics: Let A be a reference point. If a number of nuclei N is distributed randomly in space, and grow radially with the growth rate G , a Poisson distribution describes the probability for point A to be hit c times by a growth front up to time t (Gedde 1999):

$$P(c) = \frac{E(t)^c}{c!} \exp[-E(t)] \quad (3.36)$$

P : probability, c , $E(t)$: considered and average number of crystal fronts that pass point A .

For $c = 0$, i.e., for the case that A was not hit by a crystal front, Equation 3.36 reduces to:

$$P(0) = \exp[-E(t)] \quad (3.37)$$

The average number of crystal fronts $E(t)$ that pass point A can also be interpreted as an *extended volume* counting all transformed domains (impingement is not taken into account). It can be expressed by the product of the number of nuclei N per unoccupied volume V_{total} times their individual volumes V_0 :

$$E(t) = V_0 \cdot \frac{N}{V_{\text{total}}} = \frac{4}{3} \pi (Gt)^3 \cdot \frac{N}{V_{\text{total}}} \quad (3.38)$$

$E(t)$: extended occupied volume, G : growth rate, t : time, N : number of nuclei, V_{total} : total unoccupied volume.

The volume-related relative crystallinity ϕ_c / ϕ_c^∞ is given by:

$$\phi_c / \phi_c^\infty = 1 - P(0) = 1 - \exp[-E(t)] = 1 - \exp\left(-\frac{4}{3} \pi (Gt)^3 \cdot \frac{N}{V_{\text{total}}}\right) \quad (3.39)$$

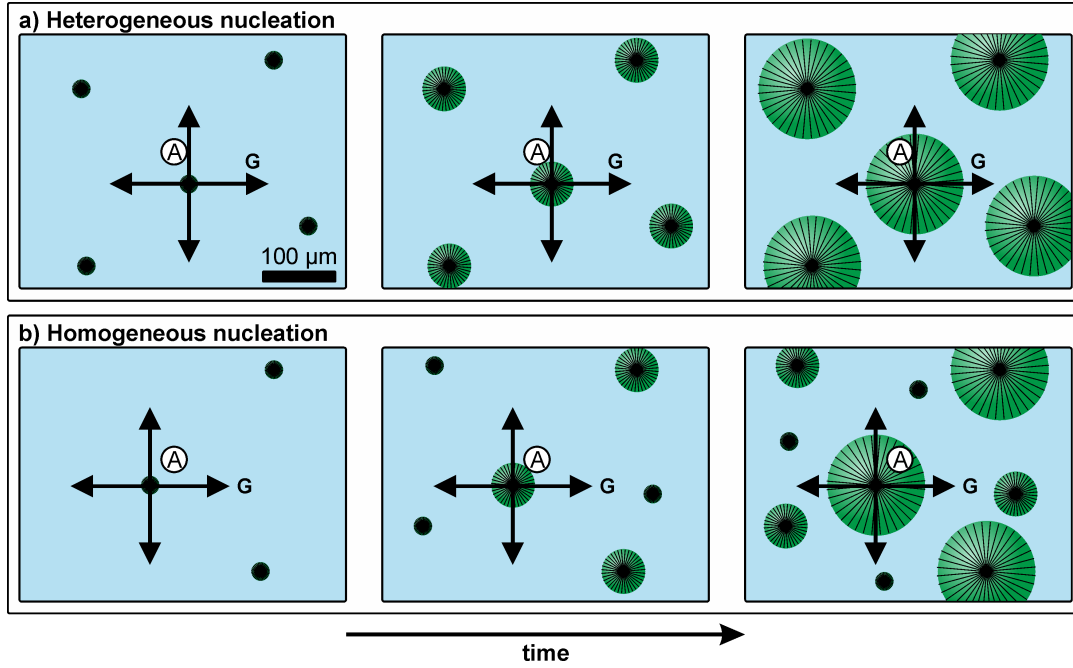


Figure 3.13: Illustration for three points in time during isothermal crystallizations of polymers under heterogeneous (a) or homogeneous (b) nucleation conditions.

In case of homogeneous nucleation with a nucleation rate I (Figure 3.13b; see also subsection 3.3.3), the instantaneous change in occupied extended volume dE is given by:

$$dE = I \cdot 4\pi r^2 \left(t - \frac{r}{G} \right) dr \quad (3.40)$$

Integration from $r = 0$ to $r = Gt$ at time t yields:

$$E(t) = \int_{r=0}^{Gt} dE = \int_{r=0}^{Gt} I \cdot 4\pi r^2 \left(t - \frac{r}{G} \right) dr = \frac{\pi}{3} I G^3 t^4 \quad (3.41)$$

Inserting Equation 3.41 into Equation 3.39 yields:

$$\phi_c / \phi_c^\infty = 1 - \exp\left(-\frac{\pi}{3} I G^3 t^4\right) \quad (3.42)$$

Generalization of Equation 3.39 and Equation 3.42 leads to the Avrami equation², and is often linearized to be able to perform a linear regression (Avrami 1939, 1940, 1941):

$$\boxed{\phi_c / \phi_c^\infty = 1 - \exp[-(Kt)^n] = 1 - \exp[-kt^n]} \quad (3.43)$$

$$\log[-\ln(1 - \phi_c / \phi_c^\infty)] = n \cdot \log(K) + n \cdot \log(t) = \log(k) + n \cdot \log(t) \quad (3.44)$$

² Equation 3.43 is also called the JMAK equation after the researchers W. A. Johnson, R. F. Mehl, M. Avrami, and A. Kolmogorov who contributed to its derivation.

The dimensionality parameter n adopts different values for 1D, 2D, and 3D growth depending on the type of nucleation (homogeneous: $n = \text{dim} + 1$, heterogeneous: $n = \text{dim}$, see Figure 3.14). Care has to be taken when experimentally obtained dimensionality parameters are discussed without complementing structural information (Wunderlich 1976; Lorenzo *et al.* 2007). Experimental factors that may lead to wrong mechanistic conclusions are temperature gradients, a prolonged induction period, and confined sample spaces. Furthermore, the Avrami equation describes only the early stages of growth before crystal impingement and secondary growth. Thus, fitting experimental data is usually only reliable in the range of $0 < \phi_c / \phi_c^\infty < 0.5$ (Lorenzo *et al.* 2007).

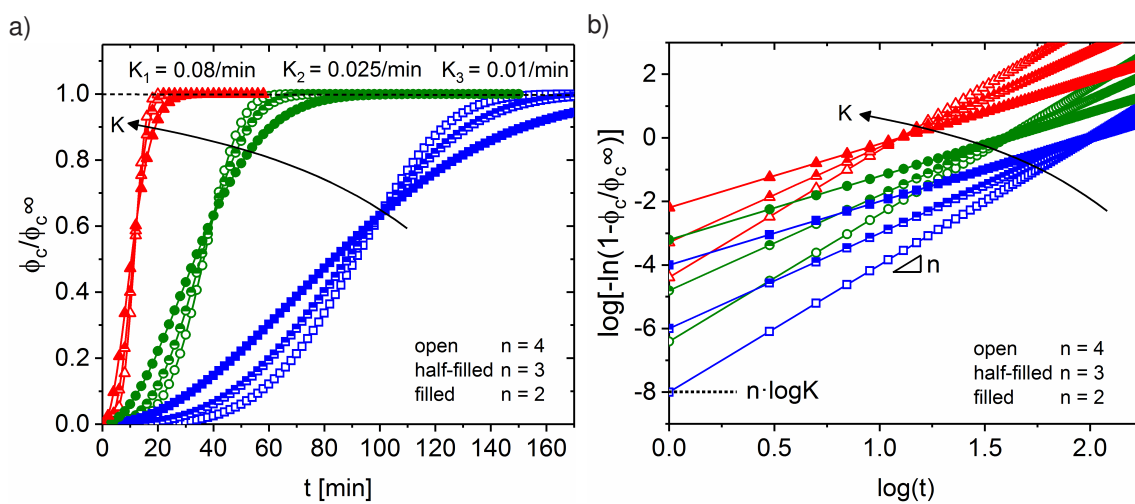


Figure 3.14: a) Calculated crystallization curves based on Equation 3.43 for different values of K and n . b) Avrami plot of the calculated crystallization curves based on Equation 3.44.

3.4 Flow-induced crystallization

3.4.1 General remarks

Early on, polymer scientists noticed that the application of flow has significant effects on the crystallization kinetics, the morphology, and ultimately the material properties of semi-crystalline polymers. Initial works by Lagasse and Maxwell (1976), Mackley and Keller (1973); Mackley *et al.* (1975), and the group of Janeschitz-Kriegl (Eder and Janeschitz-Kriegl 1988; Eder *et al.* 1990, 1992; Janeschitz-Kriegl 1992; Liedauer *et al.* 1993, 1995) showed that flow leads to increased nucleation and row-nucleated structures above a certain threshold of applied flow stress and strain. These anisotropic structures are characterized by a high degree of chain orientation in the direction of flow as shown in Figure 3.15. The high degree of orientation drastically increases the mechanical strength of the materials. For semi-crystalline fibers and films, this structural feature is essential as it permits the creation of thin, yet strong, filaments and layers due to the presence of strain-hardening.³

³ The quantification of chain orientation in fibers is frequently analyzed using Herman's orientation function, which will be presented and discussed in section 7.4 of chapter 7.

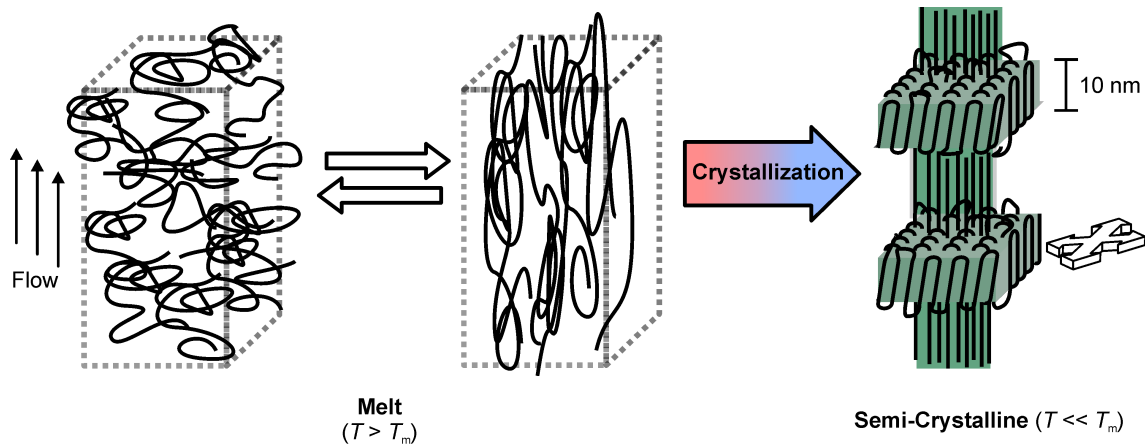


Figure 3.15: Pathway of flow-induced crystallization: flow alters the polymeric chain conformation. If chain relaxation is slower than crystallization under the chosen conditions, row-nucleated morphologies are obtained that exhibit a high degree of chain orientation in the nucleus.

The mechanism behind flow-induced crystallization involves the competition between chain deformation and relaxation. In other words, if the application of flow overrides the tendency of polymeric chains to form random coils, a substantial degree of orientation is maintained. An important consequence is that the timescale of deformation has to be equal or shorter than the one of polymer relaxation. As commercially available semi-crystalline polymers have usually high polydispersities (broad molecular weight distributions), the slowest relaxing components of the highest molecular weights are the first to display a substantial degree of chain orientation. Consequently, the formation of row-nucleated morphologies is molecular-weight-dependent and can be altered by incorporating additional long polymeric chains (e.g., UHMWPE as shown by Wingstrand *et al.* (2017)). Main works on the elucidation of this mechanism have been carried out by the group of Julie Kornfield at Caltech, USA (Kumaraswamy *et al.* 1999, 2000, 2002; Kimata *et al.* 2007), the group of Benjamin Hsiao at Stony Brook University, USA in collaboration with the group of Francisco Baltá-Calleja at the Institute for Structure of Matter, CSIC, Spain (Nogales *et al.* 1999; Somani *et al.* 2000, 2001, 2002, 2003; Agarwal *et al.* 2003), and the group of Jean-Marc Haudin at MINES ParisTech, France (Jay *et al.* 1999; Duplay *et al.* 2000). Most works were carried out using set-ups of X-ray scattering or microscopy equipped with flow apparatuses. Especially, small angle X-ray scattering (SAXS) was used extensively in these works as it is sensitive to the size and orientation of the formed lamellae (tens of nanometers).

3.4.2 Effects of flow on the morphology of crystallizing polymers

As discussed in section 3.3, nucleation in semi-crystalline polymers always involves de-coiling and reorganization to form stable nuclei. Flow promotes these processes and substitutes the otherwise stochastic diffusion of polymeric chains under quiescent conditions. Furthermore, it directs crystal growth by a template-based mechanism: once row-nuclei have been formed under the influence of flow, lamellar growth takes over and leads to lamellae perpendicular to the flow direction. This phenomenon is responsible for the persisting structural anisotropy

during flow-induced crystallization even after the cessation of flow. In Figure 3.16, the effects of flow on the microstructure of crystallizing polymers is displayed. At relatively mild flow conditions, an increase in nucleation density and reduction in spherulite sizes is observed. With increasing flow stress and strain, elongated and ultimately row-nucleated morphologies are obtained. The latter are also known as *cylindrites* (Varga 1983, 1992; Varga and Karger-Kocsis 1996).

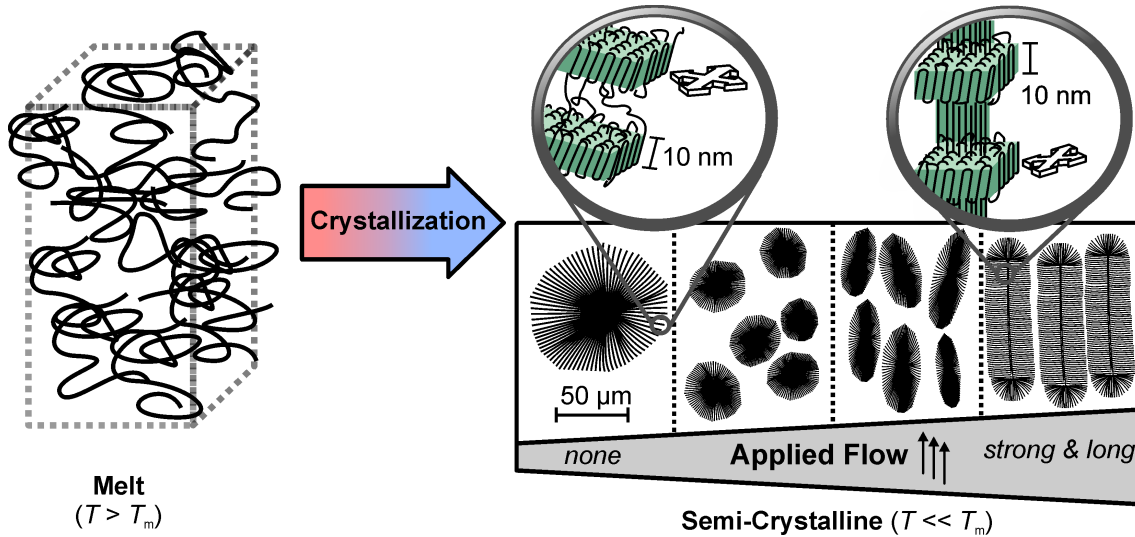


Figure 3.16: Effects of flow on the microstructure of crystallizing polymers. With increasing flow stress and strain, higher nucleation densities, elongated spherulites, and row-nucleated morphologies (*cylindrites*) are observed. The lamellar substructure shows strong orientation perpendicular to the flow direction for more vigorous flow conditions.

If the applied flow stress is further increased, the induced row-nucleated structures become smaller and smaller. For typical processing conditions of injection molding or fiber spinning with strain rates of $\dot{\gamma} > 1000/\text{s}$, the lamellae perpendicular to the flow direction extend only for a few tens of nanometers. This nano-sized morphology is oftentimes called *shish kebab* after a Turkish meat dish and is usually found in semi-crystalline fibers or the skin layer of injection molded parts (Figure 3.17).

Depending on the processing method, the type of applied flow can be predominantly extensional, shear, or a combination of both (e.g., fiber spinning: extensional, injection molding: shear flow, thermoforming: both). The flow conditions needed to achieve the different regimes shown in Figure 3.16, can be divided into time-dependent terms (flow duration and strain rate) and time-independent terms (total strain and specific work). As already pointed out in the introduction, the competition between distorted chain conformation and chain relaxation plays an important role in the formation of row-nucleated morphologies. It has been shown independently by different research groups that the applied strain rate most probably has to be larger than the inverse of the longest relaxation time to achieve persistent chain orientation (Lellinger *et al.* 2003; Elmoumni *et al.* 2003, 2005; Elmoumni and Winter 2006; Steenbakkers 2005). However, the number and spatial dimensions of row-nucleated morphologies are also connected to the time-independent quantities, i.e., total strain and specific work (Mykhaylyk

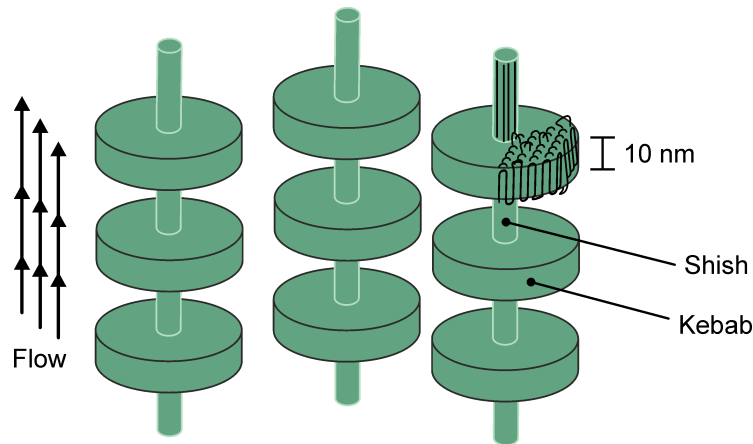


Figure 3.17: Shish kebab morphology for high strain rates present in injection molding or fiber spinning (e.g., $\dot{\gamma} > 1000/\text{s}$). Different from the micron-sized row-nucleated cylindrites, shish kebabs consist of stacked lamellae with lateral dimensions of some tens of nanometers.

et al. 2008, 2010). For more complex material systems with incorporated additives or fillers, the presence of additional surfaces leads to a facilitated formation of row-nucleated morphologies (Byelov *et al.* 2008; Szkudlarek *et al.* 2013).

3.4.3 Modeling flow-induced crystallization

Initial works on modeling flow-induced crystallization were carried out by Janeschitz-Kriegl and Eder at the Johannes Kepler University Linz (Austria) (Eder *et al.* 1990; Janeschitz-Kriegl 1992; Eder *et al.* 1992). They made important contributions to the description of the low strain rate regime and pointed out the importance of separating temperature from flow effects concerning polymer crystallization. Another very active group of researchers around Han Meijer and Gerrit W. Peters at Eindhoven University of Technology (Netherlands) published a number of very systematic studies and thorough theoretical treatments of flow-induced polymer crystallization (Vleeshouwers and Meijer 1996; Zuidema *et al.* 2001; van Meerveld *et al.* 2004; Housmans, Peters and Meijer 2009; Custódio *et al.* 2009; Housmans, Steenbakkens, Roozemond, Peters and Meijer 2009; Housmans, Gahleitner, Peters and Meijer 2009; Roozemond *et al.* 2014). Further works have been carried out by Coppola *et al.* (2001); Acierno *et al.* (2002); Coppola *et al.* (2004), Koscher and Fulchiron (2002), and Mykhaylyk *et al.* (2008); Graham (2014). Plots of the onset time t_{onset} (see Figure 6.6 in chapter 6) or half crystallization time $t_{1/2}$ vs. the applied shear strain rate $\dot{\gamma}$ help to classify the effects of strain rate, total strain, and temperature on the morphology of crystallizing polymers. In Figure 3.18, the generally observed trends are shown based on articles by Eder *et al.* (1990) and Housmans, Peters and Meijer (2009). Lowering the crystallization temperature decreases the induction time t_{onset} as expected. Above a critical strain rate $\dot{\gamma}_{\text{min}}$ the applied flow leads to a further decrease of t_{onset} , thereby acting as an apparent lower crystallization temperature (note: the induction time t_{onset} is frequently defined as the intersecting point of two linear extrapolations for the induction and growth period in isothermal crystallization experiments (see e.g., Figure 6.6, p. 101 in chapter 6).

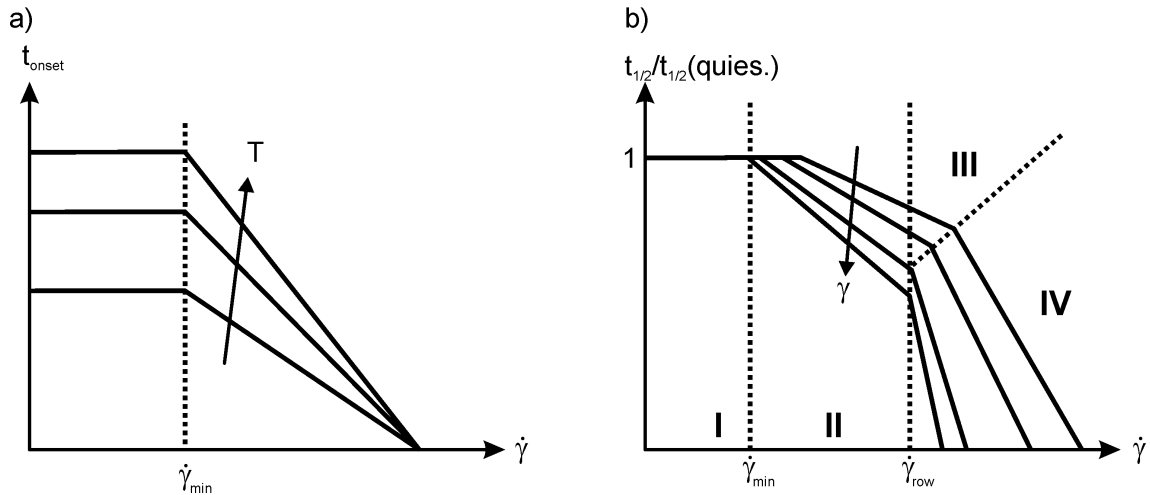


Figure 3.18: Induction time t_{onset} (a) and normalized half crystallization time $t_{1/2}/t_{1/2}(\text{quiesc.})$ (b) vs. the applied strain rate $\dot{\gamma}$. Multiple regimes are observed, differing in morphological and kinetic aspects. Adapted from Eder *et al.* (1990) and Housmans, Peters and Meijer (2009).

The crystallization half time $t_{1/2}$ is usually normalized to the half time under quiescent conditions, thereby removing any temperature-dependent effects. In the literature, this ratio is sometimes also called θ . Four different regimes can be distinguished:

- I: No significant influence of flow on the crystallization behavior;
- II: Increased nucleation, spherulitic growth;
- III: Increased nucleation and formation of ellipsoid morphologies;
- IV: Increased nucleation and formation of long extending row-nucleated structures;

Housmans *et al.* discussed the occurrence of these multiple regimes based on the characteristic flow relaxation times of polymeric melts (Housmans, Peters and Meijer 2009). In regime I, the applied strain rates were assumed to be smaller than the inverse of the reptation time τ_d (for the definitions of the reptation time τ_d and Rouse time τ_R see e.g., Larson *et al.* (2003)). As τ_d characterizes the slowest relaxation mode, all relaxation processes would be fast compared to the applied strain rate. In regime II, the strain rate was thought to be larger than the inverse of τ_d , but smaller than the inverse of the Rouse relaxation time τ_R . Polymeric chains would be oriented, but not significantly stretched. In regimes III and IV, the strain rate was assumed to be higher than the inverse of τ_R , leading to chain stretching and row-nucleated morphologies. The difference between regime III and IV was explained by the need of a certain total strain to achieve substantial chain stretching. However, Coppola *et al.* (2001) already noted earlier that the formation of row-nucleated morphologies was experimentally found to happen at much lower strain rates than the inverse of the Rouse time τ_R , thereby ruling out the argument of pronounced chain stretching as a requirement for the formation of row-nucleated structures. More likely, preventing the longest polymer chains from reptating in combination with substantial disentanglement and orientation for shear rates above the inverse of the reptation time τ_d leads to regimes III and IV.

The theoretical treatments of flow-induced crystallization range from purely phenomenological, over semi-microscopic, to fully microscopic models. The shared main goal is to connect the observed features with the applied flow conditions, thereby having to bridge the gap from microscopic chain conformation, over mesoscopic semi-crystalline morphology, to macroscopic continuum mechanics. Models that merely focus on kinetic aspects are oftentimes modifications of the treatments by Avrami, Ozawa, and Nakamura for the polymer crystallization under quiescent conditions (see subsection 3.3.6). For isothermal experiments, the Avrami model provides the following expression for athermal nucleation and spherulitic growth:

$$\phi_c/\phi_c^\infty = 1 - \exp(-E(t)) \quad \text{with} \quad E(t) = \frac{4}{3}\pi(\mathbf{G}t)^3 \cdot \frac{N}{V_{\text{total}}} \quad (3.45)$$

ϕ_c/ϕ_c^∞ : volume-related relative crystallinity, $E(t)$: extended occupied volume, \mathbf{G} : growth rate, t : time, N : number of nuclei, V_{total} : total unoccupied volume.

More generally, $E(t)$ can be defined as the integral over all individual spherulitic volumes $v(t, t_0)$ that started to grow at time t_0 multiplied by the nucleation rate \dot{N} :

$$E(t) = \int_0^t v(t, t_0) \dot{N} dt \quad (3.46)$$

The total number of nuclei N is given by the sum of all created nuclei under quiescent crystallization conditions N_q and the additional flow-induced nuclei N_s :

$$N = N_q + N_s \quad (3.47)$$

Koscher and Fulchiron (2002) linked the appearance of additional flow-induced nuclei N_s to the first normal stress coefficient N_1 by:

$$\dot{N}_s = FN_1 \quad (3.48)$$

\dot{N}_s : Flow-induced nucleation rate, F : Finger strain tensor, N_1 : first normal stress difference.

Equation 3.48 was justified by the fact that the first normal stress difference N_1 is a measure of elasticity and thus the distortion of the chain conformation. The model by Koscher *et al.* predicts the increased nucleation density and speed up of crystallization upon the application of flow. However, it doesn't take into account the modified semi-crystalline morphology in regimes III and IV at higher flow stresses and strains. A more sophisticated model was proposed by Zuidema *et al.* (2001) considering also morphological changes during flow-induced crystallization, especially the formation of row-nucleated structures above certain critical strain rates.

4 Theory of Characterization Techniques

In the following chapter, the used concepts in terms of theory, experimental design, and data analysis will be presented for each characterization method. Experimental details such as instrumental specifications, test parameters, etc. will be given in the individual chapters together with the results and discussion sections.

4.1 Rheology

Rheology is the science of flow and deformation of matter (from Greek *rheo* – "flow" and *logia* – "study of"). It combines the theoretical concepts of fluid and solid mechanics with observed flow phenomena for a range of mostly soft materials such as simple liquids, emulsions, suspensions, polymers, solutions, or gel formers that show both fluid- and solid-like character. The complexity of these materials strongly affects their flow behavior. Thus, unraveling structure-property relationships has a high importance for process engineering and product development. In the following sections, some fundamentals, common experiments, and data analysis will be presented based on books by Macosko (1994); Larson (1999); Morrison (2001); Dealy and Larson (2006); Shaw (2012); Dealy and Wang (2013).

4.1.1 Fundamentals

Flow and deformation of matter can be described by fluid and solid mechanics, which rely on the conservation of mass, momentum, and energy. The main goal in rheological experiments is to obtain information on the material properties under defined flow and deformation conditions in shear or elongation. In a simple shear experiment, the shear stress σ , the shear strain γ , and the shear strain rate $\dot{\gamma}$ are defined as intensive quantities¹ (Figure 4.1):

$$\sigma = \frac{F}{A} \quad [\sigma] = \text{Pa} \quad (4.1)$$

$$\gamma = \frac{\Delta x}{h} \quad [\gamma] = 1. \quad (4.2)$$

$$\dot{\gamma} = \frac{d\gamma}{dt} = \frac{v}{h} \quad [\dot{\gamma}] = \text{s}^{-1} \quad (4.3)$$

σ : shear stress, γ : shear strain, $\dot{\gamma}$: shear strain rate, F : force, A : area, h : height, Δx : displacement, v : velocity, t : time.

¹ For simplicity, stress σ and strain γ are treated as scalars here. In a three dimensional treatment, they would have to be defined as tensorial quantities.

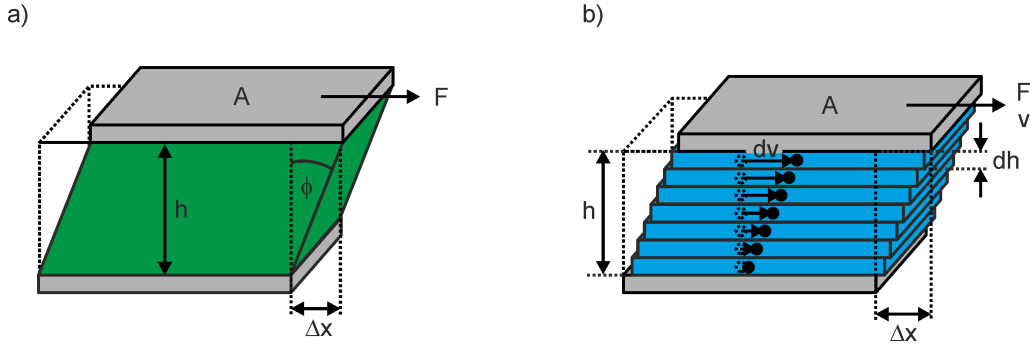


Figure 4.1: Illustration of simple shear applied to an ideal elastic solid (a) and an ideal viscous fluid (b). The definitions of stress, strain, and strain rate together with their respective relationships for the two cases are given by Equation 4.1, Equation 4.2, Equation 4.3, Equation 4.4, and Equation 4.5.

In rheology, two limiting cases of material behavior are distinguished: elasticity and viscosity. Ideal solids (Figure 4.1a) are assumed to respond purely elastic, i.e., the material will return to its original size and shape once a mechanical load is removed. This can be expressed by a proportionality between the stress σ and the strain γ with the proportionality coefficient G (the shear modulus), which corresponds to Hooke's law for a shear experiment:

$$\sigma(\gamma) = G \cdot \gamma \quad (4.4)$$

On the other hand, ideal fluids under laminar flow conditions show a proportionality between the stress σ and the strain rate $\dot{\gamma}$ with the proportionality coefficient η (the dynamic viscosity), and was found by Newton in 1687 (Figure 4.1b):

$$\sigma(\dot{\gamma}) = \eta \cdot \dot{\gamma} \quad (4.5)$$

Many real substances exhibit both elastic and viscous properties and are therefore called viscoelastic materials. In order to describe their behavior, the relationships for the limiting cases (Equation 4.4, Equation 4.5) are combined into differential equations, visually corresponding to a connection of spring and dashpot elements. A model that describes liquids with a low elastic contribution sufficiently well is the Maxwell model, which is based on a serial connection of an elastic and a viscous element. Its differential form is given by:

$$\dot{\gamma} = \dot{\gamma}_{\text{Newton}} + \dot{\gamma}_{\text{Hooke}} = \frac{\sigma}{\eta} + \frac{\dot{\sigma}}{G} \quad (4.6)$$

$$\sigma(t) = \eta \dot{\gamma} - \frac{\dot{\sigma} \eta}{G} = \eta \dot{\gamma} - \dot{\sigma} \lambda \quad (4.7)$$

$$\dot{\sigma}(t) = G \dot{\gamma} - \frac{\sigma G}{\eta} = G \dot{\gamma} - \frac{\sigma}{\lambda} \quad (4.8)$$

σ : stress, $\dot{\gamma}$: strain rate, G : shear modulus, η : viscosity, λ : relaxation time.

Solving the differential Equation 4.8 for a given problem leads to the material functions $G(t)$ and $\eta(t)$. In a stress relaxation experiment for example, the strain rate vanishes once the load is removed ($\dot{\gamma} = 0$). Thus, Equation 4.8 can be rewritten as:

$$\dot{\sigma}(t) = -\frac{\sigma}{\lambda} \quad (4.9)$$

After a separation of variables and integration, the time-dependent quantities are obtained (Macosko 1994):

$$\sigma(t) = \sigma_0 \exp\left(-\frac{t}{\lambda}\right) \quad (4.10)$$

$$G(t) = G_0 \exp\left(-\frac{t}{\lambda}\right) \quad (4.11)$$

$$\eta(t) = \eta_0 \exp\left(-\frac{t}{\lambda}\right) \quad (4.12)$$

The relaxation time $\lambda = \eta/G$ is a material parameter (e.g., molecular weight-dependent for polymers). In many cases, a single relaxation time λ is not sufficient to describe the observed relaxation behavior of complex materials and weighted sums of relaxation terms (Equation 4.13) or even full relaxation spectra (Equation 4.14) have to be considered:

$$G(t) = \sum_{k=1}^N G_k \exp\left(-\frac{t}{\lambda_k}\right) \quad (4.13)$$

$$G(t) = \int_0^{\infty} \frac{H(\lambda)}{\lambda} \exp\left(-\frac{t}{\lambda}\right) d\lambda \quad (4.14)$$

The inversion of measured experimental $G(t)$ data into relaxation time distributions $H(\lambda)$ can be carried out using regularization approaches (Thimm *et al.* 1999). From a $H(\lambda)$ distribution one can then estimate molecular properties such as the molecular weight distribution of polymers. However, a discrete number of relaxation terms is oftentimes sufficient to describe the material behavior sufficiently well (Baumgaertel *et al.* 1992).

4.1.2 Rotational and oscillatory shear rheometry

The branch of rheology that deals with apparatuses and experiments is called rheometry. Measurements of rheological quantities such as G and η can be carried out in pressure driven or drag flows. The latter offers a high versatility of different test geometries (parallel-plate, cone-plate, Couette cylinder, etc.) that can be selected depending on the type of material and the desired experimental conditions. The geometries are designed to provide different flow fields, e.g., a radius-independent shear rate $\dot{\gamma}$ in case of a cone-plate, and allow the precise calculation of stress, strain, and strain rate depending on the torque, angular velocity, and sample dimensions (Morrison 2001). There are two basic types of experiments in shear rheometry: rotational and oscillatory experiments. The former are suitable for the determination

of viscosity curves for low viscous liquids, whereas the latter are an appropriate choice for materials such as polymer melts, gels, or highly filled suspensions. As this thesis deals with crystallizing polymer melts, some features of oscillatory tests will be outlined briefly. When an oscillatory excitation is applied to a sample, the stress σ , strain γ , and strain rate $\dot{\gamma}$ become time-dependent quantities:

$$\gamma(t) = \gamma_0 \cdot \sin(\omega_1 t) \quad (4.15)$$

$$\dot{\gamma}(t) = \omega_1 \gamma_0 \cdot \cos(\omega_1 t) \quad (4.16)$$

$$\sigma(t) = \sigma_0 \cdot \sin(\omega_1 t + \delta) = G^* \cdot \gamma(t) \quad (4.17)$$

The material parameter G^* can be separated into an imaginary and a real part, and is connected to the phase angle δ by a trigonometric relation:

$$|G^*| = \sqrt{(G')^2 + (G'')^2} \quad \text{and} \quad \tan(\delta) = \frac{G''}{G'} \quad (4.18)$$

The storage modulus G' represents the elastic contributions, whereas the loss modulus G'' is a characteristic measure of all viscous contributions. This definition is based on the observation that the response of solids shows a phase angle of $\delta = 0$, i.e., the stress evolution is synchronous to the strain (ideal elasticity – see subsection 4.1.1). For viscous materials, the phase angle $\delta = 90^\circ$, standing for a maximum phase lag between the excitation and response.

Strain- and frequency-dependent measurements

For the characterization of viscoelastic materials, two rheometric tests based on a variation of strain or frequency are oftentimes used. In a strain or amplitude sweep, a sinusoidal excitation using a fixed frequency ω_1 and a varying strain amplitude $\gamma_0(t)$ is applied. In contrast, a frequency sweep is carried out using a fixed strain amplitude γ_0 in combination with a variation of the excitation frequency $\omega_1(t)$:

$$\gamma(t) = \gamma_0(t) \cdot \sin(\omega_1 t) \quad (4.19)$$

$$\gamma(t) = \gamma_0 \cdot \sin[\omega_1(t) \cdot t] \quad (4.20)$$

The strain sweep test is usually performed to distinguish the linear viscoelastic (LVE) from the non-linear viscoelastic (NLVE) regime (Figure 4.2a). At relatively low strain amplitudes γ_0 models based on linear differential equations such as the Maxwell model describe the material behavior sufficiently well. At high strain amplitudes γ_0 , the stress response becomes a non-linear function of shear rate and strain (subsection 4.1.3). In contrast to a strain sweep, a frequency sweep is used to characterize the time-dependent flow behavior of viscoelastic materials (Figure 4.2b).

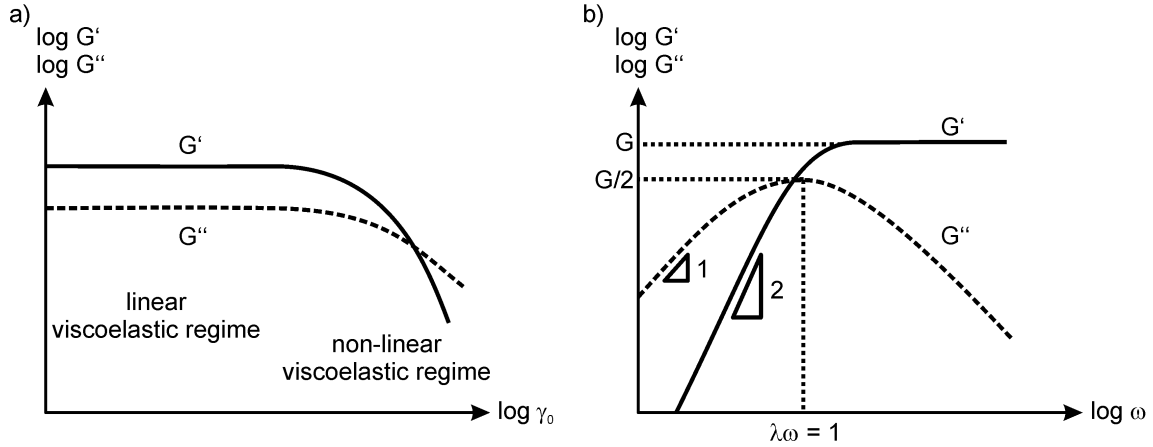


Figure 4.2: a) Strain-sweep test of a predominantly elastic material. The linear and nonlinear viscoelastic regimes are separated by a critical strain γ_{\max} . b) Frequency-dependent test of a sample that shows a Maxwell behavior according to Equation 4.21.

As discussed in the context of the Maxwell model, many materials exhibit relaxation processes that can be probed using frequency-dependent tests. For a single relaxation time λ , the frequency-dependence of storage G' and loss modulus G'' are given by (Macosko 1994):

$$G' = G \frac{(\lambda\omega)^2}{1 + (\lambda\omega)^2} \quad G'' = G \frac{\lambda\omega}{1 + (\lambda\omega)^2} \quad (4.21)$$

These relations lead to characteristic frequency-dependent curves in a log-log plot as indicated in Figure 4.2b (slope of 1 for G'' , slope of 2 for G' , at $G' = G''$ the relaxation time λ is equal to the frequency ω). Real materials are oftentimes characterized by a distribution of relaxation times. For frequency-dependent experiments, a superposition of multiple Maxwell modes usually provides a good description of measured experimental data:

$$G' = \sum_i \left[G_i \frac{(\lambda_i\omega)^2}{1 + (\lambda_i\omega)^2} \right] \quad G'' = \sum_i \left[G_i \frac{\lambda_i\omega}{1 + (\lambda_i\omega)^2} \right] \quad (4.22)$$

The time-temperature superposition principle (TTS)

The accessible frequency range in a measurement can be artificially increased by making use of the time-temperature superposition principle (TTS). For many materials, an inverse proportionality between frequency and temperature with respect to the rheological response is observed. Simply speaking, a lower frequency is mimicked by an increased temperature and vice versa. This relationship is usually expressed in the WLF-equation after its inventors Williams, Landel, and Ferry (Williams *et al.* 1955):

$$\log(a_T) = -\frac{C_1 \cdot (T - T_{\text{ref}})}{C_2 + (T - T_{\text{ref}})} \quad (4.23)$$

a_T : shift factors, T_{ref} : reference temperature, $C_1 \approx 17.4$ and $C_2 \approx 51.6$ K for $T_{\text{ref}} = T_g$.

The shift factors a_T provide the conversion ratio for all rheological quantities:

$$\log(a_T) = \log\left(\frac{\omega}{\omega_{\text{ref}}}\right) = \log\left(\frac{\eta}{\eta_{\text{ref}}}\right) = \log\left(\frac{G'}{G'_{\text{ref}}}\right) = \log\left(\frac{G''}{G''_{\text{ref}}}\right) \quad (4.24)$$

The time-temperature superposition principle is mainly used for the creation of rheological master curves. Multiple frequency-dependent measurements are recorded for different temperatures and shifted with respect to the reference temperature T_{ref} using numerical minimization algorithms. The resulting curve spans many orders of magnitude in frequency and allows the analysis of the relaxation behavior in frequency domains that are usually not accessible by experiment or would be very time consuming (Figure 4.3).

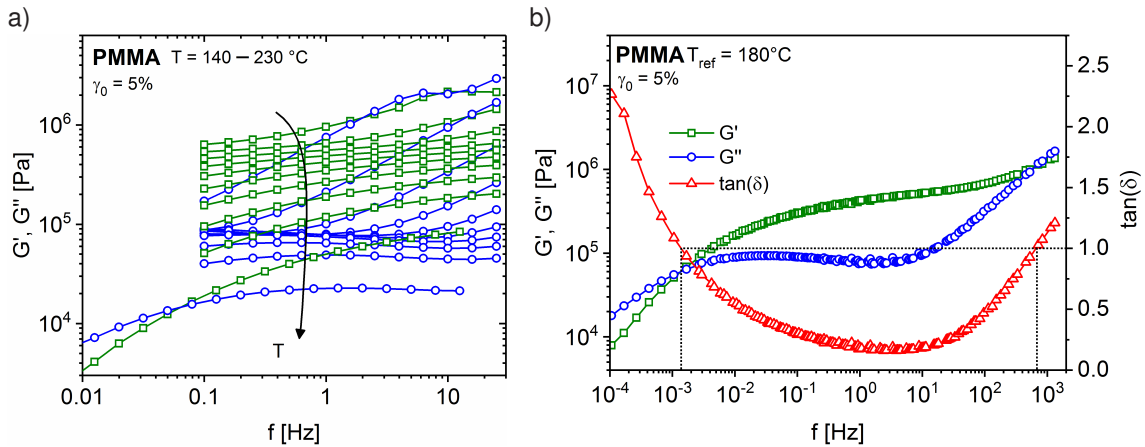


Figure 4.3: a) Frequency-dependent measurements of a poly methyl methacrylate (PMMA, M_w : 320 kg/mol, D : 2.2) at different temperatures. b) By shifting the individual frequency curves with respect to a reference temperature T_{ref} , a master curve is obtained that spans seven orders of magnitude.

4.1.3 Nonlinear rheology

Many soft materials exhibit non-linear rheological behavior, i.e., the stress response is a function of strain or strain rate. Phenomena such as shear-thickening (dilatant fluids) or shear-thinning (pseudoplastic fluids) have its origin in the microscopic structure of the materials. For example, polymers show shear-thinning, which is a consequence of the decreasing number of chain entanglements at higher strains and shear rates. Other materials such as concentrated suspensions and pastes exhibit shear-thickening as they form elastic clusters at higher strains and shear rates. In some materials, a network of associative forces has to be destroyed before a material exhibits flow, resulting in a yield stress behavior (e.g., for mayonnaise, toothpaste, or blood)². As most processing methods such as pumping, spraying, or molding involve high shear forces, the study of nonlinear rheology is of high relevance for many industries.

²Also a time-dependent behavior can be observed: thixotropy (time-dependent shear-thinning) and rheopexy (time-dependent shear-thickening).

Oscillatory nonlinear rheology

For oscillatory shear measurements, one distinguishes between experiments in the linear viscoelastic regime under small amplitude oscillatory shear (SAOS) conditions, and experiments in the nonlinear viscoelastic regime under large amplitude oscillatory shear (LAOS) conditions. The transition region is sometimes referred to as the medium amplitude oscillatory shear (MAOS) regime (Hyun and Wilhelm 2008). The nonlinear stress response of a material under LAOS conditions is characterized by a non-sinusoidal waveform that can be visualized in Lissajous or Bowditch curves as shown in Figure 4.4b, where the stress σ is plotted vs. the strain γ (Ewoldt *et al.* 2008). However, this type of representation is hardly suitable for the visualization of changing nonlinear material behavior during processes such as gel formation, crystallization, or phase separation. Additionally, a quantification of nonlinearity using geometric analysis is limited. More sophisticated approaches to quantify nonlinear behavior are the stress composition method by Ewoldt and McKinley (Ewoldt *et al.* 2008; Hyun *et al.* 2011) using Chebychev polynomials and the Fourier transform (FT) rheology method by Wilhelm (Wilhelm *et al.* 1998; Wilhelm 2002).

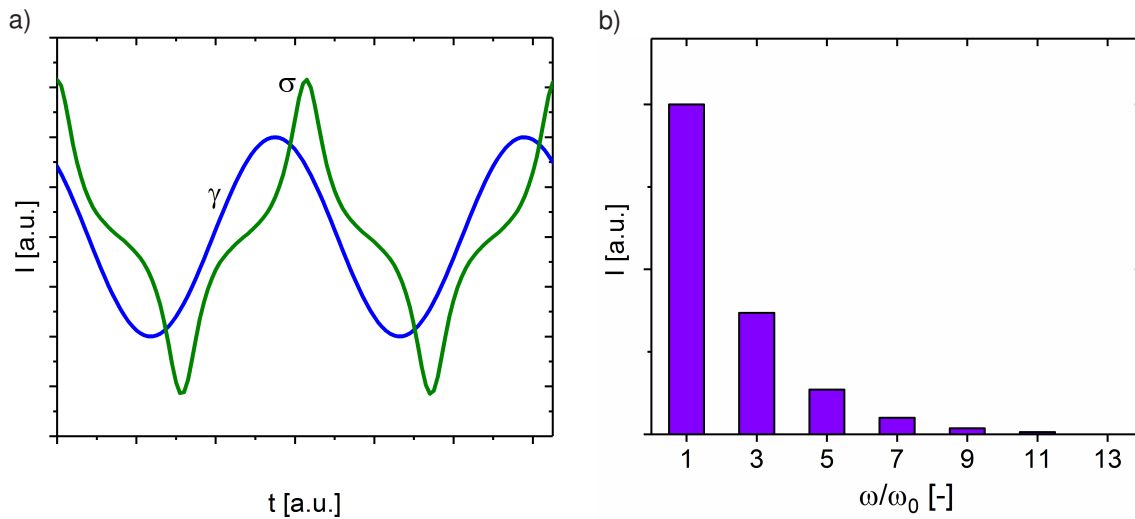


Figure 4.4: a) Schematic shear strain γ and nonlinear oscillatory stress response σ . b) Harmonic analysis based on the FT framework by Wilhelm *et al.* (1998).

The Fourier transform rheology approach is based on a harmonic analysis of the stress responses using Fourier transforms \mathcal{F} (Fourier analysis). The Fourier transform of a time-dependent signal $f(t)$ is defined as:

$$\mathcal{F}\{f(t)\} = F(\omega_1) = \int_{-\infty}^{+\infty} e^{-i\omega_1 t} \cdot f(t) dt \quad (4.25)$$

Inversely, the time-dependent signal $f(t)$ can be represented by a combination of waves:

$$f(t) = \frac{1}{2\pi} \int_{-\infty}^{+\infty} e^{i\omega t} \cdot F(\omega) d\omega. \quad (4.26)$$

Applying Fourier analysis to a stress signal leads to a corresponding frequency spectrum. For oscillatory experiments under LAOS conditions, monotonically decaying higher harmonics are observed (Figure 4.4c). As right and left turns in oscillatory experiments should yield identical responses, the stress exhibits a periodicity of 180° , which implies that even harmonics are not observed. The intensity of the third harmonic over the fundamental $I_3/I_1 = I_{31}$ has the highest sensitivity for nonlinearity and can be compared readily or as an intrinsic parameter ($Q = I_{31}/\gamma_0^2$, Hyun and Wilhelm (2008)) for different materials such as emulsions, colloidal gels, or polymer melts (Reinheimer *et al.* 2011; Kim *et al.* 2014; Cziep *et al.* 2016). Furthermore, the evolution of nonlinear behavior during transformation process like order-disorder transitions in block copolymers, gel formations, or crystallizations can be monitored and quantified (Langela *et al.* 2002; Hilliou *et al.* 2009; Dötsch *et al.* 2003; Malek *et al.* 2013).

4.2 Nuclear magnetic resonance (NMR)

Nuclear magnetic resonance (NMR) is an interaction between nuclei and electromagnetic waves in magnetic fields as well as the terminology for all corresponding characterization techniques. The earliest reported NMR experiments were carried out by Bloch *et al.* (1946). Since then a number of powerful techniques including Fourier-transform spectroscopy, multi-dimensional NMR spectroscopy, and magnetic resonance imaging (MRI) have been developed. The most important applications of NMR are the structural elucidation of mostly organic molecules and clinical *in-vivo* imaging. In the following sections, the fundamentals of NMR will be presented based on texts by Schmidt-Rohr and Spiess (1994); Slichter (1996); Kimmich (1997); Keeler (2011); Kimmich (2012).

4.2.1 Fundamentals

Nuclei consist of protons and neutrons that possess angular momentum (spin). The magnetic moment $\hat{\mu}$ is proportional to the spin angular momentum \hat{I} :

$$\hat{\mu} = \gamma \cdot \hbar \cdot \hat{I} \quad (4.27)$$

$\hat{\mu}$: magnetic moment, γ : magnetogyric ratio, \hbar : reduced Planck constant, \hat{I} : spin angular momentum.

The magnetogyric ratio γ is characteristic for each isotope and determines the sensitivity of NMR towards that specific nucleus (Table 4.1). As the most abundant isotopes of carbon (^{12}C) and oxygen (^{16}O) are undetectable by NMR ($I = 0$), the analysis of organic matter is mostly based on hydrogen nuclei / protons ($I = 1/2$, high γ and abundant, see Table 4.1). By analyzing the interactions of nearby protons, detailed information about molecular structures and their dynamics can be obtained.

Nucleus	I	Abundance [%]	Magnetogyric ratio $\gamma/2\pi$ [MHz/T]	Relative sensitivity
^1H	1/2	99.9	42.6	1
^{19}F	1/2	100	40.1	$8.32 \cdot 10^{-1}$
^{11}B	3/2	80.1	13.7	$1.65 \cdot 10^{-1}$
^{31}P	1/2	100	17.2	$6.65 \cdot 10^{-2}$
^{13}C	1/2	1.07	10.7	$1.59 \cdot 10^{-2}$
^2H	1	0.0115	6.54	$9.65 \cdot 10^{-3}$

Table 4.1: Abundances, magnetogyric ratios, and relative sensitivities for selected nuclei.

In a static magnetic field $\vec{B}_0 = (0, 0, B_0)$, the spin angular momentum \hat{I} adopts an orientation along the z -direction. The longitudinal component \hat{I}_z is quantized with $2I + 1$ eigenstates:

$$m = I, I - 1, \dots, -I \quad (4.28)$$

m : magnetic quantum number.

The absolute magnetic moment in z -direction is given by:

$$\hat{\mu}_z = m \cdot \gamma \cdot \hbar \quad (4.29)$$

The energy E is the product of the magnetic moment $\hat{\mu}$ times the static magnetic field \vec{B}_0 and leads to discrete energy levels E_m depending on the magnetic quantum number m :

$$E_m = -\hat{\mu} \cdot \vec{B}_0 = -m \cdot \gamma \cdot \hbar \cdot B_0 \quad (4.30)$$

Consequently, the energy difference ΔE_m depends on the \vec{B}_0 field as discovered by Pieter Zeeman in 1896 (Figure 4.5):

$$\Delta E_m = \gamma \cdot \hbar \cdot B_0 \quad (4.31)$$

Transitions between these energy levels can be induced by irradiating the sample with electromagnetic waves with the Larmor frequency ω_L :

$$\Delta E_m = \hbar \omega_L = \gamma \cdot \hbar \cdot B_0 \quad \Rightarrow \quad \boxed{\omega_L = \gamma \cdot B_0} \quad (4.32)$$

ω_L : Larmor precession angular frequency, γ : magnetogyric ratio, B_0 : static magnetic field.

The macroscopic net magnetization \vec{M}_0 for an ensemble of n nuclei is given by the sum of all individual magnetic moments $\vec{\mu}_i$:

$$\vec{M}_0 = \sum_{i=1}^n \vec{\mu}_i \quad (4.33)$$

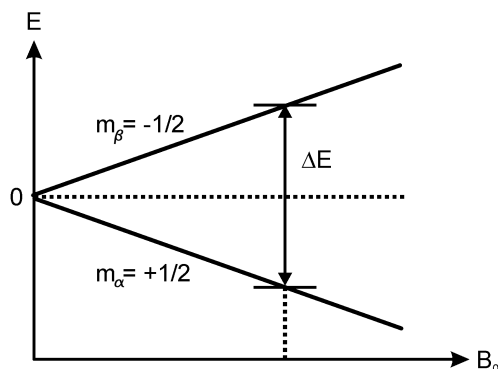


Figure 4.5: Energy E vs. static magnetic field strength B_0 for a spin $1/2$ nucleus. The two orientations of the spin angular momentum \hat{I} in the \vec{B}_0 field lead to an energy splitting ΔE (Zeeman interaction).

The population of energy levels (ground and excited eigenstates) for an ensemble of n nuclei follows a Boltzmann distribution:

$$\frac{N_\beta}{N_\alpha} = g_i \cdot \exp\left(-\frac{\Delta E_m}{kT}\right) \quad (4.34)$$

N_β/N_α : population ratio of excited vs. ground state, g_i : degeneracy of the state i .

For NMR experiments at room temperature, kT is relatively large compared to ΔE_m . Therefore, \vec{B}_0 is desired to be as large as possible to obtain the highest possible difference between the population of the ground and excited states (Figure 4.5). In modern high-field NMR spectrometers $B_0 = 10 - 20$ T using superconducting magnets with a substantial gain in signal-to-noise ratio (SNR) compared to permanent magnets (0.2 - 2 T). Overall, higher fields reduce the required measurement time for achieving a specified signal-to-noise ratio ($SNR \propto \sqrt{t}$).

NMR interactions

In molecules, nuclei are in close proximity to each other, which leads to strong interactions through chemical bonds and space. There are different types of NMR interactions such as the chemical shift, homo- and heteronuclear dipolar coupling, or J -coupling. All of them can be treated as quantum mechanical perturbations of the spin system in its unperturbed state defined by the Zeeman interaction. The basis for quantum mechanical treatments are the time-independent and time-dependent Schrödinger equations:

$$\hat{H}\psi = E\psi \quad (4.35)$$

$$i\hbar \frac{\partial \psi(t)}{\partial t} = \hat{H}\psi(t) \quad (4.36)$$

\hat{H} : Hamilton operator, E : energy, ψ : wave function, \hbar : reduced Planck constant, t : time.

Equation 4.35 leads to the energy eigenstates for a selected system that is defined by the Hamilton operator (Hamiltonian) \hat{H} . On the other hand, Equation 4.36 is relevant for all

time-dependent processes such as the excitation to and the relaxation from different energy levels, and its integration yields the time evolution of a selected system. Some important NMR interactions and their respective Hamiltonians are shown in Table 4.2. Quantum mechanical perturbation theory separates the overall Hamiltonian into a non-perturbed and perturbation term. This separation is valid for perturbations that are small compared to the entire energy of the system. Depending on the problem, calculations have to be carried out using first or higher order approximations and potentially including time-dependence. More information on the quantum mechanical description can be found in textbooks by e.g., Schmidt-Rohr and Spiess (1994); Slichter (1996); Mehring (1983).

Type of interaction	Hamiltonian	Effect
Zeeman	$\hat{H}_Z = -\gamma \hat{I}_z B_0$	Resonance at ω_L
Chemical shift	$\hat{H}_{CS} = \gamma \hat{I} \sigma \vec{B}_0$	Shift relative to ω_L
Dipolar coupling	$\hat{H}_D = -\frac{\mu_0 \hbar \gamma_1 \gamma_2}{4\pi r^3} \cdot \frac{1}{2} (3 \cos^2 \theta - 1) \{3 \hat{I}_{1z} \hat{I}_{2z} - \hat{I}_1 \cdot \hat{I}_2\}$	Line broadening / splitting
J-coupling	$\hat{H}_J = -2\pi J (\hat{I}_1 \cdot \hat{I}_2)$	Line splitting
Quadrupolar coupling	$\hat{H}_Q = \frac{eQV}{2I(2I-1)\hbar} \frac{1}{2} \{3 \hat{I}_{1z} \hat{I}_{2z} - \hat{I}_1 \cdot \hat{I}_2\}$	Line broadening / splitting
RF irradiation	$\hat{H}_{RF} = \omega_1 \hat{I}_{x/y} = -\gamma B_1 \hat{I}_{x/y}$	Rabi oscillation

Table 4.2: Hamiltonians for different interactions in frequency units and their effects on NMR. \vec{B}_0 : static magnetic field, \vec{B}_1 : induced magnetic field, γ : magnetogyric ratio, σ : chemical shift tensor, r : distance, μ_0 : vacuum permeability, θ : orientation angle between the spin pair vector and \vec{B}_0 , Q : quadrupolar moment, e : elemental charge, V : field gradient (Schmidt-Rohr and Spiess 1994; Mehring 1983).

Pulsed NMR

To rapidly investigate a large frequency range and to exploit the multiplex advantage in NMR experiments, modern spectrometers make use of short radio frequency (RF) pulses. A frequency generator with $f \simeq \omega_L/2\pi$ is turned on for short times τ (e.g., 1 – 100 μ s), producing a square wave with a corresponding spectral bandwidth of several hundred kHz. The interaction of RF pulses with nuclei in a static magnetic field can be rationalized using a vector model in a coordinate system that's rotating with ω_L . At equilibrium, the macroscopic magnetization \vec{M}_0 is aligned along the \vec{B}_0 field, which is defined as being oriented along z . Once an RF pulse is applied, the \vec{B}_1 field in the NMR probe coil interacts with the magnetization \vec{M}_0 , leading to a rotation of \vec{M}_0 along the field axis of the induced field \vec{B}_1 in a ω_L rotating frame.

The most often applied pulses have defined pulse angles of $\theta = 90^\circ$ ("90° pulse") and $\theta = 180^\circ$ ("180° pulse"). During an ideal 90° pulse, the magnetization is completely transferred to the xy plane, whereas during a 180° pulse, the magnetization is inverted along the z -axis. The NMR signal can be regarded as a magnetic field inducing a voltage into the NMR probe coil. Once an RF pulse has ended, the magnetization gradually relaxes back to equilibrium. These

processes are divided into transverse relaxation in the xy plane, and longitudinal relaxation along the z -axis (\vec{B}_0 field direction). NMR relaxation can be empirically described by a set of differential rate equations that were proposed by Bloch (1946) (Nobel prize 1952):

$$\frac{dM_z(t)}{dt} = -\frac{M_z(t) - M_{z,0}}{T_1} + \gamma [\vec{M}(t) \times \vec{B}(t)]_z \quad (4.37)$$

$$\frac{dM_y(t)}{dt} = -\frac{M_y(t)}{T_2} + \gamma [\vec{M}(t) \times \vec{B}(t)]_y \quad (4.38)$$

$$\frac{dM_x(t)}{dt} = -\frac{M_x(t)}{T_2} + \gamma [\vec{M}(t) \times \vec{B}(t)]_x \quad (4.39)$$

In a static magnetic field $\vec{B}_0 = (0, 0, B_0)$ and upon a 90°_ϕ pulse ($M_{z,0} = 0$), the solutions for Blochs linear differential equations are given by:

$$M_z(t) = M_{z,\infty} \cdot \left[1 - \exp\left(-\frac{t}{T_1}\right) \right] \quad (4.40)$$

$$M_y(t) = M_{y,0} \cdot \exp\left(-\frac{t}{T_2}\right) \quad (4.41)$$

$$M_x(t) = M_{x,0} \cdot \exp\left(-\frac{t}{T_2}\right) \quad (4.42)$$

The relaxation times T_1 and T_2 describe the respective buildup or decay of magnetization and contain information about interactions between different nuclei. T_1 is called the spin-lattice relaxation time, and T_2 is referred to as the spin-spin relaxation time. Multiple phenomena lead to a decaying behavior in the time domain or the corresponding broadening of resonance lines in a spectrum. They can be classified as coherent and incoherent interactions (Schmidt-Rohr and Spiess 1994). An important difference is that whereas coherent interactions can be refocused, incoherent interactions lead to an irreversible decay of magnetization. The former type is usually caused by dipolar dephasing in multispin systems and the coherent part can be refocused using echo pulse sequences. The latter is a consequence of stochastic local field fluctuations and is referred to as NMR relaxation in a more narrow sense.

4.2.2 Theory of NMR relaxation

The origin of NMR relaxation in ensembles of n nuclei with $I \neq 0$ lies in incoherent interactions of stochastically fluctuating fields that are caused by molecular motion. A frequently applied theory of NMR relaxation was described by Bloembergen *et al.* (1948), and is usually referred to as the Bloembergen-Purcell-Pound (BPP) model. An important prerequisite for the theory is that motions have to be fast compared to the inverse of the induced coupling frequencies. The BPP model is well suited for the description of liquids, but is limited in its applicability to solids. More elaborate theories are based on density operator formalisms (Redfield 1957).

Molecular motion and the spectral density

Similar to other techniques such as dynamic light scattering, X-ray scattering, or dielectric spectroscopy, stochastic fluctuations are accounted for by an autocorrelation or memory function $G(\tau)$. For the most simple case of a single characteristic correlation time τ_c , the autocorrelation function of local field fluctuations can be assumed to follow a mono-exponential decay:

$$G(\tau) = \exp\left(-\frac{\tau}{\tau_c}\right) \quad (4.43)$$

The autocorrelation function $G(\tau)$ can be converted into a frequency-dependent quantity $J(\omega)$ by applying a Fourier transform (Equation 4.26):

$$J(\omega) = \int_{-\infty}^{+\infty} e^{-i\omega\tau} \cdot G(\tau) d\tau \quad (4.44)$$

The spectral density $J(\omega)$ contains information on the magnitude of individual frequency components $d\omega$. By inserting Equation 4.43 into Equation 4.44 and integration over all $d\tau$, the spectral density for a single correlation time τ_c is given by:

$$J(\omega, \tau_c) = \frac{2\tau_c}{1 + \omega^2\tau_c^2} \quad (4.45)$$

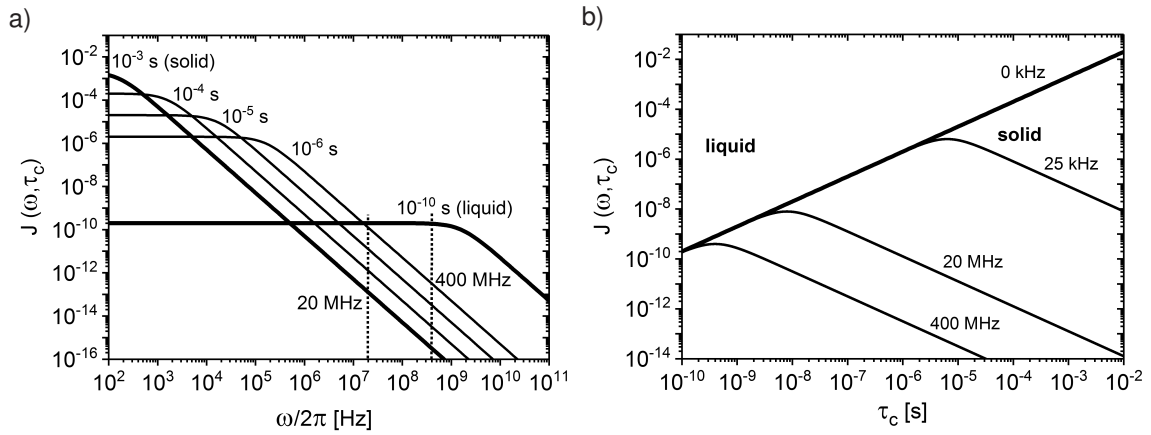


Figure 4.6: Spectral density $J(\omega, \tau_c)$ plotted vs. $\omega/2\pi$ (a) and τ_c (b) for different material states (liquid to solid), Larmor frequencies ω_0 , and interaction frequencies $\Delta\omega$ according to Equation 4.45.

The characteristic correlation time τ_c has a strong temperature-dependence, and can e.g., be described by an Arrhenius (or WLF, Equation 4.23) activation behavior if phase transitions are absent:

$$\tau_c = \tau_\infty \exp\left(-\frac{E_A}{kT}\right) \quad (4.46)$$

Thus, the τ_c -axis can also be seen as an inverse temperature axis, suggesting temperature-dependent experiments to obtain information on the correlation times and related molecular dynamic processes.

The BPP model of NMR relaxation

NMR relaxation is caused by local magnetic field fluctuations induced by molecular motion. The local magnetic field $\vec{B}_{\text{loc}}(t)$ can be treated as a quantum mechanical perturbation. The Hamiltonian has the form of a magnetic field-induced perturbation (similar to e.g., an RF pulse – see Table 4.2):

$$\hat{H} = -\gamma \hat{I}_x B_{x,\text{loc}}(t) \approx -\gamma \hat{I}_x B_{x,\text{loc}}(0) f(t) \quad (4.47)$$

The Bloch equations (Equation 4.40, Equation 4.41, Equation 4.42) can be seen as special cases of a general transition process:

$$\frac{dN(t)}{dt} = \frac{dM(t)}{dt} \propto -k \cdot M \quad (4.48)$$

NMR relaxation is a second order transition involving multiple spins, and its treatment necessitates second order perturbation theory. The transition rate for second order transitions is given by Fermi's Golden Rule No. 1 (Fermi (1950), p. 148)³:

$$\frac{dN_\gamma(t)}{dt} = \frac{2\pi}{\hbar} \left[\frac{\langle \gamma | \hat{H} | \alpha \rangle \cdot \langle \beta | \hat{H} | \gamma \rangle}{E_\alpha - E_\gamma} \right]^2 \rho(E) \quad (4.49)$$

$\rho(E)$: density of eigenstates.

Application of Equation 4.49 to NMR relaxation by including the homonuclear dipolar coupling Hamiltonian (Equation 4.47) and the spectral density $J(\omega)$ as $\rho(E)$, and integration of the differential form leads to the BPP model expressions for the transverse and longitudinal relaxation times:

$$\frac{1}{T_1} = \left(\frac{\mu_0 \hbar}{4\pi} \right)^2 \frac{\gamma^4}{5r^6} I(I+1) [J(\omega_0, \tau_c) + 4J(2\omega_0, \tau_c)] \quad (4.50)$$

$$\frac{1}{T_2} = \left(\frac{\mu_0 \hbar}{4\pi} \right)^2 \frac{\gamma^4}{10r^6} I(I+1) [3J(\Delta\omega = 0, \tau_c) + 5J(\omega_0, \tau_c) + 2J(2\omega_0, \tau_c)] \quad (4.51)$$

Inserting the respective spectral density terms $J(\omega)$ for a single correlation time τ_c (Equation 4.45) leads to a characteristic τ_c -dependence for T_1 and T_2 (Figure 4.7).

The spin-lattice relaxation time T_1 is governed by the Larmor frequency ω_0 , and exhibits a minimum, whereas T_2 is governed by the term $\Delta\omega = 0$. The BPP model assumes relaxation in the motional averaging limit where the product of the static coupling angular frequency and the motional correlation time $\Delta\omega\tau_c \ll 1$. The interaction term $\Delta\omega$ in Equation 4.51 is assumed to be zero, and consequently a monotonic decay is observed in Figure 4.7. If motional averaging is not as effective, a non-vanishing term $\Delta\omega$ (e.g., 25 kHz) can be taken into account, leading to a non-monotonic decay (Zimmer *et al.* 1994, 1995).

³ Fermi's Golden Rule No. 2 is the other well-known *Golden Rule* for first order transitions.

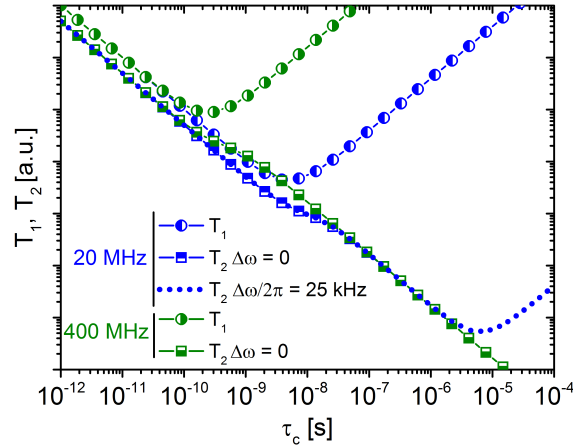


Figure 4.7: Calculated longitudinal T_1 and transverse T_2 relaxation time curves based on Equation 4.51 for different Larmor frequencies ω_0 and interaction terms $\Delta\omega$ plotted against the correlation time τ_c (inversely proportional to temperature). T_1 shows a minimum, whereas T_2 shows a monotonic decrease for $\Delta\omega = 0$. For a non-vanishing interaction term of e.g., $\Delta\omega = 25$ kHz, T_2 exhibits a minimum, too.

A third type of relaxation is observed when a sample is being continuously irradiated with an additional electromagnetic wave or, i.e., is exposed to an additional \vec{B}_1 field (spin-locking):

$$\frac{1}{T_{1\rho}} = \left(\frac{\mu_0 \hbar}{4\pi} \right)^2 \frac{\gamma^4}{10r^6} I(I+1) [3J(2\omega_1, \tau_c) + 5J(\omega_0, \tau_c) + 2J(2\omega_0, \tau_c)] \quad (4.52)$$

ω_1 : spin locking frequency – directly to the applied \vec{B}_1 field.

This third type is called relaxation in the rotating frame and can be used to probe relaxation at specific angular frequencies. Experimentally, a prolonged relaxation behavior with increased relaxation times is frequently observed.

4.2.3 NMR pulse sequences

The development of NMR pulse sequences is a very important branch of NMR research, as molecular structure and dynamics can be investigated selectively using clever combinations of pulses (Kimmich 2012). Some basic sequences for the determination of transverse and longitudinal relaxation times will be presented briefly in the following.

Transverse relaxation – Determination of T_2

The most simple experiment for measuring transverse relaxation is a single 90° pulse experiment. The succeeding signal decay is called a free induction decay (FID) and has the characteristic transverse relaxation time T_2^* . For highly mobile samples, T_2^* is usually governed by the \vec{B}_0 field homogeneity, i.e., the decay is not sample-, but magnet-specific. In order to obtain transverse relaxation times even for mobile samples, the spin echo sequence can be performed (Figure 4.8a, Hahn (1950)). The coherence of a spin system is gradually lost upon

the application of a 90° pulse (e.g., as if many watches are not perfectly in sync). An additional 180° pulse is applied after time τ , leading to an effective time reversal, and phase coherence is re-obtained after another time τ . Varying τ , the full relaxation curve can be obtained by analyzing the echo maxima.

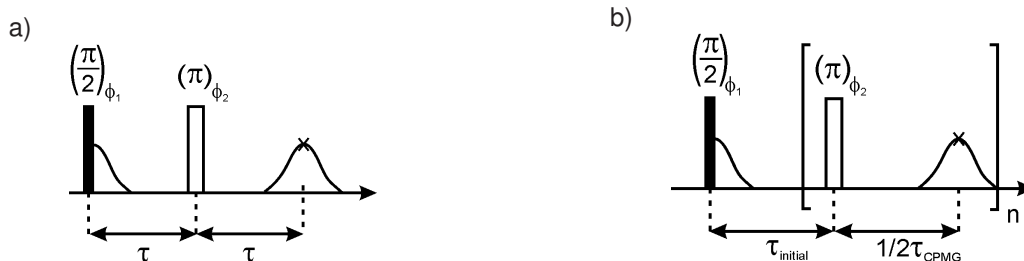


Figure 4.8: a) Spin echo sequence for studying transverse relaxation in mobile samples (Hahn 1950). b) Carr-Purcell-Meiboom-Gill sequence as a time-saving alternative to a spin echo sequence for the study of transverse relaxation in mobile samples (Carr and Purcell 1954; Meiboom and Gill 1958).

The variation of τ in a spin echo sequence is very time consuming and prevents the use of such a sequence for e.g., rapid monitoring of T_2 relaxation. An alternative is the CPMG sequence after its inventors Carr and Purcell (1954); Meiboom and Gill (1958). Following a 90° pulse, transverse relaxation is studied by a train of 180° pulses and corresponding echoes. In its original form, the time between all 180° pulses is exactly twice that of the time between the initial 90° pulse and the first 180° pulse. However, the timing between the second and all further 180° pulse can also be chosen differently. The benefit of the CPMG sequence is that it enables the measurement of a full relaxation curve in a single experiment. It can lead to substantial heating of the sample, and can be compensated by strong gas flow to ensure a constant sample temperature. Furthermore, short pulse timing can cause spin-lock type relaxation (Equation 4.52). Phase cycles such as MLEV-4, XY-16, etc. suppress this effect (Gullion *et al.* 1990). In solids, the spin system is not fully refocused by a 180° pulse, which is a consequence of the fast dipolar dephasing caused by homonuclear dipolar coupling. However, a 90° pulse leads to phase coherence for a strongly coupled two spin system as shown by Powles and Strange (1963) and Ostroff and Waugh (1966). This phenomenon can be theoretically predicted using density operator formalisms, and is referred to as a solid echo (Figure 4.9a).

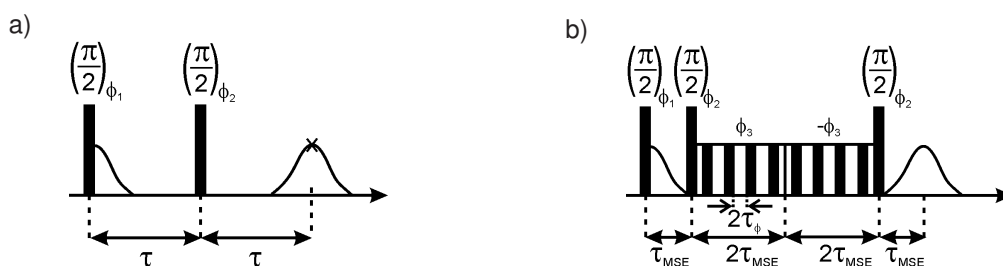


Figure 4.9: a) Solid echo sequence for studying transverse relaxation in solid samples (Powles and Strange 1963). As the solid echo does not fully refocus multi-body interactions, the mixed magic sandwich echo sequence (b) is a more quantitative alternative (Rhim *et al.* 1971; Pines *et al.* 1972; Takegoshi and McDowell 1985; Hafner *et al.* 1996).

Multi-body interactions are not completely refocused by a solid echo sequence. A more quantitative alternative for real solid materials are magic echo sequences (Rhim *et al.* 1971; Pines *et al.* 1972; Takegoshi and McDowell 1985; Hafner *et al.* 1996). The sequence shown in Figure 4.9b is one example, and is called the mixed magic sandwich echo sequence (MSE). All magic echo sequences are based on an effective time reversal of the phase coherence evolution in a multi-body spin system. The quantitative refocusing of even strongly dipolar coupled systems makes the MSE sequence a preferential candidate for reconstructing the initial part of an FID of solid samples, which is usually not accessible due to the dead time of NMR probes. However, if stochastic motions act on the time scale of the MSE refocusing block, the time reversal does not work properly, and consequently attenuated echo intensities are observed. Furthermore, the duration τ_ϕ has to be optimized for each individual set-up with respect to the echo intensity and occurrence of the maximum intensity after the duration $\tau_{\text{MSE}} = 4\tau_\phi + 4.5p_{90}/2$.

Longitudinal relaxation – Determination of T_1

Longitudinal relaxation cannot be studied directly in z -direction, as the strong \vec{B}_0 field inhibits its measurement. By flipping the magnetization into the xy plane using appropriate pulse sequences, the M_z magnetization can be detected. Two common pulse sequences are inversion recovery and saturation recovery (Figure 4.10). The former is based on an full inversion of the magnetization vector by applying a 180° pulse. Increasing the waiting time τ and flipping the recovered magnetization into the xy plane, leads to a buildup curve from which the longitudinal relaxation time T_1 is extracted. The saturation recovery sequence is based on a cascade of 90° pulses that destroys all magnetization (saturation). By increasing the waiting time τ , the buildup of magnetization in z -direction can be studied, leading again to the longitudinal relaxation time T_1 . Instead of evaluating the FID upon a 90° pulse, one can also add a CPMG sequence to the respective inversion or saturation recovery sequences.

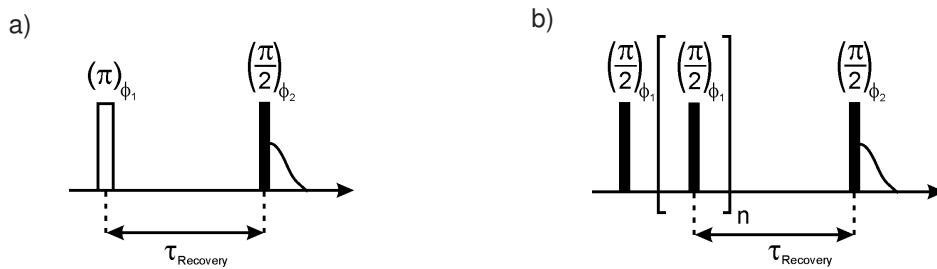


Figure 4.10: Pulse sequences for the study of longitudinal relaxation: a) Inversion recovery sequence. b) Saturation-recovery sequence. Both sequences can also be combined with refocussing sequences in the transverse plane for the detection of recovered magnetization.

4.3 X-ray scattering

The scattering of X-rays with wavelengths of 10 pm to 10 nm is widely used in material science to study structural order on a nanometer to Ångström scale (soft to hard X-rays with photon energies of 100 eV to 100 keV). The term "scattering" indicates that the fundamental concepts are similar to visible light and electron scattering and can be categorized into two types: elastic and inelastic with either no or some change in photon energy, respectively⁴. For polymers, the elucidation of crystal structures, the study of nano-scale morphologies, and the structure of polymers in solution are the most important applications. In the following sections, the fundamentals of X-ray scattering will be presented based on texts by Baltá-Calleja and Vonk (1989); Guinier and Fournet (1955); Glatter and Kratky (1982); Chu and Hsiao (2001).

4.3.1 Fundamentals

The scattering of X-rays can be treated as a collision of X-ray photons with the electrons surrounding atomic nuclei or as an interaction between the electrons and the \vec{E} -field component of light (see e.g., (Baltá-Calleja and Vonk 1989)). In Figure 4.11, the scattering of incident X-rays by a single electron is shown schematically.

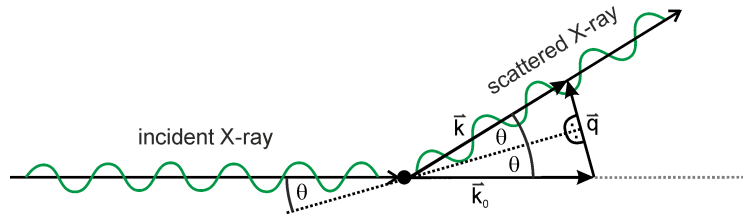


Figure 4.11: Elastic scattering of X-rays by a single electron at an angle 2θ ($|\vec{k}| = |\vec{k}_0|$).

The deflection of an incident beam is usually expressed using the angle 2θ or the corresponding scattering vector \vec{q} (Equation 4.53)⁵:

$$|\vec{q}| = |\vec{k} - \vec{k}_0| = \frac{4\pi\sin\theta}{\lambda} \quad (4.53)$$

θ : scattering angle, \vec{q} : scattering vector, $|\vec{k}| = 2\pi/\lambda$: wave vector, λ : wavelength.

Generally, one distinguishes between scattering at small and wide angles (SAXS and WAXS, respectively) with $2\theta_{\text{SAXS}} \leq 5^\circ \leq 2\theta_{\text{WAXS}}$ ($q_{\text{SAXS}} \leq 0.5/\text{\AA} \leq q_{\text{WAXS}}$ for $\lambda = 1.5 \text{\AA}$) as available experimental set-ups are optimized for these two regimes. In Figure 4.12, a typical experimental set-up for SAXS experiments is shown. The scattering intensities are detected in two dimensions as a function of the scattering vector \vec{q} and the azimuthal angle χ . In addition to the characteristic length scales provided by the scattering vector \vec{q} , the azimuthal angle

⁴ The elastic scattering from crystalline materials is also referred to as X-ray diffraction (XRD), thereby stressing the wave nature of light.

⁵ In older literature, definitions based on the scattering vector $\vec{s} = \vec{q}/2\pi$ can be found.

contains information on the degree of orientation of ordered structures. For time-resolved experiments, usually synchrotron X-ray radiation is needed to achieve a substantial photon count per unit area in a given time interval. Most synchrotron sources provide a large bandwidth of X-ray wavelengths, which can be tailored to the needs of the individual experiment by using monochromators (for $\lambda = 1.5 \text{ \AA}$ e.g., Si333 or Ge333 crystals).

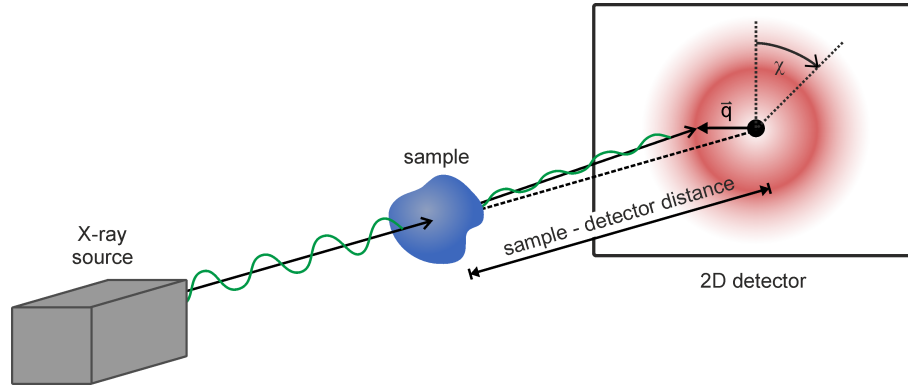


Figure 4.12: Set-up for small-angle X-ray scattering (SAXS) including the source, a sample, and the 2D detector.

4.3.2 Theory of scattering

For a single electron, the observed scattering intensity corresponds to a spherical angular-independent wave. However, for multiple scattering centers, the intensity or number of photons measured at a given angle 2θ is determined by the interference pattern of the scattered X-rays (see Figure 4.13). In case of constructive interference, a strong signal is detected, whereas for destructive interference the intensity vanishes at any given angle 2θ . The condition for constructive interference was described by W. L. and W. H. Bragg in 1913:

$$\frac{4\pi\sin\theta}{n\lambda} = \frac{2\pi}{d} = |\vec{q}| \quad (\text{Bragg's law}) \quad (4.54)$$

θ : scattering angle, \vec{q} : scattering vector, d : distance between two electrons in real space (long period), n : order of scattering, λ : wavelength.

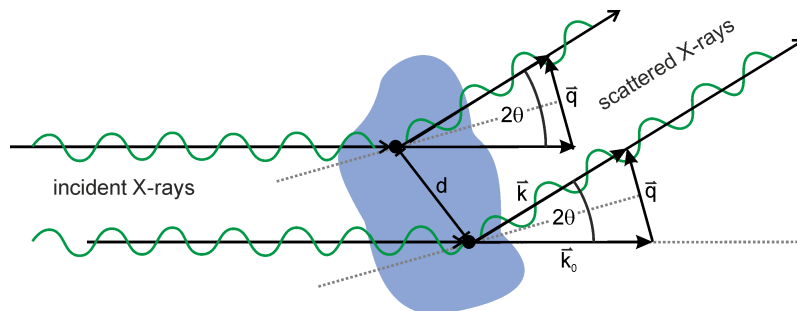


Figure 4.13: Scattering of X-rays by two electrons. Constructive interference of the scattered X-rays leads to a detectable signal intensity at an angle 2θ .

For every spatial arrangement of electrons in real space, there exists a corresponding lattice in \vec{q} -space (reciprocal space). The Bragg condition (Equation 4.54) can be rationalized using the Ewald sphere construction shown in Figure 4.14. The intersection of the Ewald and reciprocal space spheres determines the scattering pattern. In case there is a reciprocal lattice point exactly on the intersecting ring, a scattering reflex is observed. For highly ordered single crystals, a map of the reciprocal lattice is obtained, whereas for polycrystalline materials, rings of different $|\vec{q}|$ values are found as shown in Figure 4.15. Furthermore, semi-circular patterns can be observed when a substantial degree of orientation is present in polycrystalline materials.

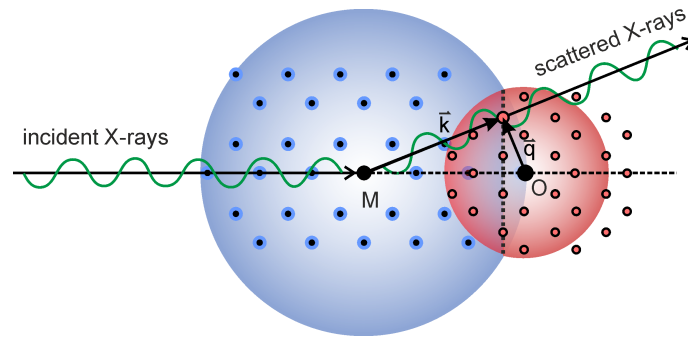


Figure 4.14: Construction of the Ewald sphere at point M and the reciprocal sphere at point O . In case there are reciprocal lattice points on the intersecting ring, scattering reflexes are observed.

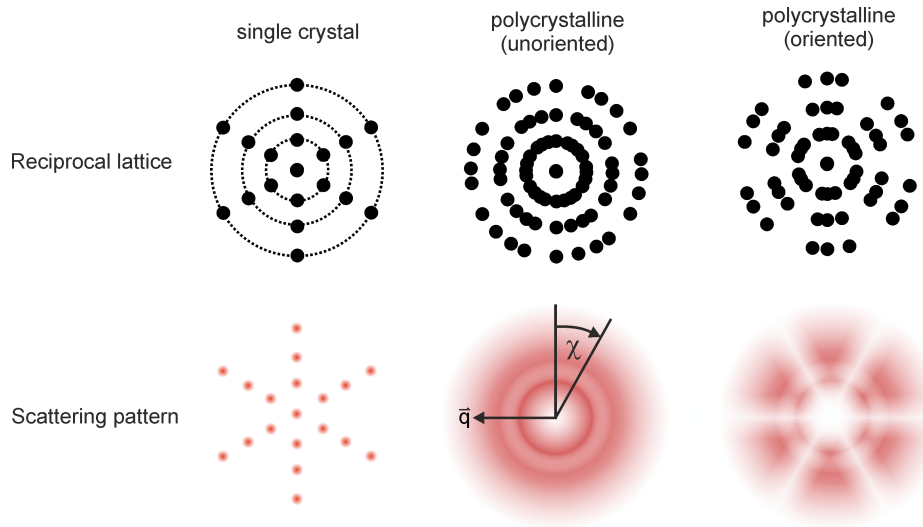


Figure 4.15: Reciprocal lattices and scattering patterns for a single crystal and unoriented / oriented polycrystalline materials (see also Figure 4.12).

In real materials, many scattering centers (electrons) are present that all contribute to the observed intensity profile $I(q)$. One distinguishes between contributions from electrons of the same or other scattering objects by introducing the form and structure factor:

$$I(q) \propto P(q)S(q) \tag{4.55}$$

$I(q)$: intensity, $P(q)$: form factor, $S(q)$: structure factor, $q = |\vec{q}|$: absolute scattering vector.

The form factor $P(q)$ is related to the shape of the scattering object, whereas the structure factor $S(q)$ describes the degree of order in a set of multiple scattering objects. For dense materials, the structure factor is the dominating part, and it is related to its electron density correlation function $\rho(z)$ by a Fourier cosine transform:

$$S(q) = \int_0^{\infty} \rho(z) \cdot \cos(qz) dz \quad (4.56)$$

$S(q)$: structure factor, $\rho(z)$: correlation function, z : distance in real space.

Scattering from lamellar systems

Materials with a high degree of order and periodicity in one dimension present a special case for the analysis of X-ray scattering data as their electron density fluctuates only in one dimension. Theoretical treatments by Vonk and Kortleve (1967); Vonk (1978) and later by Strobl and Schneider (1980) on the basis of one-dimensional correlation functions showed good agreement with experiment data and will be presented briefly. The starting point for these models is the reduction of the measured three-dimensional intensity profile $I(q)$ into a one-dimensional one by applying the Lorentz correction (Baltá-Calleja and Vonk 1989):

$$I_1(q) = I(q) \cdot q^2 \quad (4.57)$$

$I_1(q)$: one-dimensional intensity, $I(q)$: measured intensity, q : absolute scattering vector.

In Figure 4.16, both, the measured and the Lorentz-corrected intensity profiles are shown for a material with a periodic lamellar structure. The Lorentz correction shifts the scattering maxima to higher values, corresponding to a slightly smaller long period $d = 2\pi/q$.

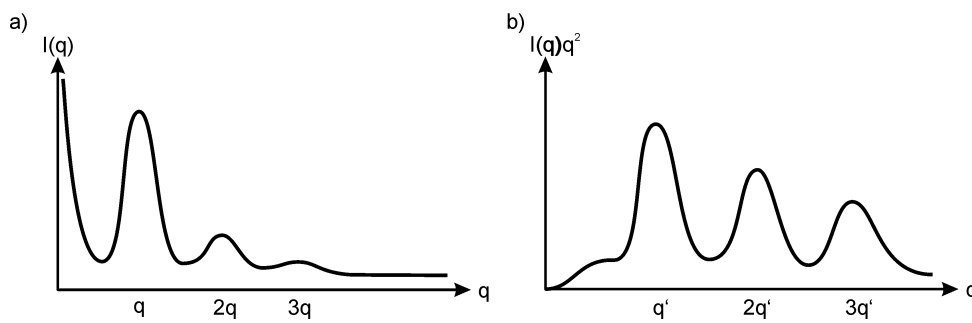


Figure 4.16: $I(q)$ intensity profile for a lamellar material (a) and the Lorentz-corrected profile (b).

From the Lorentz-corrected intensity profiles $I_1(q)$, a correlation function $K(z)$ can be deduced:

$$K(z) = \int_0^{\infty} I_1(q) \cdot \cos(qz) dq \quad (4.58)$$

$K(z)$: correlation function, z : distance in real space, q : absolute scattering vector.

For an ideal lamellar structure with equidistant spacing of perfect lamellae of only one single thickness, the correlation function becomes a triangular function (Figure 4.17b). For less ideal systems the correlation function $K(z)$ shows a damped oscillating behavior (Figure 4.17d, Strobl and Schneider (1980)).

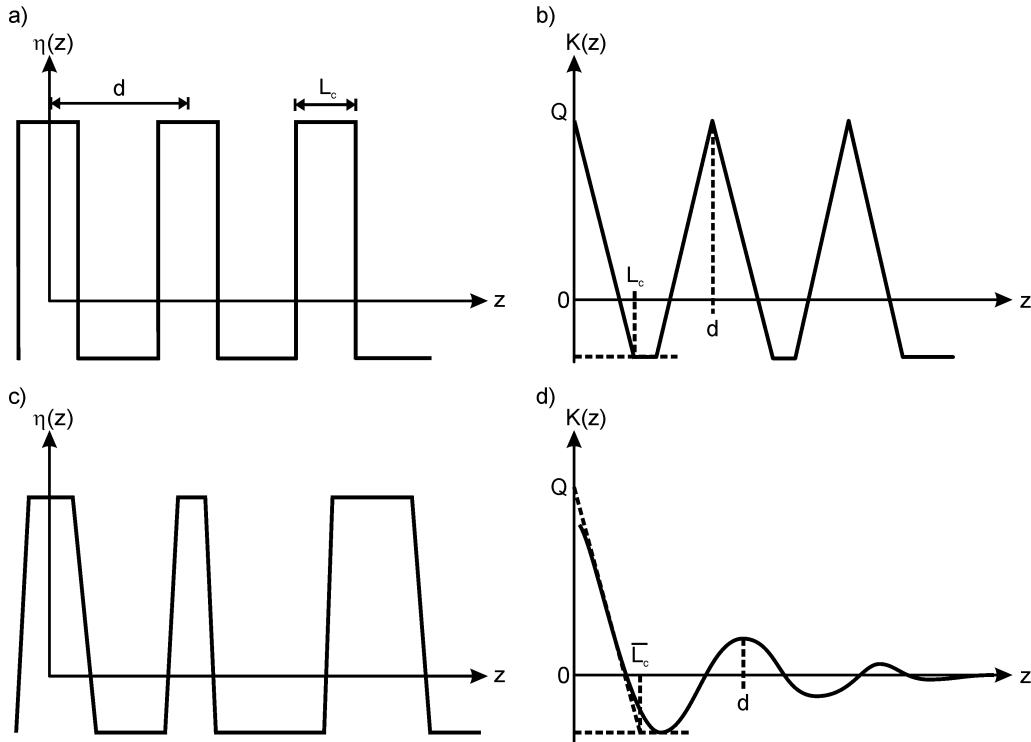


Figure 4.17: Electron density distribution $\eta(z)$ and related correlation functions $K(z)$ for an ideal lamellar system (a, b) and a less perfect material with variations in the thickness L_c , spacing between the lamellae, and surface thickness variations. Figure adapted from Strobl and Schneider (1980).

By determining the correlation function $K(z)$ from experimental scattering data, the mean lamellar thickness $\overline{L_c}$ can be extracted together with other quantities as the invariant Q , and can be converted into a crystallinity X_c for semi-crystalline polymers. As for these materials, lamellar thicknesses are on the order of 10 – 20 nm, the commonly employed technique to characterize them is small-angle X-ray scattering (SAXS). The obtained results on the lamellar thickness can be readily compared with theoretical predictions by the Gibbs-Thomson equation (Equation 3.15). Ultimately, SAXS measurements triggered Strobl to propose his multistage model (see subsection 3.3.5), as his group detected differences in the lamellar thicknesses upon crystallization and melting. In addition, SAXS reflexes at small q values that occurred prior to the formation of lamellae were assigned to density fluctuations and gave rise to the spinodal decomposition model of Olmsted *et al.* (see subsection 3.3.4).

5 Molecular Dynamics of Semi-Crystalline Polymers Studied by NMR

Nuclear magnetic resonance (NMR) techniques were used to study semi-crystalline polymers with a main focus on the investigation of the temperature-dependent molecular dynamics in semi-crystalline polymers and its use for monitoring crystallization kinetics at low magnetic fields. Furthermore, the goal was to develop a routine that could also be used for *in-situ* experiments using hyphenated RheoNMR (see chapter 6). The works were carried out at the Pro²NMR facility under supervision of Prof. G. Guthausen with support from Prof. H. Horn. Parts of this chapter are based on a recently published journal article (Räntzsch *et al.* 2018).

5.1 Introduction

In addition to detailed structural information, NMR also provides substantial insight into dynamic processes on wide time and length scales depending on the type of NMR experiments (section 4.2, p. 51). Here, we focused on transverse relaxation measurements at high and low fields of 400 and 20 MHz, respectively. NMR relaxometry is sensitive to molecular mobility on a length scale of nanometers and a time scale of 10^{-10} – 10^{-2} s. Different materials with a difference in molecular dynamics have been studied by ¹H-NMR in the past, e.g., fats (Todt *et al.* 2006a,b), rubbers (Litvinov and van Duin 2002; Saalwächter *et al.* 2005), carbohydrates (Derbyshire *et al.* 2004), composites (Papon *et al.* 2011; Guthausen *et al.* 2014), and semi-crystalline polymers (Fujimoto *et al.* 1972; Kitamaru and Horii 1978; Bergmann and Nawotki 1967; Bergmann 1978, 1981; Packer *et al.* 1984; Eckman *et al.* 1997; Kristiansen *et al.* 1999; Litvinov and Penning 2004; Hertlein *et al.* 2006). Most studies on semi-crystalline polymers were conducted at high fields with a focus on the decomposition of the FID into multiple components, which is possible due to the high \vec{B}_0 homogeneities and short NMR probe dead times of $\approx 5 \mu\text{s}$ (Dadayli *et al.* 1994; Feio and Cohen-Addad 1988; Feio *et al.* 1989; Hansen *et al.* 1998; Kristiansen *et al.* 2000, 2001). However, transverse relaxation of very rigid components can be so fast that pulse sequences based on solid (Tanaka and Nishi 1986a,b) and magic echoes (Takegoshi and McDowell 1985; Sergeev *et al.* 1985; Demco *et al.* 2003; Maus *et al.* 2006) are needed to reconstruct the FID in order to obtain information on the initial relaxation behavior (0 – 5 μs) of strongly homonuclear dipolar coupled ¹H multi-body spin systems (see subsection 4.2.3, p. 58).

NMR relaxation is strongly temperature-dependent as discussed in subsection 4.2.2, p. 55. For polymers, the glass transition temperature T_g characterizes the temperature below which coordinative segmental motions are inhibited and high rigidity is observed. Far above T_g ,

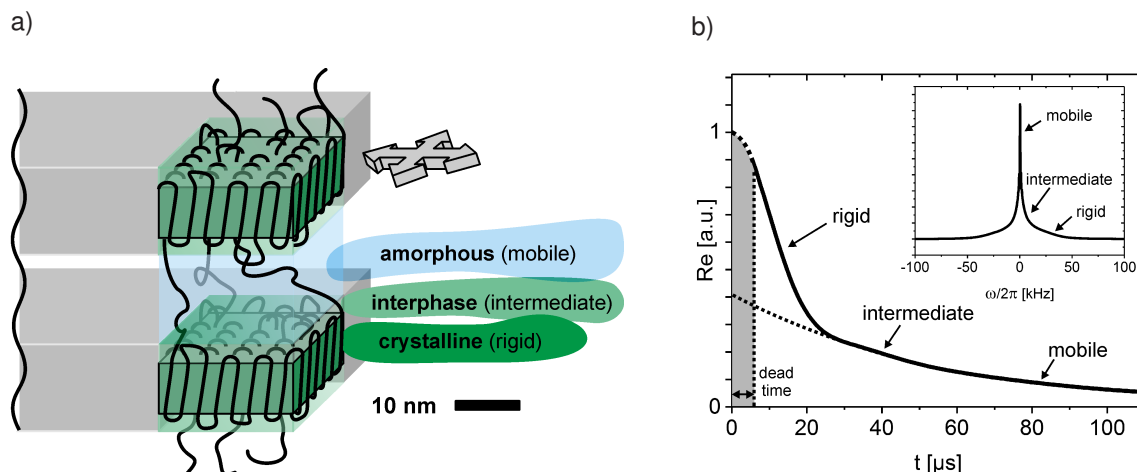


Figure 5.1: a) Lamellar substructure and assigned regions of molecular mobility. b) ^1H -NMR free induction decay (FID) and spectrum (inset) for a semi-crystalline polymer far above T_g . Homonuclear dipolar coupling leads to a strong line broadening and a fast decay in the time domain (see also section 4.2, p. 51).

protons in the center of a polymer crystal remain rigid with $\tau_{c,\text{rigid}} \approx 10^{-3}$ s, whereas interfacial protons have an intermediate mobility with $\tau_{c,\text{intermediate}} \approx 10^{-4}$ s, and amorphous ones are mobile with $\tau_{c,\text{mobile}} \approx 10^{-6}$ s (Schmidt-Rohr and Spiess (1994), exceptions are polymers with pronounced mobility in crystalline domains such as helical flips). As the transitions between phases with different mobilities are relatively smooth, choices have to be made when to call a proton "crystalline", "interfacial", or "amorphous" (Figure 5.1). This ambiguity can lead to varying results and is a reason for the differences in absolute crystallinity compared to DSC, XRD, or microscopy. Each technique measures different physical quantities (heat of fusion, unit cell order, birefringence, etc.) and therefore differences in the crystallinity X_c are also a consequence of the different sensitivity and selectivity towards the crystalline fraction.

Modeling of the transverse magnetization decay

Polymers are complex multi-spin systems where multibody interactions between nearby protons are present leading to distributions in the dipolar couplings. One can approximate the interactions using only the nearest neighbors due to the local nature of homonuclear dipolar coupling assuming that the structures are conformationally frozen (see section 4.2.1, p. 53). This simplification is applicable to polymers below their T_g and, to a good approximation, to crystalline domains above T_g . The cubic dependence of homonuclear dipolar coupling on the distance between two nuclei causes a rapid decrease in $\Delta\omega$ for larger values of r and is the reason for the local nature of homonuclear dipolar interaction (for proton-proton coupling and r in units of Å: $\Delta\omega/2\pi = 122 \text{ kHz}/r^3$ (Schmidt-Rohr and Spiess 1994)). For most synthetic polymers, the shortest proton-proton distances are found in methylene and methyl groups ($r \approx 1.8$ Å) leading to static dipolar couplings of ~ 21 kHz. The next neighbors in an alkyl chain are ~ 2.5 Å apart corresponding to a ~ 7.5 kHz coupling. The orientation-dependence of isolated spin pairs in the static \vec{B}_0 field (second Legendre polynomial, see Table 4.2) leads to characteristic line shapes discovered by Pake (1948) with line splittings depending on the

orientation. In the time-domain the Gaussian-broadened sinc-function suggested by Abragam (1989) describes the static coupling of spin pairs sufficiently well (Equation 5.1).

$$A(t) = \frac{\sin(2\pi\delta t)}{2\pi\delta t} \times \exp\left[-\left(\frac{t}{T_{2\text{Abr}}}\right)^2\right] \quad (5.1)$$

$$A(t, i) = \sum_i f_i \left\{ \frac{\sin(2\pi\delta_i t)}{2\pi\delta_i t} \times \exp\left[-\left(\frac{t}{T_{2\text{Abr},i}}\right)^2\right] \right\} \quad (5.2)$$

$\delta = 3/2 \times \Delta\omega/2\pi$: homonuclear Pake anisotropy parameter, $T_{2\text{Abr}}$: transverse relaxation time, f_i : weighting factor, t : time.

Calculated decays based on Equation 5.1 are shown in Figure 5.2 for different values of $\Delta\omega/2\pi$, which are characteristic for a conformationally frozen alkyl chain (a simple model for linear polyethylene below T_g). Decomposition of any measured $A(t)$ into an unknown number of weighted terms (Equation 5.2) can be challenging. An approximation including only the most dominant interaction and an average Gaussian component for all higher-order terms is often sufficient to model experimentally obtained relaxation data.

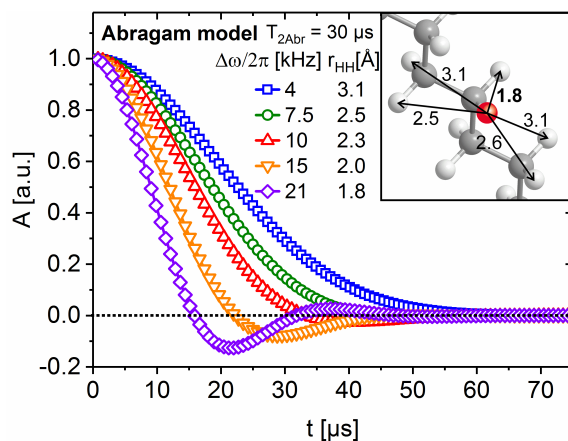


Figure 5.2: Calculated decays based on Equation 5.1 for various individual coupling frequencies $\Delta\omega/2\pi$ and corresponding proton-proton distances r_{HH} . Pronounced oscillation is observed for $\Delta\omega/2\pi \gtrsim 10$ kHz. Reprinted from Röntzsch *et al.* (2018).

The selection of a model that accurately describes the transition from static dipolar coupling behavior (Abragamian type) to relaxation in the rigid lattice limit (Gaussian type), and finally to the motional averaging limit (exponential type) is challenging, especially as static dipolar couplings are specific for each polymer. Several semi-empirical models have been proposed, which rely on combinations of Abragamian, Gaussian, and exponential functions (Dadayli *et al.* 1994; Hansen *et al.* 1998; Kristiansen *et al.* 2000). For this work, a model was selected that features a combination of an Abragamian with a single coupling constant and a Gaussian to model rigid strongly coupled protons, a Weibullian for intermediately mobile protons with remaining residual dipolar couplings, and a mono-exponential for mobile protons under the effect of motional averaging (AGWE model, Equation 5.3).

$$\begin{aligned}
 A(t) = A_{\text{Abr}} \left\{ \frac{\sin(2\pi\delta t)}{2\pi\delta t} \times \exp\left[-\left(\frac{t}{T_{2\text{Abr}}}\right)^2\right] \right\} + A_{\text{G}} \left\{ \exp\left[-\left(\frac{t}{T_{2\text{G}}}\right)^2\right] \right\} \\
 + A_{\text{Wb}} \left\{ \exp\left[-\left(\frac{t}{T_{2\text{Wb}}}\right)^n\right] \right\} + A_{\text{exp}} \left\{ \exp\left[-\left(\frac{t}{T_{2\text{exp}}}\right)\right] \right\}
 \end{aligned} \quad (5.3)$$

The rigid fraction $\chi(T)$ was defined as:

$$\chi(T) = (A_{\text{Abr}} + A_{\text{G}}) / (A_{\text{Abr}} + A_{\text{G}} + A_{\text{Wb}} + A_{\text{exp}}) \quad (5.4)$$

In Figure 5.3, the expected temperature-dependence of $\chi(T)$ for an amorphous and a semi-crystalline polymer is shown. Above T_g one expects a softening phase, which leads to a mobile material with sufficient motion to pre-average dipolar coupling for an amorphous polymer according to the Williams-Landel-Ferry (WLF) model of motional activation energies. For semi-crystalline polymers, the crystalline domains remain rigid above T_g , so that $\chi(T)$ becomes a measure of the crystallinity X_c in a plateau region preceding melting (Figure 5.3).

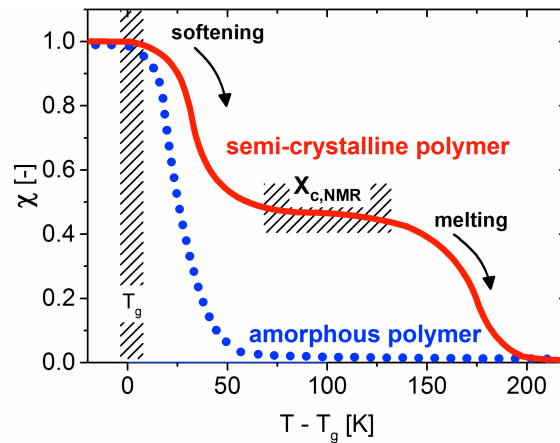


Figure 5.3: Schematic temperature-dependence of the rigid fraction $\chi(T)$ for an amorphous and a semi-crystalline polymer. The plateau for which $\chi(T) \approx X_c$ is expected to be observed around $T_g + 100$ K and ends when the polymer starts to melt. Reprinted from Röntzsch *et al.* (2018).

5.2 Experimental

NMR equipment and experimental procedures

All ^1H -NMR experiments were performed at the Pro²NMR facility under supervision of Prof. G. Guthausen with support from Prof. H. Horn. The high-field experiments were carried out on a Bruker AVANCE 400 WB spectrometer (Bruker BioSpin GmbH, Rheinstetten, Germany) with $B_0 = 9.4$ T, $\omega_L/2\pi = 400$ MHz for ^1H and equipped with a 4 mm CP-MAS ^1H probe. The NMR probe characteristics were: dead time 4.5 μs , pulses 2.5 μs (p_{90}), 5.0 μs (p_{180}). The sample temperature was controlled from -15 to +120 $^\circ\text{C}$ by a Bruker Variable Temperature

(BVT) unit operated with pressurized air and a flow rate of 1200 l/h in combination with a home-built cooling system using a mixture of dry ice and ethanol. All data were acquired by 90°-dead time-FID pulse programs (zg). The MAS rotors were packed using ~100 mg of polymer pellets. All data were accumulated (16 scans) with a 5 s recycle delay and phase cycling: $\phi_1 = \phi_{\text{rec}} = x\bar{x}x\bar{x}y\bar{y}y\bar{y}$, and digitized using the ADC+ digitization mode. The ^1H -NMR relaxometry experiments at low field were performed on a Bruker "the minispec" mq20 (Bruker BioSpin GmbH, Rheinstetten, Germany) with $B_0 = 0.5 \text{ T}$, $\omega_L/2\pi = 20 \text{ MHz}$ for ^1H . The sample temperature was controlled from -115 to +205 °C by a Bruker Variable Temperature (BVT) unit. The NMR probe characteristics were: dead time 10 μs , pulses 2.6 μs (p_{90}), 5.1 μs (p_{180}) for 0 dB pulse attenuation, and bandwidth ~500 kHz FWHM. All data were accumulated (16 scans) with a 3.5 s recycle delay and phase cycling: $\phi_1 = x\bar{x}x\bar{x}$, $\phi_2 = \bar{y}y\bar{y}$, $\phi_3 = x\bar{x}x\bar{x}$, $\phi_4 = y\bar{y}y\bar{y}$, $\phi_{\text{rec}} = x\bar{x}x\bar{x}$. On-resonance was ensured for all experiments and the phase was adjusted using a zero order phase correction. The real part was selected for analysis of the decay decomposition. In all crystallization experiments, a combination of a MSE decay and a succeeding CPMG echo train with phase cycling was employed (see subsection 4.2.3, p. 58). Approximately 20 – 30 polymer pellets (in total ~1 cm³) were put into 10 mm borosilicate glass NMR tubes, which were purged a couple of times with Argon, evacuated, and finally sealed to reduce convection and oxidative degradation.

Additional characterization

Isothermal and non-isothermal differential scanning calorimetry (DSC) were performed on a Mettler DSC30 with a TC15 temperature controller and a liquid nitrogen cooling unit (Mettler-Toledo GmbH, Gießen, Germany). The temperature profile for isothermal crystallization experiments was: RT to T_{isomelt} at 10 K/min, hold at T_{isomelt} for 12 min, T_{isomelt} to T_{cryst} at -60 K/min, hold at T_{cryst} for 2 – 3 h where T_{isomelt} was set to 40 K above the peak maximum temperature of the respective DSC melting endotherms and T_{cryst} was chosen to yield complete crystallization within the given time interval of 2 – 3 h. X-ray diffraction (XRD) experiments were carried out on a Bruker D8 Discover (Bruker AXS GmbH, Karlsruhe, Germany) with a Cu X-ray tube (40 kV, 40 mA), Göbel mirror, an Anton Paar HTK1200N heating chamber (Anton Paar, Graz, Austria), a 0.2 mm Soller slit, and a LYNXEYE XE detector (0D mode). The diffractograms were acquired by continuous scanning between $2\theta = 5$ to 34° first at 30 °C, then at elevated temperatures of +40 K above the peak maximum melting temperature observed in non-isothermal DSC experiments, and finally again at 30 °C after cooling from the melt at approximately -10 K/min. The heating chamber was evacuated to reduce X-ray background scattering and polymer degradation.

Materials

The materials used in this chapter were selected grades of the most common synthetic semi-crystalline polymers (polyolefins, polyamides, and polyesters). Information on the suppliers, the molecular weight distributions, the glass transition temperatures, and the nominal melting points can be found in section 2.4, p. 19.

5.3 Solid-state ^1H -NMR experiments at 400 MHz

5.3.1 Temperature-dependent static solid-state ^1H -NMR experiments

In order to obtain information on the transverse relaxation behavior of semi-crystalline polymers, free induction decays (FIDs) were recorded for all selected polymers varying the sample temperature from -15 to $+115$ °C in 10 °C steps (static, no drive pressure applied to CP-MAS ^1H probe). The FIDs were zero order phase-corrected and Fourier-transformed using Bruker TopSpin 4.0. Figure 5.4 shows such a temperature series of spectra for i-PP-1 (spectra of all other semi-crystalline polymers can be found in Appendix A). The broad and indifferent line below the glass transition temperature $T_g = -10$ °C gradually changed into a multi-component line with increasing temperature, and displayed an almost invariant shape for temperatures of $T > T_g + 100$ K. The origin of this line narrowing behavior is the increasing molecular motion in the amorphous domains at higher temperatures, which leads to slower transverse relaxation and more narrow lines as described by the NMR theory of relaxation (subsection 4.2.2, p. 55).

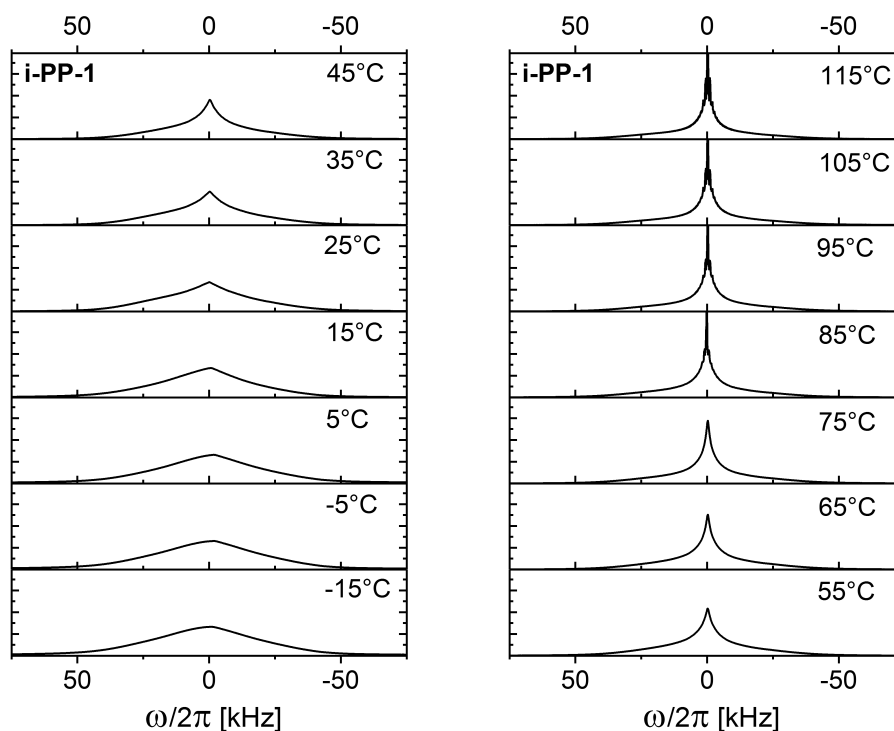


Figure 5.4: Temperature-dependent ^1H -NMR solid-state spectra of i-PP-1 ($T_g = -10$ °C) recorded in static mode at 400 MHz. Motional narrowing with increasing temperature led to a multi-component line, which displayed an invariant shape at temperatures of $T > T_g + 100$ K.

In Figure 5.5, ^1H -NMR solid-state spectra of different semi-crystalline and amorphous polymers are shown, which were recorded at different temperatures with respect to the glass transition temperature. Spectral lines are expected to be Lorentzian for highly mobile components (Fourier transform of an exponential FID), whereas for strongly dipolar coupled systems Gaussian lines are observed. The latter can be rationalized as a superposition of Pake patterns with a broad distribution of dipolar coupling frequencies (see section 5.1).

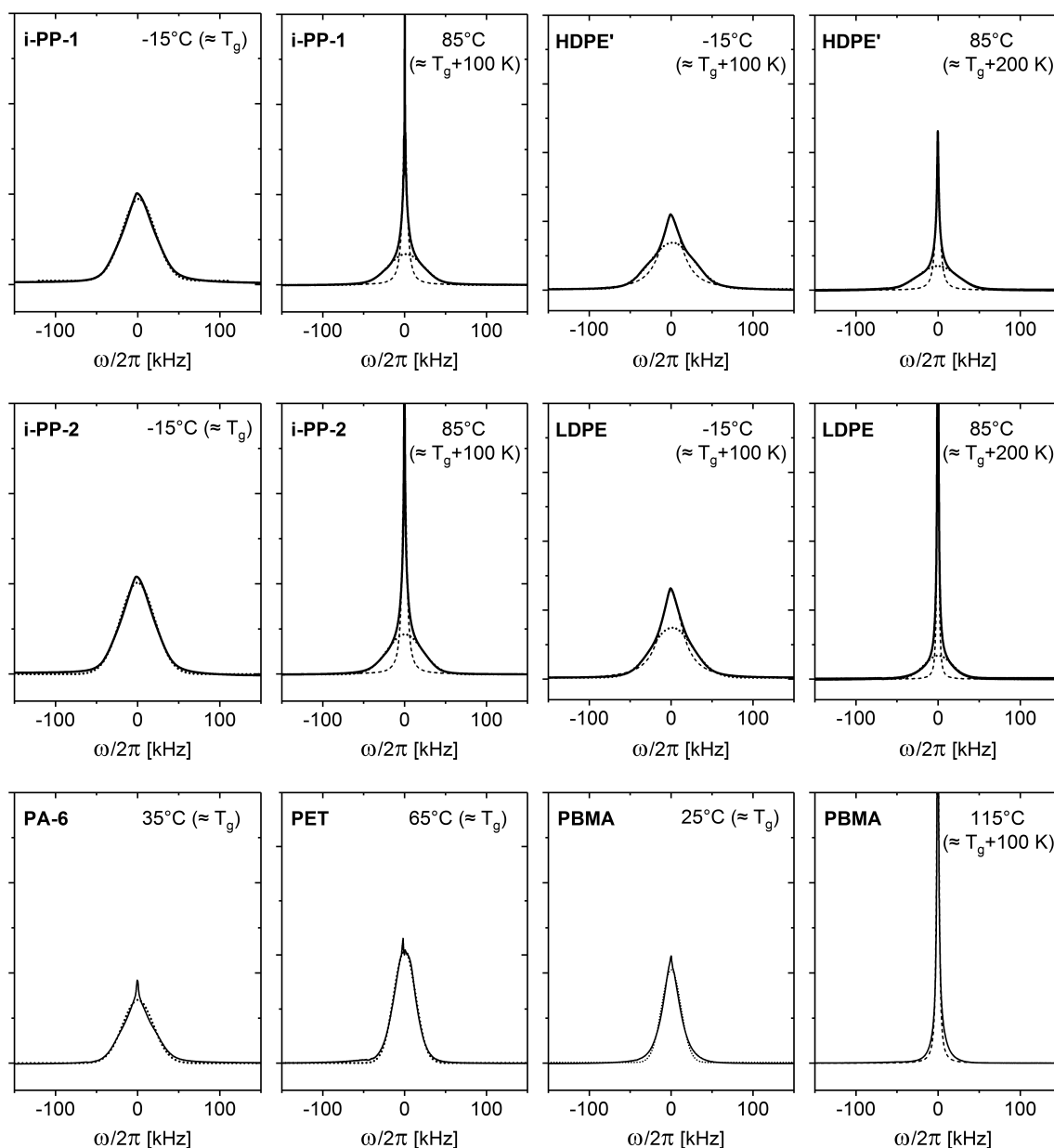


Figure 5.5: ^1H -NMR spectra of semi-crystalline and amorphous polymers recorded at $T_g + 100$ K in static mode at 400 MHz with indicated Lorentzian and Gaussian lines to separate mobile from rigid components (dotted lines: Gaussian model fits, dashed lines: Lorentzian model fits).

The spectra recorded close to the glass transition temperature T_g of the respective polymers could be described by a single Gaussian function (i-PP-1, i-PP-2, PA-6, PET, PBMA). For temperatures $T = T_g + 100$ K, the polypropylenes exhibited a combination of a narrow Lorentzian for the motional-averaged mobile components and a Gaussian (broad feet) due to the strong dipolar coupling within the crystalline domains. Interestingly, the polyethylenes displayed rather broad lines for both components at temperatures of $T_g + 100$ K, which indicated that motional narrowing was not as effective as for the other polymers. Spiess *et al.* made similar observations when analyzing ^2H -NMR spectra and associated this behavior with a small number of possible conformations that are accessible by CH_2 groups at these temperatures (Spiess 1983). Additionally, the glass transition temperature $T_g \approx -120$ °C (Mark 2007; Swan 1960;

Stehling and Mandelkern 1970) is related to the γ -relaxation process in polyethylene (Boyd 1985a,b) and has been questioned to be a proper thermodynamic glass transition by multiple researchers (Davis and Eby 1973; Gaur and Wunderlich 1980). In case of the amorphous atactic poly(butyl methacrylate) (PBMA), a single narrow Lorentzian line shape was observed for $T \approx T_g + 100$ K, which was expected because of the absence of crystalline domains.

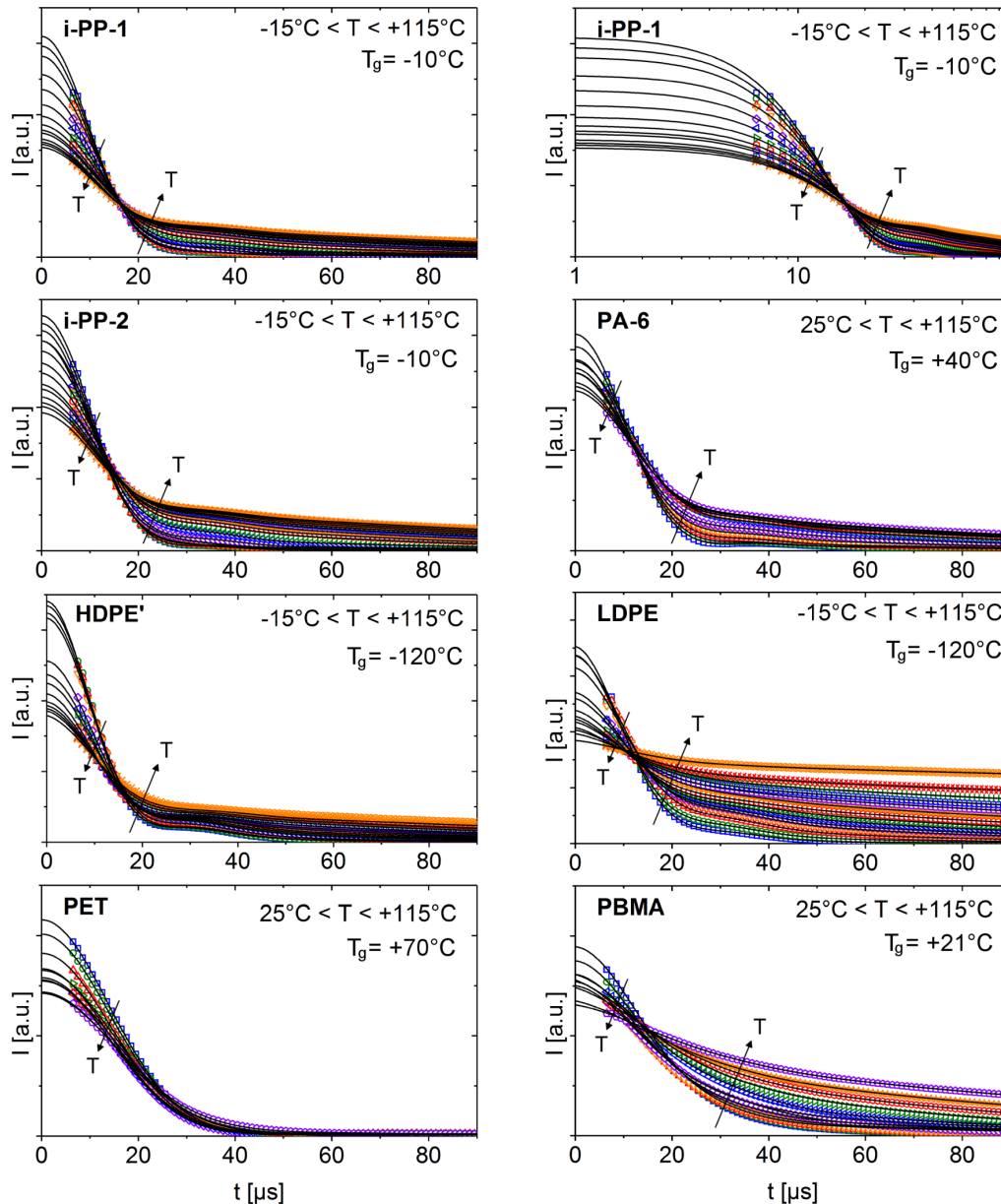


Figure 5.6: Series of temperature-dependent free induction decays (FID) recorded in static mode at 400 MHz for different polymers in the accessible temperature range of -15°C to $+115^\circ\text{C}$ ($\Delta T = 10^\circ\text{C}$, black lines: fits based on Equation 5.3 – constraints described in the text.).

In Figure 5.6, temperature-dependent free induction decays (FIDs) of all investigated polymers are depicted. At temperatures close to the respective glass transitions, all polymers showed rapid decays to zero within $\sim 50 \mu\text{s}$ which is a consequence of the high rigidity and absence of cooperative segmental motion at T_g . Plateau-like behavior was observed between 20 –

50 μs for the polyethylenes, the polypropylenes, and PA-6, which were an indication of Pake-type interactions between coupled methylene protons. The data for PET and PBMA displayed monotonically decaying curves without any notable plateau. With increasing temperature, the relative intensity of the slowly relaxing component (mobile / amorphous) increased, while the total intensity went down due to a lower overall NMR intensity (Boltzmann distribution, see section 4.2, p. 51).

For a quantitative compositional analysis, the free induction decays (FID) were modeled using the described fitting function (Equation 5.3). As all polymers contain methylene groups, a dedicated Abragamian with $\delta = 30$ kHz and $T_{2\text{Abr}}$ as a free parameter (30 – 50 μs) was chosen to account for the strong oscillations and plateau-like behavior observed in the data. The weak motional narrowing observed for the polyethylenes at temperatures of $T_g + 100$ K as revealed by the ^1H -NMR spectra, was also reflected in the free induction decays and required a different modeling approach compared to all other polymers. For the polyethylenes, the Gaussian component was not needed to achieve an accurate representation of the data and high numerical fitting stability, presumably because of its simple repeat unit consisting only of methylene protons and a regular zig-zag conformation in a polymer crystal (see section 2.2, p. 7). The Gaussian component was however necessary for the other polymers to describe the free induction decays sufficiently well, possibly due to the higher structural complexity and the associated multiple couplings. The Weibullian component could be set to zero while still providing a good representation of the data and with the benefit of fewer free parameters for all polymers except of the polyethylenes. This behavior was presumably another consequence of the low motional averaging, as the protons displayed some remaining residual dipolar coupling, and thus had to be described by a combination of a Weibullian ($n = 1.5$) and an exponential function as an approximation of the Brereton function described by Dadayli *et al.* (1994); Hansen *et al.* (1998).

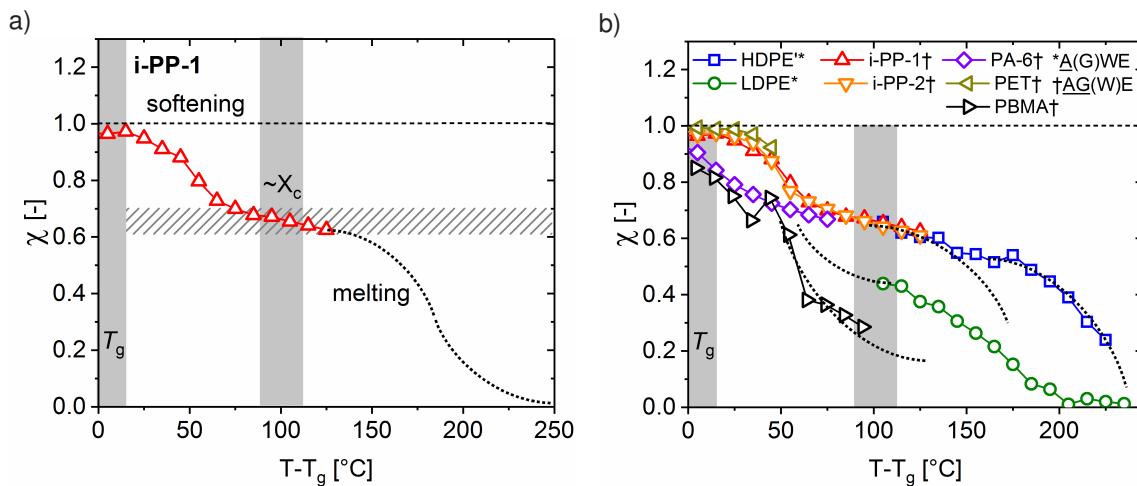


Figure 5.7: Evolution of the rigid proton fraction $\chi(T)$ for i-PP-1 (a) and in comparison with all other investigated polymers (b). Due to the limited accessible temperature range, the full softening and melting behavior could not be examined for the polymers under investigation.

In Figure 5.7a, the evolution of the rigid fraction $\chi(T)$ is shown for i-PP-1, which followed the expected decreasing behavior during the softening phase above T_g . A constant plateau was reached at temperatures $T \approx T_g + 100$ K. Because of the limited accessible temperature regime with the current solid-state NMR probe, the melting behavior could not be examined. Figure 5.7b shows a comparison of the respective $\chi(T)$ curves for all investigated polymers with indicated extrapolations to higher or lower relative temperatures (dotted lines). As the temperature interval was limited to experiments between -15 and $+120$ °C, the intended temperature-dependent study of $\chi(T)$ could only be carried out for small sections of Figure 5.3, especially in the cases of polymers with very low or high glass transition temperatures (polyethylenes: $T_g \approx -120$ °C, PET: $T_g \approx +70$ °C). As the solid-state NMR probe exhibited a dead time of $4.5 \mu\text{s}$, the available information on the decay of the very rigid components was limited (see plot in Figure 5.6). Thus, modeling the data with multiple component functions presented an ill-defined problem, especially for the estimation of the total intensity. Consequently, the observed plateau for $80 < T - T_g < 120$ °C was prone to a certain error and did not necessarily reflect an absolute mass crystallinity. In case of the amorphous PBMA, the observed softening did not reach a state of $\chi(T) = 0$, which was presumably again a consequence of the missing data points for the initial $5 \mu\text{s}$. By using a static NMR probe with an even shorter dead time or magic echo pulse sequences together with a broader specified temperature range, the full interval of $0 < T - T_g < 200$ °C could be investigated and reliable values for the mass crystallinity could be obtained. An alternative based on low-field ^1H -NMR relaxometry will be presented in section 5.4.

5.3.2 Magic angle spinning (MAS)-NMR experiments

Static NMR lines of solid samples, e.g., polymers below their respective glass transition temperatures are dominated by strong dipolar coupling in the kiloHertz regime that obscures chemical shift or J -coupling (see ^1H -NMR spectra in the previous section 5.3)¹. By a fast rotation of the sample at the magic angle $\theta = 54.7^\circ$ with respect to the static \vec{B}_0 field, the angle-dependent term $3\cos^2\theta - 1$ of the dipolar coupling Hamiltonian can be effectively suppressed (Figure 5.8, see Table 4.2). Thus, significant line narrowing is observed, which enables the structural analysis of functional groups and ultimately an identification of unknown compounds.

In Figure 5.9a, the effect of magic angle spinning (MAS) on the NMR spectra of i-PP-1 at room temperature is shown for different spinning frequencies. The expected line narrowing was observed including the appearance of spinning sidebands at multiples of the spinning frequency, which are caused by field modulations. Even for 10 kHz spinning the centerband was relatively broad and didn't exhibit chemical shift resolution. Similar observations were made for all other investigated semi-crystalline polymers. However, when the materials were heated to temperatures above their respective T_g 's in combination with magic angle spinning

¹ Another frequently observed property of solid materials is the chemical shift anisotropy (CSA), which can also be reduced by MAS and is oftentimes studied using ^{13}C -NMR spectroscopy.

at spinning frequencies of ~ 10 kHz, the spectra exhibited the expected resonances caused by different chemical shifts of the functional groups (Figure 5.9b).

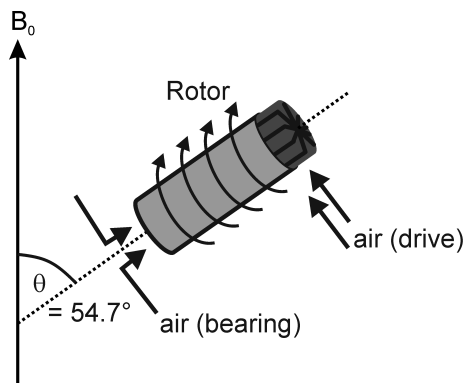


Figure 5.8: Magic-angle spinning (MAS) at the magic angle $\theta = 54.7^\circ$ to suppress dipolar coupling (Schmidt-Rohr and Spiess 1994).

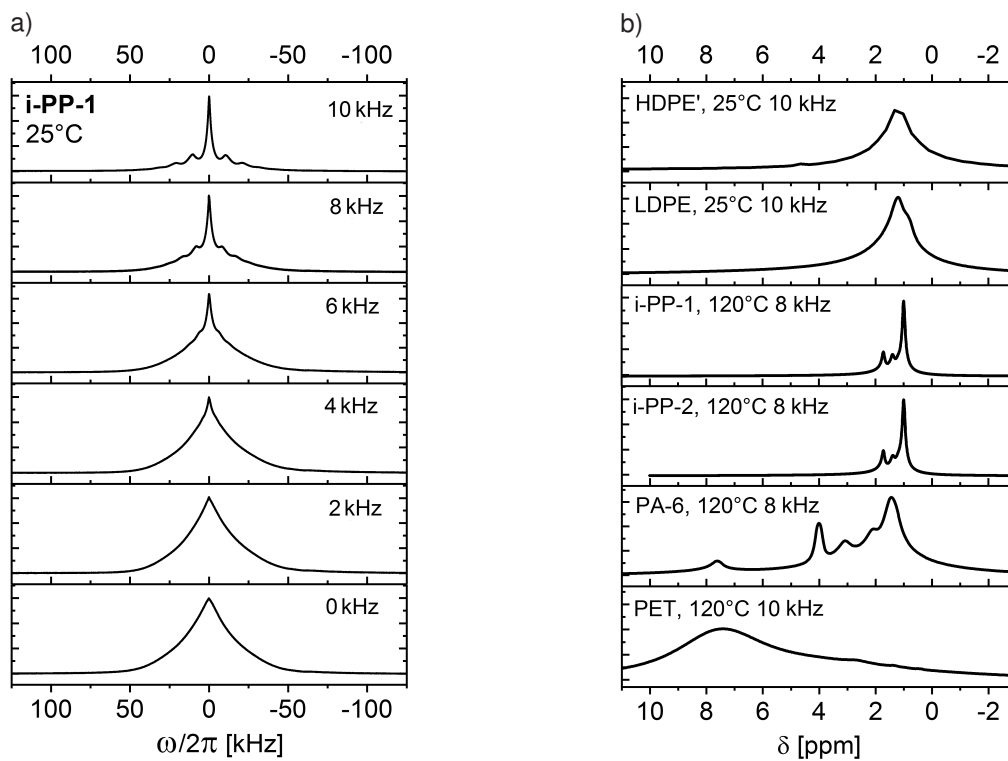


Figure 5.9: a) ^1H -NMR spectra of i-PP-1 at room temperature for different magic angle spinning frequencies. Line narrowing and spinning sidebands at multiples of the spinning frequency were observed. b) By combining magic angle spinning with an increased temperature above the respective glass transition temperatures, the different polymers showed expected resonances due to the chemical shift of their respective functional groups.

5.4 Polymer crystallinity determined by low-field NMR relaxometry

At low \vec{B}_0 fields, NMR shows lower sensitivity (Equation 4.31, p. 52) and is usually accompanied by lower B_0 homogeneity as commercial NMR instruments such as the Bruker mq20 minispec come without shim systems. On the other hand, low-field NMR has the advantage that it can be adapted to serve as an *in-situ* detector of molecular dynamics, e.g., in combination with rheology which is presented in chapter 6. In this section, the applicability of ^1H -NMR relaxometry to determine the crystallinity of solid samples was investigated by analyzing temperature-dependent NMR relaxation data. The most commercially relevant semi-crystalline polymers were studied, and the results were compared with DSC and XRD, which are based on thermodynamic and structural quantities and therefore are expected to show a slight difference in the distinction between crystalline and amorphous fractions (see section 5.1).

5.4.1 Temperature-dependent experiments on various polymers

To overcome the dead time of the low-field NMR probe ($10\ \mu\text{s}$), a mixed magic sandwich echo sequence was used to study the transverse relaxation behavior of all investigated materials (see subsection 4.2.3, p. 58 for a detailed description of the MSE sequence). The parameter τ_ϕ was adjusted to obtain the echo maximum after a duration of $\tau_{\text{MSE}} = 4\tau_\phi + 4.5p_{90}/2$ (Figure 5.10). It was found that a value of $\tau_\phi = 2.2\ \mu\text{s}$ resulted in the highest echo intensity and closest match between the echo maximum and the corresponding duration of $\tau_{\text{MSE}} = 15\ \mu\text{s}$. For lower values of τ_ϕ the re-creation of spin coherence was not complete after τ_{MSE} , which led to a distorted decay. For higher values of τ_ϕ the echo maximum was shifted to earlier times with a lower signal intensity and overemphasized oscillations in the time range of $10 - 30\ \mu\text{s}$.

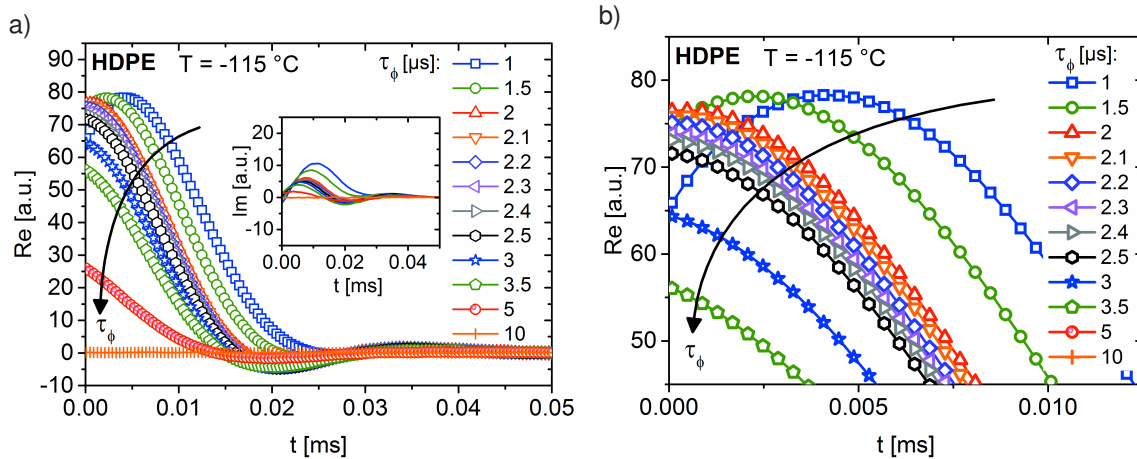


Figure 5.10: Mixed magic sandwich echo signals for different values of τ_ϕ (see subsection 4.2.3, p. 58). The optimal τ_ϕ value for the highest echo intensity and a close match between the occurrence of the echo maximum and the duration τ_{MSE} was found to be $\tau_\phi = 2.2\ \mu\text{s}$.

MSE echoes were recorded over a large temperature interval to study the transition from a fully rigid state below T_g to a state of increased softness above T_g , and finally to a highly mobile melt state (Figure 5.11). All datasets were normalized to the MSE maximum in order to remove the effect of different intensities based on the Boltzmann distribution of ground

and excited spin states. The polymers investigated in this study contain different functional groups, e.g., methylene, methyl, or phenylene units. Thus, multiple proton-proton dipolar couplings are present and consequently different patterns were observed at temperatures below and close to T_g .

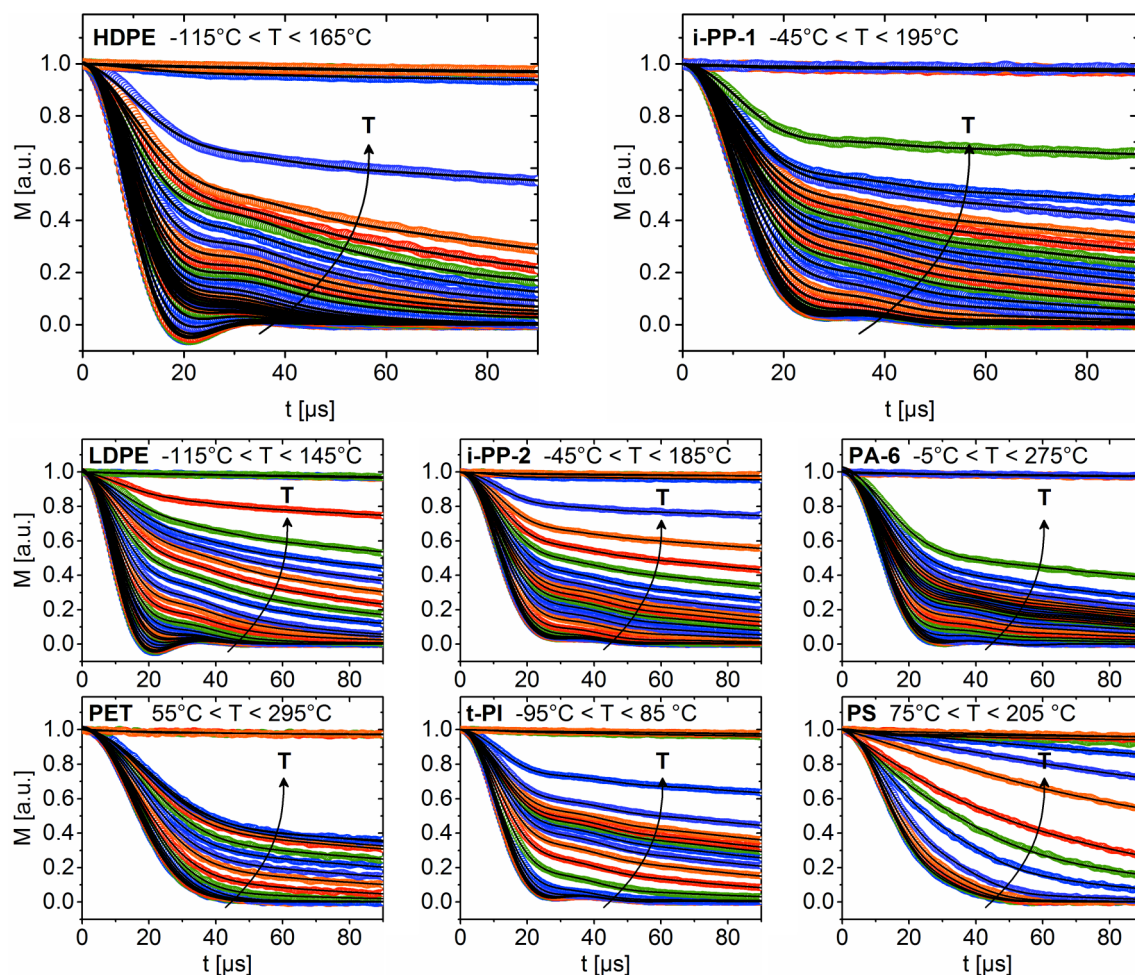


Figure 5.11: Normalized mixed magic sandwich echo (MSE) decays for different semi-crystalline polymers and temperatures measured at 20 MHz. Strong static coupling was observed for the polyethylenes below T_g , whereas i-PP, PA-6, and t-PI showed a plateau-like decay in the region of 20 – 50 μs . PS and PET exhibited a Gaussian decay without an oscillation. The lines represent the fitted model and describe the curves well over the large temperature range (Equation 5.3, $\delta = 30$ kHz, $T_{2\text{Abr}}$: free parameter with values of 30 – 50 μs). Reprinted from Röntzsch *et al.* (2018).

All polymers showed rapid decaying behavior within ~ 50 μs after the formation of the mixed magic sandwich echo at the lowest measured temperatures, which was similarly observed for the high-field free induction decays in section 5.3. Pronounced oscillations between 20 – 50 μs were visible for the polyethylenes and this was presumably caused by Pake-type interactions between coupled methylene protons. The data for all other polymers displayed less pronounced oscillations and monotonically decaying curves, which were probably a result of the more complex dipolar network and a summation of multiple coupling terms. A slowly decaying component appeared with increasing temperature that originated from the rising mobility

in the amorphous and interfacial regions. The strong oscillation at low temperatures over the time interval of 20 – 50 μs transformed into a plateau-like behavior with increasing temperature, which is probably associated with the fraction of semi-rigid protons (Maus *et al.* 2006). In comparison to the high field experiments discussed in section 5.3, the Gaussian-type decay was clearly resolved due to the reconstruction of the full magnetization decay and vanished gradually with increasing temperature for all polymers. Finally, at temperatures above the nominal melting points, an almost straight line was observed on the time scale of a few tens of μs , reflecting T_2^* relaxation dominated by the \vec{B}_0 homogeneity.

All mixed magic sandwich echo (MSE) decays were analyzed using the described AGWE model (Equation 5.3) to extract information on the fractions of rigid, intermediately mobile, and mobile protons (black lines in Figure 5.11). As for the high-field FIDs, a dedicated Abragamian with $\delta = 30$ kHz and $T_{2\text{Abr}}$ as a free parameter (30 – 50 μs) was chosen to account for the strong oscillations and plateau-like behavior observed in the data. As shown by the high-field experiments in section 5.3, polyethylenes are characterized by a relatively weak motional narrowing at temperatures of $T_g + 100$ K compared to other semi-crystalline polymers. Consequently, analyzing the decays in the time domain requires a different modeling approach. For the polyethylenes, the Gaussian component was again omitted to achieve high numerical fitting stability and an accurate representation of the data, which might be a consequence of the simple repeat unit structure consisting only of methylene protons and the regular zig-zag conformation in the crystalline domains. Due to the structural complexity of the other polymers and the associated multiple couplings, an additional Gaussian component was however necessary for these polymers to describe the relaxation behavior sufficiently well. The Weibullian component could be set to zero for all polymers except of the polyethylenes while still providing a good representation of the data and with the benefit of fewer free parameters. Hence, for polymers with a rather complex repeat unit, the domains of intermediate mobility and high rigidity cannot easily be separated by the selection of one or two dedicated Abragamians and a Weibullian. The reduction to a simplified two-phase model (crystalline + amorphous) was necessary to achieve high numerical fit stability. In addition, the different relaxation behavior of the polyethylenes might also be a consequence of the usually very high nucleation density (large interfacial area – large content of intermediately mobile protons), which is associated with the high polydispersity compared to all other polymers.

The temperature dependence of the rigid fraction $\chi(T)$ is shown for all polymers in Figure 5.12. Below T_g the curves exhibit a plateau ($\chi(T) = 1$) that ends shortly above T_g when the amorphous part of the material started to soften due to increased molecular motion. For the amorphous polystyrene sample, $\chi(T)$ effectively decayed to zero for $T \approx T_g + 50$ K. Depending on the type of semi-crystalline polymer, the softening phase extended until $T \approx T_g + 100$ K where another short plateau was observed marking the region over which the mobility difference between protons in crystalline and amorphous domains is sufficient to determine the crystallinity X_c . Notably, the temperature that is required to reach this second plateau did not exactly match the mobile plateau $\chi(T) = 0$ for the amorphous polystyrene, which suggests

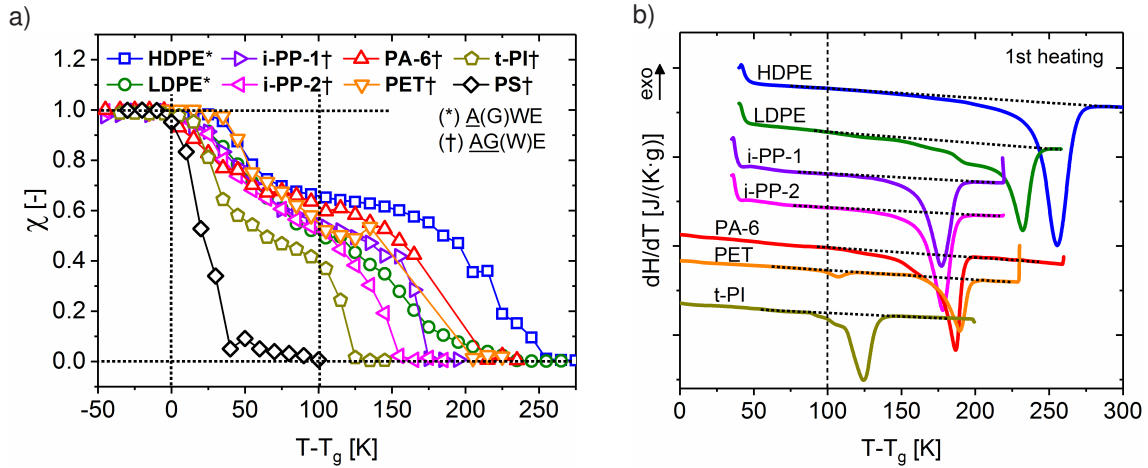


Figure 5.12: a) Temperature-dependence of the rigid fraction $\chi(T)$ for different semi-crystalline polymers and amorphous polystyrene. A plateau-like behavior was observed for all semi-crystalline polymers at $T \approx T_g + 100$ K, marking the temperature interval over which there is sufficient mobility difference between the protons of amorphous and crystalline domains to determine $X_{c,NMR}$. Melting set in at relatively low temperatures for t-PI, i-PP-2, and LDPE. b) DSC melting endotherms, which exhibited the onset of melting at temperatures slightly above $T = T_g + 100$ K. Reprinted from Röntzsch *et al.* (2018).

that the activation behavior of molecular motion is higher for semi-crystalline polymers and that some rigidity is retained, i.e., through linkages of amorphous chains to crystalline domains or additional local physical constraints that shifted the average activation barrier E_A to higher values. With a further increase in temperature, melting started and led to a second decline of $\chi(T)$ until the parameter vanished completely when the samples were fully molten (compare with DSC melting endotherms shown in Figure 5.12b). The materials investigated here were neat pellets in a non-equilibrium state, which makes it very likely that there were many small and thin lamellae present in the samples which caused melting at relatively low temperatures, shortly after the plateau at $T \approx T_g + 100$ K was reached.

The mixed magic sandwich echo sequence used in the experiments led to higher intensities than a simple solid echo. However, it was still not able to refocus all magnetization (approx. 10 % signal reduction compared to the melt). In addition, for temperatures at which motional modes have a similar time scale as the refocusing block duration (10 – 20 μ s), the magic sandwich echo intensity decreased significantly (e.g., for $T_g + 50$ K for segmental motion of amorphous chains and $T_g + 200$ K for helical flips of crystalline chains). However, at this stage there was no alternative to the mixed magic sandwich echo, and the trends agreed with the experiments carried out at high field (section 5.3). The values of $\chi(T)$ at $T = T_g + 100$ K were chosen as a measure of crystallinity $X_{c,NMR}$ for further interpretation. A relative error of $\pm 10\%$ was estimated for $X_{c,NMR}$, mainly given by fitting uncertainties over the time interval of 20 – 50 μ s and assuming a certain ambiguity in the assignment of protons in crystalline vs. rigidified amorphous domains.

5.4.2 Comparison with DSC and XRD

Differential scanning calorimetry (DSC) heating traces of "as received" pellets were integrated and compared with literature values for theoretically 100% crystalline samples (Mark 2007). An example of such a melting endotherm is given for i-PP-1 in Figure 5.13a. An average of three samples was calculated with a relative error of approximately $\pm 10\%$, which was presumably resulting from different cooling conditions for each pellet during processing and the experimental error. Frequent sources of error in DSC are the selection of suitable integration limits, setting of the baseline, and the literature values for theoretically 100% crystalline samples (Wunderlich 2005).

X-ray diffractograms were recorded for "as received" pellets at room temperature and above the nominal melting point to obtain information on the amorphous signal shape. The amorphous halo was adjusted in the vertical and horizontal directions to match the minima of the measured diffractograms at room temperature. Figure 5.13b shows the results for i-PP-1 with the black line being the shifted amorphous halo. A comparison of the integrals yielded the XRD crystallinity. This method was found to be more reliable than a simple Gaussian fit because the amorphous halo is not necessarily symmetric and its shape depends on the polymer type and experimental set-up. Generally, the sources of error in X-ray diffraction measurements are the estimation of the amorphous halo, the selection of integration limits and the baseline, and angle-dependent intensity shifts when a Bragg-Brentano geometry is used for non-flat samples.

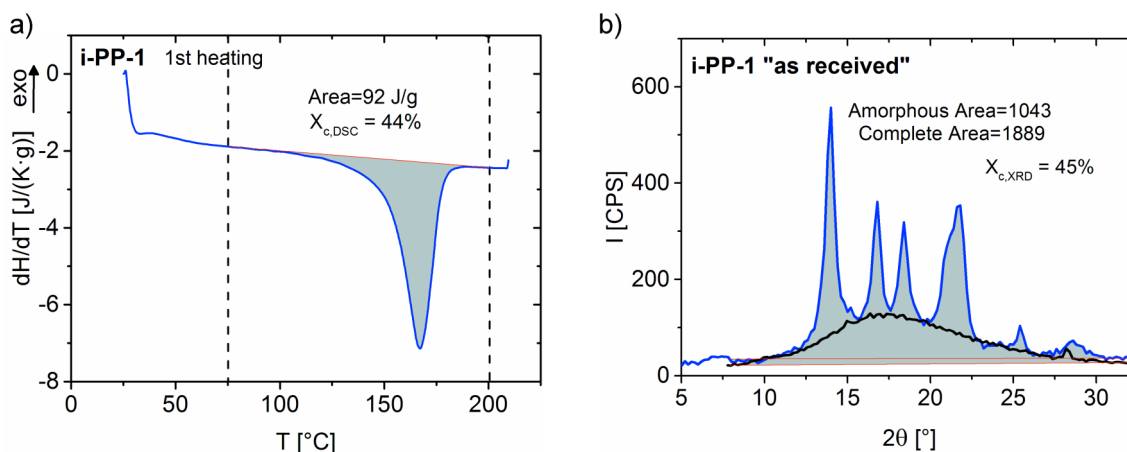


Figure 5.13: a) DSC heating trace of i-PP-1 ("as received" pellets) recorded at 10 K/min. Integration of the melting endotherm and comparison with literature values for a theoretically 100% crystalline sample yielded a DSC crystallinity of 44%. b) XRD diffractogram of i-PP-1 at 30 °C (blue line) and a shifted amorphous halo (black line) recorded at 200 °C. A comparison of the integrals yielded an XRD crystallinity of 45% (additional data in Appendix A). Reprinted from Röntzsch *et al.* (2018).

A comparison of crystallinity values X_c determined by DSC, XRD, and NMR is shown in Figure 5.14 for all investigated polymer types. The obtained values agreed relatively well within the estimated experimental errors of $\pm 10\%$ for X_c . Each characterization technique measures a different physical quantity (heat of fusion, unit cell order, molecular dynamics, etc.). There-

fore, the structural assignment to crystalline, interfacial, and amorphous domains varied based on the different length and time scales involved in the measurements. For the NMR experiments, the selected model and data analysis method were found to be a good compromise between an accurate description of the data and high numerical fit stability. At temperatures of $T > T_g + 100$ K, the mobility difference between the protons of amorphous and crystalline domains was sufficient for a determination of the crystallinity in semi-crystalline polymers.

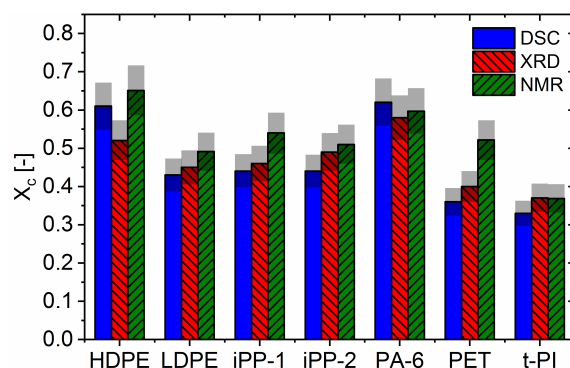


Figure 5.14: Crystallinities X_c for different polymers as determined by DSC, XRD, and NMR. The methods agreed well within an estimated relative error of $\pm 10\%$ (indicated in grey), which could be attributed to experimental uncertainties (temperature control, sensitivity, etc.) and to the data analysis (baselines, integration ranges, data fitting models, etc.). Reprinted from Röntzsch *et al.* (2018).

5.5 Monitoring polymer crystallization using low-field NMR relaxometry

Following the buildup of crystallinity $X_c(t_{\text{exp}})$ from an isotropic melt using NMR relaxometry at low field provides important information on crystallization kinetics (subsection 3.3.6, p. 35), which depend on chain topology, additives, and processing conditions (temperature, pressure, flow). For such phase transitions, sophisticated decay decomposition tends to be numerically unstable, and can generally not be applied to measurements on magnets of low \vec{B}_0 homogeneity, for which T_2^* is dominated by the \vec{B}_0 field and not by the sample. The use of a combined MSE-CPMG sequence is a robust alternative to distinguish between protons in rigid / crystalline and mobile / amorphous domains (Figure 5.15a, subsection 4.2.3, p. 58). The main idea behind this approach is that only relatively mobile (amorphous) protons are detected by the CPMG sequence (Carr and Purcell (1954); Meiboom and Gill (1958)), because of the 180° pulse refocusing properties and an appropriate duration of the relaxation phase before the first 180° CPMG pulse. The mixed magic sandwich echo (MSE) is recorded as a measure of all protons for each point in experimental / crystallization time. Examples of transverse relaxation decays of an isotactic polypropylene in a super-cooled melt state and after complete isothermal crystallization as measured by a combined MSE-CPMG sequence are given in Figure 5.15b. The determination of evolving crystallinities $X_c(t_{\text{exp}})$ can be carried out either by a direct or indirect method, which is similar to the solid fat content (SFC) determination of fats (AOCS-Cd 16b-93 1997; AOCS-Cd 16-81 2009).

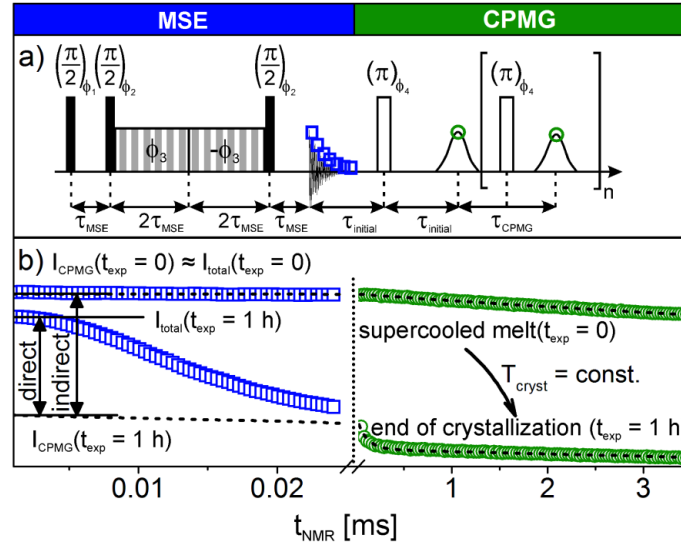


Figure 5.15: a) Combined mixed magic sandwich echo (MSE) and CPMG sequence to refocus the signal of a homonuclear dipolar coupled spin system, and to differentiate between rigid and mobile protons (Maus *et al.* 2006). b) MSE (open squares) and CPMG data (open circles) for a super-cooled i-PP melt ($t_{\text{exp}} = 0$ h) and at the end of isothermal crystallization ($t_{\text{exp}} = 1$ h). Direct or indirect data processing approaches similar to the SFC determination of fats (AOCS-Cd 16b-93 1997; AOCS-Cd 16-81 2009) can be applied to extract the buildup in crystallinity $X_c(t_{\text{exp}})$. Reprinted from Röntzsch *et al.* (2018).

Direct method. CPMG intensities $I_{\text{CPMG}}(t_{\text{exp}})$ are back-extrapolated to $t_{\text{NMR}} = 0$ ms for every point in the experimental / crystallization time (t_{exp}) and compared with the total intensity $I_{\text{total}}(t_{\text{exp}})$ at $t_{\text{NMR}} = 0$ ms:

$$X_{c,\text{direct}}(t_{\text{exp}}) = 1 - \frac{C \times I_{\text{CPMG}}(t_{\text{exp}})}{I_{\text{total}}(t_{\text{exp}})} \quad (5.5)$$

The direct method is applicable to any type of iso- and non-isothermal protocols because the point of reference (I_{total}) is directly detected within each relaxation curve. However, the pulse sequences employed to measure I_{total} can be non-quantitative if motions within the solid are on the time scale of the refocusing pulses blocks (e.g., chain flips in polyethylene, Hu *et al.* (1999); Bärenwald *et al.* (2012, 2014)). As $X_{c,\text{direct}}(t_{\text{exp}})$ has to be zero for the super-cooled melt at $t_{\text{exp}} = 0$ min, a correction factor $C = I_{\text{total}}(t_{\text{exp}} = 0 \text{ min}) / I_{\text{CPMG}}(t_{\text{exp}} = 0 \text{ min})$ is needed, which depends on fitting uncertainties, the \vec{B}_0 homogeneity, and MSE performance.

Indirect method. For the indirect analysis, CPMG intensities $I_{\text{CPMG}}(t_{\text{exp}})$ are back-extrapolated to $t_{\text{NMR}} = 0$ ms and compared with the back-extrapolated CPMG intensity at $t_{\text{exp}} = 0$ min at which the sample was in a super-cooled melt state at T_{cryst} :

$$X_{c,\text{indirect}}(t_{\text{exp}}) = 1 - \frac{I_{\text{CPMG}}(t_{\text{exp}})}{I_{\text{CPMG}}(t_{\text{exp}} = 0)} \quad (5.6)$$

The indirect approach is readily applicable to isothermal protocols and to non-isothermal protocols if a Curie intensity correction is applied (multiplying by the absolute temperature). Furthermore, even polymers with a significant crystal mobility can be investigated as the method

only relies on the decreasing CPMG intensities. It can be used to analyze data acquired on magnets of low homogeneity as the CPMG sequence is more robust against gradients in \vec{B}_0 than the MSE sequence (Hürlimann and Griffin 2000). Both data analysis methods require short pulse timings for the CPMG sequence and a distinguished separation between the rigid and mobile signals to achieve high fit stability. The echo timing is desired to be short in order to provide a large number of data points and is mainly limited by the acquisition time, the probe dead time, and the 180° pulse length. To quantitatively detect all mobile protons with the CPMG sequence, we propose the use of a short MSE recording interval of $\tau_{\text{initial}} = 25 \mu\text{s}$ during which only the signal that originates from protons in crystalline domains is decaying.

5.5.1 Experiments on common semi-crystalline polymers

Isothermal crystallizations were carried out for all polymers² at temperatures that led to complete crystallization within 1 – 2 h. Figure 5.16a shows an isothermal crystallization experiment monitored by a combined MSE-CPMG sequence for i-PP-1 at $T_{\text{cryst}} = 136^\circ\text{C}$. The MSE part exhibited a Gaussian-type decay with progressing crystallization, which is in perfect agreement with the temperature-dependent experiments (section 5.4). The CPMG decays decreased in intensity with the progression of crystallization and transformed from slow mono-exponential into bi-exponential decays. The gradual increase of the rigid component pointed towards a nucleation and growth mechanism, especially as the relaxation behavior of the amorphous fraction during the transition from the melt to the semi-crystalline state was almost invariant. Consequently, the mesomorphic phase prior to crystallization proposed by Strobl *et al.* had to be small compared to the overall sample volume (see subsection 3.3.5, p. 33). The evolution of CPMG data in "experimental" / "crystallization" and "NMR" time exhibited the inverse S-shape for the decline in CPMG intensity caused by an effective signal loss during crystallization (Figure 5.16b).

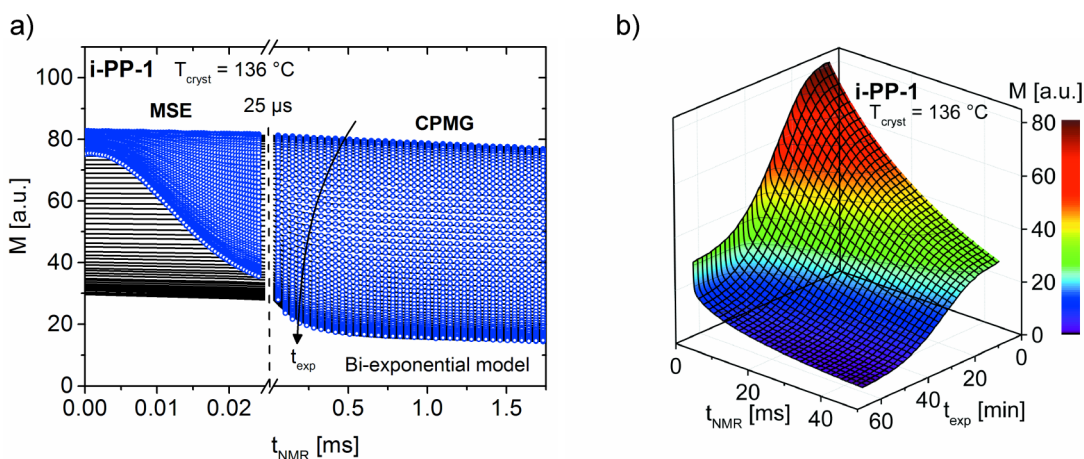


Figure 5.16: a) Time-series of MSE-CPMG data for an isothermal crystallization of i-PP-1 at 136°C (black lines are back-extrapolations to $t_{\text{NMR}} = 0$ ms). b) At $t_{\text{NMR}} = 0$ ms the time evolution of CPMG intensities shows an inverse S-shape, caused by an effective signal loss during crystallization. Reprinted from Röntzsch *et al.* (2018).

² The temperatures needed for a relatively slow crystallization of PET ($T_{\text{cryst}} > 230^\circ\text{C}$) could not be reliably maintained, and the data was excluded from further analysis.

The CPMG data was analyzed using a bi-exponential over the range of 0.05 – 10 ms to quantify the decline of the amorphous fraction. Crystallization curves based on the direct and indirect data analysis are shown in Figure 5.17a. The shapes were very similar as they mainly depended on the CPMG part and the final plateaus differed only slightly (final crystallinity $\approx 57\%$). The observed scattering of $X_c(t)$ was almost identical and was mainly due to the stability of the CPMG data fitting. A short echo time ($\tau_{\text{CPMG}} = 25 \mu\text{s}$) improved the numerical stability as a sufficient number of echoes had to be recorded during the initial 200 μs to achieve stable fitting with a minimal number of iterations. However, partial spin-locking might occur in a classical CPMG experiment. As the scope of this work was to analyze intensity ratios rather than absolute relaxation times, this effect played a minor role in the determination of the crystallization curves. Isothermal crystallization curves of i-PP-1 obtained by NMR and DSC are shown in Figure 5.17b. As mentioned before, relative crystallinities were analyzed with respect to their curve shapes and associated kinetics since isothermal DSC experiments cannot readily be integrated to yield absolute values and the plateaus of the NMR crystallization curves depended on the selection of the pulse timings. The trend of slower crystallization with increasing crystallization temperature for $T_{\text{cryst}} > (T_m^0 + T_g)/2$ was well captured by both, DSC and NMR. The DSC data exhibited slightly more symmetric S-shapes, i.e., a lower slope at the beginning but higher slope at the turning point, which was probably a result of the smaller sample size and therefore lower temperature gradient compared to the NMR set-up (40 μl^3 vs. 1 cm^3).

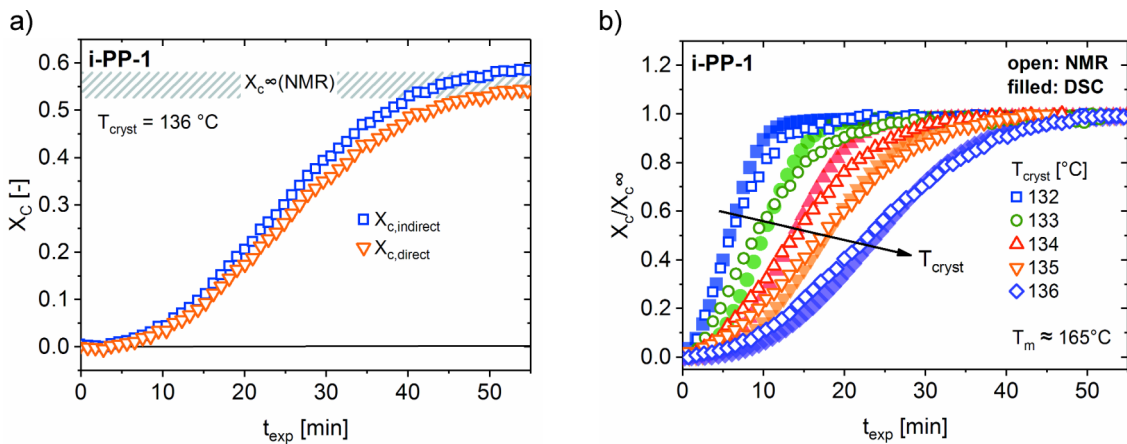


Figure 5.17: a) Direct and indirect data analysis (Equation 5.5 and Equation 5.6) yielded similar values with $X_{c,NMR}^{\infty} \approx 57\%$. b) Isothermal crystallization curves of i-PP-1 as measured by NMR (20 MHz, indirect data analysis) and corresponding DSC data. Reprinted from Röntzsch *et al.* (2018).

In Figure 5.18, isothermal crystallization curves measured at different temperatures are shown for all investigated semi-crystalline polymers. The trend "higher crystallization temperature leads to slower crystallization" for $T_{\text{cryst}} > (T_m^0 + T_g)/2$ was observed for all polymers. Over the investigated temperature intervals, the results for the polyethylenes showed the strongest dependency on the crystallization temperature. The immediate increase in ϕ_c for HDPE and LDPE upon reaching the crystallization temperature was probably caused by a gradient in temperature of ~ 1 K within the sample volume of $\sim 1 \text{ cm}^3$.

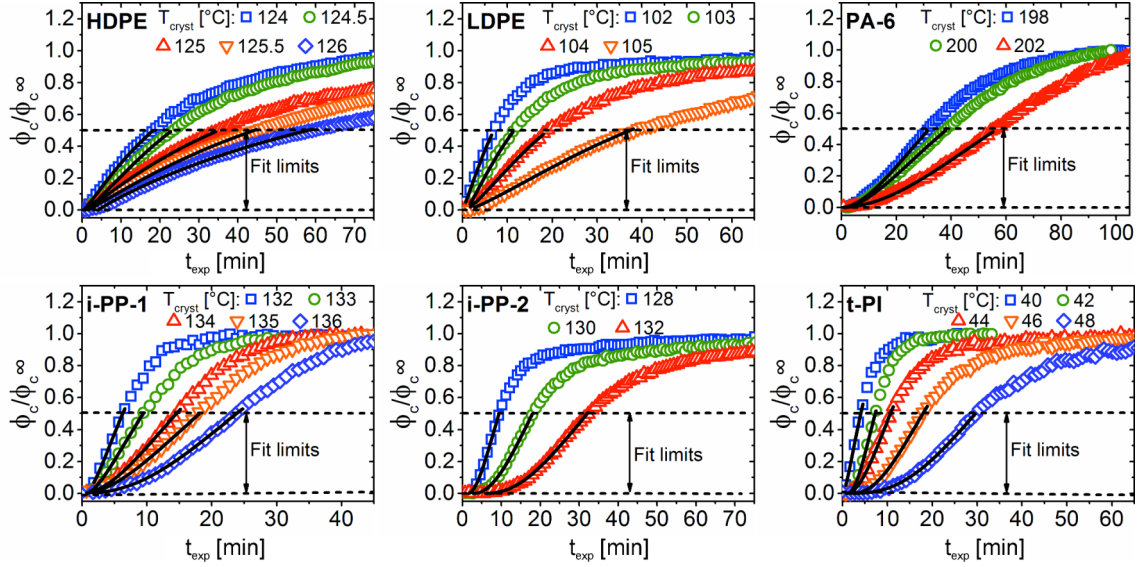


Figure 5.18: Isothermal crystallization traces for several different polymers and their crystallization temperatures (indirect data analysis). All curves exhibit the trend "higher crystallization temperature leads to slower crystallization" which is usually observed for $T_{\text{cryst}} > (T_m^0 + T_g)/2$. The immediate increase in the relative crystallinity of HDPE and LDPE upon reaching the crystallization temperature may have been caused by a temperature gradient in the sample. All curves were fitted using an Avrami model up to 50% relative crystallinity to obtain the kinetic rate K and the exponent n . Reprinted from Rantzsch *et al.* (2018).

The data shown in Figure 5.18 is presented in the form of volume-related crystallinities, which are related to the mass-dependent counterparts by:

$$\phi_c(t) = \frac{\rho_a}{\frac{\rho_c}{X_c(t)} + \rho_a - \rho_c} \quad (5.7)$$

All curves were directly fitted using the volume-related Avrami model up to 50% relative crystallinity to obtain the kinetic rate K and the exponent n (Avrami (1941), subsection 3.3.6, p. 35):

$$\frac{\phi_c(t)}{\phi_c^\infty} = 1 - \exp\{-[K(t - t_0)]^n\} \quad (5.8)$$

ϕ_c : volume crystallinity, ϕ_c^∞ : final volume crystallinity, K : rate, n : exponent, t : time, t_0 : induction time, X_c : mass crystallinity, ρ_a, ρ_c : densities of the fully amorphous and crystalline material (Van Krevelen and Te Nijenhuis 2009).

The direct Avrami modeling of crystallization curves and the analysis using linearized Avrami plots were compared and no major difference was found between these two approaches (Figure 5.19). However, for incomplete crystallization runs and fast experiments with only a small number of data points, differences in the estimation of the induction time t_0 and kinetic parameters K and n might be found. In the present work the induction time t_0 is merely regarded as a fitting parameter to shift the Avrami curve on the t -axis. Therefore, it includes contributions from the time needed for cooling and from the actual induction or pre-nucleation process. Such a pro-longed nucleation period with no significant change in crystallinity was observed

for different polymers, especially at higher crystallization temperatures (Lorenzo *et al.* 2007). Some researchers attribute it to the pre-nucleation process of cluster formation as discussed in subsection 3.3.2, p. 25, whereas others suspect that it might be a question of sensitivity to detect a small number of nuclei at the very beginning of polymer crystallization.

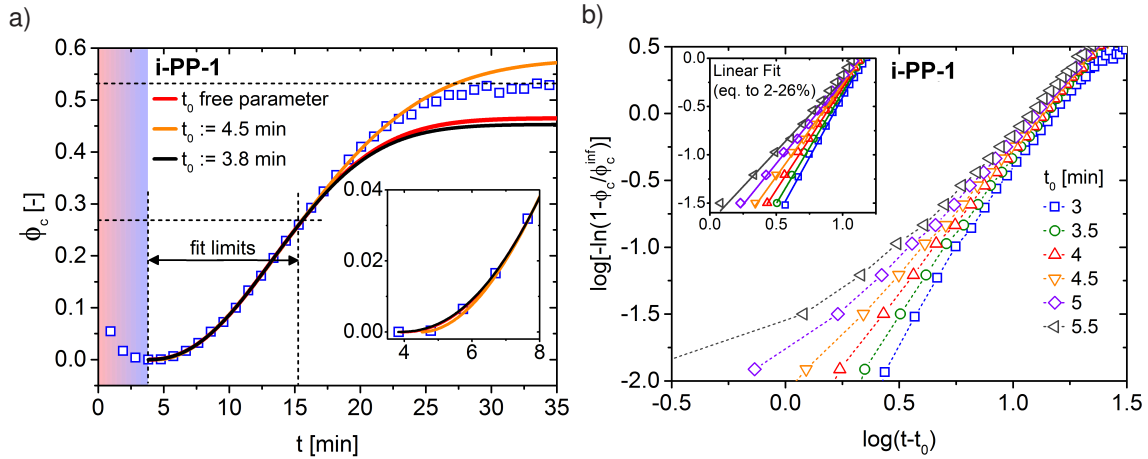


Figure 5.19: a) Direct modeling of crystallization data for i-PP-1 recorded at 132 °C using the Avrami equation up to $\phi_c/\phi_c^\infty = 0.5$. An induction time $t_0 \approx 4$ min was estimated. b) Corresponding Avrami plot for different values of t_0 . The value of $t_0 = 4$ min showed the expected linear relationship, whereas higher and lower values led to nonlinear curves (see also subsection 3.3.6, p. 35).

All crystallization curves for the two i-PPs, PA-6, and t-PI were well described by the direct Avrami fit over the range of $0 \leq \phi_c/\phi_c^\infty \leq 0.5$, which is an indication of predominantly primary growth up to that point (Figure 5.18). Since the Avrami model does not account for a growth rate distribution, it is strictly applicable only in the absence of any temperature gradient, which is experimentally difficult to achieve for the sample volume of ~ 1 cm³ in a 10 mm NMR probe. The immediate increase in ϕ_c for all polyethylene crystallization curves (Figure 5.18) and the resulting non-symmetric S-shape indicate that there was a temperature gradient across the sample as these two samples are highly sensitive to even the smallest crystallization temperature differences over the chosen temperature interval.

5.5.2 Comparison with DSC

Isothermal DSC crystallization experiments were carried out for all polymers using the protocol established by Lorenzo *et al.* (2007) (melting, fast cooling with -60 K/min, isothermal crystallization). As the buildup of crystallinity is obtained by an integration of time-dependent heat flux curves in DSC (Figure 5.20a), the highest measurable crystallization temperature is limited by the sensitivity of the instrument, which is different from NMR where in principle no limitations are pre-determined with respect to the highest crystallization temperature. Furthermore, the absolute area under isothermal crystallization heat flux curves ΔH is strongly dependent on the baseline, therefore usually values relative to the total area ΔH_{total} are compared (Lorenzo *et al.* 2007). These relative enthalpy ratios are identical to relative crystallinity ratios ϕ_c/ϕ_c^∞ , which are comparable to the relative crystallinity values obtained by NMR.

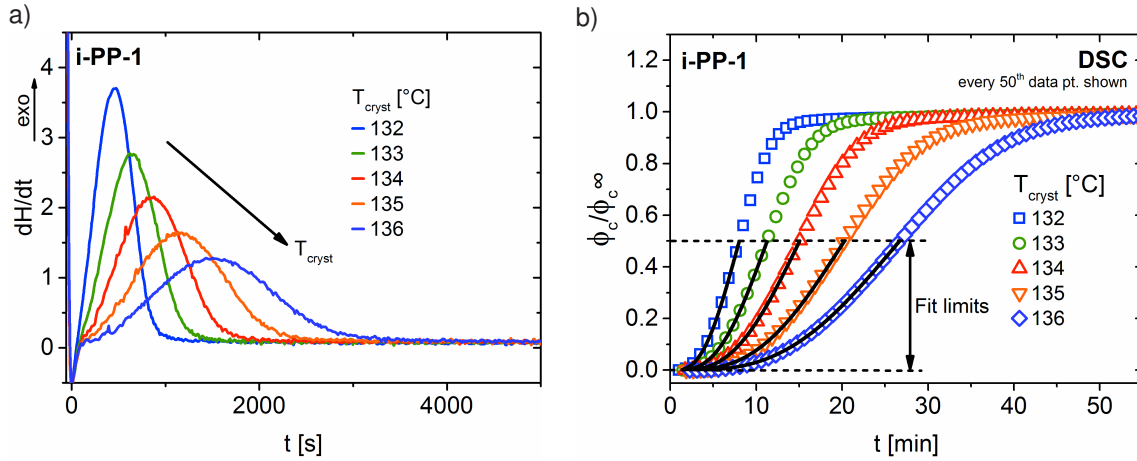


Figure 5.20: a) DSC heat flux curves for isothermal crystallizations of i-PP-1 at different temperatures. Integration of the time-dependent heat flux curves and normalization led to relative crystallinity ratios ϕ_c/ϕ_c^∞ (b), which were analyzed using the Avrami model (Equation 5.8).

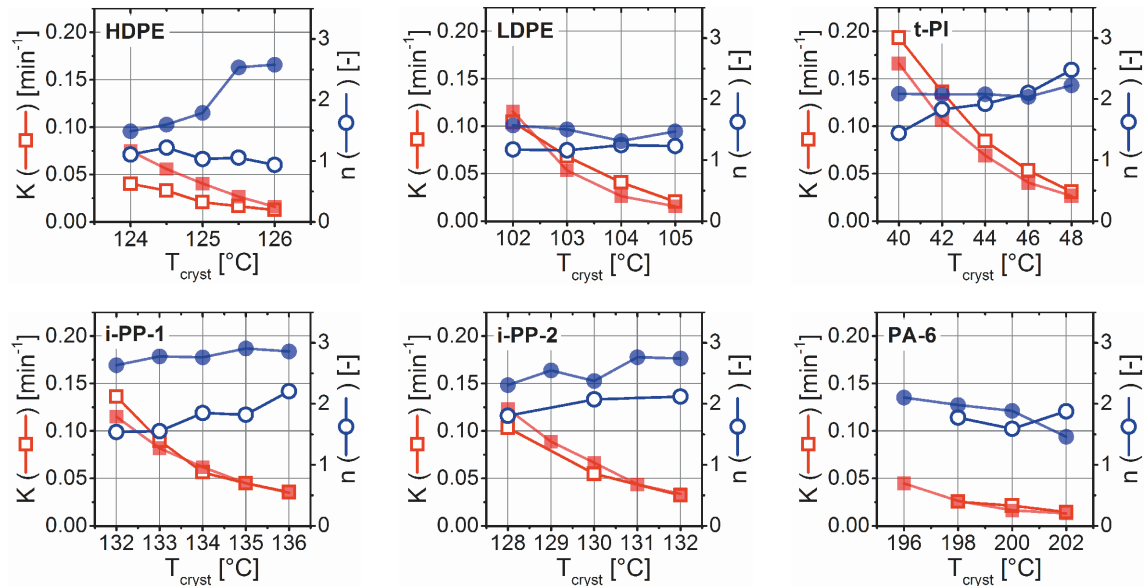


Figure 5.21: Avrami rate K and exponent n for isothermal crystallization experiments of different polymers measured by DSC (filled symbols) and NMR (open symbols). The rate K showed a good level of agreement for all polymers. On the other hand, the values for the exponent n only agreed well for LDPE, t-PI, and PA-6, whereas, for the polypropylenes and especially HDPE, a lower value was determined by NMR. The origin of this discrepancy is probably a temperature gradient of ~ 1 K across the sample for the NMR experiments. Reprinted from Röntzsch *et al.* (2018).

For all polymers, the Avrami rate K extracted from NMR was in good agreement with the values obtained by isothermal DSC experiments (Figure 5.21). The Avrami exponent n was comparable for LDPE, t-PI, and PA-6, whereas, for the polypropylenes and HDPE, a lower value was determined by NMR. The origin of this discrepancy was the earlier rise in the NMR crystallinity parameter compared to DSC, and could have been the consequence of the temperature gradient of ~ 1 K across the sample for the NMR experiments. In (Figure 5.22), the effect of a growth rate distribution is illustrated using a linear superposition of five curves with different values for the growth rate K , but identical dimensionalities n . Modeling the

superposition curve with only a single set of Avrami parameters led a significantly decreased exponent $n' = 1.4$, which didn't indicate a change in dimensionality, but was an artifact caused by the distribution of growth rates. By optimizing the temperature control and NMR probe design, a reduction of temperature gradients and a better comparability could be achieved.

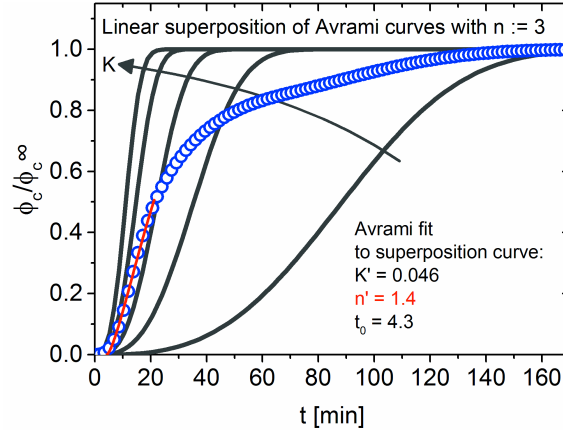


Figure 5.22: Linear superposition of five curves with $K = 0.01, 0.025, 0.04, 0.06, 0.08$ 1/min, and identical dimensionalities $n = 3$. Modeling the superposition curve with a single set of Avrami parameters led to an average growth rate $K' \approx 0.046$ /min, which was in good agreement with the third curve of intermediate K . However, the obtained apparent dimensionality $n' = 1.4$ was significantly lower than the dimensionalities n of the individual curves.

5.6 Development of a high-temperature LF-NMR probe and an active Q-switch

Motivation

As NMR has an inherently low sensitivity because of the \vec{B}_0 -dependent Zeeman splitting, much effort is put into minimizing losses and improving signal transmission. In order to achieve the highest possible sensitivity, probes with high quality factors Q are desirable. The quality factor Q is a dimensionless parameter that characterizes the damping behavior of tank circuits caused by its internal resistance (high $Q =$ low damping, low $Q =$ high damping). It has a strong effect on the sensitivity and the ring-down characteristics of NMR probes (high Q – long dead time, see Figure 5.1b). For a tank circuit, the quality factor is given by:

$$Q = \frac{1}{R} \cdot \sqrt{\frac{L}{C}} \quad (5.9)$$

R : resistance, L : inductance, C : capacitance.

The NMR probe bandwidth $\Delta\omega$ and the quality factor Q are connected by:

$$Q = \frac{\omega_0}{\Delta\omega} \quad (5.10)$$

The maximum possible NMR probe Q factor is limited by the circuit design, the needed bandwidth for excitation, and the relaxation behavior of the material under study. For liquid samples with slow transverse relaxation, high Q probes (> 150) with long dead times of $> 20 \mu\text{s}$ can be constructed as the magnetization of liquid samples hasn't decayed significantly on this time scale. However, for solid samples the rapid signal decay due to dipolar dephasing limits the possible quality factor to values $Q < 50$ with corresponding dead times of $\sim 10 \mu\text{s}$. Pulse sequences such as the magic sandwich echo (MSE) are a way to reconstruct the initial magnetization decay (see subsection 4.2.3, p. 58). However, they are prone to errors if dynamic processes act on the time scale of the refocusing pulses. A different approach is to use an active Q -switching device in combination with a high- Q NMR probe, which allows for a switching between states of high and low Q as shown in Figure 5.23 (Conradi 1977; Hoult 1979; Andrew and Jurga 1987; Anklin *et al.* 1995; Peshkovsky *et al.* 2005; Corver *et al.* 2005; Guthausen and Kamlowksi 2009; Aissani *et al.* 2014). For pulsing and data acquisition the Q -switch is open, enabling fast signal transmission and high sensitivity. Right after an NMR pulse, the Q -switch is closed, which lowers Q and leads to an effective damping of the ring-down.

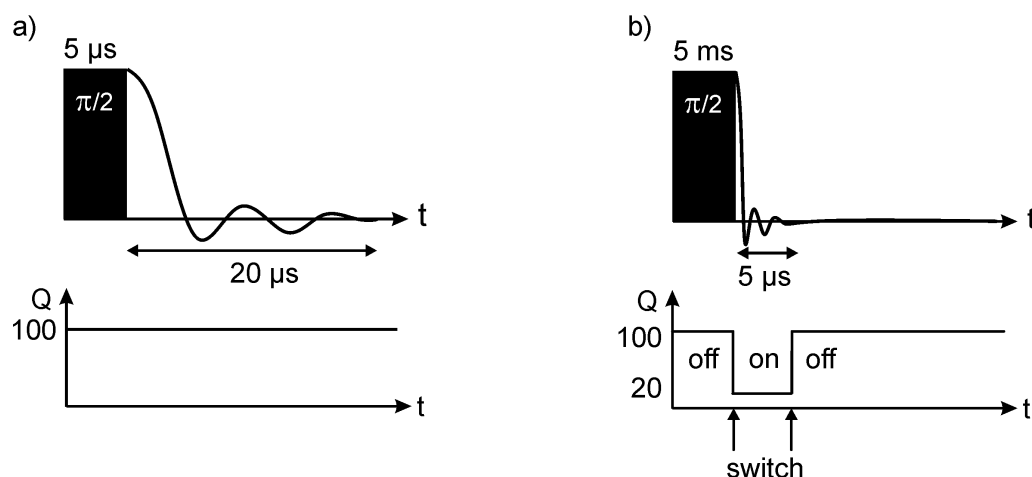


Figure 5.23: Schematic representation of a high- Q NMR probe with a long dead time (a) and the same probe together with an active Q -switching device to dampen the pulse and shorten the dead time (b).

Design

A new high-temperature NMR probe for the Bruker "the minispec" spectrometer operating at 20 MHz with high Q , an improved thermal insulation, and simplified match- / tunability was developed at the Pro²NMR facility under supervision of Prof. G. Guthausen (Figure 5.24). All metal, plastic, and glass parts were made in-house by colleagues at the ITCP workshop and the glass blowing facility. Silvering of a glass Dewar and evacuation were carried out by KGW Isotherm GmbH (Karlsruhe, Germany). NMR probes are designed to resonate at the Larmor frequency (here: 20 MHz) which is defined by the magnetic field \vec{B}_0 . The parameters of the tank circuit (capacitance C , inductance L) are related to the angular frequency ω_0 by:

$$\omega_0 = \frac{1}{\sqrt{LC}} \quad (5.11)$$

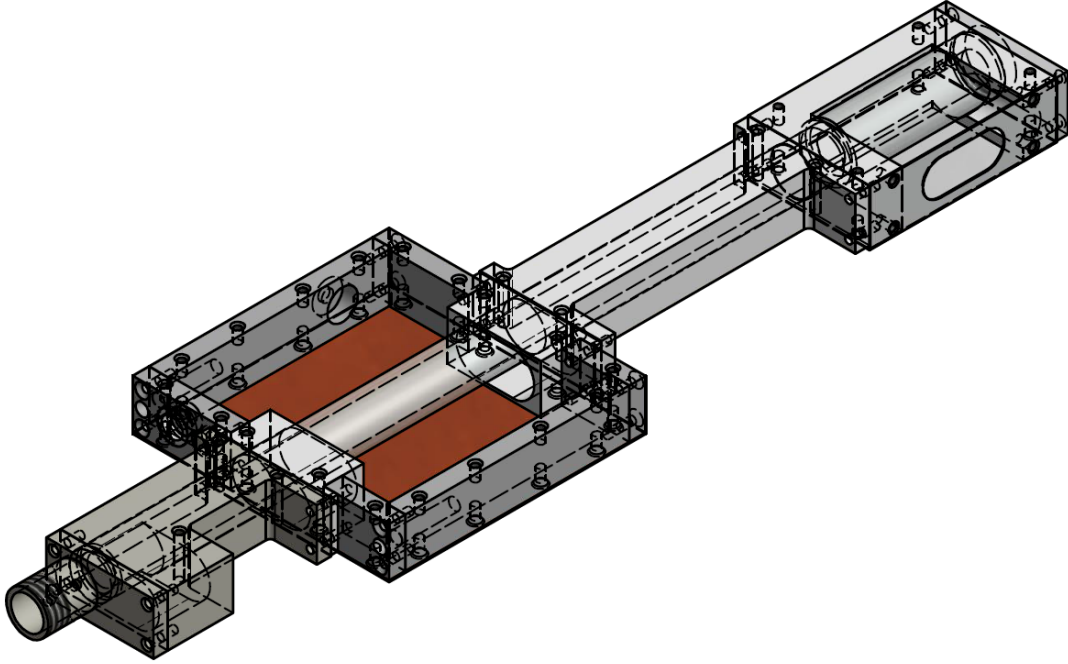


Figure 5.24: CAD drawing of the developed high-temperature probe for the Bruker "the minispec" spectrometer (20 MHz) at the Pro²NMR facility with a shielded housing for the tank circuit and a silvered Dewar for thermal insulation (photograph in Appendix A).

For a solenoid coil, the inductance is proportional to the square of the number of turns N^2 times the area A , divided by the length l :

$$L \approx \frac{\mu_0 \cdot N^2 \cdot A}{l} \quad (5.12)$$

μ_0 : vacuum permeability, N : number of turns, A : area, l : length.

The tank circuit shown in Figure 5.26a was built using two non-magnetic trim capacitors (Voltronics NMTM120CE, 2 – 120 pF) and flat silver wire (1.5 mm diameter, 999 silver, Götze GmbH, Berlin) for the solenoid coil ($d = 18$ mm, $N = 12$, $l = 45$ mm). The Q factor was determined to be ~ 130 by measuring the bandwidth at full width half maximum (FWHM) using an Agilent 8712ET RF network analyzer.³

The Q -switch was developed in a joint project between the Pro²NMR facility led by Prof. Gisela Guthausen and Dr. Martin Sack (Institute for Pulsed Power and Microwave Technology - IHM, group of Prof. John Jelonnek) and his student Paul Dietrich who worked on this project during his Bachelor thesis. It was designed as an accessory that could be used together with different NMR probes. Its position in the set-up was selected to be in between the pre-amplifier and the NMR probe (Figure 5.25). Triggering the Q -switch was carried out by transistor–transistor logic (TTL) pulses using the Bruker minispec software. The circuit was designed by Dr. Mar-

³ The definition of bandwidth $\Delta\omega$ differs between the communities of NMR and electrical engineering. The latter group measures the bandwidth at -3 dB, which leads to lower Q values. For this work, the NMR convention of measuring bandwidth at FWHM of the resonance was employed.

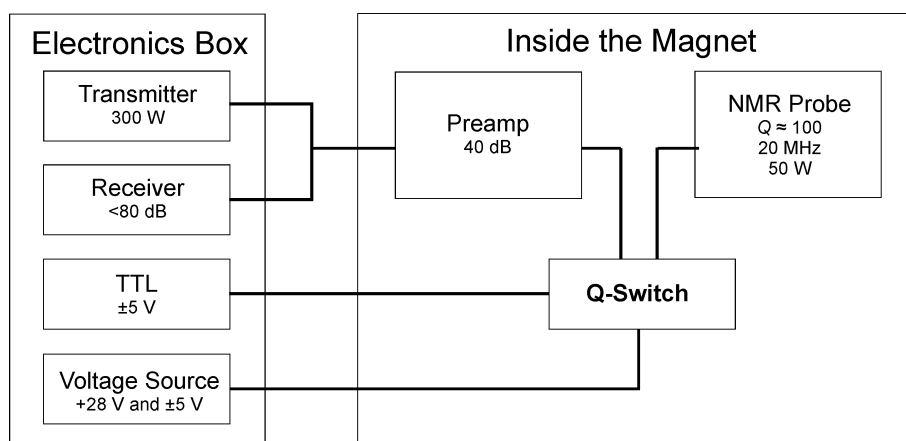


Figure 5.25: Schematic layout of the Bruker minispec with the Q-switch as an accessory that can be used together with different NMR probes. Its position in the set-up was selected to be in between the pre-amplifier and the NMR probe to ensure high flexibility and accessibility.

tin Sack and Paul Dietrich based on works by Anklin *et al.* (1995); Peshkovsky *et al.* (2005); Corver *et al.* (2005); Guthausen and Kamlowski (2009). The main components were a transformer (ferrit core) for transferring energy into the Q-switch, two transistors T_1 and T_2 for switching (SPP04N60S5 type, max. 600 V and 4.5 A), three trim capacitors C_{Prim} , C_{Sec1} and C_{Sec2} for power matching, and two resistors R_{Q1} and R_{Q2} for energy absorption (max. 3 W, combinations of SMD 1210 type resistors).

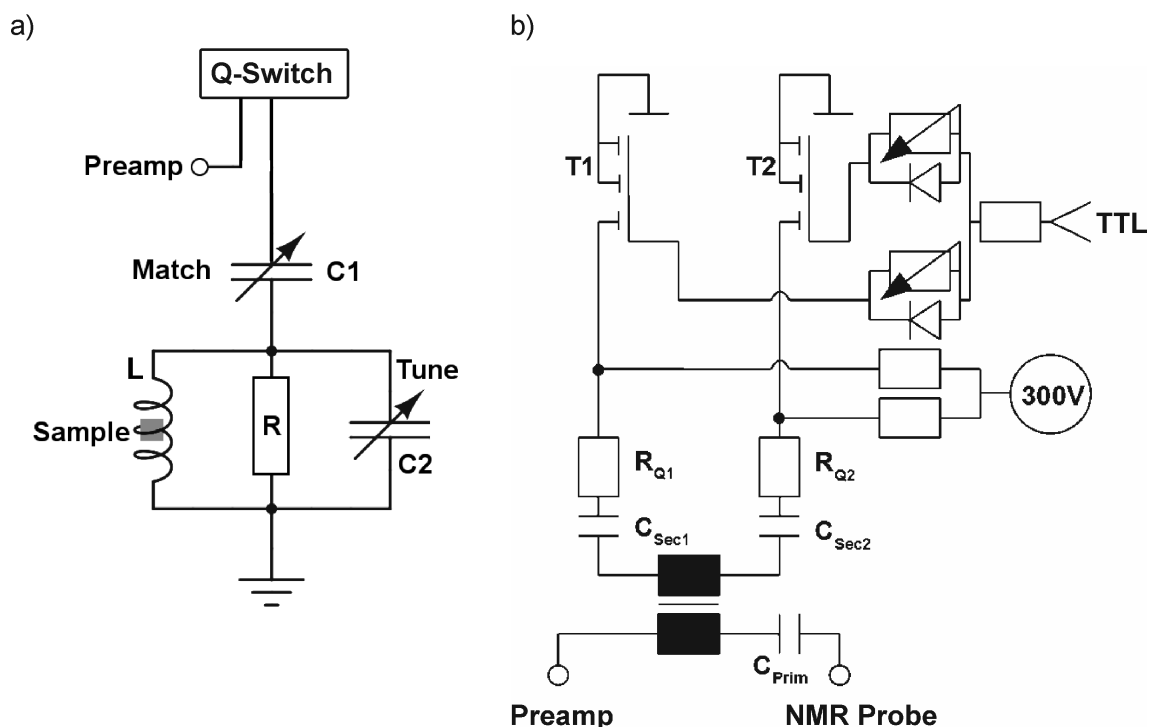


Figure 5.26: a) Circuit design of the developed high-Q NMR probe operating at 20 MHz. b) Q-switch circuit developed by Dr. Martin Sack and Paul Dietrich (photograph in Appendix A).

Performance Tests

The Q-switch was tested externally using an oscilloscope to evaluate and optimize the damping performance. The data shown in Figure 5.27a was obtained for a transformer with three windings and a NiZn ferrit type 67 core (Fair Rite Corp., Wallkill, USA). It showed almost no signal loss in the open case, and a damping of -11 dB in the closed state (TTL on). The signal needed only 2 – 3 ns to reach stable damping conditions.

For performance testing under real conditions, the developed NMR probe and the Q-switch were assembled inside of the Bruker minispec and matched iteratively to ensure the highest energy transfer ($50\ \Omega$ matching). The switching functionality was tested using a 90° -FID pulse program (dead time measurement). To prevent arcing within the NMR probe, a pulse attenuation of 24 dB was applied, which led to a 90° pulse length of $7.8\ \mu\text{s}$. TTL-triggering was carried out by inserting Bruker ExpSpel st-commands right after the pulse. In Figure 5.27b, results are shown for different experimental configurations. Notably, the mere presence of the Q-switch in the signal path led to a lower dead time. The reason was certain coupling to the Q-switch even in its open state. Turning the Q-switch on and off produced substantial crosstalk. Therefore, the active damping functionality of the Q-switch was tested using a $50\ \mu\text{s}$ closed state following the 90° pulse. The data showed a prolonged decay and not the damping effect which was seen in the experiments using an oscilloscope. This was presumably associated with a lower energy transfer in the switched case due to a modified impedance ($\neq 50\ \Omega$). Inserting cables of different lengths between the preamp and the Q-switch didn't change this trend significantly. Placing the Q-switch electrically on the other side of the capacitor C_1 (Figure 5.26a) might help to improve the energy transfer and to lower the dead time. Alternatively, an inductive coupling to the NMR coil as suggested by Peshkovsky *et al.* (2005) could in the future be realized at the cost of lower flexibility.

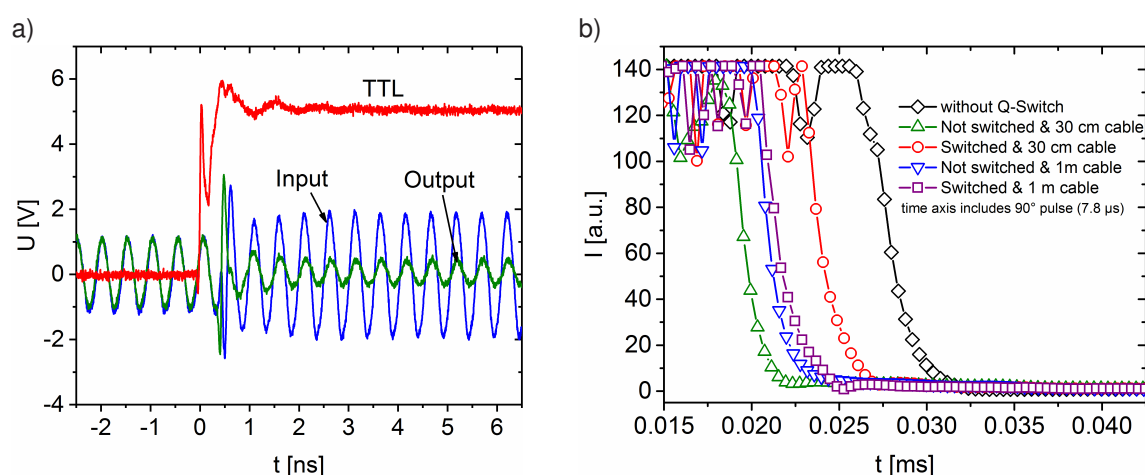


Figure 5.27: a) External measurements of the Q-switch damping performance using an oscilloscope. The loss in the open state was minimal, whereas in the closed state a damping of -11 dB was observed. b) NMR probe dead time measurements for different experimental configurations in combination with the Q-switch (not switched / switched, different cable lengths between the preamp and the Q-switch).

5.7 Concluding remarks

In this chapter, the molecular dynamics of commercially relevant semi-crystalline polymers were investigated using ^1H -NMR. In the first part, high-field solid-state NMR experiments were presented, which displayed the broad line shape of semi-crystalline polymers due to strong homonuclear dipolar coupling. Free induction decays were analyzed using semi-empirical models to describe the temperature-dependent relaxation of semi-crystalline polymers. The experiments were limited by the accessible temperature range that didn't allow for a full series of measurements between the glass transition temperature and the nominal melting points.

In the second part, low field ^1H -NMR relaxometry was used to investigate the temperature-dependent relaxation behavior over a wider temperature range and $T = T_g + 100$ K was identified as the minimum temperature for which the mobility difference between protons in crystalline and amorphous fractions is sufficient for an unambiguous determination of polymer crystallinity. The obtained bulk crystallinities X_c were compared to DSC and XRD data, and showed good agreement for all polymers within an estimated relative error of $\pm 10\%$ for the respective methods. Additionally, we focused on the determination of crystallization kinetics, i.e., monitoring of isothermal crystallization, which required a robust design of the pulse sequence, precise temperature calibration, and careful data analysis. We found the combination of a mixed magic sandwich echo (MSE) with a short acquisition duration followed by a CPMG echo train with short pulse timings to be the most suitable sequence for crystallization experiments. For all polymers, the relaxation behavior within the amorphous domains was rather invariant during crystallization, pointing towards a nucleation and growth mechanism for polymer crystallization. Two different methods of data analysis (direct, indirect) were evaluated. The indirect data analysis was found to be more robust because it relies only on the analysis of CPMG data and is independent of the MSE efficiency. When compared to isothermal DSC experiments, a quantitative analysis using the Avrami model showed good agreement for the rate K , but certain deviations in the exponent n were seen that were presumably caused by temperature gradients.

In the third part of this chapter, the use of an active Q -switching device for lowering the dead time of high- Q NMR probes was studied in a joint project between the Pro²NMR facility led by Prof. Gisela Guthausen and Dr. Martin Sack and Paul Dietrich (Institute for Pulsed Power and Microwave Technology - IHM, group of Prof. John Jelonnek). The developed NMR probe had an improved thermal insulation and simplified match- and tunability. When tested externally using an oscilloscope, the closed Q -switch dampened a 20 MHz signal by -11 dB, whereas in the open state it showed almost no signal loss. When tested together with the built high- Q NMR probe, no substantial signal dampening could be observed. This behavior was presumably caused by an impedance mismatch once the Q -switch was turned on. By placing the Q -switch electrically closer to the NMR coil, the performance could be improved.

6 Interplay between Molecular Dynamics and Rheology in Polymer Crystallization: RheoNMR

In the following chapter, simultaneous investigations of molecular dynamics and the associated hardening behavior during polymer crystallization are presented, which are an important cornerstone in understanding the rheology of crystallizing polymer melts. In this context, the influence of crystallization temperature, polymer grade, fillers, and additives were analyzed. Furthermore, the effect of well-defined flow profiles on the process of polymer crystallization with respect to the changes in molecular dynamics and rheology is discussed. Finally, the morphology as revealed by *ex-situ* scanning electron microscopy was connected with the observed flow phenomena and the changes in molecular dynamics. Parts of this chapter are based on recently published conference contributions (Räntzsch *et al.* 2017a,b).

6.1 Introduction

The flow and deformation behavior of polymer melts can be thoroughly studied using rheology, whereas low-field NMR relaxometry is a powerful technique for the characterization of molecular dynamics (chapter 5). To achieve a substantial insight into the interplay of these domains, especially under flow, these two methods were combined into one set-up (Rätzsch *et al.* 2017; Räntzsch *et al.* 2017b). This approach is different from other RheoNMR set-ups, as its main purpose is the study of molecular dynamics rather than molecular or macroscopic structure via NMR spectroscopy (Grabowski and Schmidt 1994; Lukaschek *et al.* 1995; Schmidt 2006; Ohgo *et al.* 2008; Medronho *et al.* 2010) and magnetic resonance imaging (Callaghan 1999; Callaghan and Gil 2000; Callaghan and Komlosh 2002; Callaghan 2006, 2008; Galvosas and Callaghan 2006; Hollingsworth *et al.* 2004; Kilfoil and Callaghan 2000; Lopez-Gonzalez *et al.* 2006). The length and time scales of rheometry are millimeters and seconds whereas in low-field NMR relaxometry (also called Time Domain (TD)-NMR) they are both $10^3 - 10^6$ times smaller. Besides polymer crystallization, low-field RheoNMR can also be used to study the curing of resins, the cross-linking of rubbers, or the crystallization of edible fats. Based on the changes in molecular dynamics, a quantitative compositional analysis of multiphase soft matter systems during or upon the application of linear and non-linear shear deformations can be obtained (chapter 5).

The buildup of semi-crystalline spherulites in a polymer melt leads to strong thickening, which has some similarity to a suspension of rigid, potentially interacting particles in a viscoelastic fluid. Early studies by Pogodina and Winter (1998); Pogodina *et al.* (1999, 2001) showed

a gelation-like transition during polymer crystallization similar to small molecules that form into a gel. The suspension-like hardening behavior of crystallizing polymer melts was described in great detail by Lamberti *et al.* (2007); Lamberti (2012); Pantani, De Meo, Speranza and Titomanlio (2015) and incorporated into a hardening model by Roozmond *et al.* (2012). However, the detailed physics behind this process remain a subject of debate. Due to the extremely high temperature-dependence of polymer crystallization, the correlation of data on the evolving crystallinity and flow behavior from separate instruments (e.g., DSC and rheology) is very difficult to practically achieve. *In-situ* techniques such as low-field RheoNMR determine polymer crystallinity and flow properties simultaneously, leading to a substantially better correlation of data with the additional benefit of being able to apply shear protocols.

6.2 Experimental

RheoNMR set-up

The hyphenated low-field RheoNMR set-up was developed by Dr. Karl-Friedrich Ratzsch and is based on a portable ^1H NMR unit ($\vec{B}_0 = 0.7\text{ T}$, $\omega_L/2\pi = 30\text{ MHz}$ for ^1H) that was integrated into a commercial strain-controlled TA / Rheometrics ARES shear rheometer (Figure 6.1, Ratzsch *et al.* (2017), see Appendix A for a photograph). This unique combination can be employed to make a full rheological characterization (G' , G'' , $|\eta^*|$, FT-Rheology: $I_{3,1}$, Q_0) and to apply well-defined shear protocols while monitoring molecular dynamics *in-situ* via ^1H NMR relaxometry.

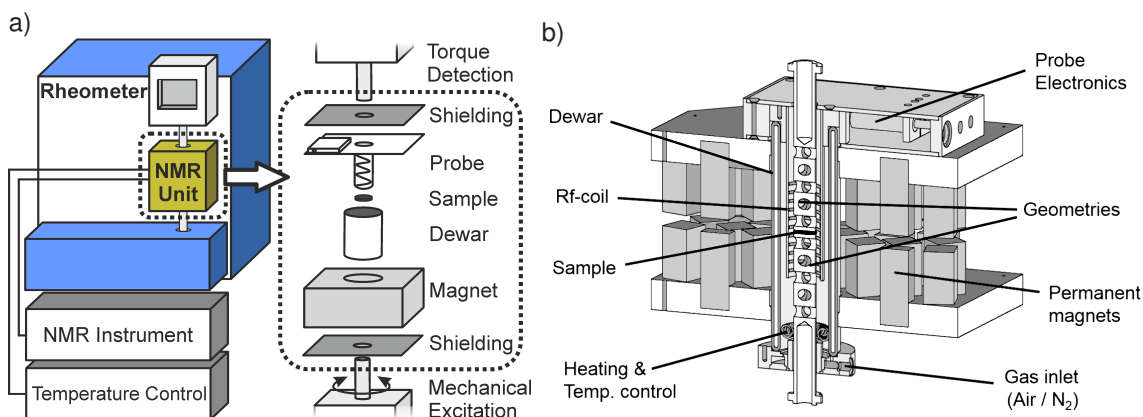


Figure 6.1: Low-field RheoNMR set-up based on a portable ^1H time domain (TD)-NMR unit (30 MHz) implemented in a strain-controlled shear rheometer (TA ARES). Adapted from Ratzsch *et al.* (2017); Rätzsch *et al.* (2017b).

The NMR magnet consists of a Halbach array of 92 NdFeB permanent magnets that permits its facile integration into a rheometer due to its low stray field, light weight and small dimensions (Figure 6.1). A Dewar was placed between the temperature-sensitive permanent magnets and sample space to achieve good thermal insulation (silvered glass with an un-silvered window to avoid ring currents). The sample temperature can be controlled from -15 to $+210\text{ }^\circ\text{C}$ using a N_2 -based convective heating system and a Bruker Variable Temperature unit (BVT). The broadband NMR probe used in these experiments is based on a parallel tank circuit equipped

with a solenoid coil ($l = 33$ mm, $d = 16$ mm) and two capacitors (match & tune) exhibiting a dead time of $12 \mu\text{s}$ and pulse lengths of $\sim 3 \mu\text{s}$ (90°) and $\sim 6 \mu\text{s}$ (180°) at 0 dB pulse attenuation, respectively. Pulsing, data acquisition and processing were performed by a Bruker "the minispec" electronic unit. A requirement for ^1H NMR experiments are proton-free and non-conducting geometries, which were made from ceramics (13 mm parallel-plate and cone-plate). Such an NMR unit can also be used e.g., in combination with an extruder to monitor flow instabilities and polymer crystallization simultaneously by NMR and a pressure-sensitive detection system (Ratzsch *et al.* 2013).

The characteristics of the magnet were tested by recording free induction decays of a silicone oil for different positions inside of the magnet (Appendix A). The middle position resulted in the longest FID with the corresponding most narrow resonance (FWHM ≈ 50 kHz). In all cases, the FID exhibited certain oscillations, which were probably caused by the two stacked Halbach arrays. The \vec{B}_0 homogeneity was substantially lower than on the Bruker minispec mq20 (FWHM ≈ 250 Hz), which was used in chapter 5. Consequently, a multi-component analysis of the FID or a reconstructed counterpart (e.g., a mixed magic sandwich echo) was not possible. However, the performance was sufficient for monitoring polymer crystallizations using a combined MSE-CPMG pulse sequence as described in section 5.5, p. 82.

Procedures

Quiescent and flow-induced crystallization of isotactic polypropylene were studied under isothermal conditions in a temperature interval of $+130$ to $+150^\circ\text{C}$. The nominal average sample temperature was calibrated prior to all experiments using a digital thermometer (RS Components, Mörfelden-Walldorf, Germany) equipped with a type K thermocouple (see Appendix A for a calibration curve). Due to a temperature uncertainty of $\pm 1^\circ\text{C}$, the effective average crystallization temperatures denoted in this chapter are given based on a comparison with results from DSC and standalone NMR to ensure at most comparability (subsection 5.5.2, p. 87). Prior to all crystallization experiments, the polypropylene samples were molten at 200°C for 15 min to erase the thermal history. The changes in molecular dynamics and the buildup of crystallinity from an isotropic melt were monitored by ^1H NMR relaxometry as described in section 5.5, p. 82 using a combined MSE-CPMG pulse sequence. A bi-exponential function was fitted to the CPMG data to extrapolate to the theoretical initial intensity I_{CPMG} at $t_{\text{NMR}} = 0$. Based on the indirect data evaluation approach the evolving mass fraction of crystalline material was determined (Equation 5.6, p. 83). Different from our paper presented at the Novel Trends in Rheology Conference VI (Rätzsch *et al.* 2017b), no density-dependent correction term was included, the temperature was re-calibrated, and relative crystallinities were evaluated. In some experiments, the CPMG part was acquired without a preceding magic sandwich echo, as it was unnecessary for the indirect data evaluation. Obtained mass crystallinities $X_c(t)$ were converted to volume fractions $\phi_c(t)$ by considering the densities for a fully amorphous and a theoretically 100% crystalline sample (Mark 2007).

All polymer crystallizations were monitored by rheological time sweeps with low strain amplitude $\gamma_0 = 0.5\%$ and angular frequency $\omega = 1$ rad/s to detect the change in flow behavior without disturbing crystal formation. For all flow-induced crystallizations, a steady shear step was included right after the desired crystallization temperature was reached (Figure 6.2). Parallel-plate geometries (13 mm) with a gap of 1.5 mm were used in all experiments, as the contraction of the sample during crystallization required step-wise lowering of the upper geometry, which prevented the use of cone-plate geometries with a fixed gap.

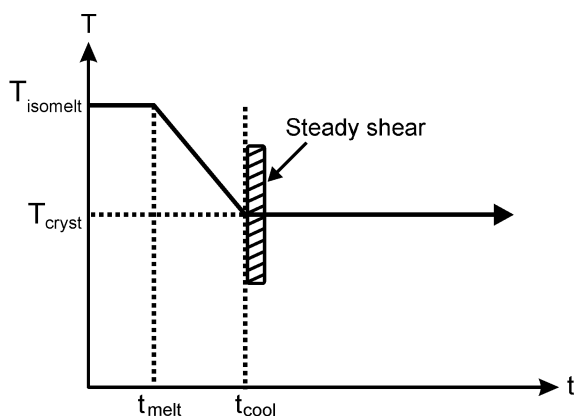


Figure 6.2: Short-term shear protocol proposed by Janeschitz-Kriegl and co-workers to separate the influences of temperature and flow on polymer crystallization (Janeschitz-Kriegl 1992; Eder *et al.* 1992). For i-PP: $t_{\text{melt}} \approx 15$ min, $t_{\text{cool}} - t_{\text{melt}} \approx 5$ min, $T_{\text{isomelt}} \approx T_m + 35$ K, $T_{\text{cryst}} \approx T_m - 35$ K.

The semi-crystalline morphologies were analyzed using *ex-situ* scanning electron microscopy (SEM). All samples were etched with an acidic permanganate solution (0.2 mol/l KMnO_4 in 10:4:1 H_2SO_4 (96%), $\text{o-H}_3\text{PO}_4$ (85%), H_2O for 2 h at room temperature with subsequent washing using H_2O_2 (30%)/ H_2O and sonication for 30 min in acetone). A 2 nm thick coating of Pt was deposited onto the specimens using a Leica EM ACE 600 sputter coater. SEM images were taken using a Zeiss Gemini/LEO 1530 system with 5 kV and 30/60 μm aperture.

Materials

The main material of investigation was a Ziegler-Natta polypropylene grade i-PP-1 (batch 1: $M_w = 246$ kg/mol, $D = 2.7$, batch 2: $M_w = 282$ kg/mol, $D = 3.4$). Additional experiments were performed on a metallocene-catalyzed polypropylene grade i-PP-2 ($M_w = 202$ kg/mol, $D = 1.9$) in order to unravel the effect of regio-defects on the crystallization behavior (see section 2.4, p. 19 for further information on the used polymer grades). The influence of nucleating agents was studied using compounds of i-PP-1' (batch 2) with 250, 500, 750, 1500 ppm of N, N', N''-tris(3-methylbutyl)-1,3,5-benzene tricarboxamide (DH677), which were prepared by our collaborators Dr. K. Kreger and D. Kremer in the group of Prof. H.W. Schmidt (University of Bayreuth, Germany) using a lab-scale twin-screw extruder. Furthermore, the effect of fillers on the crystallization behavior was analyzed using compounds of i-PP-1 with 1 – 5 wt% fumed silica (CAB-O-SIL TS-530, Cabot Corporation, Alpharetta, USA), which were compounded by Dr. J. Palacios in the group of Prof. A. Müller (Universidad del País Vasco, San Sebastián, Spain).

6.3 Quiescent crystallization of isotactic polypropylene

The isothermal crystallization behavior of neat isotactic polypropylene i-PP-1 was investigated by simultaneous monitoring of the flow behavior via rheology and the emerging polymer crystallinity ϕ_c via ^1H NMR relaxometry. The sample kept at 200 °C for 15 min was rapidly cooled to the crystallization temperature $T_{\text{cryst}} \approx 130$ °C. The experimental parameters for monitoring G' , G'' and $\tan(\delta) = G''/G'$ during crystallization were chosen as $\gamma_0 = 0.5\%$ and $\omega = 1$ rad/s to stay in a non-perturbing regime with regard to the crystallization kinetics. In Figure 6.3a, simultaneously measured evolving moduli G' and G'' are plotted together with the volume-related crystallinity ϕ_c extracted from NMR relaxation data by the indirect data analysis (Figure 6.3b, see also section 5.5, p. 82).

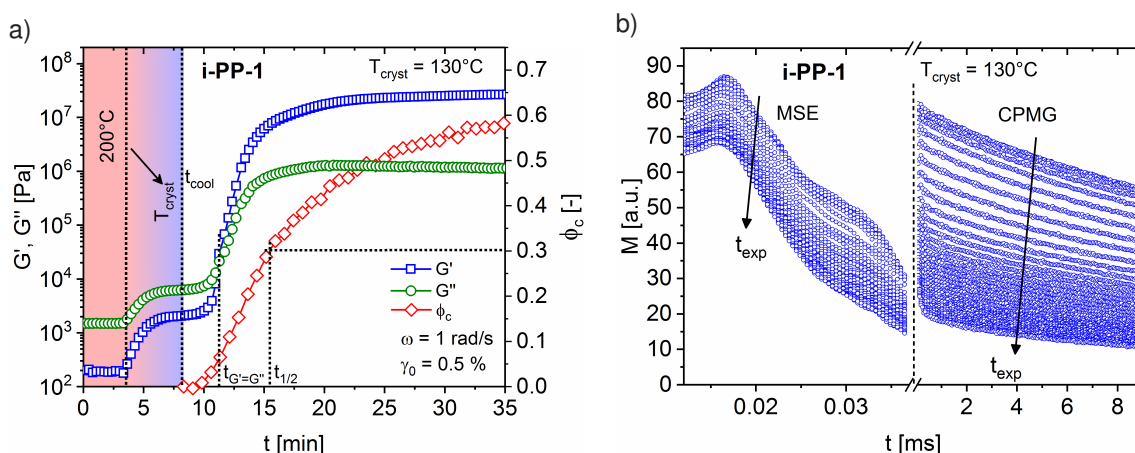


Figure 6.3: Simultaneously measured low-field RheoNMR data on the isothermal crystallization of isotactic polypropylene i-PP-1. a) Evolution of the rheological moduli G' and G'' plotted together with the volume-related crystallinity ϕ_c as determined by NMR. b) Corresponding series of transverse relaxation data as captured by an MSE-CPMG sequence.

An immediate increase in both the storage modulus G' and the loss modulus G'' was observed when the temperature was decreased ($t \approx 3$ min in Figure 6.3a). The time needed for cooling was approximately 5 min, which resulted in a nominal cooling rate of ~ 15 K/min. Crystallization started right after the temperature $T_{\text{cryst}} \approx 130$ °C was reached, which was indicated by another rise in the moduli G' and G'' , and the crystallinity ϕ_c . With further progression of crystallization, the material became increasingly elastic and a crossover ($G' = G''$) was observed at $t = 11$ min. Notably, the absolute crystallinity ϕ_c was as low as $\sim 5\%$ when the crossover occurred, which will be extensively discussed later in this section. The time $t_{1/2}$ needed to reach half crystallinity ($\phi_c = 0.3$) was identified as a second characteristic time of the crystallization process. By that time, the moduli reached almost their final plateau values on a log scale, whereas the crystallinity ϕ_c kept further increasing until a final crystallinity of $\phi_c = 0.6$ was obtained. The magic sandwich echoes recorded prior to the CPMG echo train showed a decaying behavior that was mainly determined by the \vec{B}_0 homogeneity (Figure 6.3b). Different deconvolution approaches were tested, but no analytical expression was found that could accurately describe the magnet-inherent decaying behavior and allowed a separation from

additional relaxation contributions caused by the sample. Results of the direct and indirect data analysis for obtaining crystallinity values are shown in Figure 6.4a. The direct approach is based on a comparison of CPMG intensities with the respective MSE maxima within one combined MSE-CPMG experiment, whereas the indirect approach relies on a comparison of CPMG intensities with the initial CPMG intensity of the supercooled melt. It was found that the indirect approach led to less noisy data and its final crystallinities were in the range of the values determined in chapter 5.

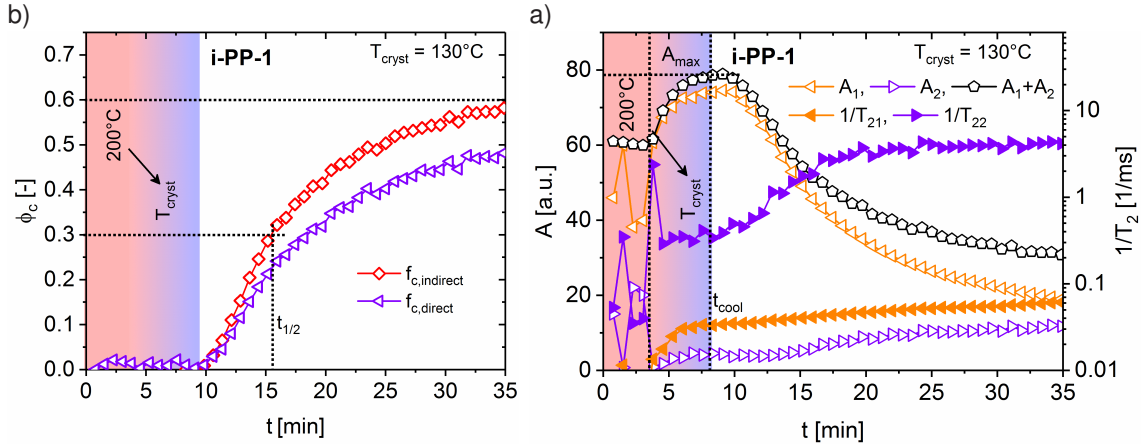


Figure 6.4: a) Comparison of the direct and indirect data evaluation methods of RheoNMR decay data for monitoring of the crystallinity buildup curves (section 5.5, p. 82). b) Transverse relaxation rates and intensities extracted from NMR relaxation data as captured by an MSE-CPMG sequence.

Characteristic transverse relaxation rates $1/T_{2,1}$ and $1/T_{2,2}$ and their corresponding intensities were obtained by modeling the NMR relaxation data with a bi-exponential function:

$$A(t) = A_1 \cdot \exp\left(-\frac{t}{T_{2,1}}\right) + A_2 \cdot \exp\left(-\frac{t}{T_{2,2}}\right) \quad (6.1)$$

The relaxation rates $1/T_{2,1}$ and $1/T_{2,2}$ showed an inverse evolution compared to the corresponding intensities A_1 and A_2 (Figure 6.4b). The highly mobile component was characterized by the relaxation rate $1/T_{2,1}$, which increased only slightly during the crystallization process. This indicated the buildup of additional physical constraints during crystallization that hindered molecular motion to some degree. Both, the relaxation rate $1/T_{2,2}$ and the corresponding intensity A_2 of the semi-mobile or intermediately mobile component increased during crystallization. The early appearance of this intermediately mobile component might be an indication of a pre-forming mesomorphic phase which is located at the growth front as proposed by Strobl (see subsection 3.3.5, p. 33, Strobl (2000, 2009)). Overall, the transformation process had a comparable effect on the local molecular dynamics ($1/T_{2,1}$, $1/T_{2,2}$) and the macroscopic flow behavior (G' , G''), which was in accordance with previous isothermal crystallization experiments on trans-polyisoprene (Räntzsch *et al.* 2014).

Repeatability

The test-retest reliability or repeatability of the RheoNMR set-up was analyzed by carrying out multiple isothermal crystallizations of i-PP-1 at a relatively high crystallization temperature of $T_{\text{cryst}} \approx 136$ °C, which ensures the detectability of variations in the crystallization kinetics due to its strong temperature-dependence and a large total number of data points. In Figure 6.5a, rheological time sweep data from different experiments is shown in an overlay plot. The corresponding evolution of the relative crystallinities ϕ_c/ϕ_c^∞ as monitored by NMR relaxometry is shown in Figure 6.5b. The earliest measurement from November 2015 (no. 1) displayed higher moduli than the later experiments, which might have been caused by a slightly too low gap using the thermal expansion correction feature of the TA ARES. In all later experiments, the zero-gap routine was carried out at the crystallization temperature, which didn't require the use of a thermal expansion correction. All experiments performed in July 2016 showed similar curve behavior. The two measurements from July 25 (no. 2/3) were done using the exact same sample, whereas for the experiment on July 26 (no. 4), a new sample was loaded into the setup. Importantly, the NMR unit was not disassembled between these tests, which ensured a similar average temperature and temperature distribution within the sample. In contrast, the measurement in August 2016 (no. 5) was done using a re-calibrated set-up and a new sample, which led to slightly different results.

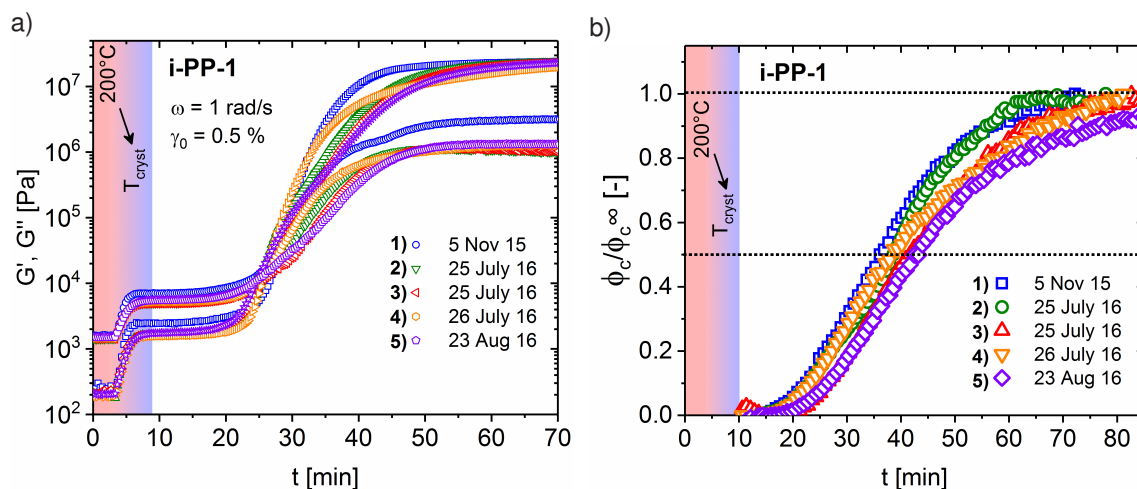


Figure 6.5: a) Overlay plot of multiple rheological time sweeps in chronological order following the isothermal crystallization of i-PP-1 at nominal crystallization temperatures $T_{\text{cryst}} \approx 136$ °C. b) Corresponding evolution of the relative crystallinities ϕ_c/ϕ_c^∞ .

For further comparison, the times needed for the onset and endset of crystallization were determined by estimating the intersection of linear extrapolations of the storage modulus G' (Figure 6.6). On an absolute time scale, t_{endset} showed the highest variation, whereas t_{onset} and $t_{G'=G''}$ were rather similar and not that much affected by potential differences in the average sample temperature and its distribution. Again, the experiments carried out in a short period of time (July 2016) showed strong correlation with a low variation of $t_{G'=G''}$ below ± 0.5 min, which was lower than the respective standard deviations.

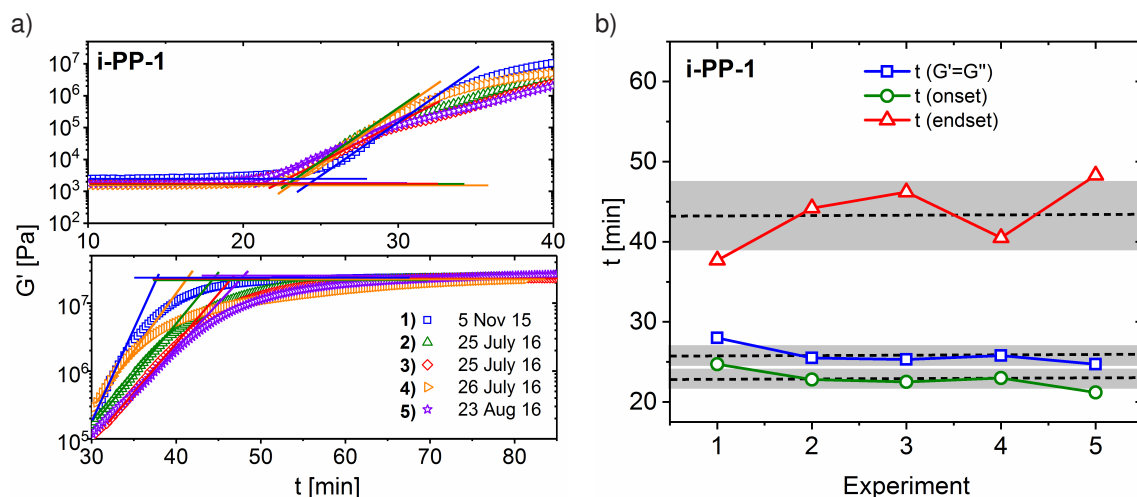


Figure 6.6: a) Determination of the on- and end-set crystallization times using linear extrapolations of the storage modulus G' from the experiments shown in Figure 6.5. b) Resulting times extracted from the experiments no. 1-5. The crossover time $t_{G'=G''}$ and the onset time t_{onset} showed low variations for experiments conducted close in time (dashed lines: mean, grey areas: standard deviation).

6.3.1 Temperature-dependence of isothermal crystallization

The temperature-dependence of isothermal polymer crystallization was investigated by simultaneously monitoring the flow behavior and the emerging relative polymer crystallinity ϕ_c/ϕ_c^∞ . In Figure 6.7, the evolution of the moduli G' , G'' , and relative crystallinities ϕ_c/ϕ_c^∞ is shown for i-PP-1. The sensitivity of polymer crystallization towards temperature is high in the chosen interval: a decrease of 2 K led to a two times faster crystallization as detected by the crossover times. The trend of faster crystallization with decreasing crystallization temperature for $T_{\text{cryst}} > (T_m^0 + T_g)/2$ assuming a Gaussian distribution of growth rates was well captured by both, the moduli G' , G'' and the relative crystallinity ϕ_c/ϕ_c^∞ . To further evaluate the data, all crystallinity curves were directly fitted using the Avrami model up to $\phi_c/\phi_c^\infty = 0.5$ to obtain the kinetic rate K and the exponent n (Avrami (1941), subsection 3.3.6, p. 35):

$$\frac{\phi_c(t)}{\phi_c^\infty} = 1 - \exp\{-[K(t - t_0)]^n\} \quad (6.2)$$

ϕ_c : volume crystallinity, ϕ_c^∞ : final volume crystallinity, K : rate, n : exponent, t : time, t_0 : induction time.

All crystallinity curves shown in Figure 6.7b were well described by an Avrami fit using nonlinear regression up to 50% relative crystallinity. As the number of data points acquired during the initial nucleation period was rather low, the numerical Avrami fit showed strong dependencies between the dimensionality parameter n and the induction time t_0 . The interval t_0 included the experimental time spent for acquiring a melt signal (~ 3 min), the time needed for cooling (~ 5 min for 200 to 136 °C), and the reorganization time preceding nucleation. The most reasonable set of t_0 values was found to be: 8.5 min (130 °C), 9 min (132 °C), 10 min (134 °C), and 12 min (136 °C) and kept constant during the nonlinear fit using a

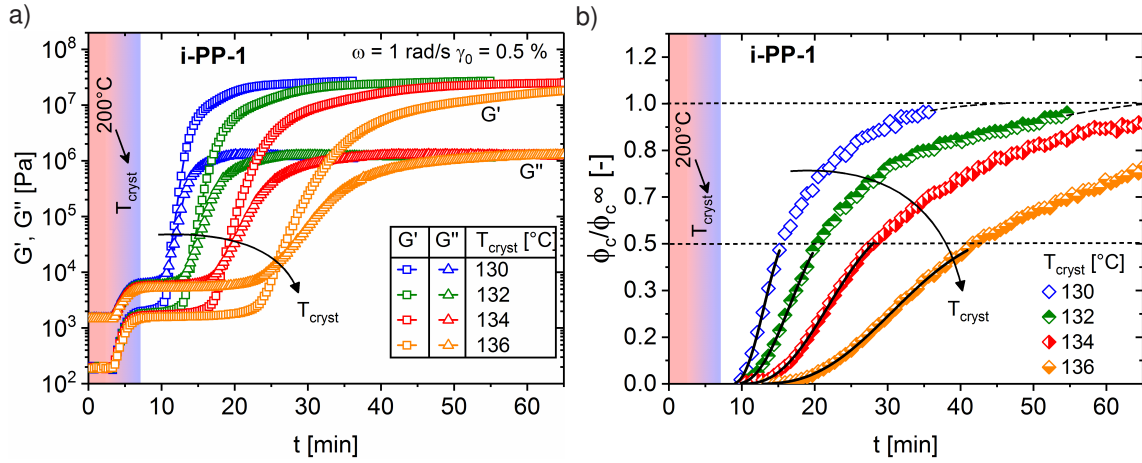


Figure 6.7: Simultaneously acquired moduli G' , G'' (a) and relative crystallinities ϕ_c/ϕ_c^∞ (b) during isothermal crystallization of isotactic polypropylene (i-PP-1) from the melt at different crystallization temperatures. The known trend "higher temperature leads to slower crystallization" for $T_{\text{cryst}} > (T_m^0 + T_g)/2$ was well reflected. For every crystallinity curve, a direct Avrami fit was performed over the interval $0 \leq \phi_c/\phi_c^\infty \leq 0.5$ to facilitate the correlation of rheological parameters with polymer crystallinity from NMR relaxometry.

Levenberg-Marquardt algorithm (Figure 6.8a). As the curves showed an asymmetric behavior, an additional pre-factor of ~ 0.6 was needed on the right hand side of Equation 6.2 to account for the nominal lower final crystallinity caused by primary crystallization. This set of parameters led to a good representation of the curves up to 50% relative crystallinity, which was the main goal of this analysis.

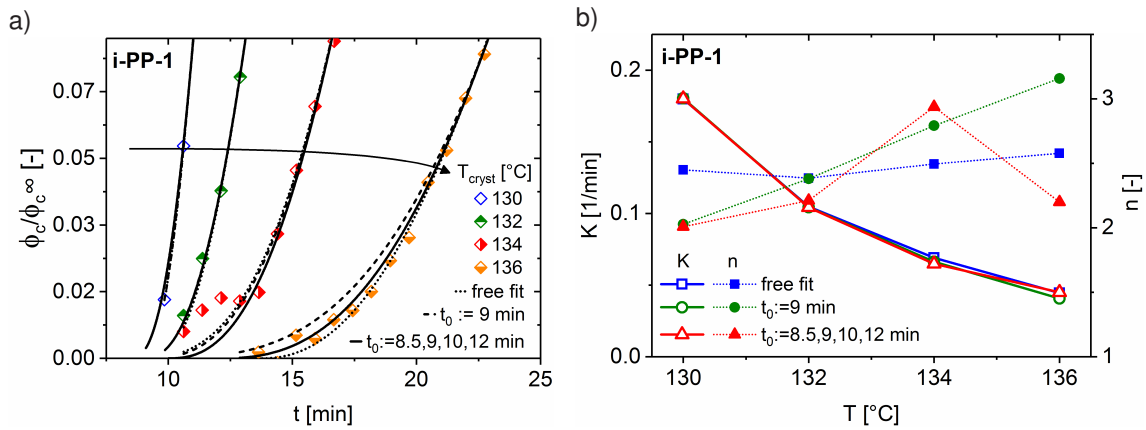


Figure 6.8: a) Detailed Avrami fits using different parameter sets for t_0 . b) Kinetic data obtained by modeling the crystallization curves of Figure 6.7b.

The kinetic results obtained from the different evaluation methods are compared in Figure 6.8b. Overall, K decreased at higher temperatures from $\sim 0.15 \text{ min}^{-1}$ at 130°C to 0.05 min^{-1} at 136°C . The rate parameter K was independent of the chosen analysis method, whereas the dimensionality n depended on the data point density, the induction time, and the overall noise level. For the experiments presented here, the dimensionality parameter n was not found to be a reliable measure of the type of nucleation (heterogeneous / homogeneous) or the dimensionality of growth.

6.3.2 Physical gelation – characteristics and modeling

The temperature-dependent experiments discussed in the previous section were further evaluated with respect to the characteristic hardening behavior. Crystallization half times $t'_{1/2}$ for $\phi_c/\phi_c^\infty = 0.5$ were plotted against the crossover / gelation times t'_{gel} ($G' = G''$) in Figure 6.9a. The time spent at 200 °C and the time needed for cooling (in total 8 min) were subtracted: $t' = t - 8$ min. The exact gelation time t'_{gel} can be unambiguously obtained by multi-wave experiments and the detection of a frequency-independent $\tan(\delta)$ (see Figure 6.10a). As we selected a low angular velocity of 1 rad/s, the crossover time at which $G' = G''$ is practically identical to the exact gelation time (± 1 min) and thus will be considered as the gelation time t'_{gel} . The relationship between $t'_{1/2}$ and t'_{gel} is well described by the dotted line ($t'_{1/2} = 2t'_{\text{gel}}$). Before spherulitic impingement, the effective volume / degree of space filling is approximately given by the relative crystallinity ϕ_c/ϕ_c^∞ .

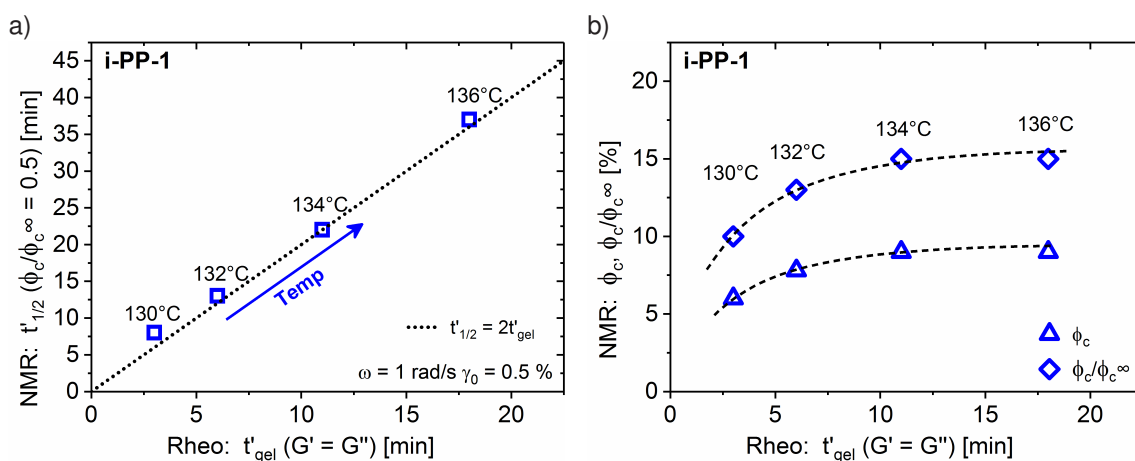


Figure 6.9: a) Crystallization half times $t'_{1/2}$ for $\phi_c/\phi_c^\infty = 0.5$ as a function of the crossover times for different crystallization temperatures. The time spent at 200 °C and the time needed for cooling (in total 8 min) were subtracted: $t' = t - 8$ min. The relationship between the two times for the temperature series is well described by $t'_{1/2} = 2t'_{\text{gel}}$. b) Absolute and relative crystallinities (degree of space filling) at the crossover vs. the crossover time. The values were extremely low compared to other material systems such as suspensions or emulsions.

In Figure 6.9b, the absolute and relative crystallinities at the crossover were plotted against the crossover time t'_{gel} . Compared to other materials such as suspensions or composites, the degree of space filling needed to achieve an elastic gel-like state with strongly increased viscosity is relatively low ($\phi_c/\phi_c^\infty \leq 15\%$). Another feature of crystallizing polymer melts is the appearance of a maximum in the relative third harmonic $I_{3,1}$ (Dötsch *et al.* 2003). In Figure 6.10b, the evolution of the relative third harmonic $I_{3,1}$ and the loss tangent $\tan(\delta)$ are compared for the temperature series of Figure 6.7. A correlation of the $I_{3,1}$ maxima and $\tan(\delta) = 1$ was found, which revealed the strong nonlinear rheological behavior close to the point of gelation. Using small angle light scattering (SALS), Pogodina and Winter identified long-range density fluctuations at the gel point, which might be the origin for the nonlinear behavior (Pogodina *et al.* 1999, 2001). The observations of low degrees of space filling and density fluctuations at the gel point will be further discussed in chapter 8 on RheoMicroscopy.

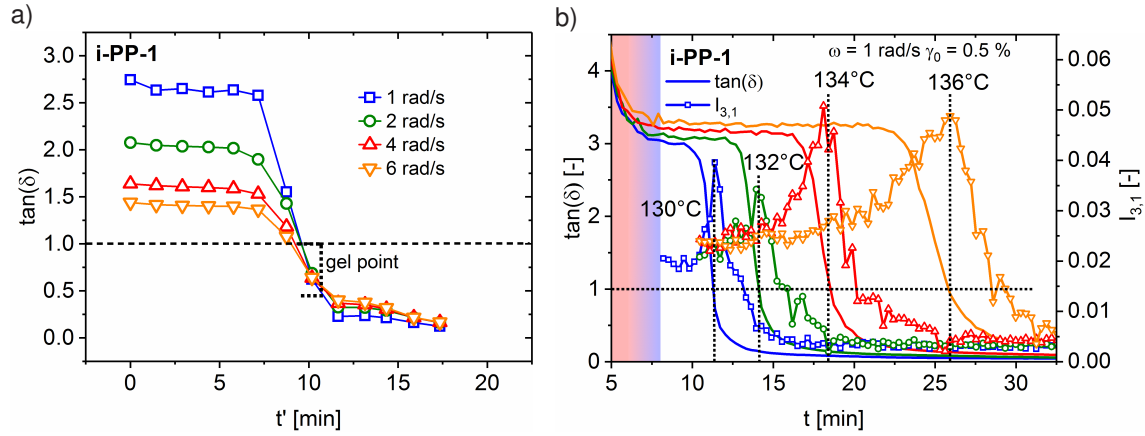


Figure 6.10: a) Multiwave oscillatory data for an isothermal crystallization of i-PP-1 at ~ 134 °C. The rheological gel point, characterized by a frequency-independence of $\tan(\delta)$ (Winter and Mours 1997), was practically identical with the crossover time ($G' = G''$, $\tan(\delta) = 1$). b) Loss tangent $\tan(\delta)$ and relative third harmonic $I_{3,1}$ vs. time for different isothermal crystallizations of i-PP-1 (nonlinearity at lower times not shown for clarity).

By plotting a normalized rheological function, e.g., the reduced absolute complex viscosity $|\eta^*|/|\eta^*|_0$, as a function of the degree of space filling (relative crystallinity) ϕ_c/ϕ_c^∞ , the effect of temperature on the time-dependence of the polymer crystallization is removed (Lamberti *et al.* 2007). In Figure 6.11, a correlation plot is shown for the temperature series of Figure 6.7. A higher viscosity was seen at lower crystallization temperatures before the curves collapsed onto one line. A strong relative increase in viscosity occurred at degrees of space filling below $\phi_c/\phi_c^\infty \approx 10$ to 15%, which indicated some form of long-range interaction between the growing spherulites (see chapter 8). As the obtained hardening curves had some similarity to those of solid-particle suspensions, they were evaluated using different suspension and semi-empirical models (Mewis and Wagner 2012; Mueller *et al.* 2009; Kotula and Migler 2018):

$$\frac{|\eta^*|}{|\eta^*|_0} = 1 + 2.5\phi \quad (\text{Einstein}) \quad (6.3)$$

$$\frac{|\eta^*|}{|\eta^*|_0} = \left[1 - \frac{\phi}{\phi_{\max}}\right]^{-2.5\phi_{\max}} \quad (\text{Krieger-Dougherty}) \quad (6.4)$$

$$\frac{|\eta^*|}{|\eta^*|_0} = \left[1 - \frac{\phi}{\phi_{\max}}\right]^{-2} \quad (\text{Quemada}) \quad (6.5)$$

$$\frac{|\eta^*|}{|\eta^*|_0} = 1 + A \left[1 - \exp\left(-\frac{\phi}{B}\right)^C\right] \approx 1 + D\phi^C \quad (\text{Sigmoidal / Power law}) \quad (6.6)$$

$$\frac{|\eta^*|}{|\eta^*|_0} = 1 + 2.5\phi + D'\phi^{C'} \quad (\text{Extended Einstein}) \quad (6.7)$$

$|\eta^*|/|\eta^*|_0$: reduced absolute complex viscosity, ϕ : degree of space filling, ϕ_{\max} : maximum packing fraction, A, B, C, D : fitting parameters.

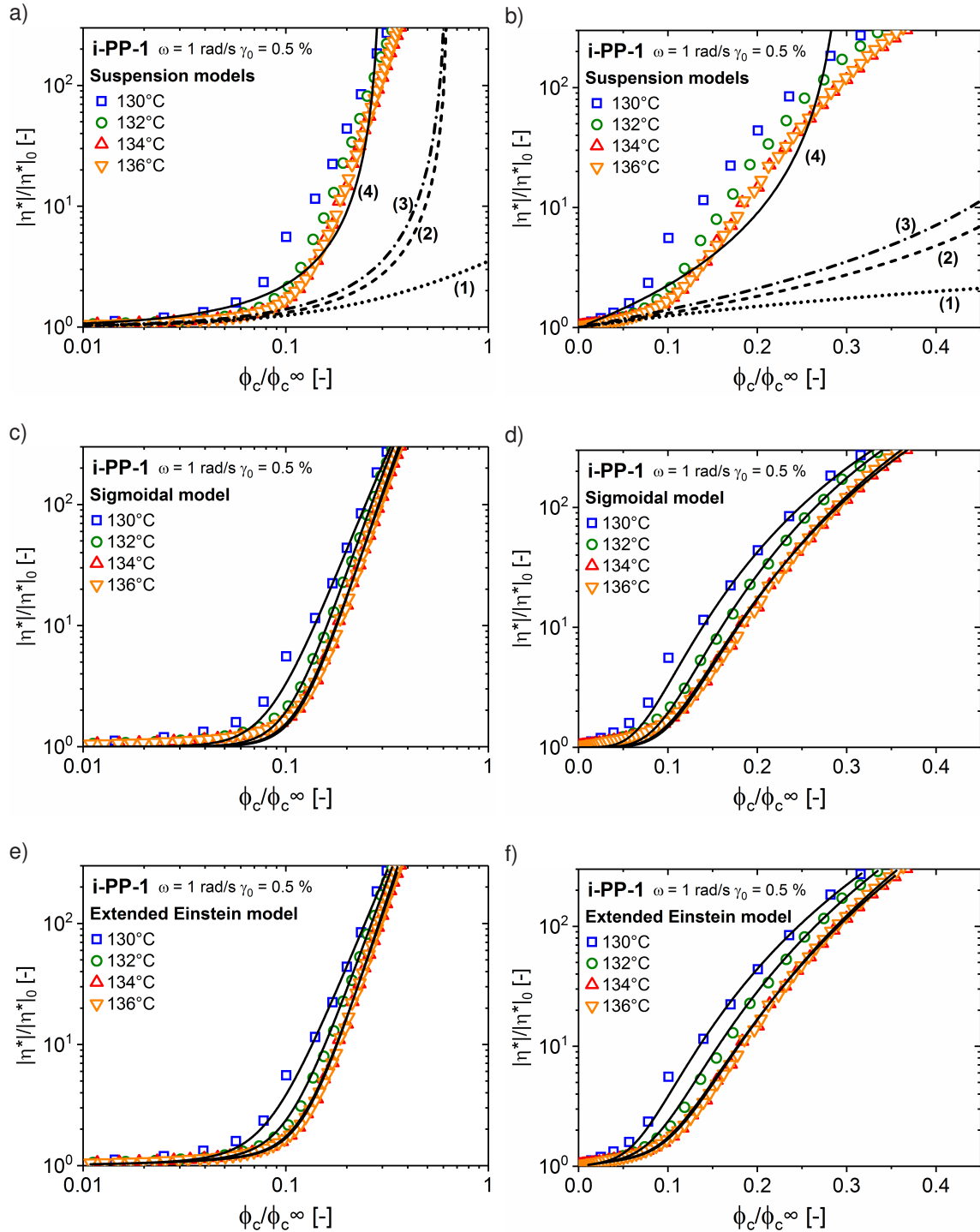


Figure 6.11: Reduced absolute complex viscosity vs. relative crystallinity (degree of space filling) for the temperature series of Figure 6.7. a & b) Suspension-like modeling: Einstein (1), Krieger-Dougherty with $\phi_{\max} = 64\%$ (2), Quemada with $\phi_{\max} = 64\%$ (3), Quemada with $\phi_{\max} = 30\%$ (4). c & d) Empirical sigmoidal model (Equation 6.6). e & f) Extended Einstein model Equation 6.7 based on a combination of Equation 6.3 and Equation 6.6.

The Einstein model is known to be valid only for very dilute systems. Consequently, it provided a relatively good fit for small values of $\phi_c/\phi_c^\infty \leq 0.05$, but did not describe the steep increase observed at $\phi_c/\phi_c^\infty \approx 0.1$ as shown in Figure 6.11a & b. Using a maximum packing fraction of

$\phi_{\max} = 64\%$, which is usually found for hard sphere suspensions (Mewis and Wagner 2012), the Krieger-Dougherty and Quemada models did not provide a good description of the experimental data. A better match was achieved, when the Quemada equation was modified by assuming a packing fraction of $\phi_{\max} = 30\%$ (Figure 6.11b, curve 4). On the other hand, the empirical three-parameter sigmoidal model described the rise around $\phi_c/\phi_c^\infty \approx 0.1$ and the curves at higher degrees of space filling sufficiently well, but showed an underestimation of the reduced viscosity at low degrees of space filling (Figure 6.11c & d). The sigmoidal model could also be simplified to a power law by using a Taylor series expansion, which reduces the amount of free parameters (C , D). The combination of an Einstein model to describe the behavior at low degrees of space filling plus a power law (extended Einstein model) gave the best fitting results (Figure 6.11c & d). Taking into account that it only requires two free parameters, it is very suitable for an analysis of the hardening curves of different samples or crystallization conditions. The parameter D' represents the dynamic range of $|\eta^*|/|\eta^*|_0$, whereas C' might be associated with the coordination of growing spherulites.

The extracted fitting parameters from the sigmoidal and extended Einstein models are given in Table 6.1 and showed a trend to higher parameter values with increasing crystallization temperature. Even though the sigmoidal model is purely empirical, there is a certain similarity to the maximum packing fraction (B) and the exponent (C) of the suspension models. Additionally, the parameter A describes the dynamic range of the hardening curves. The parameter D' was substantially higher for the extended Einstein model compared to the calculated D values from the sigmoidal model, which was presumably a consequence of the combination with the linear 2.5ϕ term of the Einstein model. Simply speaking, the sigmoidal model described the whole hardening curve with one nonlinear term, whereas the description based on the extended Einstein model was based on two distinct regimes (before and after gelation).

a)					b)		
$T_{\text{cryst}} [^\circ\text{C}]$	$A [-]$	$B [-]$	$C [-]$	$D = AC/B [-]$	$T_{\text{cryst}} [^\circ\text{C}]$	$C' [-]$	$D' [-]$
130	1423	0.46	4.2	$13 \cdot 10^3$	130	4.1	$29 \cdot 10^3$
132	1172	0.44	4.8	$13 \cdot 10^3$	132	4.6	$44 \cdot 10^3$
134	1581	0.51	4.9	$15 \cdot 10^3$	134	5.0	$46 \cdot 10^3$
136	1845	0.51	5.1	$19 \cdot 10^3$	136	5.1	$58 \cdot 10^3$

Table 6.1: Parameters determined by modeling the data in Figure 6.11 with an empirical sigmoidal model (a) (Equation 6.6), and with a semi-empirical extended Einstein model (b) (Equation 6.7).

Similar to the reduced viscosity, other parameters such as the reduced storage or loss moduli, the loss tangent, or the relative intensity of the third harmonic can be analyzed in plots against the degree of space filling (see Figure 6.12). For the moduli, the observed behavior is very similar to the reduced viscosity as expected. However, as most hardening models were derived for the reduced viscosity and not the moduli (Mewis and Wagner 2012), comparisons of different materials and conditions were usually carried out based on the reduced viscosity

by most researchers (Lamberti *et al.* 2007). The correlation of the loss tangent and the third harmonic with the degree of space filling again illustrated that the crossover ($\tan(\delta) = 1$) and the peak maximum in $I_{3,1}$ occurred always at degrees of space filling $0.1 \leq \phi_c/\phi_c^\infty \leq 0.15$. Furthermore, the loss tangent showed a dependence on crystallization temperature, especially up to the point of gelation where the correlation plots of the reduced viscosity or the moduli didn't exhibit a clear temperature dependence.

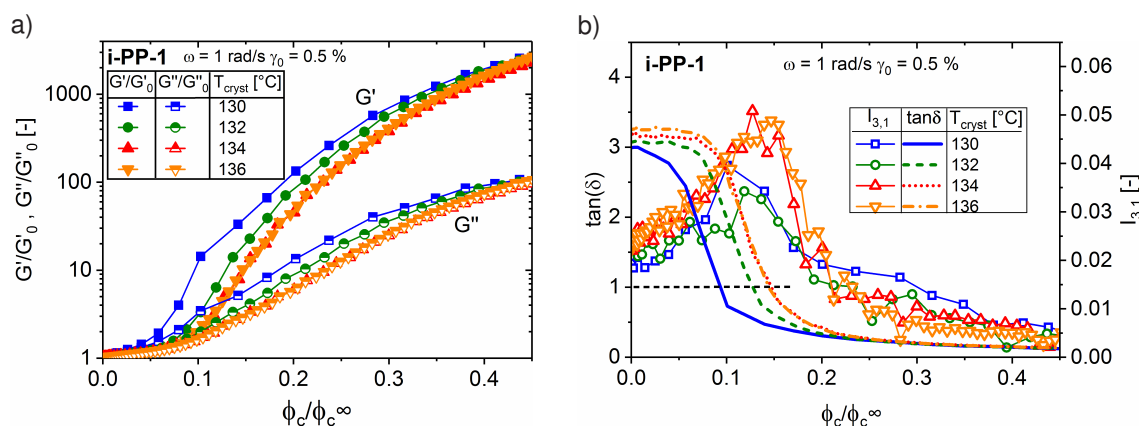


Figure 6.12: Reduced storage G'/G'_0 and loss G''/G''_0 moduli (a), and loss tangent $\tan(\delta)$ and the relative third harmonic $I_{3,1}$ (b) vs. the degree of space filling (relative crystallinity).

6.3.3 Influence of the polymer grade, fillers, and nucleating agents

To further explore the crystallization behavior of isotactic polypropylene, experiments on more complex material systems will be presented in the following. In many applications multi-component materials are used, which potentially include fillers, nucleating and clarifying agents, pigments, or processing additives. Furthermore, changing molecular weight, its distribution, stereo- / regioregularity, or branching can have a strong effect on the crystallization kinetics, the morphology, and the realized crystal structures (see section 2.3, p. 13).

Polymer grade

The metallocene-catalyzed isotactic polypropylene i-PP-2 of approximately the same molecular weight as the Ziegler-Natta grade i-PP-1 (section 2.4, p. 19) was analyzed with respect to its isothermal crystallization behavior using the RheoNMR routine described in the previous section. In Figure 6.13, simultaneously acquired moduli G' and G'' are shown together with the evolution of the relative crystallinity ϕ_c/ϕ_c^∞ as determined by NMR relaxometry. Taking into account the much lower crystallization temperatures of $T_{\text{cryst}} \approx 131 - 134$ °C compared to the experiments on i-PP-1, the crystallization was significantly slower as indicated by the rise in the moduli G' and G'' , and the relative crystallinity ϕ_c/ϕ_c^∞ , respectively. This phenomenon might have been a consequence of the 1 mol% of 2,1-erythro defects and an associated kinetic hindering effect (see Appendix A for ^{13}C NMR spectra).

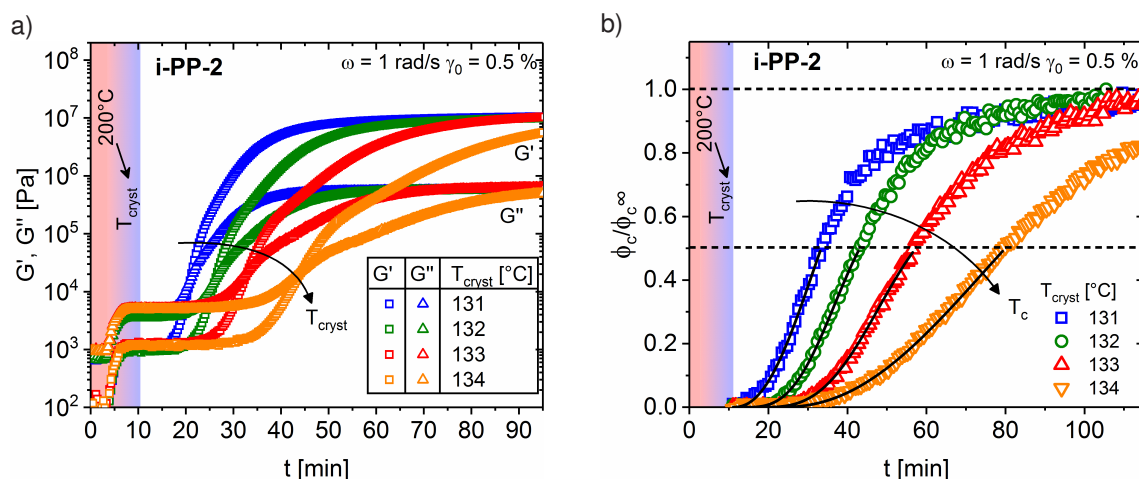


Figure 6.13: Simultaneously acquired moduli G' , G'' (a) and relative crystallinities ϕ_c/ϕ_c^∞ (b) during isothermal crystallization of isotactic polypropylene (i-PP-2) from the melt at different crystallization temperatures. For every crystallinity curve, a direct Avrami fit was performed over the interval $0 \leq \phi_c/\phi_c^\infty \leq 0.5$ to facilitate the correlation of rheological parameters with polymer crystallinity from NMR relaxometry.

All crystallinity curves were directly fitted using the Avrami model up to 50% relative crystallinity to facilitate the correlation of rheological parameters with the degree of space filling (subsection 3.3.6, p. 35). The extracted kinetic data is shown in Figure 6.14a considering the following t_0 values that provided a reasonable description of the data: 11 min (131 °C), 14 min (132 °C), 18 min (133 °C), and 23 min (134 °C). The rate K decreased at higher temperatures from $\sim 0.04 \text{ min}^{-1}$ at 131 °C to 0.015 min^{-1} at 134 °C and was lower than for i-PP-1. The dimensionality n was on the order of the value for i-PP-1 taking into account the experimental uncertainty depending on the data point density, the induction time, and the overall noise level.

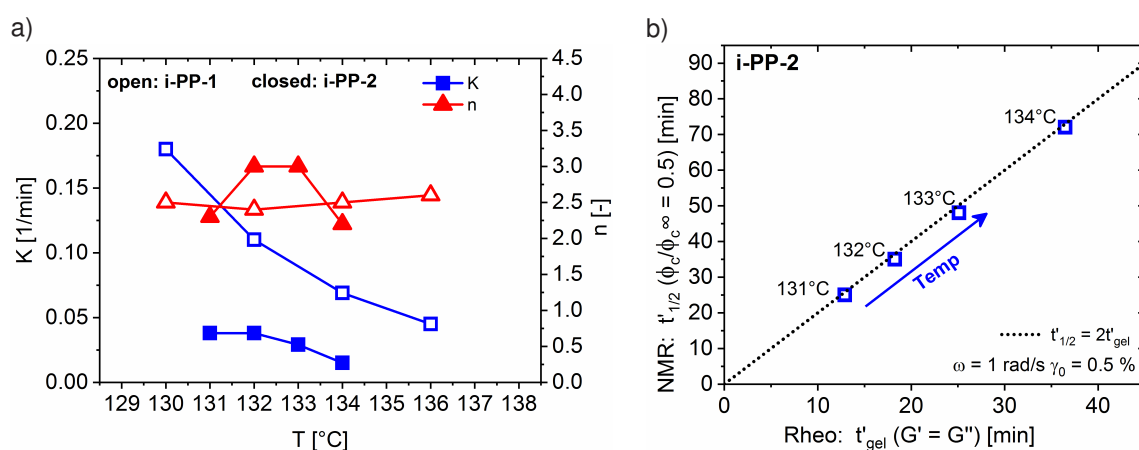


Figure 6.14: a) Kinetic crystallization data extracted from Figure 6.13b by applying an Avrami model (Equation 6.2). b) Crystallization half times $t'_{1/2}$ for $\phi_c/\phi_c^\infty = 0.5$ as a function of the crossover times for different crystallization temperatures.

In Figure 6.14, the crystallization half times $t'_{1/2}$ are plotted as a function of the crossover times for different crystallization temperatures. Despite the drastically lower crystallization rate compared to i-PP-1, the data could be well described by the linear relationship $t'_{1/2} = 2t'_{\text{gel}}$.

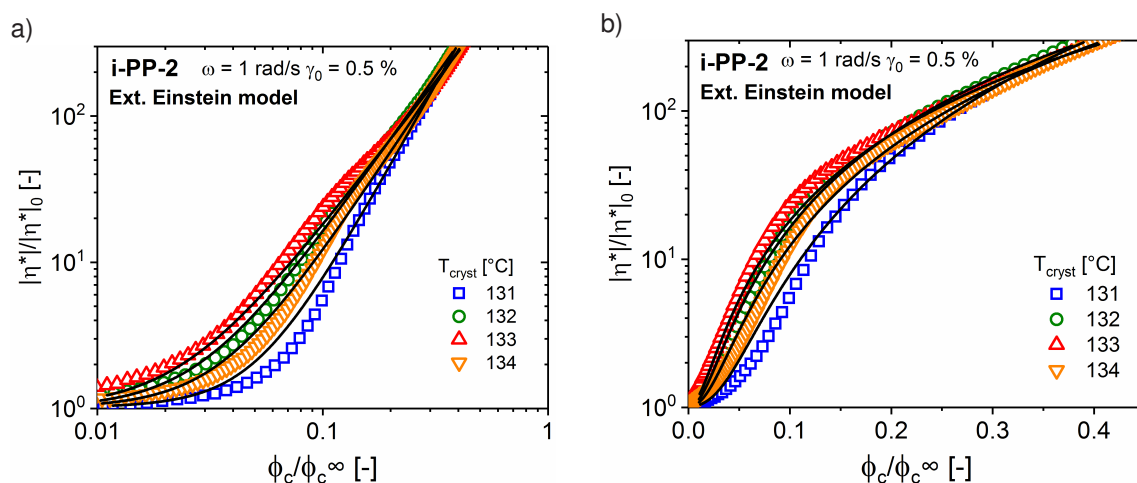


Figure 6.15: Reduced absolute complex viscosity vs. relative crystallinity (degree of space filling) for the temperature series of Figure 6.13 analyzed using an extended Einstein model (Equation 6.7).

The correlation of the reduced absolute complex viscosity $|\eta^*|/|\eta^*|_0$ with the degree of space filling ϕ_c/ϕ_c^∞ is shown in Figure 6.15. An increase at lower values of ϕ_c/ϕ_c^∞ was observed compared to i-PP-1 (Figure 6.11). This effect might have been a consequence of the inherently higher nucleation density and smaller average spherulite sizes of the regio-defective grade i-PP-2 ($d \approx 5 \mu\text{m}$ vs. $50 \mu\text{m}$, see chapter 8). Results from an analysis based on an extended Einstein model (Equation 6.7) are shown in Table 6.2. Both parameters C' and D' were lower for i-PP-2 compared to the Ziegler-Natta grade i-PP-1. The low C' values can be rationalized as showing a more parabolic curve compared to the hardening curves of i-PP-1. Consequently, the transition from the Einstein regime at low ϕ_c/ϕ_c^∞ to an increasingly solid-like material was relatively smooth.

a)			b)		
i-PP-2 (regio-defective)			i-PP-1 (regio-regular)		
T_{cryst} [°C]	C' [-]	D' [-]	T_{cryst} [°C]	C' [-]	D' [-]
131	2.8	$4.0 \cdot 10^3$	130	4.1	$29 \cdot 10^3$
132	2.2	$2.3 \cdot 10^3$	132	4.6	$44 \cdot 10^3$
133	2.0	$1.7 \cdot 10^3$	134	5.0	$46 \cdot 10^3$
134	2.3	$2.4 \cdot 10^3$	136	5.1	$58 \cdot 10^3$

Table 6.2: Parameters determined by modeling the data in Figure 6.15 with a semi-empirical extended Einstein model (a) (Equation 6.7) and compared to the values for i-PP-1 (b).

Fillers

Isothermal crystallization experiments were performed at five different temperatures ($T_{\text{cryst}} \approx 132 - 136$ °C) for a compound of i-PP-1 with 3 wt% of silica (section 2.4, p. 19) using the RheoNMR routine of the previous sections. In Figure 6.16, simultaneously acquired moduli G' and G'' are shown together with the evolution of the relative crystallinity ϕ_c/ϕ_c^∞ . The trend of faster crystallization with decreasing crystallization temperature for $T_{\text{cryst}} > (T_m^0 + T_g)/2$ was again well captured by both, the moduli G' , G'' and the relative crystallinity ϕ_c/ϕ_c^∞ . Compared to the neat i-PP-1 grade, a slightly faster crystallization was observed.

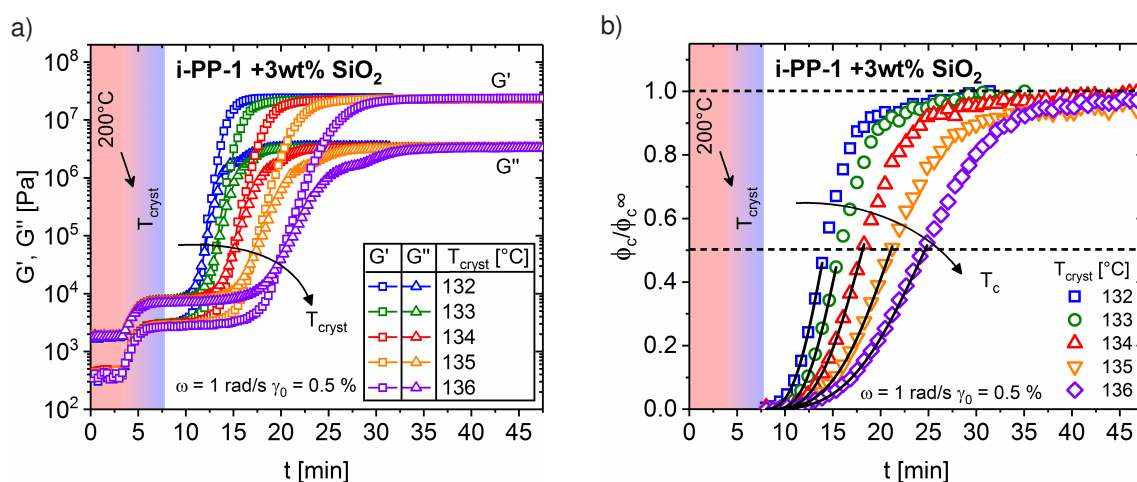


Figure 6.16: Simultaneously acquired moduli G' , G'' (a) and relative crystallinities ϕ_c/ϕ_c^∞ (b) during isothermal crystallization of isotactic polypropylene i-PP-1 with 3 wt% silica from the melt at different crystallization temperatures. For every crystallinity curve, a direct Avrami fit was performed over the interval $0 \leq \phi_c/\phi_c^\infty \leq 0.5$.

All crystallinity curves were directly fitted using the Avrami model up to 50% relative crystallinity (subsection 3.3.6, p. 35). Other than for neat i-PP-1, constant t_0 values of ~ 8 min were found to provide a good description of the data. This indicated that the time needed for crystal nucleation was decreased by the addition of silica. The extracted kinetic data is shown in Figure 6.17a. The rate parameter K was higher for the filled sample compared to neat i-PP-1 over the entire temperature range, and the difference increased for lower crystallization temperatures. The dimensionality n stayed relatively constant at ~ 3.0 , which was higher than for the neat i-PP-1 ($n \approx 2.5$), but still within the relative error of approximately $\pm 10 - 20\%$. Thus, even though heterogeneous nucleation was certainly present, no indication of a substantially lower n value as proposed by the Avrami framework was observed (compare with subsection 3.3.6, p. 35).

The speed-up of crystallization as indicated by the Avrami parameter K was presumably a consequence of increased nucleation during the early stages of polymer crystallization. Possibly, the hydrophobically modified silica offered surfaces that lowered the free surface energy of forming pre-nuclei, which then had a higher probability to grow further and survive the initial time period (see chapter 3, especially Equation 3.20, Equation 3.23, and Equation 3.26 for

details on the thermodynamics of crystal nucleation). The accelerating effect of fillers at low filler loadings has been frequently observed by other researchers (Jain *et al.* 2005; Palza *et al.* 2011; Papageorgiou *et al.* 2005). For high filler loadings ($> 5\text{wt}\%$), a reduction of the overall crystallization speed is usually observed as the dynamics of polymer chains become significantly hindered (Nitta *et al.* 2006; Fukuyama *et al.* 2013; Röntzsch *et al.* 2014). This effect can be rationalized as an increase of the activation energy in the transport term β of the Hoffman-Lauritzen model, which leads to lower nucleation rates I and growth rates G , respectively (Equation 3.27, Equation 3.35 in chapter 3).

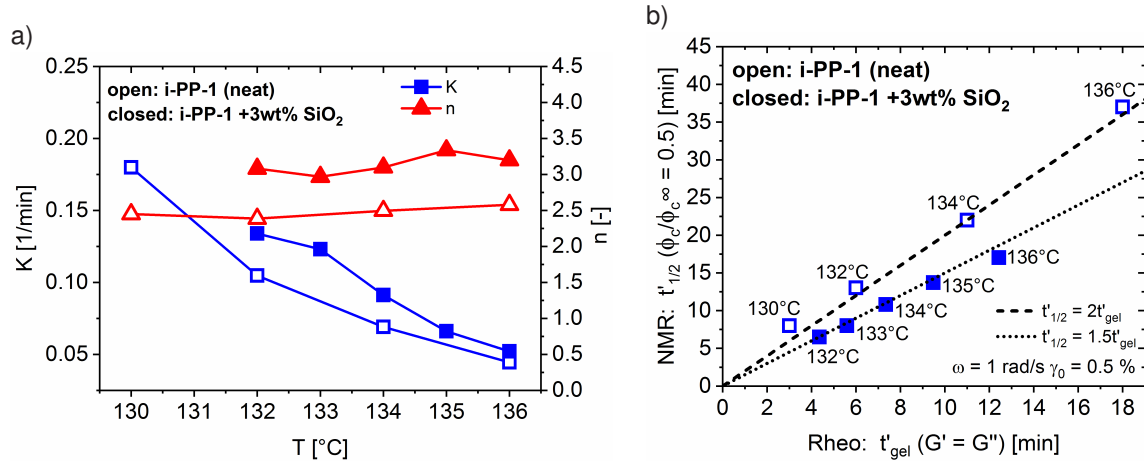


Figure 6.17: a) Kinetic crystallization data extracted from Figure 6.16b by applying an Avrami model (Equation 6.2). b) Crystallization half times $t'_{1/2}$ for $\phi_c/\phi_c^\infty = 0.5$ as a function of the crossover times for different crystallization temperatures. The relationship between the two times for the temperature series is well described by $t'_{1/2} = 1.5t'_{gel}$, which differs from the unfilled case (Figure 6.9).

In Figure 6.17b, the crystallization half times $t'_{1/2}$ for $\phi_c/\phi_c^\infty = 0.5$ are plotted as a function of the crossover times for different crystallization temperatures. Interestingly, a linear relationship $t'_{1/2} = 1.5t'_{gel}$ described the data fairly well, which was different from the neat case (Figure 6.9) and might have been a consequence of heterogeneous nucleation.

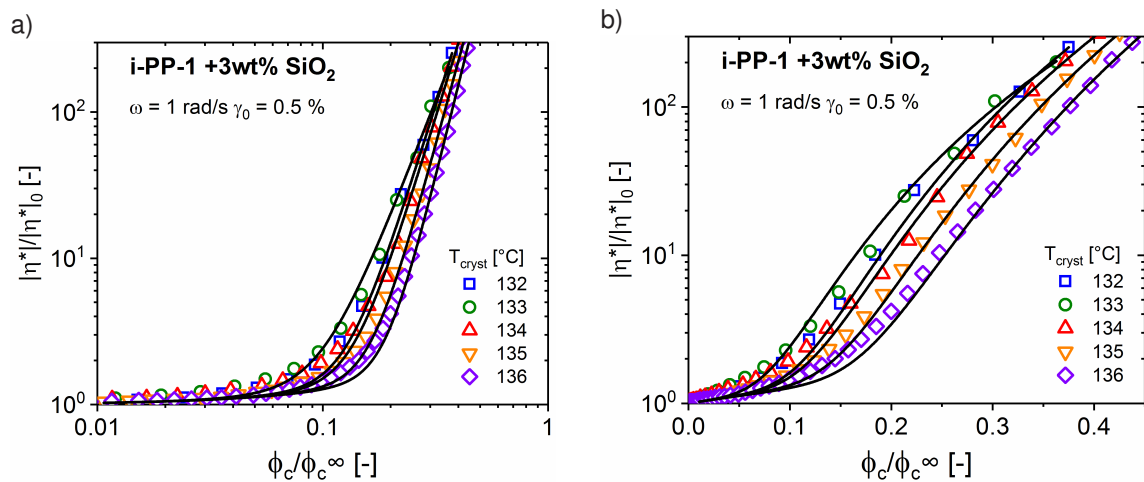


Figure 6.18: Reduced absolute complex viscosity vs. relative crystallinity (degree of space filling) for the temperature series of Figure 6.16 analyzed using an extended Einstein model (Equation 6.6).

The correlation of the reduced absolute complex viscosity $|\eta^*|/|\eta^*|_0$ with the degree of space filling ϕ_c/ϕ_c^∞ is shown in Figure 6.18. The behavior of the filled sample was very similar to the neat sample Figure 6.11 and did also display a certain shift with respect to the crystallization temperature. Results from an analysis based on an extended Einstein model (Equation 6.7) are shown in Table 6.3. All values were rather similar to the neat case and increased with increasing crystallization temperatures, except for $T_{\text{cryst}} \approx 133$ °C where the fit didn't converge. Overall, the hardening behavior was found to be relatively independent of the filler and the associated changes in the crystallization kinetics.

a)			b)		
i-PP-1 + 3wt% SiO₂			i-PP-1 (neat)		
T_{cryst} [°C]	C' [-]	D' [-]	T_{cryst} [°C]	C' [-]	D' [-]
132	4.9	$32 \cdot 10^3$	130	4.1	$29 \cdot 10^3$
133	(4.0)*	$(12 \cdot 10^3)^*$	132	4.6	$44 \cdot 10^3$
134	5.1	$31 \cdot 10^3$	134	5.0	$46 \cdot 10^3$
135	5.8	$43 \cdot 10^3$			
136	6.3	$49 \cdot 10^3$	136	5.1	$58 \cdot 10^3$

Table 6.3: Parameters determined by modeling the data of Figure 6.18 with a semi-empirical extended Einstein model (a) (Equation 6.7) and compared against the values for neat i-PP-1 (b). (*) Fit didn't converge.

Nucleating Agents

The influence of nucleating agents on the isothermal crystallization behavior of isotactic polypropylene was studied in a joint project with Dr. Klaus Kreger and Daniel Kremer (both members of Prof. Hans-Werner Schmidt's group at the University of Bayreuth) on the example of a 1,3,5-benzene tricarboxamide derivative (Figure 6.19, Kristiansen *et al.* (2009); Blomenhofer *et al.* (2005)) and i-PP-1' (Ziegler-Natta grade, batch 2). The nucleation mechanism for different nucleating agents is not fully understood in all cases. However, providing an epitaxial surface (e.g., with many alkyl groups in the case of polypropylene) and a lower surface free energy for new nuclei seems to be a common principle (see chapter 3, (Bernland 2010)). RheoNMR experiments following the same routine as in the previous sections were performed at a crystallization temperature of 136 °C for all samples (neat i-PP-1', i-PP-1' + 250, 500, 750, 1500 ppm by weight of N, N', N''-tris(3-methylbutyl)-1,3,5-benzene tricarboxamide – abbrev. "DH677"). The repeatability for selected crystallization conditions was again checked for this series of experiments, as a relatively large number of different samples had to be measured (see Appendix A). A two-step sigmoidal behavior and an earlier crossover ($G' = G''$) was observed compared to older experiments, which was potentially due to an inhomogeneous temperature distribution.

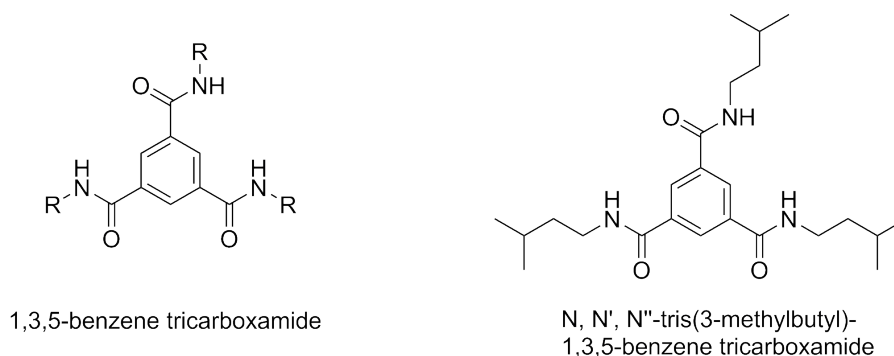


Figure 6.19: Chemical structures of generic 1,3,5-benzene tricarboxamides (a) and the used N, N', N''-tris(3-methylbutyl)-1,3,5-benzene tricarboxamide derivative (b).

In Figure 6.20, simultaneously acquired data on G' , G'' (a) and ϕ_c/ϕ_c^∞ (b) is shown as a function of experimental time t . The relative crystallinity ϕ_c/ϕ_c^∞ showed a shift to earlier times with increasing additive content up to 750 ppm. The curve for the 1500 ppm sample displayed no further speed-up and was practically identical to the curve of the 750 ppm sample. The rheological moduli G' and G'' did not exactly follow the trend seen in ϕ_c/ϕ_c^∞ , with the 250 ppm sample having had an earlier rise in the moduli than the 500 ppm sample. Differences in sample loading, edge effects, etc. might have led to this behavior. The 750 ppm sample again displayed the earliest change in G' and G'' .

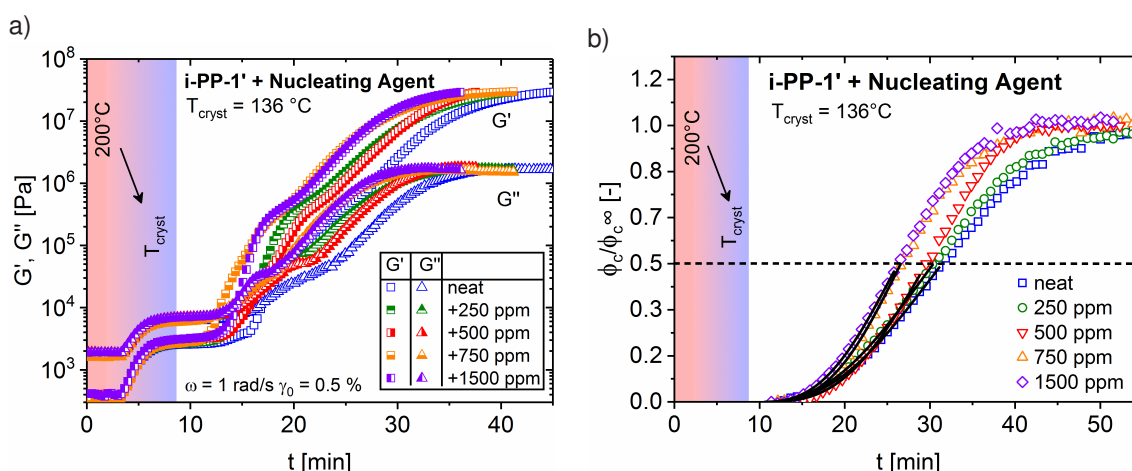


Figure 6.20: Simultaneously acquired moduli G' , G'' (a) and relative crystallinities ϕ_c/ϕ_c^∞ (b) during isothermal crystallization of isotactic polypropylene i-PP-1' with different amounts of nucleating agent (DH677) from the melt at $T_{\text{cryst}} \approx 136^\circ\text{C}$. For every crystallinity curve, a direct Avrami fit was performed over the interval $0 < \phi_c/\phi_c^\infty < 0.5$.

The crystallinity curves were directly fitted using the Avrami model up to 50% relative crystallinity to facilitate the correlation of rheological parameters with the degree of space filling (subsection 3.3.6, p. 35). Similarly to the silica filled sample in the previous section, constant t_0 values of ~ 10 min were found to provide the best description of the experimental data. The extracted kinetic results are shown in Figure 6.21a. The rate parameter K increased slightly with increasing NA content compared to neat i-PP-1 up to 750 ppm. The dimensionality n was ~ 3.0 for 500 and 750 ppm, whereas for the other samples it was closer to 2.5 as in the neat

case (relative error approximately $\pm 10 - 20\%$). A similar behavior was observed for the filled sample in the previous section, which showed no indication of a substantially lower n value as proposed by the Avrami framework (compare with subsection 3.3.6, p. 35). The speed-up of crystallization as indicated by the Avrami parameter K was potentially caused by increased nucleation during the early stages of polymer crystallization. Nucleating agents are designed to offer surfaces that lower the free surface energy of forming pre-nuclei, which then had a higher probability to grow further and survive the initial time period. In the present system, the nucleating agent precipitated at temperatures above the crystallization temperature, which is a characteristic feature of clarifying agents. However, the formed fibrils were not very effective in nucleating new spherulites as revealed by electron microscopy (see section 6.5). The 1500 ppm sample was already above the optimum concentration of ~ 750 ppm, which led to the formation of large agglomerates rather than a dispersed fibrillar network.

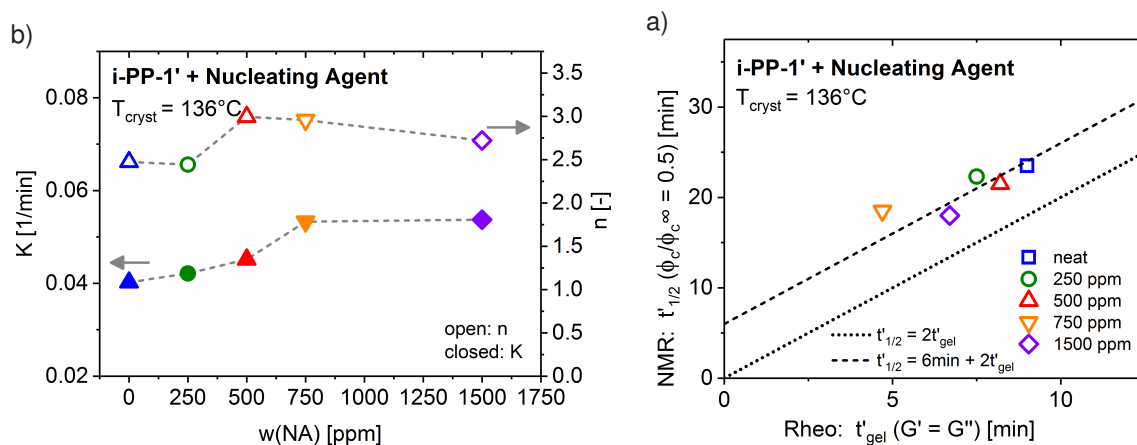


Figure 6.21: a) Kinetic crystallization data extracted from Figure 6.20b by applying an Avrami model (Equation 6.2). b) Crystallization half times $t'_{1/2}$ for $\phi_c/\phi_c^\infty = 0.5$ as a function of the crossover times for different crystallization temperatures. The relationship between the two times for the temperature series is well described by $t'_{1/2} = 2t'_{\text{gel}} + 6$ min, which differs from the non-nucleated case (Figure 6.9).

In Figure 6.21b, the crystallization half times $t'_{1/2}$ for $\phi_c/\phi_c^\infty = 0.5$ are plotted as a function of the crossover times for different crystallization temperatures. Similar to the temperature-dependent experiments, a linear relationship with a slope of 2 described the data fairly well. However, all data including the one for the neat sample exhibited low crossover times, which required a shift of the describing linear relationship by 6 min, and was presumably a consequence of an inhomogeneous temperature distribution within the sample. Overall, the addition of the nucleating agent had a similar effect on the crystallization behavior as a decrease in crystallization temperature. As the 1500 ppm sample was above the optimum concentration for the formation of a fibrillar network, it showed again a prolonged crystallization despite the overall higher NA content. In Figure 6.22, the correlation of the reduced absolute complex viscosity $|\eta^*|/|\eta^*|_0$ with the degree of space filling ϕ_c/ϕ_c^∞ is shown for all investigated samples. Over the entire range of ϕ_c/ϕ_c^∞ an increasing additive content up to 750 ppm led to higher relative absolute viscosities. The 1500 ppm sample displayed a behavior that was similar to the 500 ppm sample, which might have been caused by a lower content of nucleating

dispersed fibrils. As a nucleating agent primarily changes the nucleation density & spherulite sizes, flow behavior during crystallization from the melt was found to be sensitive to these quantities and not only on the volume fraction ϕ_c as for low-viscous suspensions. This might also be the reason for the observed trends in the temperature-dependent experiments (lower crystallization temperature – increased nucleation / smaller spherulites).

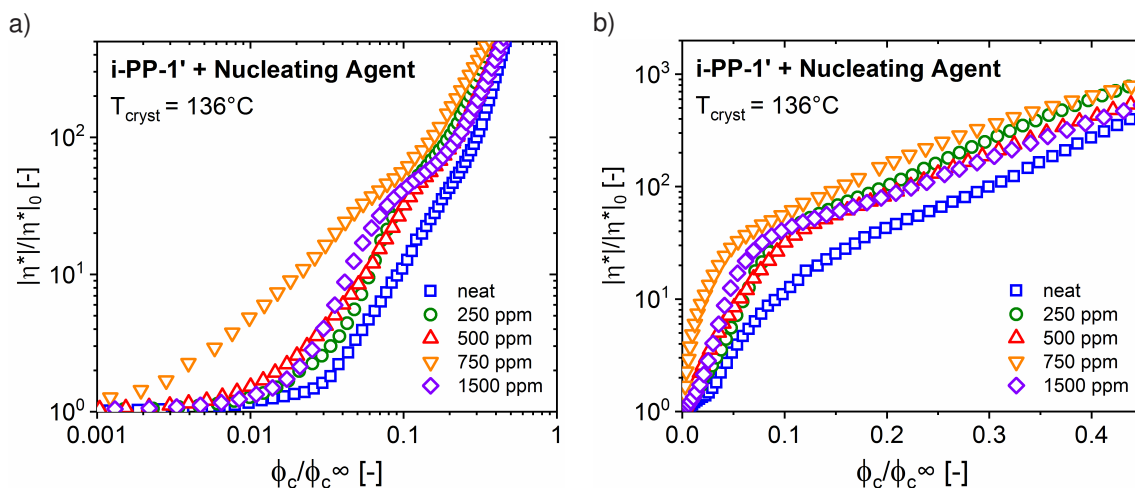


Figure 6.22: Reduced absolute complex viscosity vs. relative crystallinity (degree of space filling) for isothermal crystallization of i-PP-1' with different contents of nucleating agent.

As even the hardening curve for the neat sample showed a kink in the slope at $\phi_c/\phi_c^\infty \approx 0.2$ (Figure 6.22a), the proposed extended Einstein and empirical sigmoidal model were not suitable to describe the hardening curves and consequently no quantitative parameters C' and D' could be extracted. Likely this was not a consequence of the difference in molecular weight compared to batch 1 (see section 2.4, p. 19), but rather due to a temperature gradient across the sample. In the meantime, the heating system was improved by replacing the heating wire and including a vortex element, which opens up the possibility to carry out experiments with a more homogeneous temperature distribution in the future.

6.4 Flow-induced crystallization of isotactic polypropylene

Besides measuring the flow behavior and crystallinity evolution simultaneously at varying temperatures, for different polymer grades, or incorporated additives, one can also impose a non-equilibrium state prior to crystallization using short-term steady shear or LAOS protocols of varying shear rate, strain and duration. Flow is known to have a strong effect on the crystallization kinetics, the morphology, and material properties of semi-crystalline polymers as introduced in section 3.4, p. 38. To separate the effects of flow and crystallization temperature, the protocol by Janeschitz-Kriegl was employed in the following experiments (Figure 6.2). As the criteria for the formation of row-nucleated structures are not fully resolved yet (Kumaraswamy 2005; Lamberti 2014), experiments with variations of the strain rate, the shear duration, and the total strain were carried out at different crystallization temperatures.

6.4.1 Variations of strain rate, shear duration, and total strain

Two different temperature regimes were selected for the study of flow-induced crystallization: a high temperature regime where usually no crystallization is observed on relevant time scales (here: 146 °C), and a lower temperature regime where quiescent crystallization is observed (here: 136 °C), but shows a prolonged induction period before significant crystallinity is being developed (compare with Figure 6.7). In Figure 6.23, experimental results for flow-induced crystallizations of i-PP-1 at $T_{\text{cryst}} \approx 146$ °C are shown where the steady shear protocols were selected to have a similar total strain ($\gamma \approx 200$). As all experiments were carried out using parallel-plate geometries, the imposed shear rates and total strains were the maximum values applied to the outer parts of the sample.

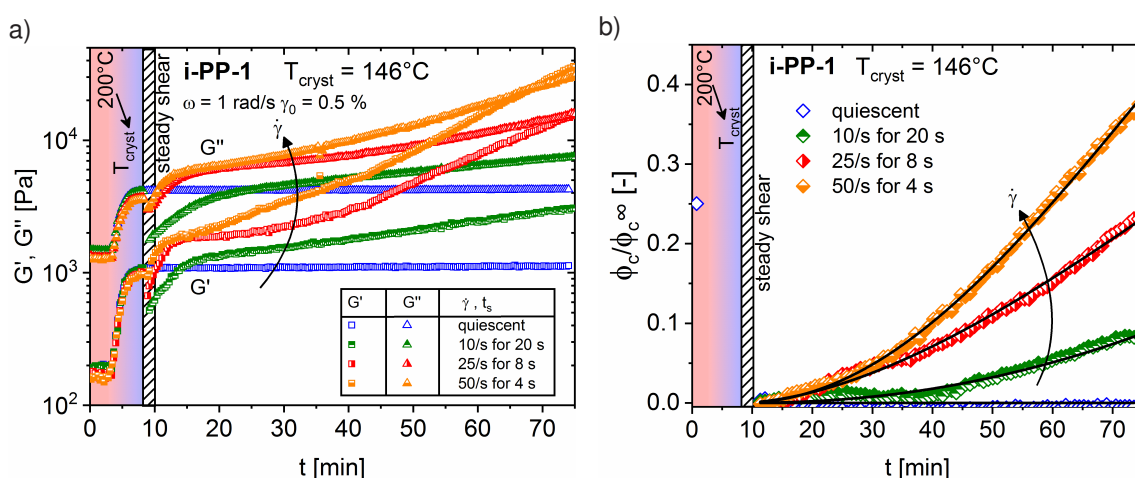


Figure 6.23: Simultaneously acquired moduli G' , G'' (a) and relative crystallinities ϕ_c/ϕ_c^∞ (b) during flow-induced crystallization of i-PP-1 at 146 °C. Upon cooling, different steady shear protocols with a similar total strain $\gamma \approx 200$ were applied.

For $T_{\text{cryst}} \approx 146$ °C, the isothermal experiment under quiescent conditions didn't show any indication of crystallization as the moduli stayed constant and the relative crystallinity ϕ_c/ϕ_c^∞ didn't grow. The behavior changed drastically when flow was applied, as then a significant increase in crystallinity and a rise in moduli were observed, which depended on the applied flow conditions. With increasing shear rate $\dot{\gamma}$, the acceleration effect was more pronounced. In the cases of $\dot{\gamma} = 25/\text{s}$ and $50/\text{s}$, the recovery from a shear-thinned state right after the cessation of flow led to moduli that were a factor of two higher compared to the plateau preceding the steady shear interval. This behavior was presumably caused by an immediate formation of athermal nuclei, which then grew further over time. Furthermore, a crossover of G' and G'' was detected for these experiments. The observation that the shear rate $\dot{\gamma}$ plays a dominant role in accelerating polymer crystallization agrees with previous works by other researchers (Somani *et al.* 2000; Somani, Yang, Hsiao, Sun, Pogodina and Lustiger 2005; Kumaraswamy 2005; Elmoumni and Winter 2006). In Figure 6.24, experimental results for flow-induced crystallizations at $T_{\text{cryst}} \approx 136$ °C are shown where the steady shear protocols were selected to have either a similar total strain ($\gamma \approx 50$) or a similar strain rate ($\dot{\gamma} \approx 10/\text{s}$). All pre-sheared

melts showed a significantly faster crystallization which was seen in the moduli G' and G'' as well as in the relative crystallinity ϕ_c/ϕ_c^∞ . For the two samples exposed to the highest strain rate (17/s for 3 s) and total strain (10/s for 20 s), the curves exhibited an almost immediate increase in moduli G' / G'' and relative crystallinity ϕ_c/ϕ_c^∞ after the cessation of flow. Even though the shear rate was lower in the "10/s for 20 s" experiment, it showed the fastest crystallization and earliest rise in the moduli G' and G'' . Hence, the higher total strain and the associated shearing time t_s were overcompensating the lower shear rate. The immediate increase in moduli and crystallinity suggested that not only the overall speed was affected, but that changes in the morphology of the crystallizing polymer might have occurred. Indeed, the presence of row-nucleated structures (cylindrites) was confirmed later on by *ex-situ* scanning electron microscopy (SEM), and will be discussed in section 6.5.

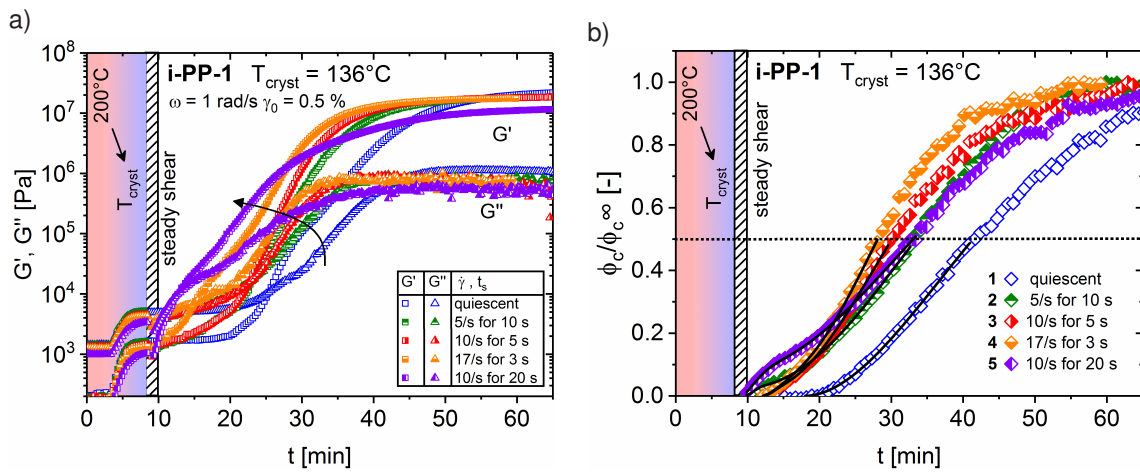


Figure 6.24: Simultaneously acquired moduli G' , G'' (a) and relative crystallinities ϕ_c/ϕ_c^∞ (b) during flow-induced crystallization of i-PP-1 at 136 °C. Upon cooling, different steady shear protocols were applied, which either had a similar total strain or strain rate. A substantial increase in the speed at which G' , G'' , and ϕ_c/ϕ_c^∞ developed was observed for all experiments, which followed the trend "higher shear rate and longer duration lead to faster crystallization".

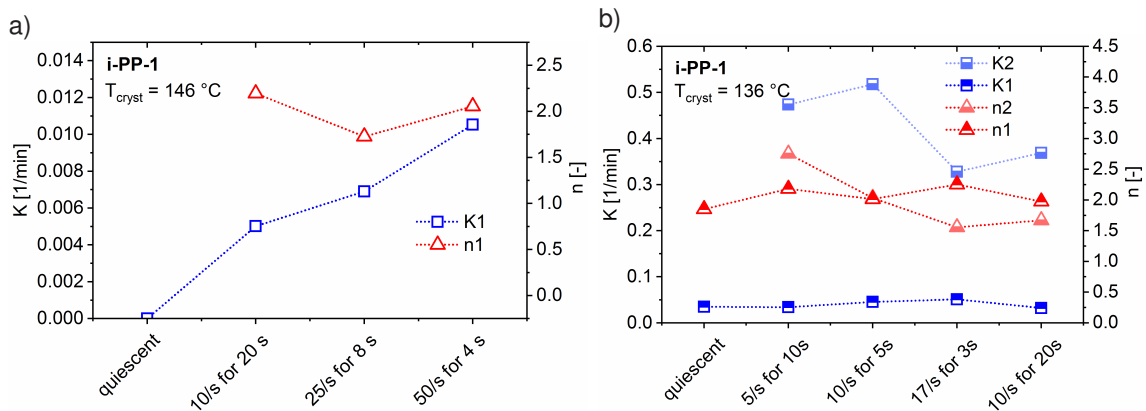


Figure 6.25: Kinetic crystallization data extracted from Figure 6.23b and Figure 6.24b by applying Avrami models (Equation 6.2). For $T_{\text{cryst}} \approx 136$ °C, a second set of Avrami parameters was added to account for the additional crystallization process induced by the applied flow (see Figure 6.24b).

All crystallinity curves were again directly fitted using the volume-related Avrami model up to 50% relative crystallinity to facilitate the correlation of rheological parameters with the degree of space filling (subsection 3.3.6, p. 35). In case of the experiments at $T_{\text{cryst}} \approx 136$ °C, a second set of Avrami parameters was added to account for the additional crystallization process induced by the applied flow. The extracted kinetic results are shown in Figure 6.25. For the experiments at $T_{\text{cryst}} \approx 146$ °C, the kinetic rate parameter K increased with higher shear rates whereas the dimensionality n stayed relatively constant within the error margin. For the experiments carried out at $T_{\text{cryst}} \approx 136$ °C, the rate parameters $K1$ and $K2$ were separated by one order of magnitude, but didn't display a clear trend. The dimensionality $n1$ and $n2$ stayed again relatively constant around $n = 2.0$. The relative contribution of the second Avrami component ($K2, n2$) increased from 2.5% for the "5/s for 10 s" experiment to 8.5% for the "10/s for 20 s" experiment. This result accorded well with the qualitatively observed trend of an additional crystallization process at earlier times for higher shear rates and longer shear durations at the chosen crystallization temperature. For the evaluation of flow-induced crystallization experiments, applied shear rates $\dot{\gamma}$ are usually compared against the characteristic flow relaxation time λ at the chosen temperature (see section 3.4, p. 38 and section 4.1, p. 44). This relationship can be expressed using the Weissenberg number $Wi = \lambda\dot{\gamma}$. A second important relationship is found between the relaxation time λ and the shearing time t_s , which is given by the Deborah number $De = \lambda/t_s$. This dimensionless quantity can be seen as a relative frequency, which helps to describe the state of the material during the application of flow (small De – liquid-like, large De – solid-like). In Figure 6.26a, temperature-dependent frequency sweeps of i-PP-1 are shown from which the relaxation time λ_{cross} was calculated as one over the crossover frequency ($\omega(G' = G'')$). An exponential decrease in the relaxation time λ_{cross} with increasing temperature was observed as the polymer dynamics became more and more mobile. Thus, applying flow at lower temperatures is more likely to have an effect on polymer crystallization compared to the application of flow at higher temperatures.

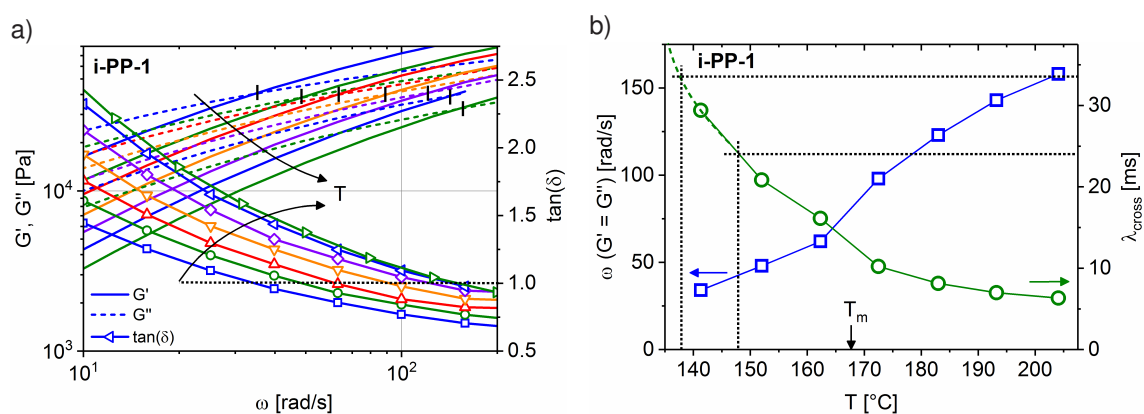


Figure 6.26: a) Temperature series of frequency sweeps for i-PP-1. b) Temperature-dependence of the crossover frequencies and corresponding relaxation times λ_{cross} .

For polydisperse polymers, the relaxation time λ_{cross} as measured by the crossover is not necessarily the longest relaxation time of the material. Experiments by Wingstrand *et al.* (2017) on blends of commercial high-density polyethylene (HDPE) with low amounts of ultra

high-molecular weight polyethylene (UHMWPE) revealed that the crossover frequency was practically identical to that of neat HDPE, whereas the terminal regime showed a modified behavior (Wingstrand *et al.* 2017). When a 6-mode Maxwell model was applied to a mastercurve constructed from the frequency data of Figure 6.26a, significant contributions of modes with higher relaxation times were observed (Figure 6.27). Similarly, the conversion of the mastercurve into a relaxation spectrum $H(\lambda)$ showed the presence of slower relaxing components (see Appendix A). Considering a minimum contribution of $>1\%$, the longest relaxation times λ_M were on the order of 1 s, which was a factor of 30 higher than λ_{cross} . These slowly relaxing components were most certainly associated with the high molecular weight tail of the rather polydisperse i-PP-1 material ($\mathcal{D} = 2.7$).

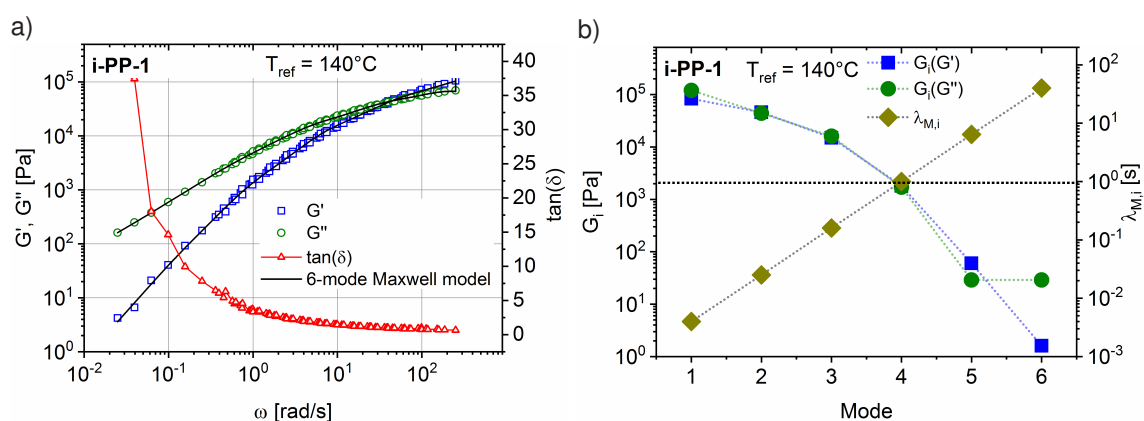


Figure 6.27: a) Rheological mastercurve for $T_{\text{ref}} \approx 140^\circ\text{C}$, which was constructed from frequency sweeps measured at different temperatures (Figure 6.26a). b) Parameter extracted from a 6-mode Maxwell model applied to the mastercurve in a).

The Deborah and Weissenberg numbers for the respective flow-induced crystallization conditions are summarized in Table 6.4. In all experiments the Deborah numbers were below 1, which implied that steady-state conditions were achieved for the majority of polymer chains after a short amount of time. It is a widely accepted rule for flow-induced crystallization that the shear rate has to be larger than the inverse of the longest flow relaxation time λ to induce row-nucleated structures ($Wi > 1$), as the altered chain conformation has to persist over certain periods of time in order to form threadlike nuclei (Elmoumni and Winter 2006). Here, the Weissenberg numbers Wi_{cross} based on the relaxation time λ_{cross} were smaller than 1, with the exception of one experiment (50/s for 4 s at 146°C). As already pointed out, the relaxation time λ_{cross} does not characterize the slowest relaxation mode, but rather the most dominant one. The Weissenberg number $Wi_{M(\text{axwell})}$ based on the longest significant relaxation time $\lambda_M \approx 1$ s extracted from a 6-mode Maxwell model exhibited values larger than 1. Even though the chosen 1% criterion for a significant contribution to the relaxation behavior was arbitrary, a certain non-negligible fraction of polymer chains was certainly affected by the applied shear rate. As will be seen in chapter 7, shear rates as low as $\dot{\gamma} = 3/\text{s}$ were able to induce row-nucleated morphologies, which accorded well with the observation that only a very small amount of long chains is needed to form row-nucleated structures (Wingstrand *et al.* 2017).

$T_{\text{cryst}} [^{\circ}\text{C}]$	$\dot{\gamma} [1/\text{s}]$	$t_s [\text{s}]$	γ	$\lambda_{\text{cross}} [\text{s}]$	De_{cross}	Wi_{cross}	$\lambda_M [\text{s}]$	De_M	Wi_M
146	10	20	200	0.026	0.0013	0.26	~ 1	0.05	10
	25	8	200	0.026	0.0033	0.65	~ 1	0.1	25
	50	4	200	0.026	0.0065	1.3	~ 1	0.3	50
136	5	10	50	0.037	0.0037	0.19	~ 1	0.1	5
	10	5	50	0.037	0.0074	0.37	~ 1	0.2	10
	17	3	51	0.037	0.012	0.63	~ 1	0.3	17
	10	20	200	0.037	0.0019	0.37	~ 1	0.05	10

Table 6.4: Characteristics of the flow-induced crystallization experiments in terms of the shear rate $\dot{\gamma}$, the shearing time t_s , the total strain γ , the relaxation times λ , the Deborah numbers De , and the Weissenberg numbers Wi , respectively.

As presented in the beginning of this chapter, NMR relaxometry not only provides information on the amount of protons in mobile or rigid fractions, but also on their respective NMR relaxation times / rates (see Figure 6.4b). Generally, the application of flow can have a substantial effect on the NMR relaxation behavior of polymer melts (Räntzsch *et al.* 2014). As in all experiments presented in this section a short-term steady shear protocol was employed and flow relaxation was relatively fast (Figure 6.27b), the overall polymer dynamics were expected to behave similarly to a non-perturbed system soon after the cessation of flow. Figure 6.28 shows a comparison of a crystallization experiment at 136 °C under quiescent conditions, and with a preceding steady shear step of 10/s for 20 s. The point density of ~ 1 data point per minute was too low to resolve the potentially increased mobility during and shortly after the application of flow as indicated by the rheological shear-thinning behavior (Figure 6.24a). For the main part of crystallization the relaxation rates $1/T_{21}$ and $1/T_{22}$ showed very similar curve shapes and absolute values for both, the quiescent and the pre-sheared case, which confirmed that there was no persistent change in polymer dynamics for the chosen experimental conditions.

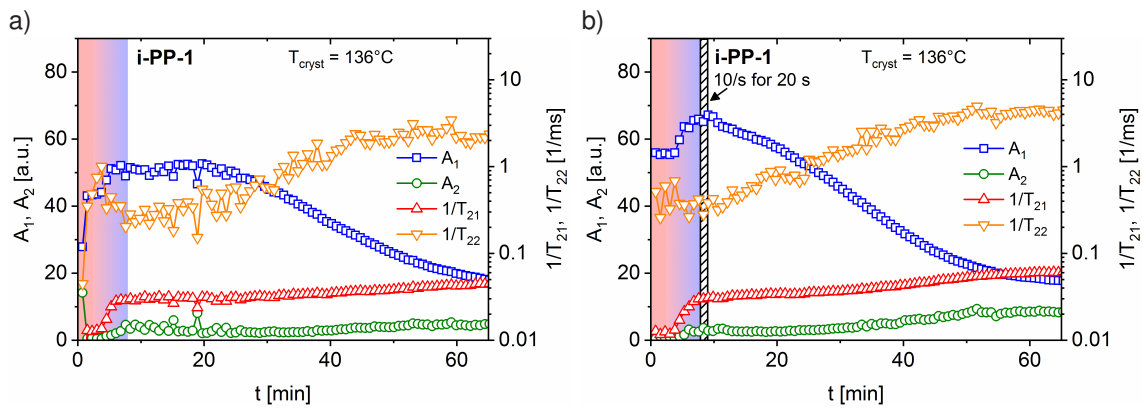


Figure 6.28: NMR transverse relaxation rates and intensities extracted from MSE-CPMG data using Equation 6.1 for the quiescent crystallization of i-PP-1 at 136 °C (a) and with a preceding steady shear step of 10/s for 20 s (b).

6.4.2 Physical gelation during flow-induced crystallization

To further compare the different flow-induced crystallization experiments, crystallization half times for $\phi_c/\phi_c^\infty = 0.5$ and crossover times for $G' = G''$ were plotted against each other in Figure 6.29. For the quiescently crystallized temperature-dependent experiments of Figure 6.7, the relationship between $t'_{1/2}$ and t'_{gel} was well described by the dotted line ($t'_{1/2} = 2t'_{\text{gel}}$). The data for the flow-induced crystallization experiments at $T_{\text{cryst}} = 146^\circ\text{C}$ roughly fell on this line, even though the uncertainty in estimating the crystallization half time was considerable (extrapolation based on the Avrami fit). For the pre-sheared experiments at $T_{\text{cryst}} \approx 136^\circ\text{C}$, a shift to lower times was observed at moderate shear conditions. At higher strain rates and total strains, the gelation times t'_{gel} decreased further and the crystallization half times $t'_{1/2}$ remained almost constant. This behavior indicated that there was a change in the nucleation and growth characteristics. Indeed, a high nucleation density and row-nucleated structures were confirmed for the "10/s for 20 s" sample by *ex-situ* scanning electron microscopy, which will be discussed in section 6.5.

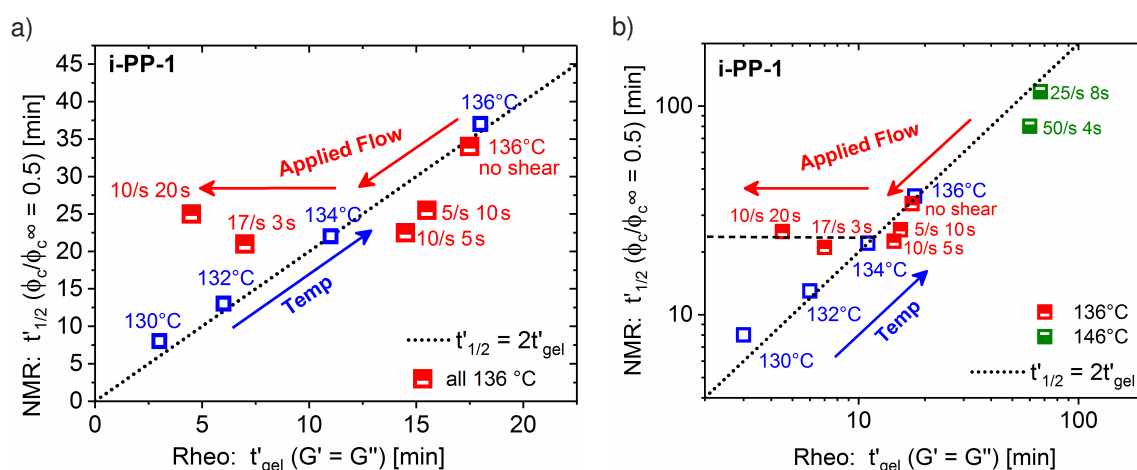


Figure 6.29: Crystallization half times $t'_{1/2}$ for $\phi_c/\phi_c^\infty = 0.5$ as a function of the crossover/gelation times t'_{gel} for $G' = G''$ at different crystallization temperatures (open squares) and pre-shear experiments (semi-filled squares) in a linear (a) and logarithmic plot (b).

The shorter time needed to achieve a gel state for higher shear rates and longer shear durations might have been a consequence of the strongly increased nucleation density and the potential influence of row-nucleated structures (cylindrites). It is well established that elongated objects have a substantial effect on the rheology of multi-component systems as seen for e.g., fiber-reinforced composites (Pötschke *et al.* 2002), and suspensions of ellipsoidal (Madivala *et al.* 2009) or rod-like particles (Abbasi *et al.* 2009). An illustration of the potential morphology at the rheological gel point is given in Figure 6.30 for three different scenarios: a) quiescent conditions; b) mild applied flow conditions; c) strong and long applied flow. At relatively mild flow conditions, nucleation is thought to be increased, which leads to lower average spherulite sizes at the gel point. For experiments under stronger and longer applied flow, the formation of row-induced structures might lead to even earlier gelation compared to experiments at lower

shear rates. However, also the strain rate distribution present in parallel-plate geometries has to be taken into account, which presumably caused faster crystallization at the outer parts of the sample. As the torque is proportional to the radius, changes at the outer parts of the sample have a strong effect on rheology, whereas NMR is sensitive to the sample average. The detailed morphology at the gel point and build-up of row-nucleated structures was further studied using RheoSAXS and RheoMicroscopy, which will be discussed in chapter 7 and chapter 8, respectively.

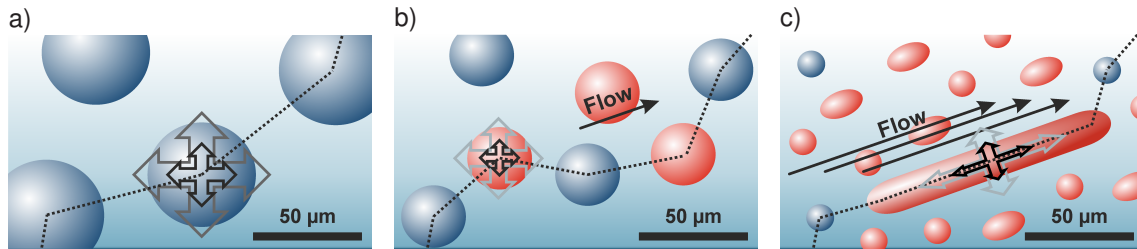


Figure 6.30: Potential morphology at the gel point for three different scenarios: a) quiescent conditions; b) mild applied flow conditions with increased nucleation; c) strong and long applied flow conditions with the formation of ellipsoidal and rod-like structures.

The correlation of the reduced absolute complex viscosity $|\eta^*|/|\eta^*|_0$ with the degree of space filling ϕ_c/ϕ_c^∞ is shown in Figure 6.31 for all experiments carried out at $T_{\text{cryst}} \approx 146^\circ\text{C}$ (a) and $T_{\text{cryst}} \approx 136^\circ\text{C}$ (b), respectively. An increase proportional to the applied shear rate $\dot{\gamma}$ at very lower values of ϕ_c/ϕ_c^∞ was observed for the experiments at $T_{\text{cryst}} \approx 146^\circ\text{C}$. This behavior might have been caused by the creation of a small number of athermal nuclei that were below the detection threshold of NMR. For higher degrees of space filling, the curve shape was similar to that of quiescently crystallized i-PP-1 (Figure 6.11). The correlation plots for the experiments at $T_{\text{cryst}} \approx 136^\circ\text{C}$ didn't exhibit a clear trend with respect to the applied flow conditions. It remained inconclusive at this stage, if this behavior was caused by a change in the nucleation and growth characteristics or the presence of a certain temperature gradient.

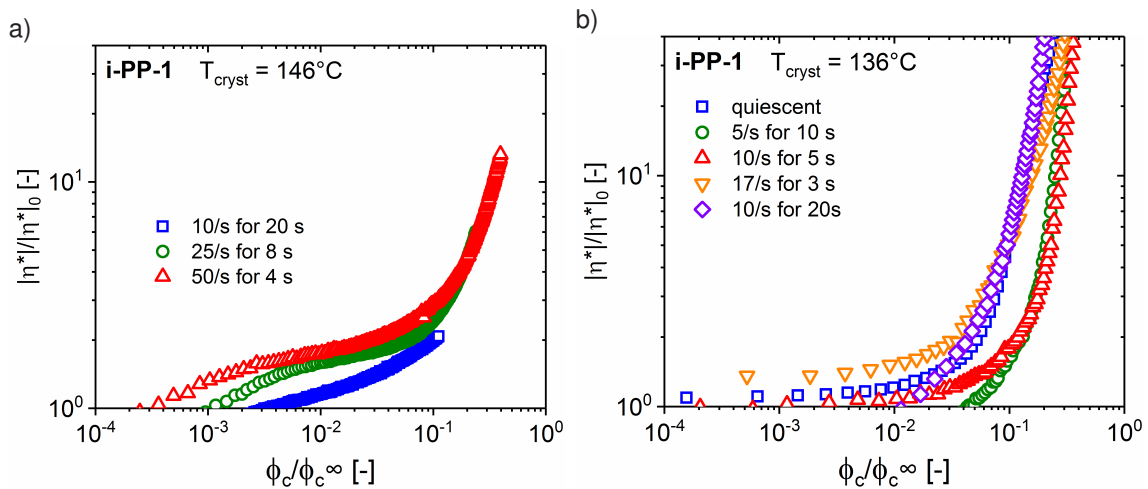


Figure 6.31: Reduced absolute complex viscosity vs. relative crystallinity (degree of space filling) for flow-induced isothermal crystallizations of i-PP-1 at 146°C (a) and 136°C (b).

6.5 Morphology investigations using scanning electron microscopy

To further evaluate the effects of different polymer grades, fillers, nucleating agents, and flow on the crystallization of isotactic polypropylene, *ex-situ* scanning electron microscopy (SEM) investigations were carried out on the recovered specimen upon complete crystallization. All samples were etched prior to SEM using an acidic permanganate solution as described by Sawyer *et al.* (2008) (experimental details were given in section 6.2). The etchant concentration and etching time were optimized to achieve a substantial removal of the amorphous fraction without heavily damaging the crystalline structure. All images presented in this section were recorded at a position of ~ 3 mm from the edge of the sample.

Quiescently crystallized isotactic polypropylene

For the Ziegler-Natta grade i-PP-1, large spherulites (~ 100 μm) were observed that formed a densely packed lattice with no observable voids (Figure 6.32). This confirmed that the degree of space filling ϕ_c/ϕ_c^∞ was close to 1 at the end of crystallization. The detailed crystalline structure (Figure 6.33) consisted of 10 – 20 nm thick stacked lamellae, which grew radially from the center of the spherulites. At the highest magnification, a cross-hatched morphology was observed with short daughter lamellae bridging the parent or primary lamellae at a splaying angle of $\sim 90^\circ$. This feature was frequently observed for isotactic polypropylene and associated with the 3-1 helix structure of the unit cell.

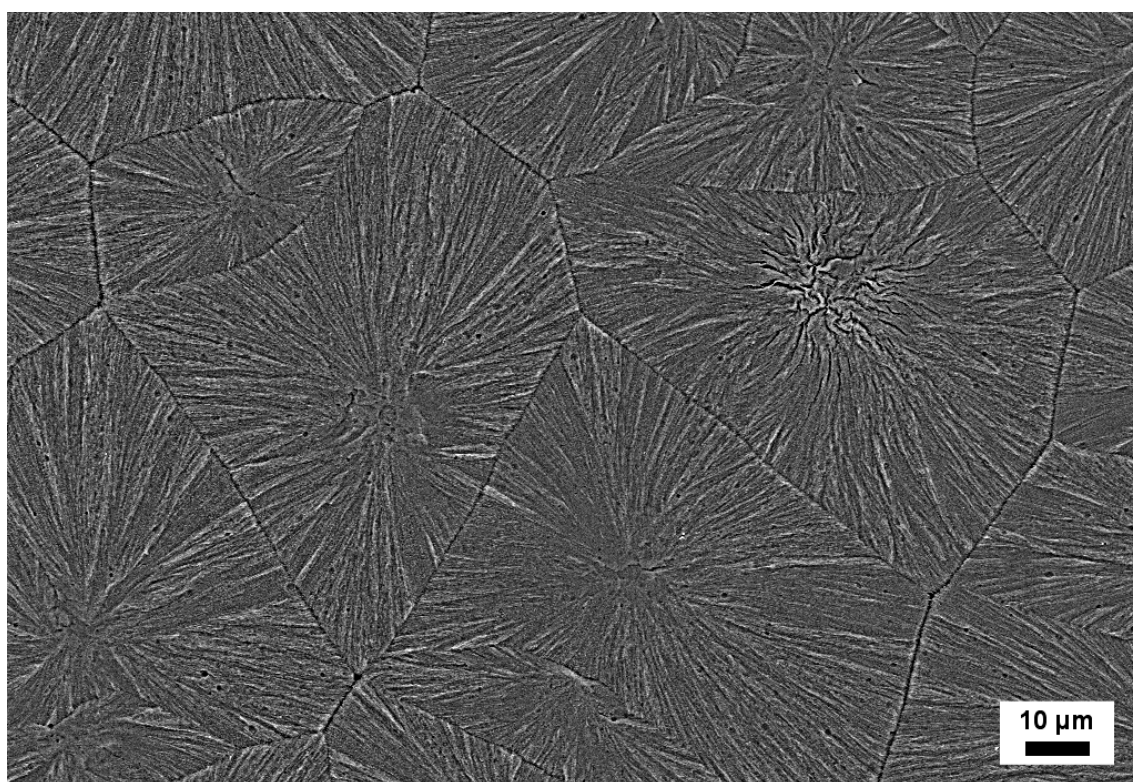


Figure 6.32: SEM images of etched i-PP-1 crystallized at 136 °C under quiescent conditions. Large spherulites with a lamellar substructure were observed throughout the sample.

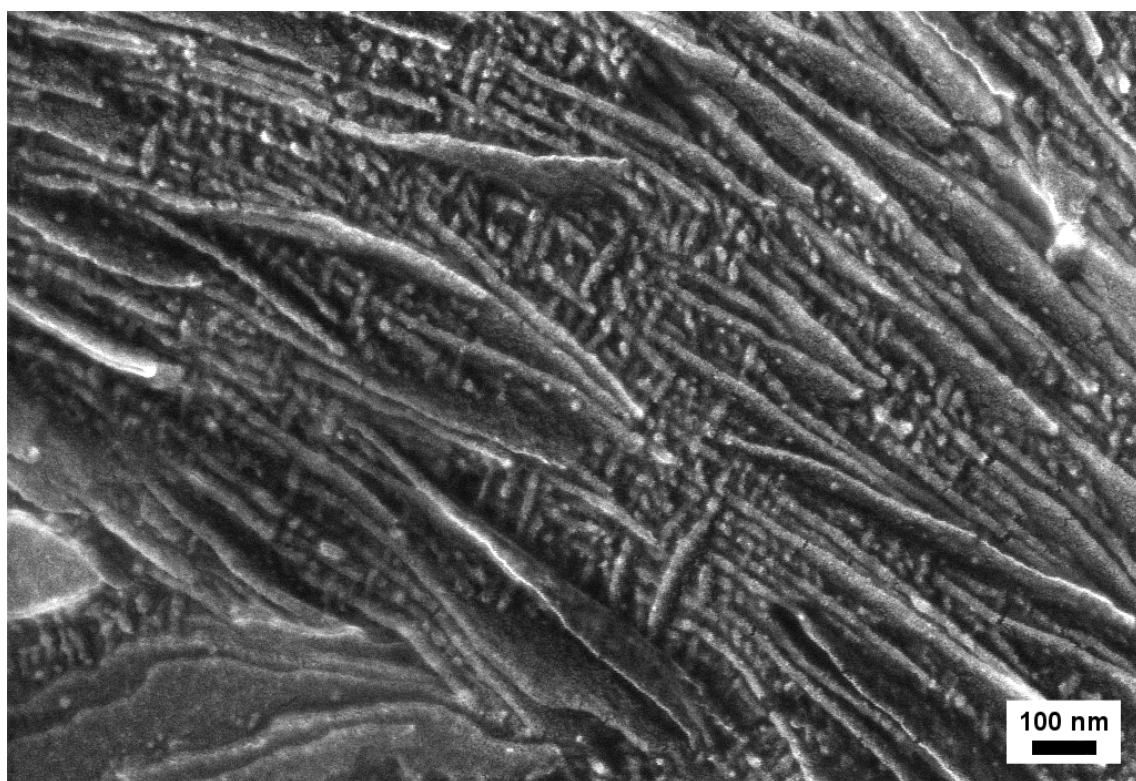
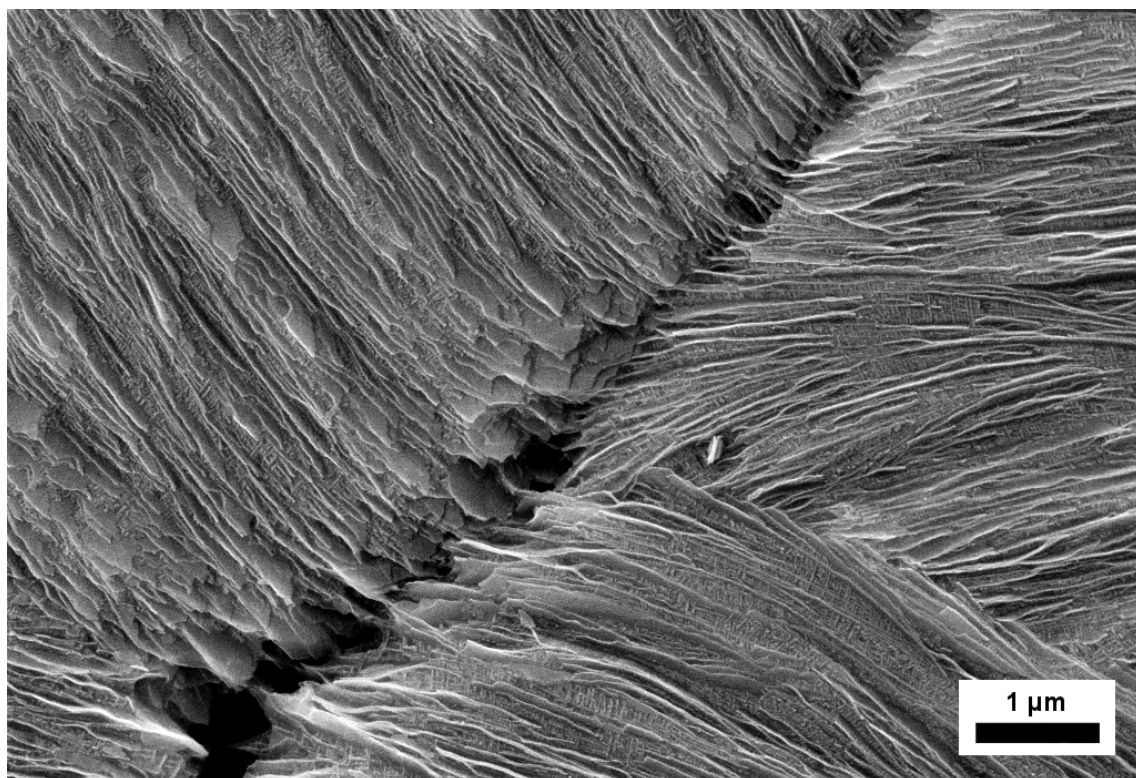


Figure 6.33: SEM images of etched i-PP-1 crystallized at 136 °C under quiescent conditions. The substructure consisted of stacked lamellae, which grew radially from the center of a spherulite and displayed some splaying.

Influence of the polymer grade

The regio-defective polypropylene grade i-PP-2 exhibited a substantially higher nucleation density compared to the regio-regular i-PP-1 sample at comparable crystallization conditions (Figure 6.34). Furthermore, it had an anisotropic, bundle-like microstructure with less clearly visible stacked lamellae. The high nucleation density and exceptional spherulitic structure are very likely a consequence of the 1 mol% 2,1-erythro regio defects (see Appendix A), which are known to induce the observed γ -form crystallization with non-parallel chain packing and a high tendency to form anisotropic lamellar structures (see section 2.3, p. 13, Thomann *et al.* (1996)).

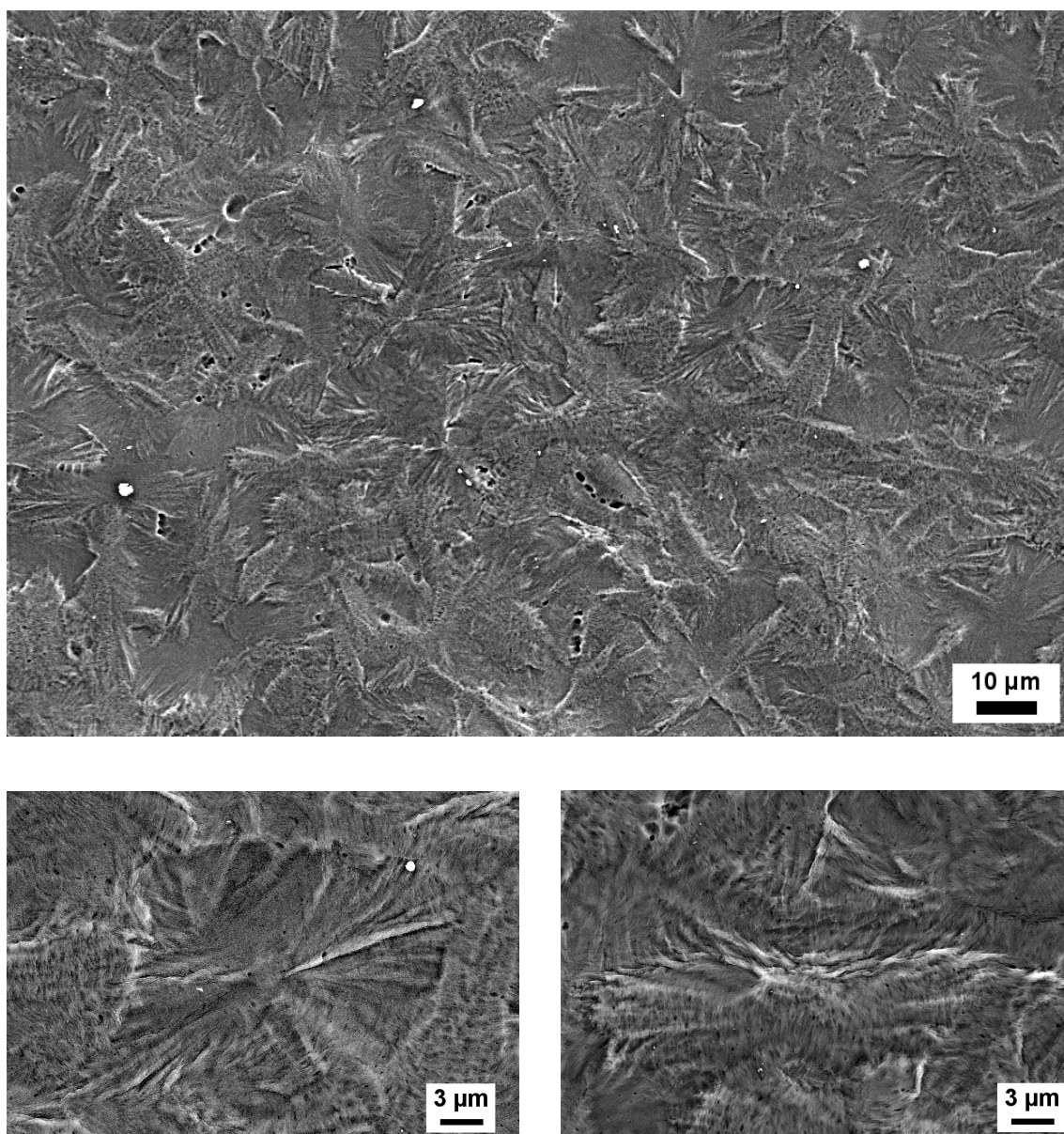


Figure 6.34: SEM image of etched i-PP-2 crystallized at 134 °C under quiescent conditions, which revealed a higher nucleation density and anisotropic spherulites compared to the regio-regular i-PP-1 grade.

Influence of fillers

The effect of fillers on the crystallization of isotactic polypropylene was studied by incorporation of 3 wt% silica into i-PP-1. An increase in the nucleation density was observed, which explained the overall faster crystallization behavior (Figure 6.35). EDX analysis confirmed that the silica was located mostly in the center of the spherulites acting as a nucleation agent. However, some larger silica agglomerates were also present in the sample.

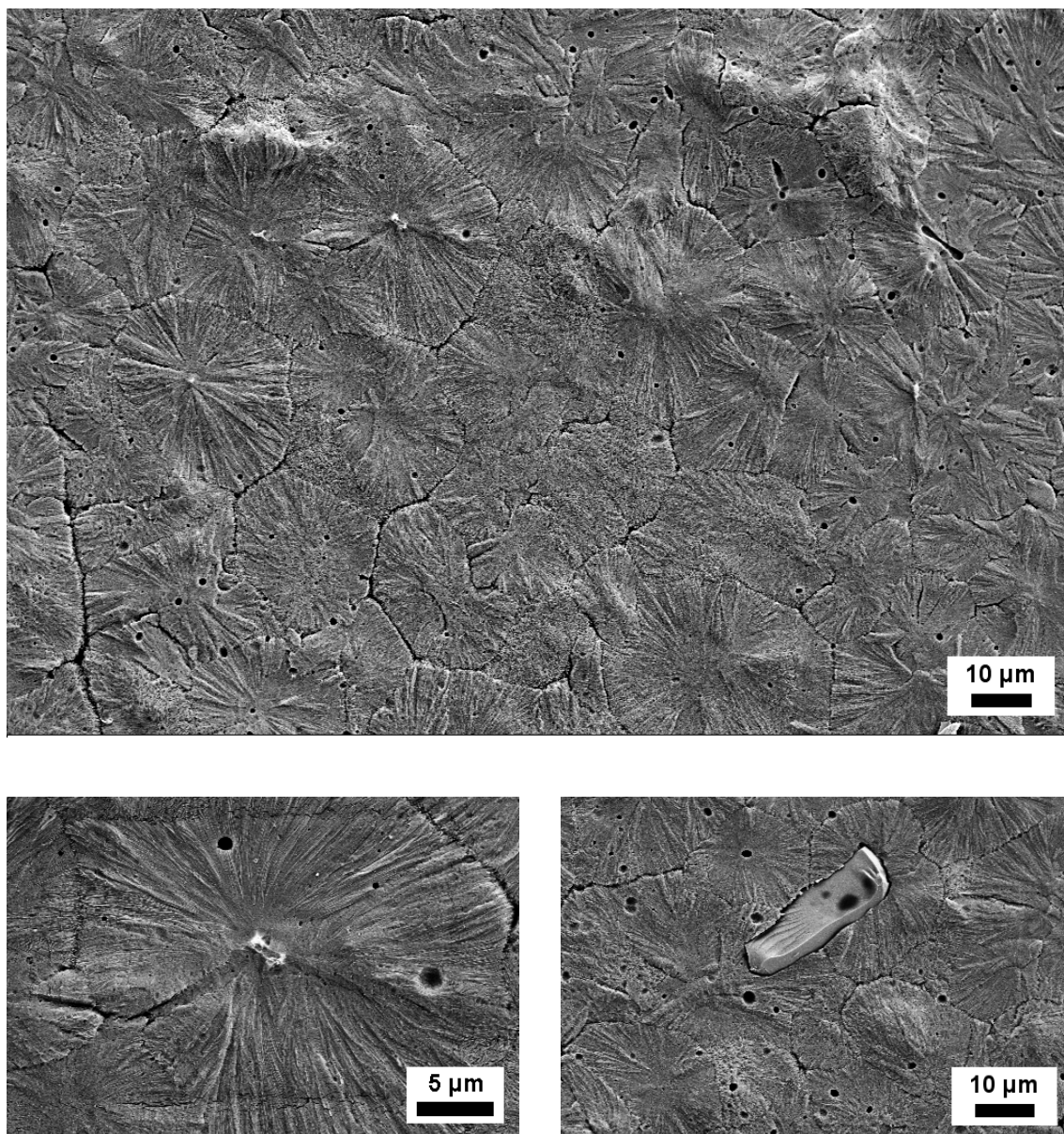


Figure 6.35: SEM image of etched i-PP-1 + 3wt% silica crystallized at 132 °C under quiescent conditions. The nucleation density was higher compared to the neat i-PP-1 sample crystallized under similar conditions (see Appendix A). The silica was confirmed by EDX analysis to be located mostly in the center of the spherulites. However, also larger agglomerates of silica were observed.

Influence of nucleating agents

The influence nucleating agents on the crystallization of isotactic polypropylene was studied by an addition of different amounts of a 1,3,5-benzene tricarboxamide derivative to the Ziegler-Natta grade i-PP-1'. An increase in nucleation density was observed up to a weight content of 750 ppm. However, the nucleation efficiency of individual nucleating agent fibrils was found to be relatively low. The diameter of the fibrils was on the order of 200 – 500 nm, whereas their length was 10 – 20 μm . For the 1500 ppm sample large agglomerates of nucleating agent were present in the sample, which explained the overall lower nucleating efficiency and slower crystallization kinetics.

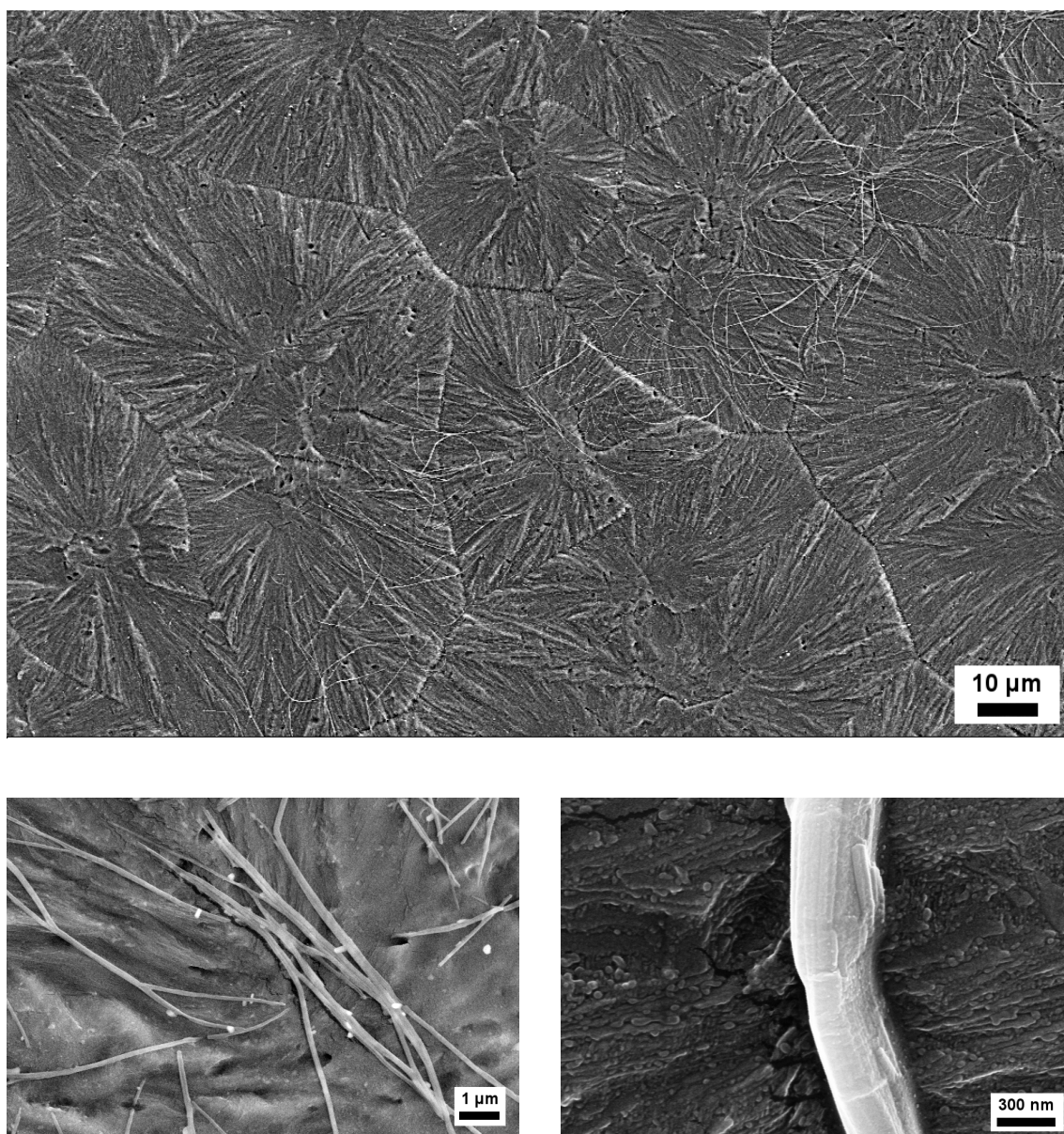


Figure 6.36: SEM image of etched i-PP-1' + 750 ppm N, N', N''-tris(3-methylbutyl)-1,3,5-benzene tricarboxamide crystallized at 136 °C under quiescent conditions. The nucleation density was the highest compared to all other samples of the series. The nucleating agent fibrils were found throughout the sample and some of them acted as nucleation points for the formation of spherulites.

Flow-induced crystallized isotactic polypropylene

The effect of flow on the morphology of isotactic polypropylene was studied by applying short-term steady shear before crystallization of i-PP-1. The recovered specimen from a test which showed the strongest speed-up of crystallization (10/s for 20 s, $T_{\text{cryst}} \approx 136$ °C) had a substantially increased nucleation density with very small spherulite sizes (~ 5 μm) compared to the quiescently crystallized i-PP-1 sample (see section 6.4). Furthermore, row-nucleated structures / cylindrites were found throughout the sample with a strong directional orientation of the grown lamellae perpendicular to the flow direction and, to a limited degree, also daughter lamellae in the direction of flow. The latter is known to be caused by the large splaying angle of $\sim 90^\circ$ in isotactic polypropylene due to the 3-1 helix structure. The lamellar thickness was similar to that measured in the quiescent case, which suggested that while nucleation was indeed strongly affected by the application of flow, growth proceeded instead rather unperturbed on the time scale of hours with the exception of template-based orientation of growth in the row-nucleated structures. The high anisotropy of these objects is a potential reason for the observed shorter gelation times t'_{gel} (Figure 6.29) for the samples that were subject to the strongest flow in these experiments (17/s for 3 s and 10/s for 20 s).

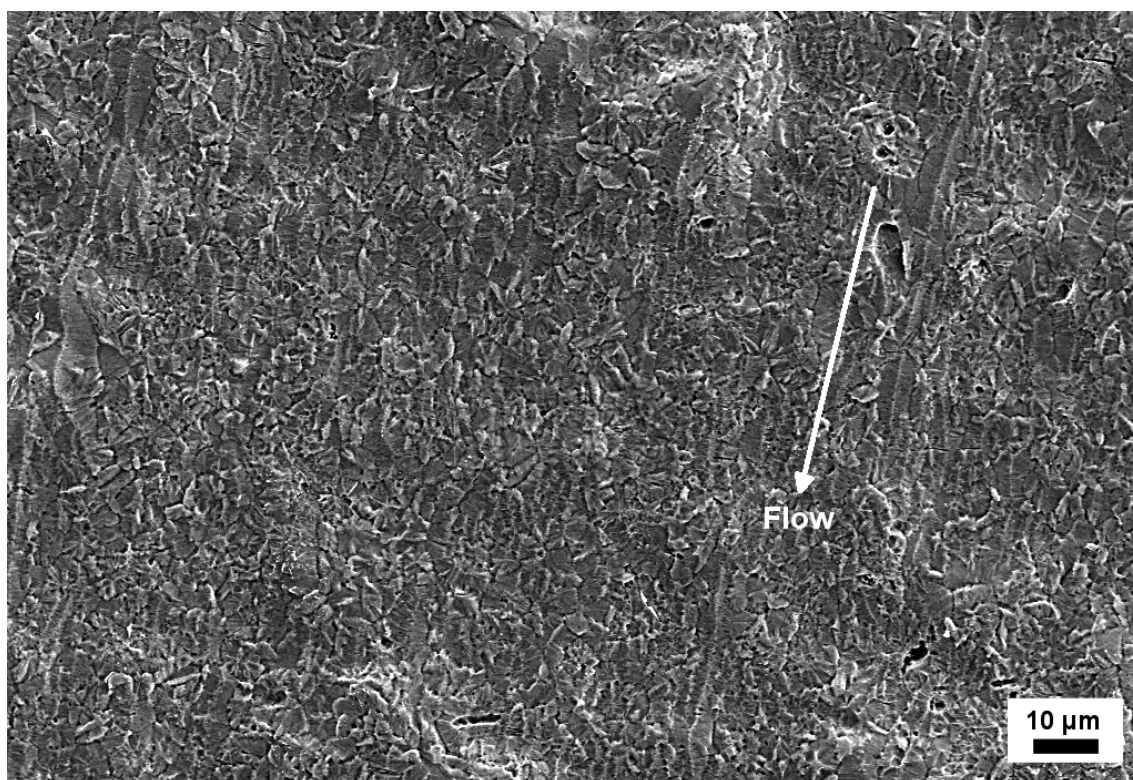


Figure 6.37: SEM images of etched i-PP-1 crystallized at 136 °C with a preceding steady shear experiment (10/s for 20 s). A very high nucleation density and row nucleated structures the direction of flow were found.

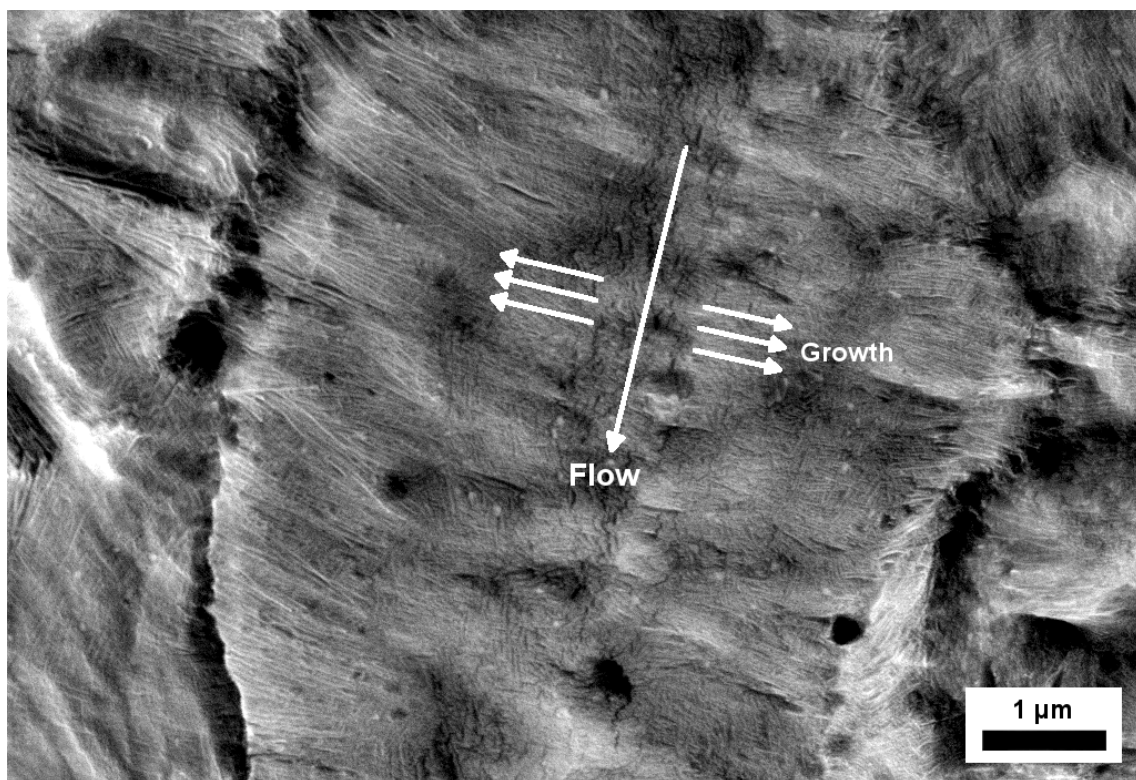
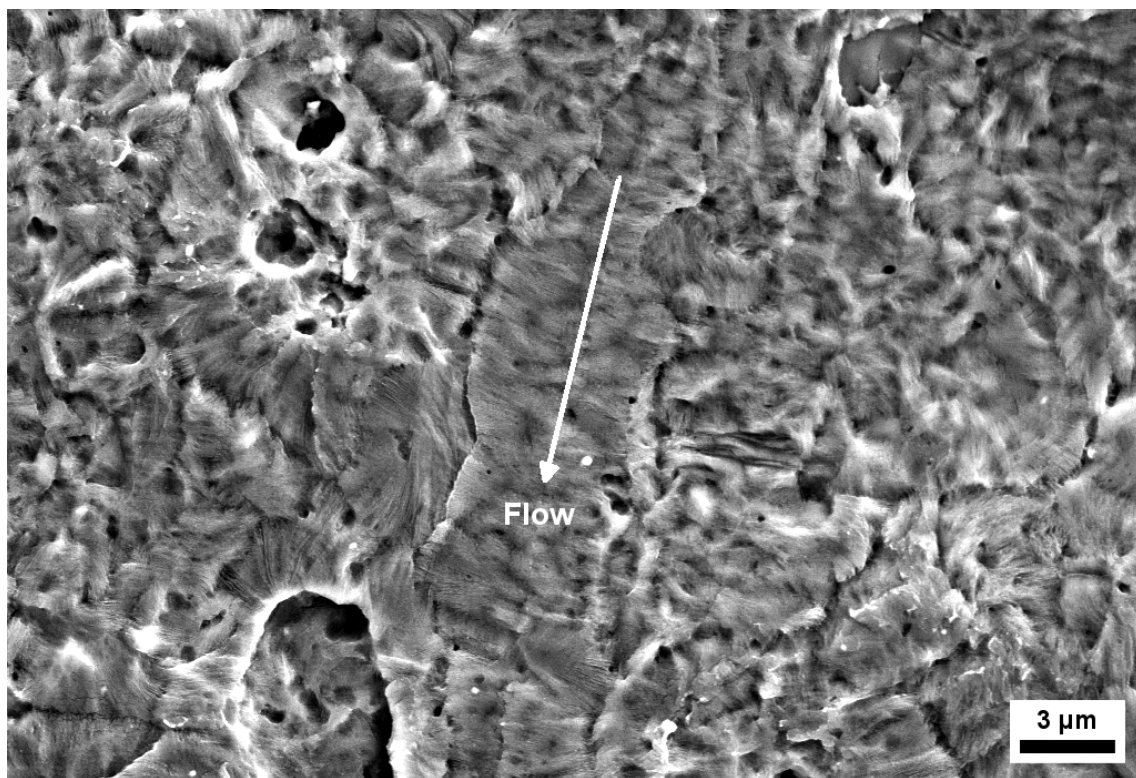


Figure 6.38: SEM images of etched i-PP-1 crystallized at 136 °C with a preceding steady shear step (10/s for 20 s). The detailed row-nucleated structure exhibited lamellae that were grown perpendicular to the direction of flow.

6.6 Concluding remarks

The crystallization of isotactic polypropylene under quiescent conditions and with preceding steady shear protocols was investigated using a hyphenated RheoNMR set-up based on a commercial strain-controlled shear rheometer with a portable low-field ^1H NMR unit. Evolving crystallinities ϕ_c were determined using a multi-echo-based NMR relaxometry sequence, which measures molecular mobility of protons. As the sample was studied simultaneously by rheology and NMR relaxometry, correlation plots such as e.g., $|\eta^*|/|\eta^*|_0$ vs. ϕ_c/ϕ_c^∞ were constructed, which were evaluated using suspension (Einstein, Quemada, Krieger-Dougherty) and semi-empirical models (sigmoidal, extended Einstein). The best description of the hardening behavior of a neat Ziegler-Natta grade i-PP was achieved using an extended Einstein model with exponents $C' \approx 4$ to 5 and dynamic ranges $D' \approx 30000$ to 60000 for the chosen crystallization temperatures of $T_{\text{cryst}} \approx 132$ to 136 °C.

Different isotactic polypropylene grades were compared with respect to their crystallization kinetics and physical gelation behavior. A metallocene-catalyzed, regio-defective polypropylene grade showed a three times slower crystallization rate at comparable temperatures and an unusually fast rising hardening curve for low degrees of space filling compared to the previously examined regio-regular Ziegler-Natta grade. The influence of fillers and nucleating agents on the crystallization behavior of i-PP was studied in close collaboration with the groups of Prof. A. Müller (Universidad del País Vasco, San Sebastián, Spain) and Prof. H.W. Schmidt (University of Bayreuth, Germany). The tested silica increased the crystallization rate by $\sim 30\%$ at 3wt% loading, which was comparable to the effect of a 2 °C lower crystallization temperature. Similarly, the employed nucleating agent of the 1,3,5-benzene tricarboxamide type showed a $\sim 30\%$ faster crystallization at the determined optimum concentration of 750 ppm by weight. Due to the simultaneous acquisition of rheology and NMR data, it was possible to correlation plots that characterized the hardening behavior of filled and nucleated isotactic polypropylene. It was found that the incorporated silica filler didn't change the hardening behavior significantly, whereas the 1,3,5-benzene tricarboxamide nucleating agent led to a faster rising hardening curve at the optimum concentration of 750 ppm.

Flow-induced crystallization was studied using short-term steady shear protocols with either similar total strains or strain rates. An increase in the speed of crystallization was detected for the pre-shear experiments, with the samples that were subjected to the strongest flow conditions of 10/s for 20 s showing an almost immediate increase in the viscosity $|\eta^*|$ upon the cessation of flow. Scanning electron microscopy confirmed that a substantially higher nucleation density with small spherulites ($\sim 5 \mu\text{m}$) was present in the sheared samples. In addition, anisotropic row-nucleated structures were observed for experiments at Weissenberg numbers $Wi \gg 1$ for at least 1% of the polymer chains that may be the origin of rigidification at very low crystallinities. Further experiments using monodisperse polymers of different molecular weights would help to fully clarify the relationship between the imposed flow as characterized by the Weissenberg number Wi and potentially formed row-nucleated morphologies.

7 Correlation between Nano-Scale Morphology and Rheology in Polymer Crystallization: RheoSAXS

In the following chapter, simultaneous RheoSAXS investigations on the nanostructure and rheology during quiescent and flow-induced polymer crystallization are presented. All experiments were carried out at the beam line P10 of the German Electron Synchrotron (DESY) in collaboration with Dr. Eric Stellamanns and Dr. Michael Sprung. The effect of flow profiles on the process of polymer crystallization with respect to the changes in the morphology and rheology will be discussed. The obtained sample morphologies were further evaluated using *ex-situ* scanning electron microscopy.

7.1 Introduction

Investigating the X-ray scattering of soft matter under flow conditions has been of high interest for several decades, since changes in the nano-scale morphology are oftentimes strongly connected with modified properties such as the tensile strength of fibers, the long-range ordering of block copolymers, or the optical properties of liquid crystals. Time-resolved experiments of phase transitions and ordering processes can usually only be performed using synchrotron radiation to achieve the required high photon intensities for a time resolution on a millisecond to second scale. Early hyphenated set-ups were based on flow cells that allowed for the application of steady shear protocols in combination with wide and small angle X-ray scattering. Investigations were conducted on e.g., liquid crystals (Hongladarom *et al.* 1996; Berghausen *et al.* 2000), copolymers (Hamley *et al.* 1998; Castelletto *et al.* 2001, 2005), and semi-crystalline polymers (Somani *et al.* 2000, 2001; Nogales *et al.* 2001; Somani *et al.* 2002; Agarwal *et al.* 2003; Kumaraswamy *et al.* 2004; Balzano *et al.* 2008, 2009). More recently, slit-flow experiments on crystallizing polymers based on a multipass rheometer were presented by Portale *et al.* (2013); Ma *et al.* (2012, 2014), and Balzano *et al.* (2016). The structure formation during polymer processing such as extrusion (Schrauwen *et al.* 2004), film blowing (van Drongelen *et al.* 2014), and fiber spinning (Samon *et al.* 1999; Kolb *et al.* 2000; Schultz *et al.* 2000; Ran *et al.* 2000) was also investigated by several groups using respective hyphenated set-ups. Despite the very valuable insights in the structural buildup during quiescent and flow-induced crystallization of polymers, these studies lacked information on the *in-situ* rheology of the materials under investigation. Hyphenated set-ups that allowed for simultaneous measurements of rheology and X-ray scattering based on shear rheometers were realized by Panine *et al.* (2003) who studied liquid crystals and polymer latices in a Couette cell rheometer, by Polushkin *et al.* (2004, 2005) who developed a tooth geometry to study the alignment of block copolymer supramolecules in the radial and tangential shear direction, by

Pfleiderer *et al.* (2014) who built a shear cell rheometer that allowed for the study of X-ray scattering of fluids in the vorticity direction, and by Struth *et al.* (2011); Meins *et al.* (2011); Stellamanns *et al.* (2013) who developed a hyphenated set-up based on a commercial stress-controlled rheometer with a unique beam path for the study of low to highly viscous samples. The latter set-up was used in the experiments on polymer crystallization presented here, and furthermore by other researchers to study block copolymers (Meins *et al.* 2012; Pulamagatta *et al.* 2012), platelet dispersions (Lettinga *et al.* 2012), and colloidal systems (Kim *et al.* 2013; Westermeier *et al.* 2016). Recently, also hyphenations of extensional rheometers and X-ray scattering techniques were presented by Yan *et al.* (2009); Liu *et al.* (2011), and Wingstrand *et al.* (2017) with the aim of understanding the interplay of the structural buildup and elongational rheology during the processing of semi-crystalline polymers.

7.2 Experimental

RheoSAXS set-up

The hyphenated RheoSAXS set-up was developed in collaboration between the groups of Prof. Wilhelm (KIT) and the beam line P10 group at the German Electron Synchrotron (DESY) (Figure 7.1, Struth *et al.* (2011); Meins *et al.* (2011); Stellamanns *et al.* (2013), see Appendix A for a photograph). A unique feature of this set-up is that the incident X-ray beam is reflected by a Ge333 crystal in order to maintain the horizontal shear flow direction of the used Haake MARS II rheometer (Thermo Scientific, Karlsruhe, Germany). The rheometer motor was flipped to open up the top space for the beam path and the 2D-SAXS detector. By using the synchrotron source DESY PETRA III in combination with a Pilatus 300k 2D-SAXS detector (Dectris, Baden-Dättwil, Switzerland), experiments with up to 500 frames per second can be conducted. The q -range of the instrument can be adjusted by selecting a respective sample-to-detector distance (limits $\sim 0.02 - 4/\text{\AA}$ for $\lambda = 1.54 \text{\AA}$). The home-built oven allows to perform experiments over a temperature interval of 10 – 300 °C under a nitrogen atmosphere.

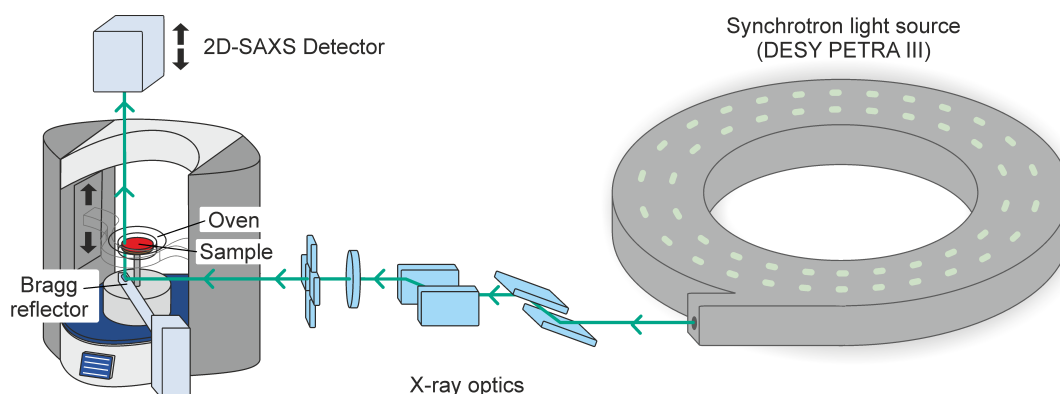


Figure 7.1: RheoSAXS set-up based on a stress-controlled Haake MARS II rheometer that was implemented into the beam path at beam line P10 of the German Electron Synchrotron (DESY). A unique feature of this set-up is the Ge333 reflector that guides the X-rays vertically to the detector, thereby allowing to maintain the horizontal shear flow direction of the rheometer.

Procedures

Quiescent and flow-induced crystallization of isotactic polypropylene were studied under isothermal conditions at temperatures of 130 – 140 °C. Prior to all crystallization experiments, the polypropylene samples were molten at 200 °C for 15 min to erase the thermal history. All polymer crystallizations were monitored by rheological time sweeps with low strain amplitude $\gamma_0 = 0.5\%$ and angular frequency $\omega = 1$ rad/s to detect the change in flow behavior without disturbing crystal formation. For all flow-induced crystallizations, a steady shear step was included right after the desired crystallization temperature was reached (Figure 6.2). Parallel-plate geometries (35 mm) with X-ray transmissive windows made from polyimide were used in the presented experiments. The X-ray beam size was $250 \times 250 \mu\text{m}$ and the position at $r = 14$ mm. The 2D-SAXS patterns were accumulated over 5 s and processed using *idltools* (Version 0.3, provided by A. Rothkirch, DESY, 2012). Upon complete crystallization, the semi-crystalline morphologies were analyzed using *ex-situ* scanning electron microscopy (SEM). All samples were etched with an acidic permanganate solution and coated with 2 nm Pt (see section 6.2, p. 96 for experimental details). SEM images were taken using a Zeiss Gemini/LEO 1530 system with 5 kV and 30/60 μm aperture.

Materials

As in chapter 6, the main material of investigation was a Ziegler-Natta polypropylene grade i-PP-1 (batch 1: $M_w = 246$ kg/mol, $\bar{D} = 2.7$). Additional experiments were performed on a metallocene-catalyzed polypropylene grade i-PP-2 ($M_w = 202$ kg/mol, $\bar{D} = 1.9$). Further information on the used materials can be found in section 2.4, p. 19.

7.3 Quiescent crystallization of isotactic polypropylene

The isothermal crystallization behavior of neat isotactic polypropylene i-PP-1 was investigated by simultaneous monitoring of the flow behavior via rheology and the emerging nano-scale morphology via 2D-SAXS. The sample was rapidly cooled from an isotropic melt (200 °C for 15 min) to the crystallization temperature $T_{\text{cryst}} \approx 138$ °C. In Figure 7.2, simultaneously measured moduli G' and G'' are plotted together with 2D-SAXS images recorded at 15, 30, 45, and 60 min, respectively. The 2D-SAXS image at 15 min was chosen as a background image to reveal the difference scattering pattern of the forming lamellar structure in contrast to the supercooled melt state. At the end of the crystallization, an isotropic ring was formed, indicating an unoriented sample morphology. Notably, the pattern at 30 min showed an increased intensity close to the beam stop at low q values, which points towards a process that preceded the nucleation of polymeric crystals. At the same time, the rheological moduli G' and G'' showed an increase and the expected hardening behavior with a crossover at $t \approx 40$ min. The final absolute G' and G'' values were lower compared to the experiments on the same polymer presented in chapter 6, which could have been a consequence of the large diameter (35 mm) in combination with the inherent compliance of the geometry.

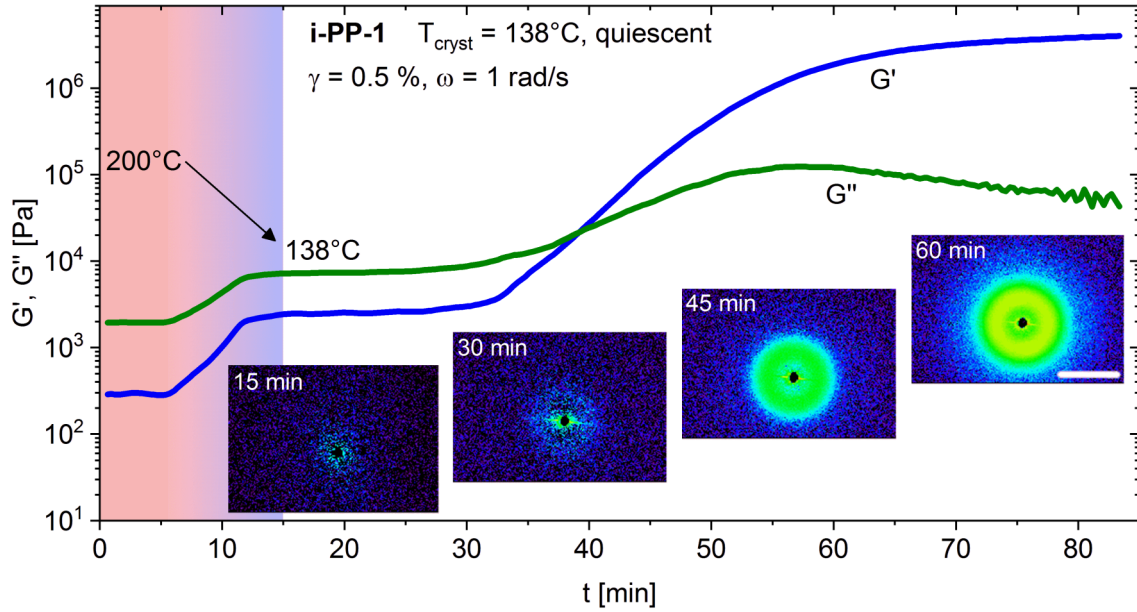


Figure 7.2: Simultaneously measured moduli G' and G'' plotted together with selected 2D-SAXS patterns for the quiescent crystallization of i-PP-1 at 138 °C (background image: 15 min, scale bar: 0.05/Å).

7.3.1 Quantitative analysis of the 2D-SAXS and rheology data

The radially averaged intensity profiles $I(q)$ shown in Figure 7.3 were extracted from the 2D-SAXS patterns acquired during quiescent crystallization of i-PP-1. The intensity of the reflex at $\sim 0.02/\text{Å}$, corresponding to the isotropic ring in Figure 7.2, increased strongly with crystallization time, whereas its position remained relatively constant. This type of scattering arises from the semi-crystalline substructure of the spherulites, which are being formed by radially growing lamellae (Baltá-Calleja and Vonk 1989).

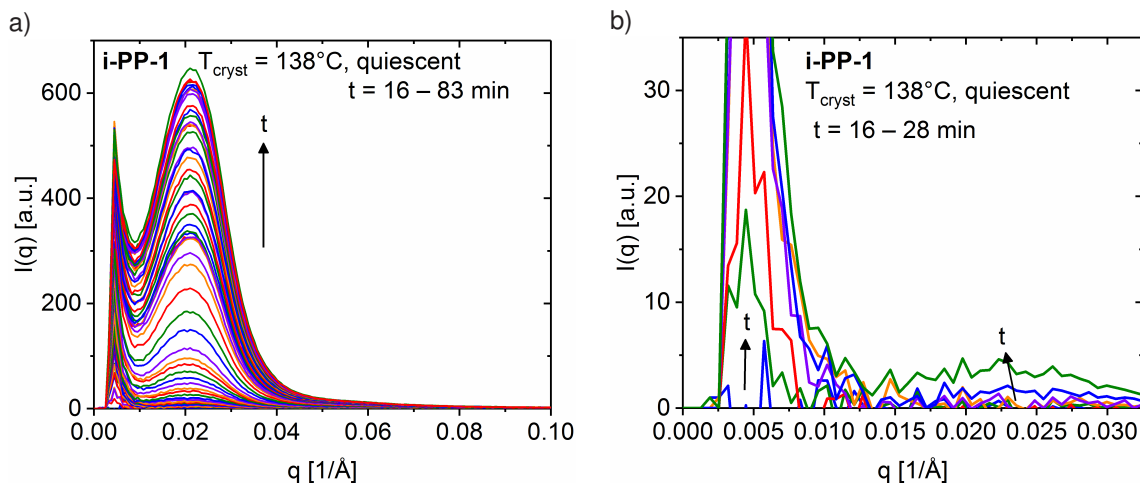


Figure 7.3: Radially averaged 2D-SAXS intensities $I(q)$ for the quiescent crystallization of i-PP-1 at 138 °C (a) and selected data for the initial pre-nucleation period (b). A substantial intensity increase for $q \leq 0.01/\text{Å}$ was observed before a reflex became visible at $q \approx 0.02/\text{Å}$.

A substantial intensity increase for $q \leq 0.01/\text{\AA}$ was observed before a reflex became visible at $q \approx 0.02/\text{\AA}$. This feature was seen by other researchers as discussed in subsection 3.3.4, p. 32 and could be rationalized by assuming long-range density fluctuations preceding crystal nucleation (Imai *et al.* 1994, 1995; Ezquerro *et al.* 1996). More recently, Hikosaka *et al.* (2003) suggested that the observed scattering is more likely a consequence of nuclei with a low degree of lamellar ordering. Potential density fluctuations were studied by e.g., Xiao and Akpalu (2007) and Baert and Van Puyvelde (2008), who came to the conclusion that the formation of small sheaf-like nuclei sufficiently well explain the observed phenomenon. To extract quantitative information on the dimensions of the growing lamellae, a Lorentz correction was performed by multiplying the intensities $I(q)$ with q^2 (Cser 2001). In Figure 7.4, the obtained corrected intensity profiles are shown for the entire crystallization process (a) and the initial nucleation period (b). The maxima were shifted to higher values of $q \approx 0.025/\text{\AA}$, corresponding to a long period $d = 2\pi/q \approx 250 \text{\AA}$, which was in the range of the lamellar substructure for this material as determined by scanning electron microscopy (see section 6.5, p. 124).

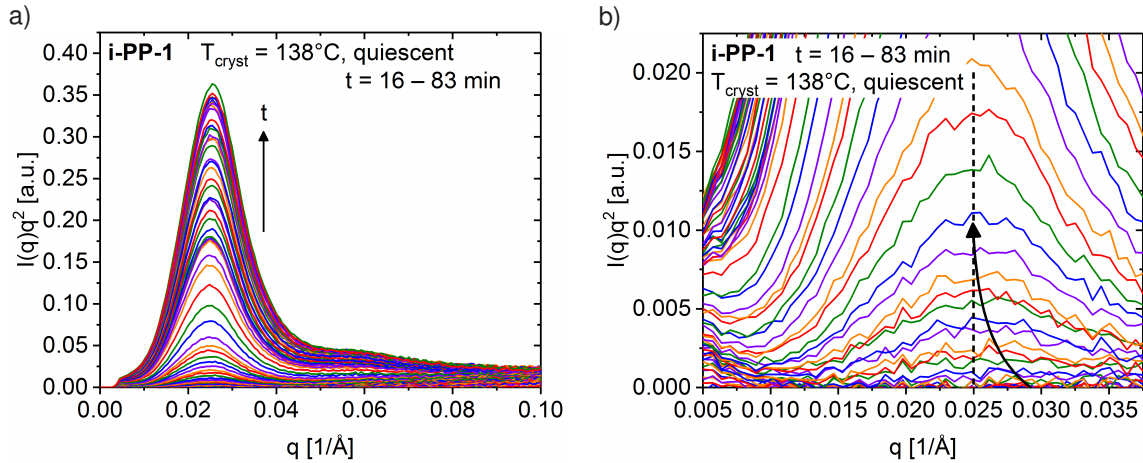


Figure 7.4: Evolution of the Lorentz-corrected intensity profiles $I(q)q^2$ for the entire crystallization process (a) and for the early stages of crystallization (b). An overall shift to higher q values was observed compared to the non-corrected intensity profiles of Figure 7.3.

By applying a Fourier transform to the baseline-corrected and smoothed intensity profile $I(q)q^2$ at the end of the crystallization (83 min), the correlation function $K(z)$ was obtained (see section 4.3, p. 61, especially Equation 4.58, p. 64). The correlation function $K(z)$ displayed a behavior that was characteristic for a lamellar system with certain variations in the spacing, thickness, and surface of the grown lamellae (Baltá-Calleja and Vonk 1989). As proposed by Strobl and Schneider (1980), the mean lamellar thickness \bar{L}_c was deduced from the intersection of a linear fit to the initial decay in Figure 7.5 (solid line) and the dashed horizontal line marking the minimum of the correlation function. The obtained value of $\bar{L}_c \sim 90 \text{\AA}$ was smaller than half of the long period $d \approx 250 \text{\AA}$, which possibly indicated an interphase of $20 - 30 \text{\AA}$ that marked the transition regime from the amorphous to the crystalline phase. However, the linear fit also depended on the selection of the fitting limits (here: 0 to 75\AA), causing an uncertainty of $\pm 10 \text{\AA}$ in the determination of the average lamellar thickness \bar{L}_c .

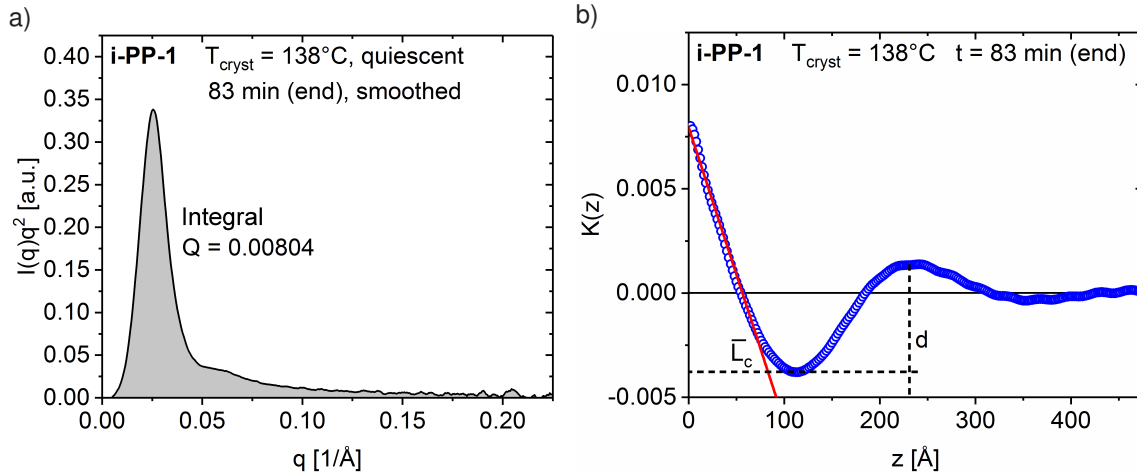


Figure 7.5: Integrated intensity profile $I(q)$ (baseline-corrected and smoothed using a 5-point moving average) for the end of the crystallization of i-PP-1 at 138°C (a) and the corresponding correlation function $K(z)$ (b).

7.3.2 Correlation of the SAXS invariants and the rheological parameters

As a quantitative measure of the evolving crystallinity, the normalized invariants Q_{norm} were calculated by integrating the Lorentz-corrected intensity profiles of Figure 7.4 from $0 - 0.1/\text{\AA}$ and normalizing the values to $[0,1]$:

$$Q = \int I(q)q^2 dq \quad (7.1)$$

The resulting buildup curve is shown in Figure 7.6a. The sigmoidal behavior was similar to the crystallinity curves in chapter 5 and chapter 6 as determined by NMR. However, a plateau at ~ 50 min ($Q_{\text{norm}} \approx 0.5$) was seen, which might have been the consequence of secondary crystallization and the associated decrease in scattering intensity due to the disruption of the periodic lamellar structure (Figure 7.6b). This cross-hatched morphology is frequently found for isotactic polypropylene and is assumed to be caused by the 3-1 helix chain structure.

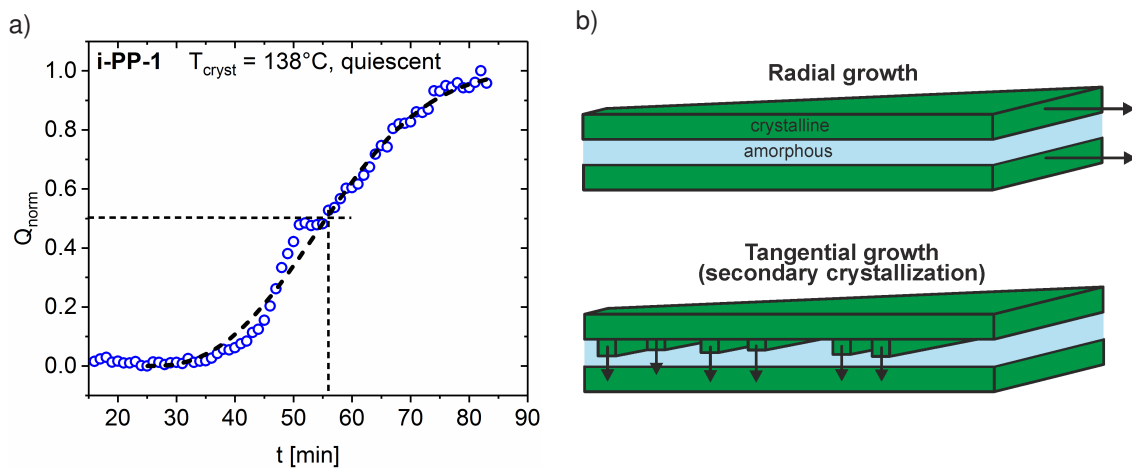


Figure 7.6: Normalized scattering invariant Q_{norm} for the crystallization of i-PP-1 at 138°C under quiescent conditions (a). Illustration of the growth processes in radial and tangential direction (b).

By plotting the reduced absolute complex viscosity $|\eta^*|/|\eta^*|_0$ as a function of the invariant Q_{norm} , a hardening curve was constructed (Figure 7.7a). Compared to the correlation plots determined by RheoNMR in the previous chapter (e.g., Figure 6.11), an increase of $|\eta^*|/|\eta^*|_0$ at lower values of Q_{norm} was observed. The extended Einstein model (Equation 6.7) was indicated by the dashed line, but could only roughly describe the hardening data. The loss tangent shown in Figure 7.7b displayed a decrease at low values of Q_{norm} , and the crossover of G' and G'' occurred at $Q \approx 0.06$. A reason for the different behavior compared to the results measured by RheoNMR could have been sensitivity towards periodic structures instead of the actual crystalline fraction. Furthermore, the position of the beam at the edge of the sample ($r = 14$ mm) in combination with the beam size of only 250×250 μm probed the material locally, whereas in the RheoNMR experiments a sample average was determined.

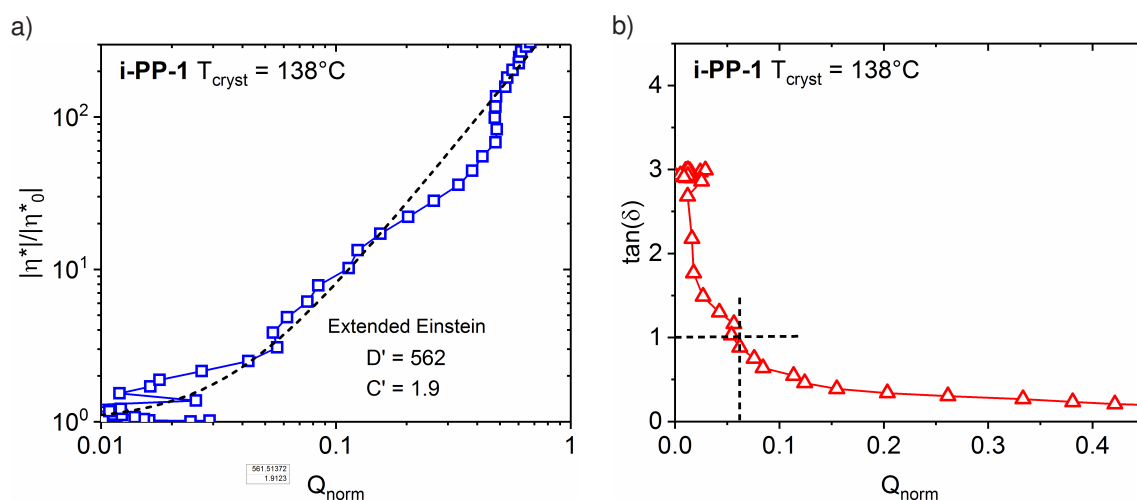


Figure 7.7: Reduced absolute complex viscosity $|\eta^*|/|\eta^*|_0$ (a) and loss tangent (b) vs. the normalized scattering invariant Q_{norm} for the quiescent crystallization of i-PP-1 at 138 °C. The absolute complex viscosity at 16 min was selected as $|\eta^*|_0$.

7.3.3 Effect of regio defects on the morphology under quiescent conditions

As in chapter 5 and chapter 6, the metallocene-catalyzed, regio-defective isotactic polypropylene i-PP-2 was analyzed with respect to its isothermal crystallization behavior using a similar RheoSAXS routine as for the Ziegler-Natta grade i-PP-1. In Figure 7.8, simultaneously acquired moduli G' and G'' are shown together with the evolution of the 2D-SAXS patterns. The crystallization was significantly slower compared to the experiments on i-PP-1 as indicated by the late rise in the moduli G' and G'' at an even lower crystallization temperature of $T_{\text{cryst}} \approx 132$ °C. Notably, the isotropic ring at $\sim 0.04/\text{\AA}$ was weak in intensity, indicating a low degree of periodic lamellar order. It appeared at an early stage of crystallization together with an increased scattering intensity at q values below $0.02/\text{\AA}$, where the moduli G' and G'' didn't show any significant rise yet. As this pattern persisted over the course of the crystallization it was likely caused by stacks of lamellae with a low periodicity and random orientation that still led to some degree of scattering rather than long-range density fluctuations as proposed by e.g., Imai *et al.* (1994); Ezquerro *et al.* (1996).

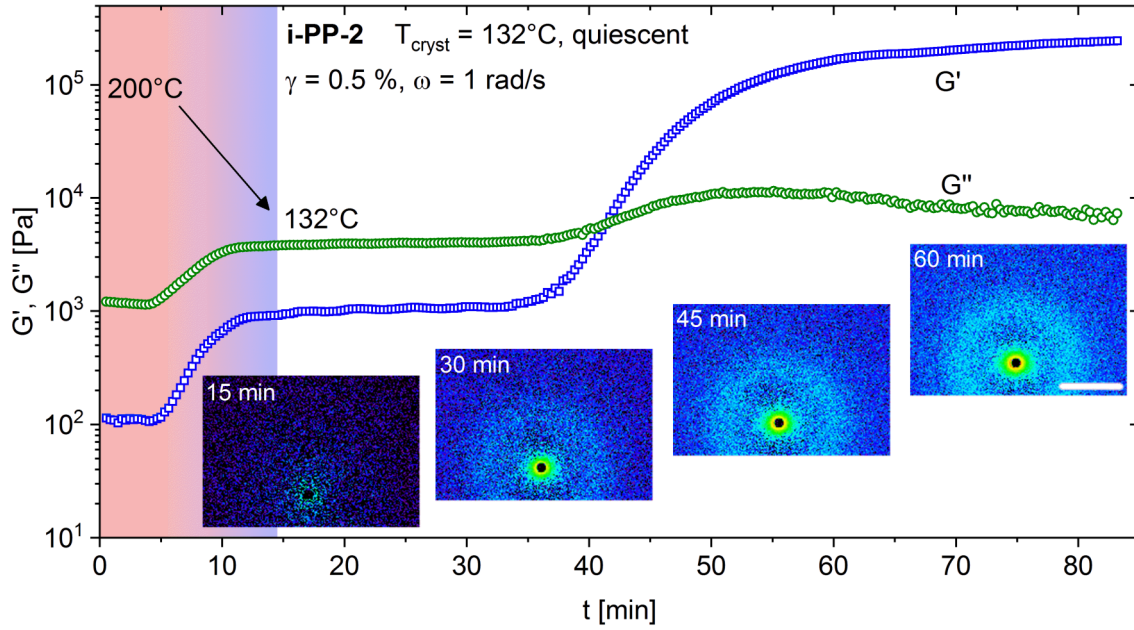


Figure 7.8: Simultaneously measured moduli G' and G'' plotted together with selected 2D-SAXS patterns for the quiescent crystallization of i-PP-2 at 132 °C (background image: 15 min, scale bar: 0.05/Å).

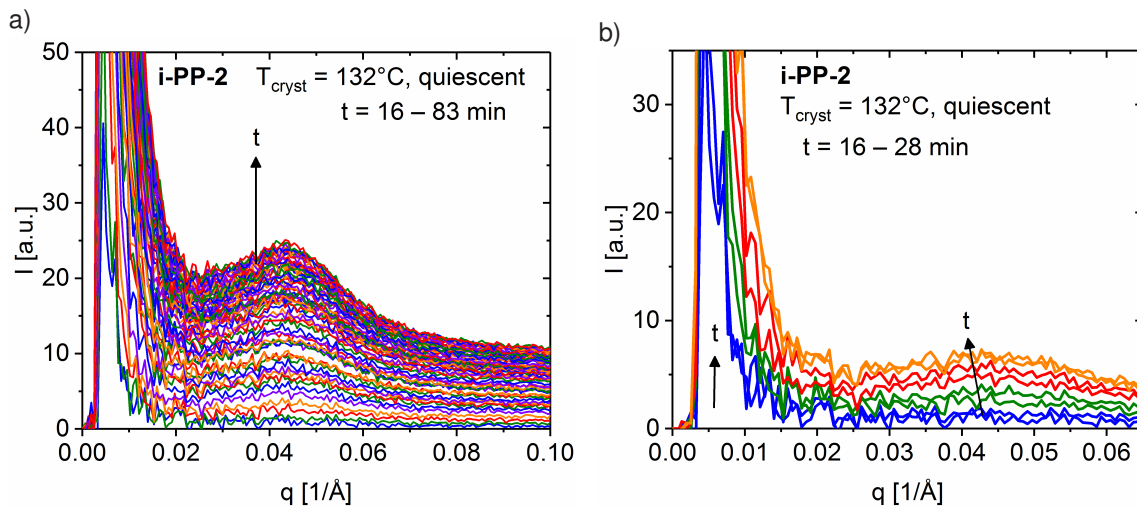


Figure 7.9: Radially averaged 2D-SAXS intensities $I(q)$ for the quiescent crystallization of i-PP-2 at 132 °C (a) and selected data for the initial pre-nucleation period (b). A substantial intensity increase for $q \leq 0.02/\text{Å}$ was observed before a reflex became visible at $q \approx 0.04/\text{Å}$.

A Lorentz correction was performed by multiplying the intensities $I(q)$ with q^2 to extract quantitative information on the dimensions of the grown lamellae. In Figure 7.10, the obtained corrected intensity profiles are shown for the entire crystallization process (a) and the initial nucleation period (b). The maxima were shifted to higher values of $q \approx 0.05/\text{Å}$, corresponding to a long period $d = 2\pi/q \approx 125 \text{ Å}$, which was half of the determined values for i-PP-1. A pronounced baseline drift was observed, potentially caused by the total increased scattering intensity that was independent of the q vector (light blue color in Figure 7.8).

Similarly to i-PP-1, the correlation function $K(z)$ was determined by applying a Fourier transform to the baseline-corrected and smoothed intensity profile $I(q)q^2$ at the end of the crys-

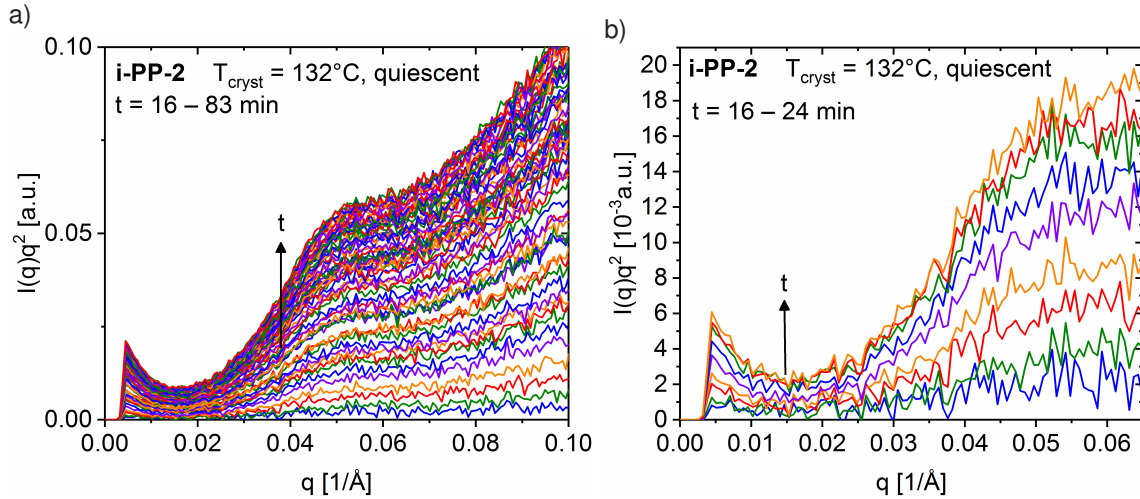


Figure 7.10: Evolution of the Lorentz-corrected intensity profiles $I(q)q^2$ for the entire crystallization process (a) and for the beginning of crystallization (b). A shift to higher maxima and a strong increase at higher q values was observed compared to the non-corrected intensity profiles of Figure 7.9.

tallization (Figure 7.11). It showed again an oscillating behavior that was characteristic for a lamellar system with certain variations in the spacing, thickness, and surface of the grown lamellae (Baltá-Calleja and Vonk 1989). As proposed by Strobl and Schneider (1980), the mean lamellar thickness \bar{L}_c was deduced from the intersection of a linear fit to the initial decay in Figure 7.5 (solid line) and the dashed horizontal line marking the minimum of the correlation function. The obtained value of $\bar{L}_c \sim 50 \text{ \AA}$ was smaller than half of the long period d , which could again indicate a potential interphase of $20 - 30 \text{ \AA}$ between the amorphous and the crystalline phase. As for i-PP-1, the linear fit also depended on the selection of the fitting limits (here: 25 to 50 \AA), causing an uncertainty of approximately $\pm 10 \text{ \AA}$ in the determination of the average lamellar thickness \bar{L}_c .

As a quantitative measure of the evolving crystallinity, the normalized invariants Q_{norm} were calculated by integrating the Lorentz-corrected intensity profiles of Figure 7.10 from $0.025 - 0.075/\text{\AA}$ and normalizing the values to $[0,1]$ (Equation 7.1, p. 137). The resulting buildup curve is shown in Figure 7.10b. Qualitatively, the curve was characterized by an almost immediate increase upon reaching the crystallization temperature at $t \approx 15$ min, indicating an instantaneous formation of some sort of a lamellar structure. Because of the rather low absolute scattering intensity compared to i-PP-1 that was potentially due to a low degree of periodicity, the invariant Q_{norm} was most probably not a quantitative measure of the total crystallinity for this polymer. The data shown in Figure 7.12a exhibited a rather uncorrelated behavior with an increase of the reduced absolute complex viscosity at high values for Q_{norm} . Consequently, the data was not well described by an extended Einstein model (Equation 6.7).

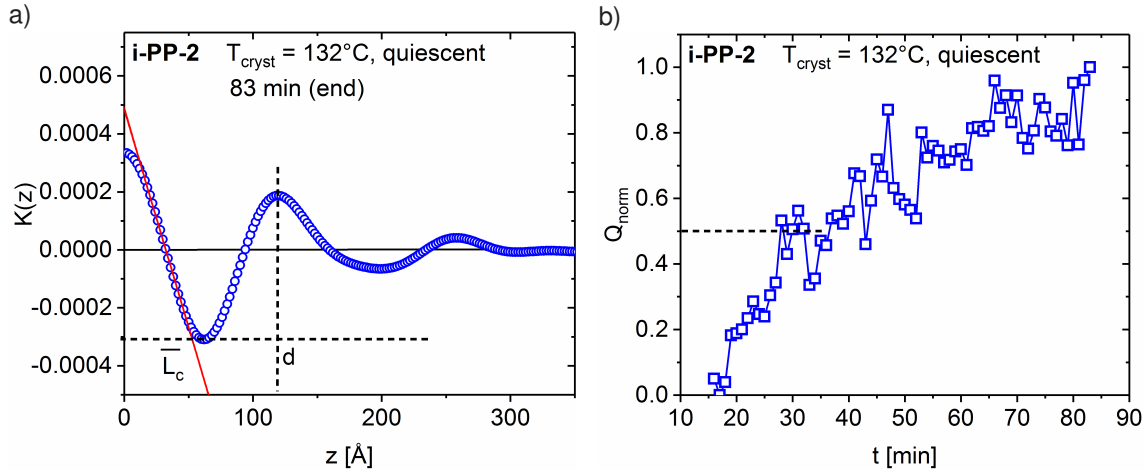


Figure 7.11: Correlation function $K(z)$ for the end of the crystallization of i-PP-2 at 132°C (a) and time evolution of the normalized scattering invariant Q_{norm} for the entire crystallization under quiescent conditions (b).

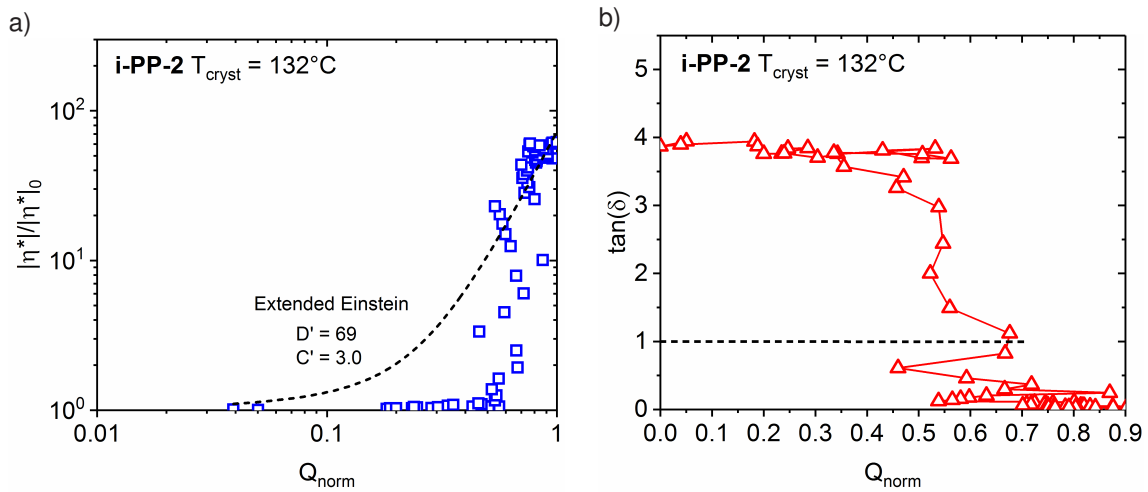


Figure 7.12: Reduced absolute complex viscosity $|\eta^*|/|\eta^*|_0$ (a) and loss tangent (b) vs. the normalized scattering invariant Q_{norm} for the quiescent crystallization of i-PP-2 at 132°C (a). The absolute complex viscosity at 16 min was selected as $|\eta^*|_0$.

7.4 Flow-induced crystallization of isotactic polypropylene

Applying flow during polymer crystallization is known to alter the semi-crystalline morphology as discussed in section 3.4, p. 38. As in chapter 6, the short-term shear protocol by Janeschitz-Kriegl (Figure 6.2) was employed to study the effects of flow independently from the chosen crystallization temperature. In Figure 7.13, rheological moduli G' and G'' (a) and the corresponding loss tangent (b) are plotted together with selected simultaneously acquired 2D-SAXS patterns (c). With increasing maximum shear rate a speed-up of crystallization was detected by the rheological parameters. All experiments under flow conditions exhibited dumbbell-shaped 2D-SAXS patterns, indicating the formation of anisotropic structures perpendicular to the flow direction. The corresponding q values were on the order of $0.02/\text{\AA}$ as for the quiescent case. Thus, the observed patterns were likely caused by lamellae that were grown perpendicular to the flow direction starting from flow-induced elongated nuclei.

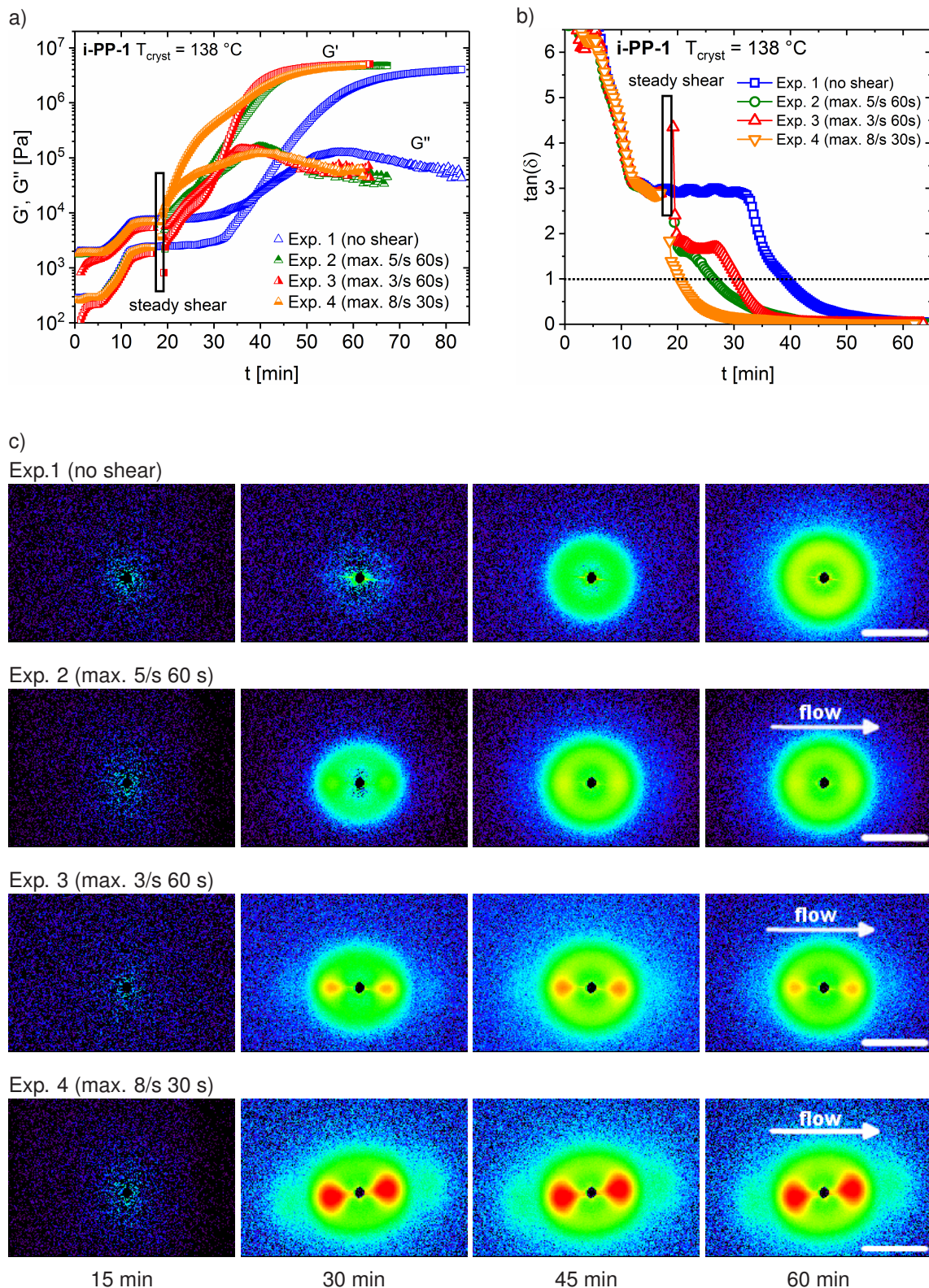


Figure 7.13: Simultaneously acquired moduli G' , G'' (a), the corresponding loss tangent (b), and selected 2D-SAXS patterns (c) for crystallizations of i-PP-1 at $138 \text{ }^\circ\text{C}$ under quiescent and flow conditions. A speed-up of crystallization with increasing maximum shear rate was detected by the rheological parameters. The 2D-SAXS data showed the formation of dumbbell-shaped patterns, indicating an anisotropic structure perpendicular to the flow direction (background images: 15 min, scale bar: $0.05/\text{\AA}$).

In contrast to the observed speed-up of crystallization with higher maximum shear rates as determined by a faster increase of G' and G'' , the 2D-SAXS patterns showed a different trend for the experiments at maximum shear rates of 5/s and 3/s. As the used stress-controlled rheometer needed some time to reach the desired shear rates, the actually applied shear rate and total strain during the initial 30 s were higher for the experiment at a maximum shear rate of 3/s (Figure 7.14). Likely, this fact led to a higher degree of conformational anisotropy and in the end a higher number of extended row nuclei for this experiment compared to the experiment at a maximum shear rate of 5/s. On the other hand, for the latter experiment an overall larger number of flow-induced nuclei (higher nucleation density) might have been attained because of the higher total strain. Further potential origins of this behavior include:

- A spatially inhomogeneous sample morphology which was probed locally by the X-ray beam of $250 \times 250 \mu\text{m}$ at $r = 14 \text{ mm}$ (however, the sample thickness was $\sim 1.5 \text{ mm}$, which should have been enough to provide an averaged signal);
- A loss of sample material at the probed position for the experiment at 5/s (however, the moduli at the end of the crystallization were similar to the other experiments);
- A pre-oriented state for the experiment at 3/s as indicated by the low moduli for $t \leq 5 \text{ min}$ (however, the longest relaxation times at the selected crystallization temperature of $138 \text{ }^\circ\text{C}$ are on the order of seconds as discussed in section 6.4, p. 116);

The difficulty in achieving steady shear using a stress-controlled rheometer could be overcome by applying a defined stress instead of a feedback-loop-controlled shear rate. However, as the granted beam time was limited, no such experiments could be conducted. In chapter 8, RheoMicroscopy experiments using the same stress-controlled rheometer are presented where controlled stresses were applied.

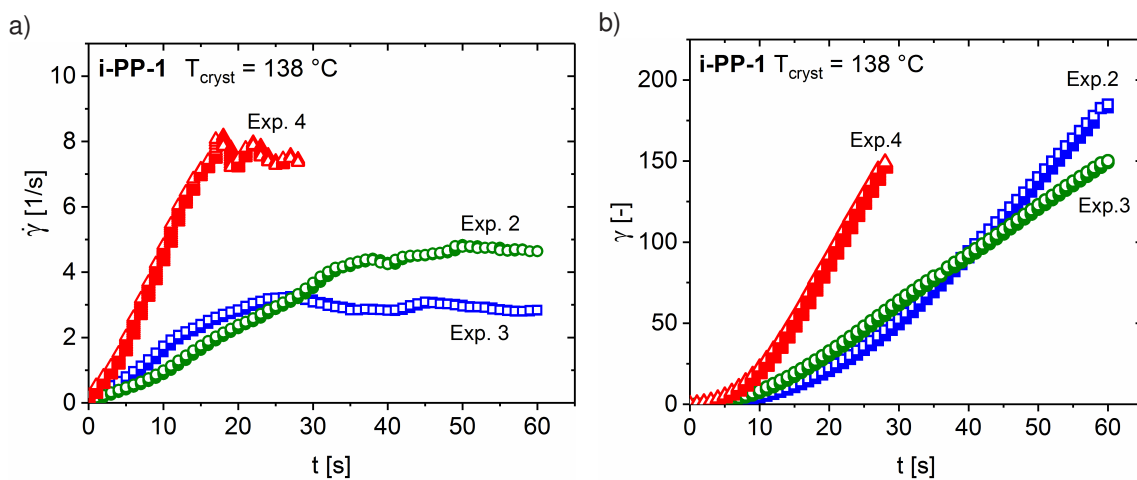


Figure 7.14: Applied shear rates (a) and total strains (b) during the short-term steady shear routine for the experiments in Figure 7.13. Notably, the experiment with a maximum shear rate of 3/s showed a higher shear rate and total strain during the initial 30 s compared to the experiments at a maximum shear rate of 5/s.

7.4.1 Quantitative analysis of the azimuthally integrated 2D-SAXS patterns

The acquired 2D-SAXS data was azimuthally integrated over a range of $0.01 \leq q \leq 0.03/\text{\AA}$ in order to extract information on the time evolution of the scattering patterns. In Figure 7.15, contour plots with identical scaling are shown for the experiments on i-PP-1 at 138 °C under different crystallization conditions (see Appendix A for the corresponding waterfall plots). In all experiments that contained short-term steady shear profiles (b – d), two characteristic stripes at $\chi_1 \approx 90^\circ$ and $\chi_2 \approx 270^\circ$ were observed, corresponding to the dumbbell patterns of Figure 7.13. Experiment 4 showed an immediate formation of this pattern upon the cessation of flow and its intensity remained almost constant over time. For experiments 2 and 3, these patterns were less pronounced and a time-wise buildup and decrease in scattering intensity was seen. The latter feature indicated a loss in anisotropy at later stages of the crystallization, which was possibly caused by a combination of secondary crystallization (cross-hatching) and a lower degree of orientation at the growth front further away from the nucleus (Kumaraswamy *et al.* 2004).

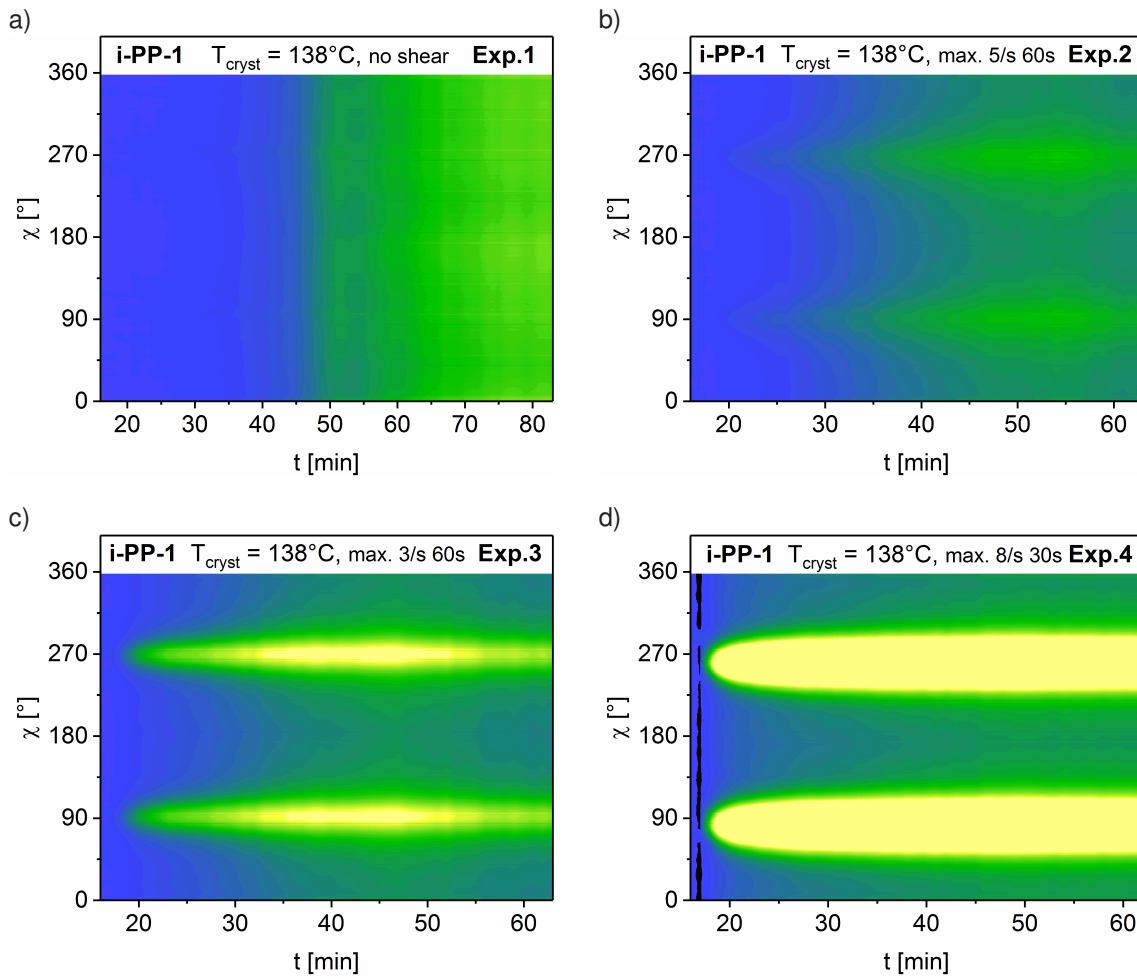


Figure 7.15: Evolution of the azimuthally integrated 2D-SAXS intensity profiles with identical scaling for crystallizations of i-PP-1 at 138 °C under different crystallization conditions. Background image: 15 min, integration from $0.01 \leq q \leq 0.03/\text{\AA}$.

Analyzing the time-dependent azimuthally integrated intensity profiles

All azimuthally integrated 2D-SAXS patterns obtained from experiments with applied flow profiles were smoothed using a 10-point moving average (adjacent averaging). Numerical fits were performed using Lorentzian functions to extract quantitative information on the time evolution of the peak widths, positions, and heights. As shown in Figure 7.16, all curves were sufficiently well described by two dedicated Lorentzian components:

$$I = \left(\frac{2A_1}{\pi} \right) \cdot \left(\frac{\Delta\chi_1}{4(\chi - \chi_1)^2 + (\Delta\chi_1)^2} \right) + \left(\frac{2A_2}{\pi} \right) \cdot \left(\frac{\Delta\chi_2}{4(\chi - \chi_2)^2 + (\Delta\chi_2)^2} \right) + I_0 \quad (7.2)$$

I : scattering intensity, I_0 : baseline intensity, A_1, A_2 : peak maximum intensities, χ_1, χ_2 : peak maximum positions, $\Delta\chi_1, \Delta\chi_2$: full width half maximum.

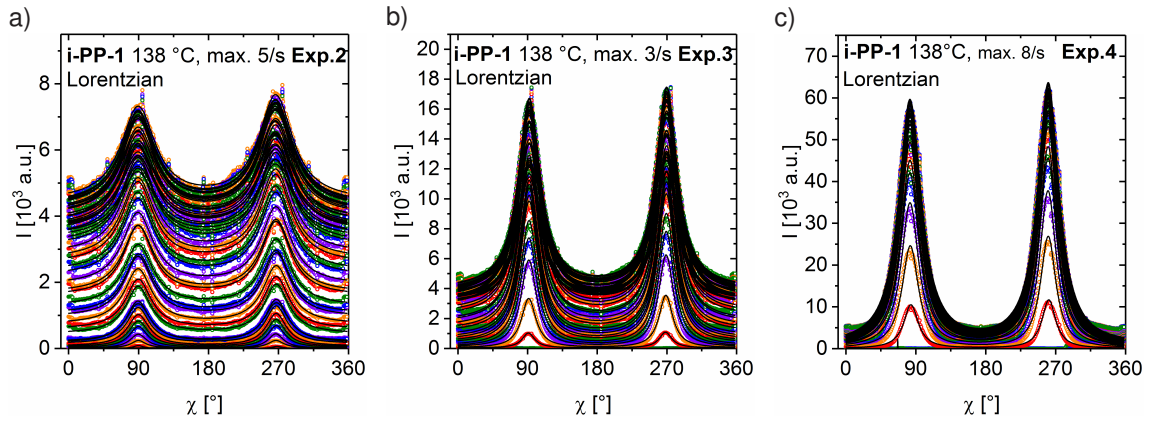


Figure 7.16: Lorentzian model fitted to the azimuthally integrated and smoothed intensity profiles for crystallization experiments of i-PP-1 at 138 °C under different flow conditions.

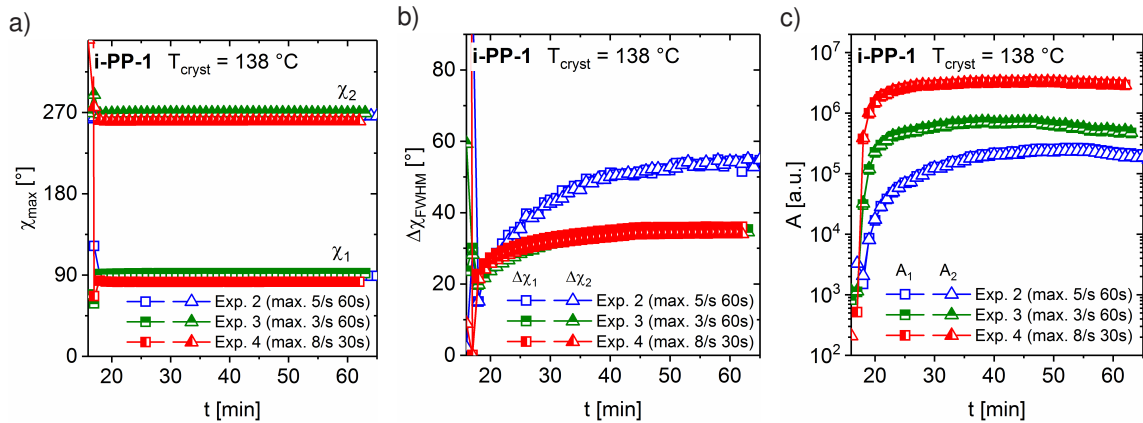


Figure 7.17: Fit parameters extracted from a peak analysis using two dedicated Lorentzian functions for crystallizations of i-PP-1 at 138 °C under different flow conditions.

The obtained results from the performed peak analysis are shown in Figure 7.17. For all experiments, the peak positions χ_1 and χ_2 remained constant over the entire crystallization process. Interestingly, the absolute χ values were lower for higher applied maximum shear rates, indicating a slightly different structural orientation. The respective peak widths $\Delta\chi$ became

larger with time as shown in Figure 7.17b, possibly because the degree of order further away from the induced nuclei was getting lower. The strongest broadening was seen for experiment 2, which might have been a result of the overall low degree of anisotropy.

Orientation analysis using Herman's orientation function

The flow-induced anisotropy during polymer crystallization as detected by the acquired 2D-SAXS patterns was further analyzed using Herman's orientation function (Hermans 1946; Wilchinsky 1968; White and Spruiell 1983):

$$F_H = \frac{3 \langle \cos^2 \phi \rangle - 1}{2} \quad (7.3)$$

F_H : orientation parameter, $\phi = \chi - 90^\circ$: orientation vector with respect to the flow direction.

Equation 7.3 was initially employed to describe the degree of orientation in drawn fibers by measuring their birefringence. As the periodicity of orientation phenomena is 180° , the second Legendre polynomial was chosen by Herman to obtain a quantitative measure of orientation (see section 4.2.1, p. 53 for the use of the second Legendre polynomial in the description of NMR dipolar coupling and chemical shift anisotropy). The average intensity term $\langle \cos^2 \phi \rangle$ in Equation 7.3 is given by the fraction of two $\sin \phi$ -weighted integrals over $d\phi$:

$$\langle \cos^2 \phi \rangle = \frac{\int I(\phi) \cos^2 \phi \sin \phi d\phi}{\int I(\phi) \sin \phi d\phi} \quad (7.4)$$

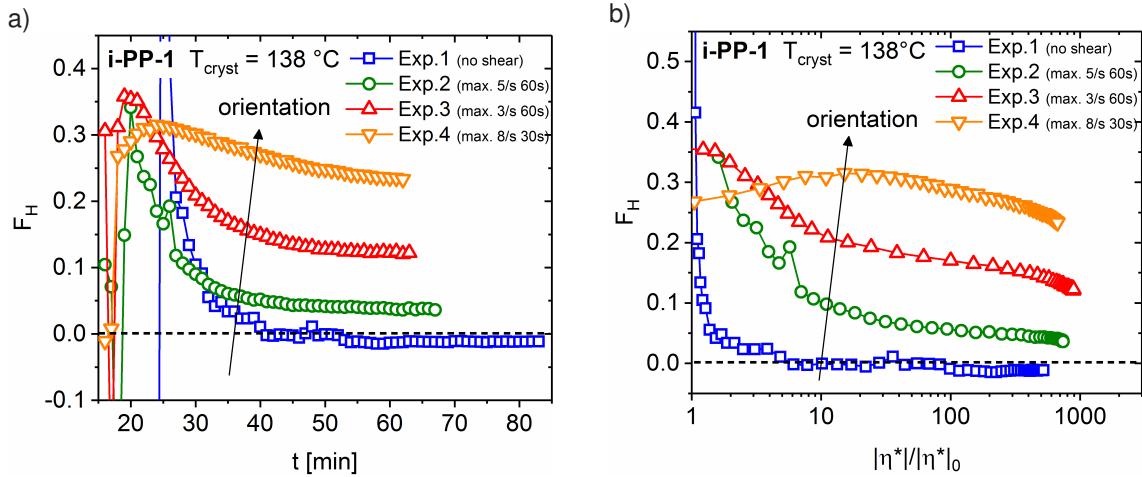


Figure 7.18: Herman's orientation parameter F_H vs. time t (a) and vs. the reduced absolute complex viscosity $|\eta^*|/|\eta^*|_0$ (b) for crystallizations of i-PP-1 at 138°C under quiescent and flow conditions.

In Figure 7.18a, the obtained orientation parameters F_H for the crystallization experiments of i-PP-1 under different conditions are plotted against time. Experiment 4 with a maximum shear rate of 8/s and the strongest overall scattering intensity showed the highest degree of orientation and a slight decrease with crystallization time. Lower degrees of orientation

were seen for the other experiments, with the experiment under quiescent conditions exhibiting a final plateau value of $F_H \approx 0$ as expected. In Figure 7.18b, all obtained orientation parameters were correlated with the reduced absolute complex viscosity. During the initial period of $1 \leq |\eta^*|/|\eta^*|_0 \leq 10$, experiments 1 – 3 showed a rapid decrease in F_H , whereas for $10 \leq |\eta^*|/|\eta^*|_0 \leq 1000$ only a minor loss in orientation was detected. The data for experiment 4 had a maximum at $|\eta^*|/|\eta^*|_0 \approx 10$, and followed the decreasing trend of the other experiments at higher values of $|\eta^*|/|\eta^*|_0$. Interestingly, all experiments including the one under quiescent conditions showed a high level of orientation for $t \approx 20 - 30$ min. Generally, even experiments under nominally quiescent conditions show some form of inherent local flow due to convection upon cooling. Thus, the observed high degrees of orientation at the beginning of all crystallization processes might have originated from the alignment of anisotropic nuclei at the very early stages of polymer crystallization (see section 8.3, p. 159 on RheoMicroscopy).

7.4.2 Effect of regio defects on the flow-induced semi-crystalline morphology

In addition to the investigations of the regio-defective grade i-PP-2 under quiescent conditions presented in section 7.3, also experiments with applied flow profiles were performed. In Figure 7.20, acquired rheological moduli G' and G'' (a) and the corresponding loss tangent (b) are plotted together with selected simultaneously acquired 2D-SAXS patterns (c). An intense cross-shaped pattern at q values below $0.02/\text{\AA}$ was formed, which was different from the dumbbell 2D-SAXS patterns that were observed for i-PP-1. As discussed in the previous section, the used stress-controlled rheometer needed some time to reach the desired shear rates due to its feedback-loop for the application of certain shear conditions. In Figure 7.19, the applied shear rate $\dot{\gamma}$ and the absolute shear deformation γ are plotted against time for experiments 6 and 7. The raw data for exp. 7 was smoothed using a 30-point moving average. In both cases, steady-state conditions were reached after approximately 20 s.

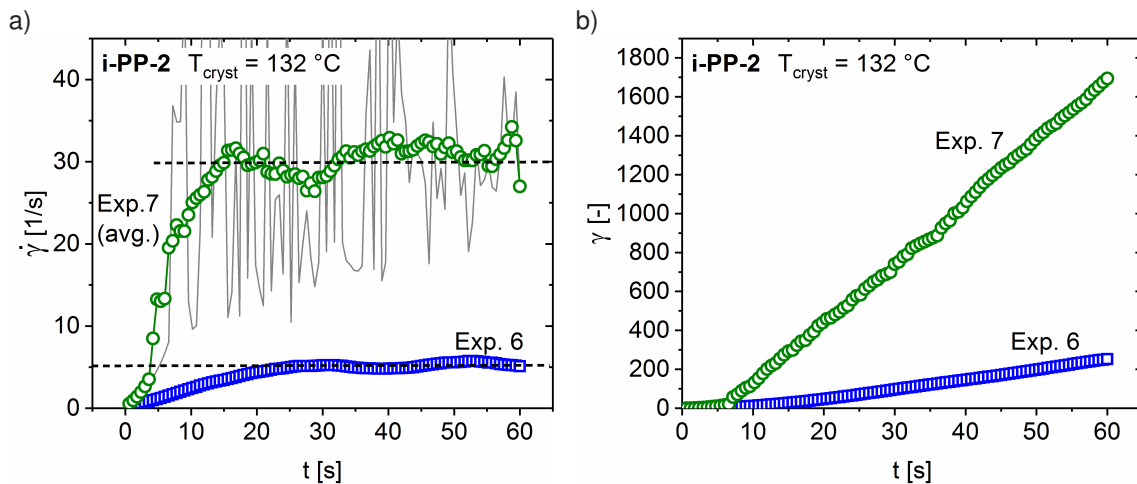


Figure 7.19: Applied shear rates (a) and total strains (b) during the short-term steady shear routine for the experiments in Figure 7.20.

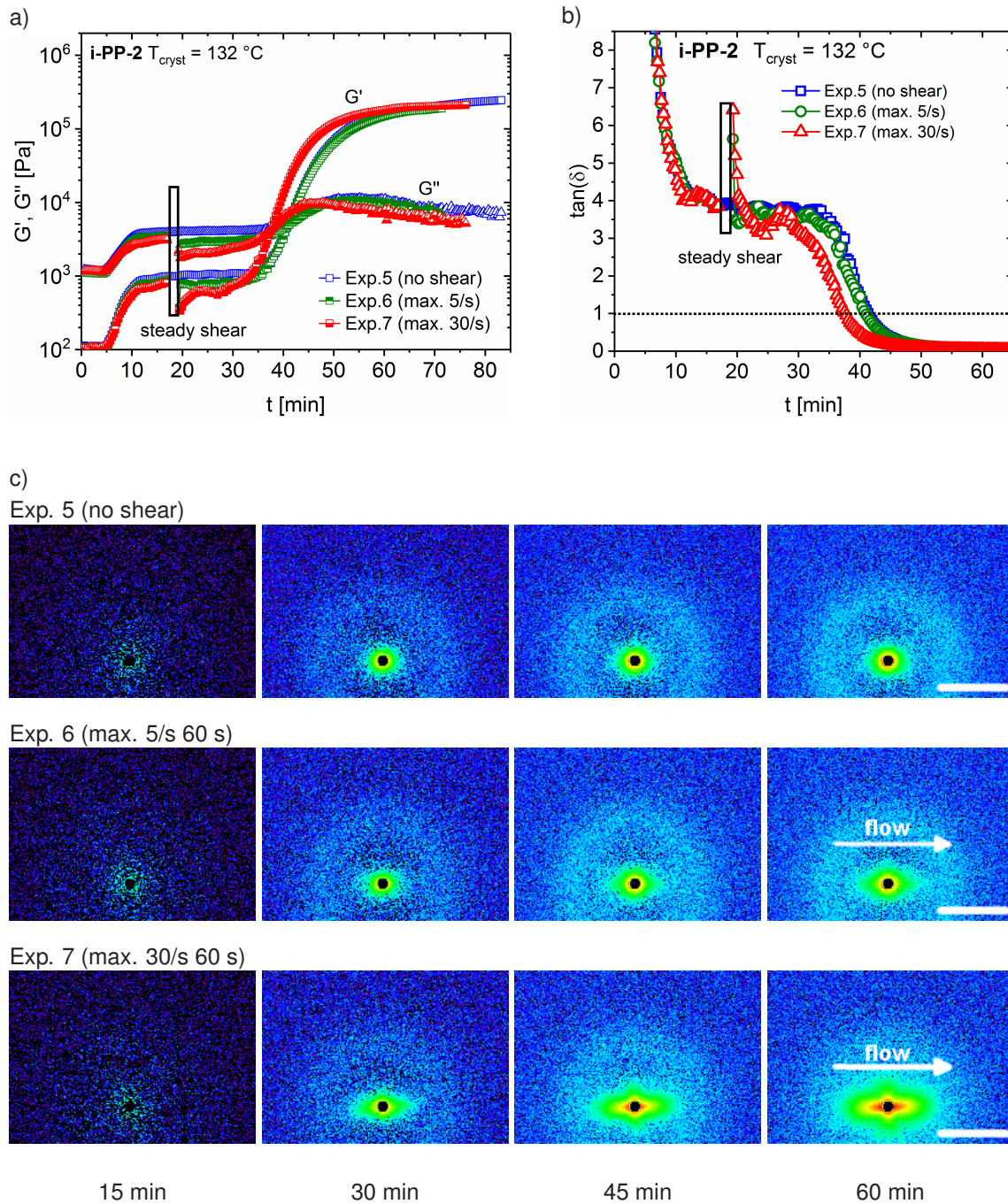


Figure 7.20: Simultaneously acquired moduli G' , G'' (a), the corresponding loss tangent (b), and selected 2D-SAXS patterns (c) for crystallizations of i-PP-2 at $132\text{ }^{\circ}\text{C}$ under quiescent and flow conditions. A speed-up of crystallization with increasing maximum shear rate was detected by the rheological parameters. The 2D-SAXS data showed the formation of cross-shaped patterns at low q values, indicating a certain degree of orientation parallel and perpendicular to the flow direction (background images: 15 min, scale bar: $0.05/\text{\AA}$).

The 2D-SAXS patterns were azimuthally integrated over a range of $0.005 \leq q \leq 0.02/\text{\AA}$ in order to extract information on the evolution of the formed patterns with time. In Figure 7.21, contour plots are shown for the experiments on i-PP-2 at $132\text{ }^{\circ}\text{C}$ under different crystallization conditions. In all experiments that contained short-term steady shear profiles (b – c), characteristic patterns at $\chi_1 \approx 90^{\circ}$ and $\chi_2 \approx 270^{\circ}$ were observed, corresponding to the equa-

torial part of the cross-shaped patterns as displayed in Figure 7.20. The meridional part was visible for experiment 7 by an increased intensity at $\chi_3 \approx 0^\circ$ and $\chi_4 \approx 180^\circ$. Different from the experiments on i-PP-1, the patterns showed up some time after the cessation of flow and increased gradually in intensity with time. Interestingly, also the experiment under quiescent conditions (Figure 7.21a) displayed an increased intensity at 90° and 270° , corresponding to the non-symmetric pattern in Figure 7.20.

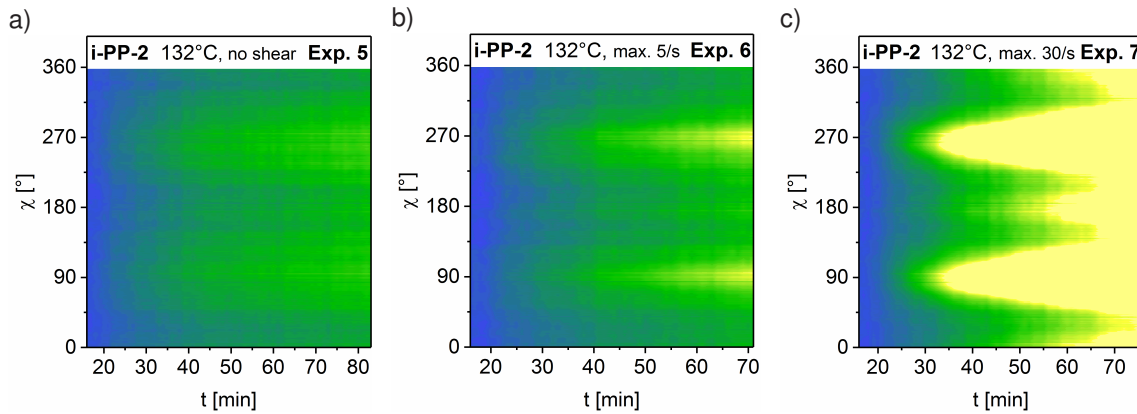


Figure 7.21: Evolution of the azimuthally integrated 2D-SAXS intensity profiles with identical scaling for crystallizations of i-PP-2 at 132 °C under different crystallization conditions.

Analyzing the time-dependent azimuthally integrated intensity profiles

All azimuthally integrated 2D-SAXS intensity profiles including the experiment under quiescent conditions were smoothed using a 10-point moving average (adjacent averaging). Numerical fits were performed on the equatorial peaks at $\chi_1 \approx 90^\circ$ and $\chi_2 \approx 270^\circ$ using Lorentzian functions to extract quantitative information on the time evolution of the peak widths, positions, and heights (Equation 7.2). As shown in Figure 7.22, the equatorial peaks were sufficiently well described by two dedicated Lorentzian components for all curves.

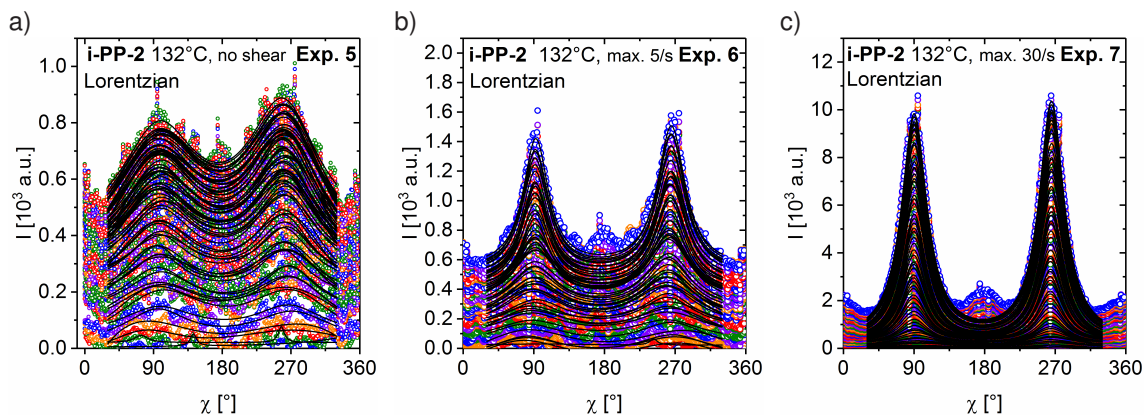


Figure 7.22: Lorentzian model fits to the azimuthally integrated intensity profiles for crystallizations of i-PP-2 under different conditions.

The obtained results from the performed peak analysis are shown in Figure 7.23. For all experiments, the peak positions χ_1 and χ_2 remained constant over the entire crystallization process. The absolute χ values were lower for higher applied maximum shear rates, indicating a slightly different structural orientation. The respective peak widths $\Delta\chi$ became larger with time as shown in Figure 7.23b, possibly because the degree of order further away from the induced nuclei was getting lower (lamellar splaying). The strongest broadening was seen for experiment 2, which might have been a result of the overall low degree of anisotropy as indicated by the lowest final scattering intensity A (Figure 7.23c).

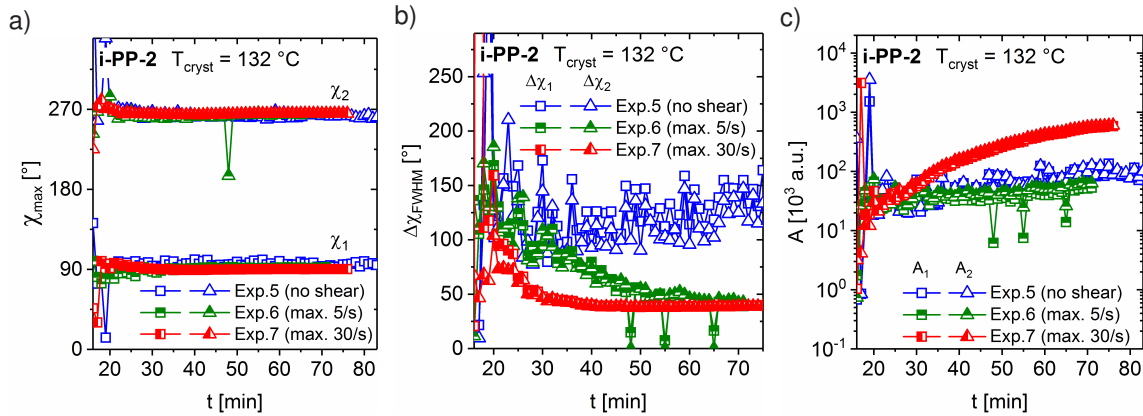


Figure 7.23: Fit parameters extracted from a peak analysis using two dedicated Lorentzian functions for crystallizations of i-PP-2 at 132 °C under different conditions.

Orientation analysis using Herman's orientation function

For all experiments on i-PP-2, an analysis using Herman's orientation function (Equation 7.3 and Equation 7.4) was performed. Similarly to the experiments on the Ziegler-Natta grade i-PP-1 (Figure 7.18), experiments 5 and 6 showed a loss in orientation for $t \approx 20 - 30$ min (Figure 7.24a). The observed high degrees of orientation at the beginning of the crystallization process might again have been a consequence from locally induced oriented nuclei.

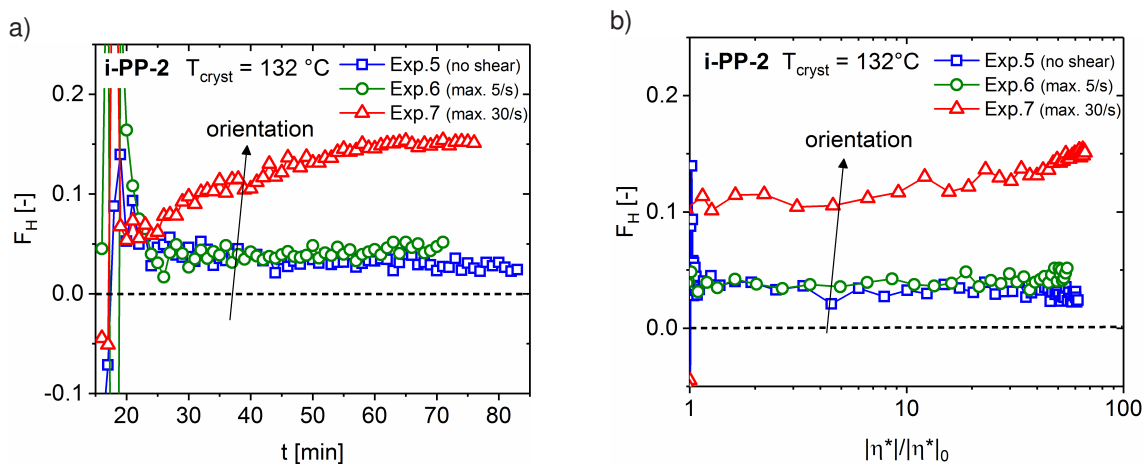


Figure 7.24: Herman's orientation parameter F_H vs. time t (a) and vs. the reduced absolute complex viscosity $|\eta^*|/|\eta^*|_0$ (b) for crystallizations of i-PP-2 at 132 °C under quiescent and flow conditions.

The experiment with a maximum shear rate of 30/s showed the highest degree of orientation at later stages of the crystallization process and no decrease, which was different from experiment 4 on i-PP-1. In Figure 7.24b, all obtained orientation parameters F_H were correlated with the reduced absolute complex viscosity. All curves stayed relatively constant over the crystallization process, which was different from the results for i-PP-1. The high nucleation density of the metallocene-catalyzed grade i-PP-2 in combination with applied flow fields possibly led to a very locally ordered morphology instead of large extended row-nucleated structures as in the case of i-PP-1.

7.5 Morphology investigations using scanning electron microscopy

To further investigate the effects of different flow profiles on the nano-scale morphology of isotactic polypropylene, scanning electron microscopy (SEM) was carried out on the recovered specimen upon complete crystallization as in section 6.5, p. 124. All samples were etched prior to SEM using an acidic permanganate solution as described by Sawyer *et al.* (2008) (experimental details were given in section 7.2). The images were recorded at a position of ~ 3 mm from the edge of the sample where the X-ray beam penetrated the material. On the following pages, only micrographs from experiments with applied flow profiles will be discussed (see section 6.5, p. 124 and Appendix A for images of quiescently crystallized samples).

The analysis of the sample from experiment 3 with a maximum shear rate of 3/s confirmed an increased nucleation density with spherulite sizes of $\sim 20 - 30 \mu\text{m}$ compared to the quiescently crystallized i-PP-1 sample (Figure 7.25, compare with section 6.5, p. 124). Furthermore a relatively small number of elongated, but still spherulitic structures was observed. Some cross-hatching was visible, especially further away from the row nucleus. This feature is known to be caused by the large splaying angle of $\sim 90^\circ$ in isotactic polypropylene due to the 3-1 helix structure and might explain the decrease in scattering intensity at later stages of the crystallization process. Unfortunately, no *ex-situ* scanning electron microscopy could be conducted on the sample from experiment 2 as it was molten prior to experiment 3, thereby preventing a direct comparison of the obtained morphologies for these two experiments.

The recovered specimen from experiment 4 (max. 8/s for 30 s) which showed the highest degree of orientation had a substantially increased nucleation density with very small spherulite sizes of $\sim 10 - 20 \mu\text{m}$ (Figure 7.26). Extended row-nucleated structures (cylindrites) were found throughout the sample with a strong directional orientation of the grown lamellae perpendicular to the flow direction. Likely, this structural motif caused the observed dumbbell-shaped scattering pattern.

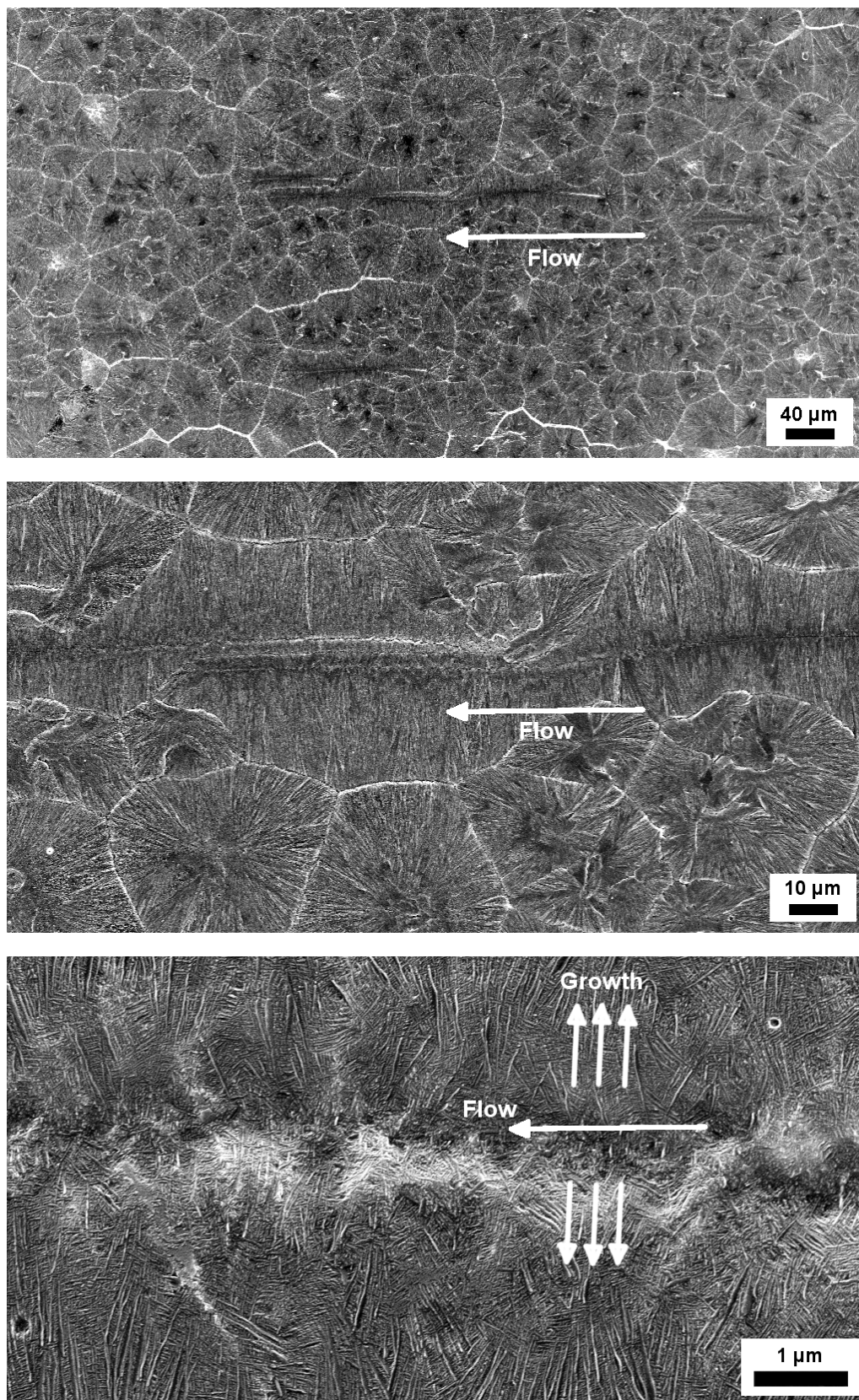


Figure 7.25: SEM images at different magnifications of etched i-PP-1 crystallized at 138 °C under flow (exp. 3, max. 3/s 60 s).

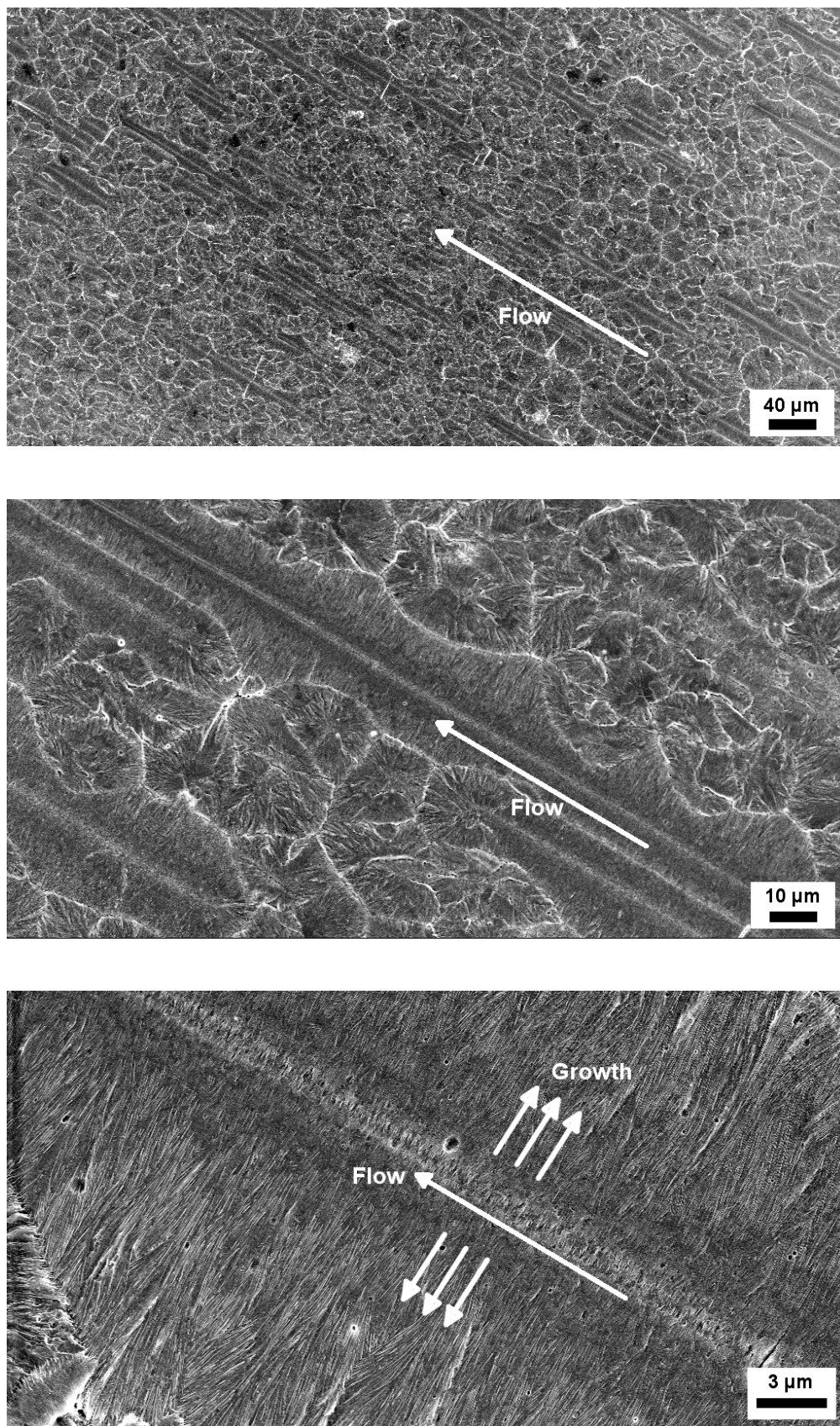


Figure 7.26: SEM images at different magnifications of etched i-PP-1 crystallized at 138 °C under flow (exp. 4, max. 8/s 30 s).

The regio-defective grade i-PP-2 sample from experiment 7 (max. 30/s 60 s) exhibited an extremely high nucleation density with spherulite sizes below 10 μm (compare with Figure 6.34 in section 6.5, p. 124). Thus, the application of flow further increased the already inherently high nucleation density due to the 1 mol% of 2,1-erythro regio defects. A strongly cross-hatched micro-structure was observed, which might explain the overall low scattering intensity due to a disruption of the periodic lamellar structure as illustrated in Figure 7.6. No long-extending row-nucleated structures with perpendicularly grown lamellae as in the case of i-PP-1 were clearly visible. Consequently, the cross-shaped scattering pattern and the increased degree of orientation probably resulted from an average alignment of the lamellae rather than from a particular structural motif.

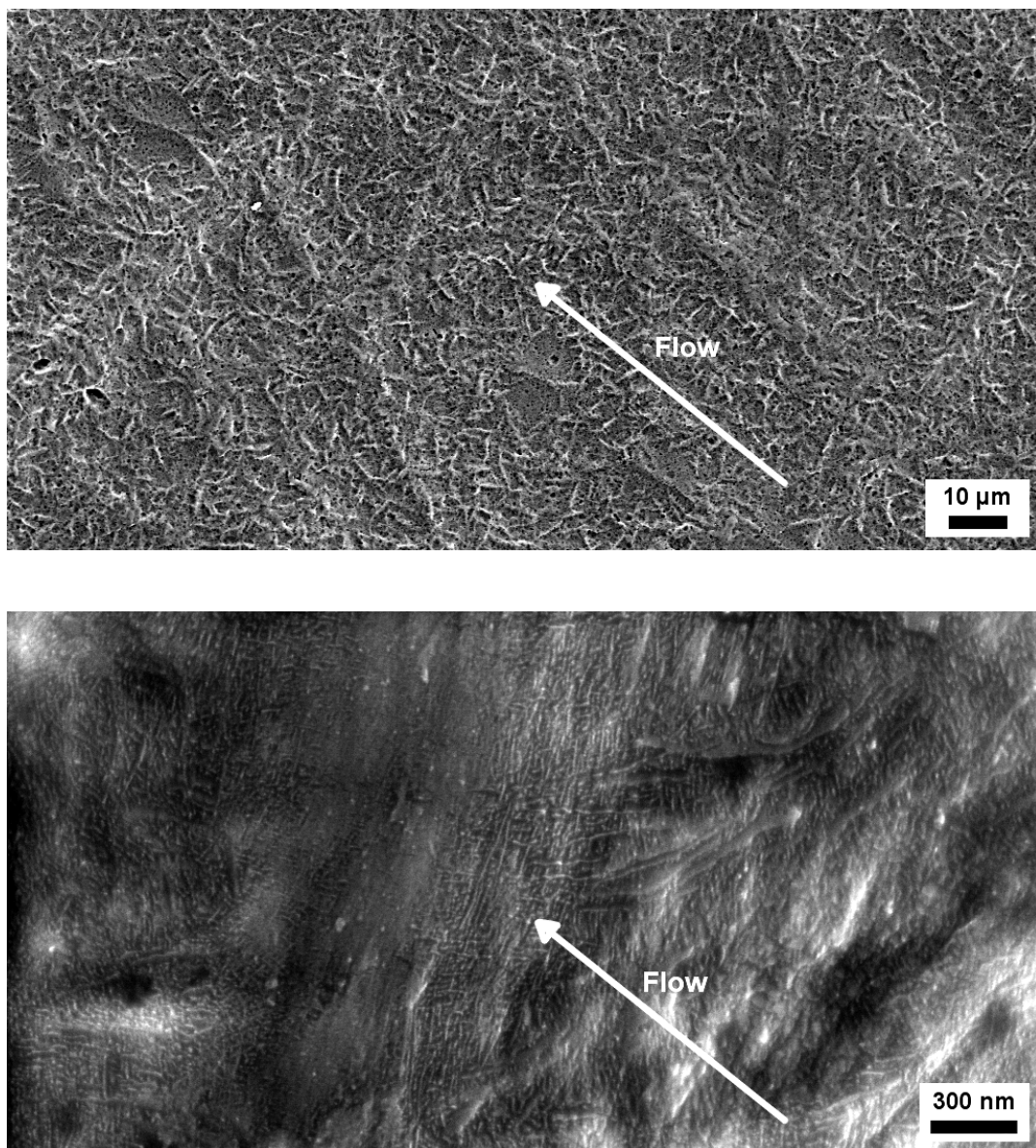


Figure 7.27: SEM images of etched i-PP-2 crystallized at 132 $^{\circ}\text{C}$ under flow conditions (exp. 7, max. 30/s 60 s).

7.6 Concluding remarks

In this chapter, the nano-scale morphology and rheology of isotactic polypropylene during crystallization under quiescent and flow conditions was investigated using hyphenated RheoSAXS. The vertical set-up was based on a commercial stress-controlled shear rheometer that was integrated into a reflected X-ray beam path of beam line P10 at the German Electron Synchrotron (DESY). All works were carried out in collaboration with Dr. Eric Stellamanns and Dr. Michael Sprung (both DESY, Hamburg, Germany).

Under quiescent crystallization conditions, the tested Ziegler-Natta and metallocene-catalyzed polypropylene grades showed the formation of ring-type scattering patterns, indicating an isotropic orientation of the grown lamellae. From the scattering curves of the fully crystallized samples correlation functions based on a lamellar scattering model were deduced and lamellar thicknesses in the range of ~ 9 nm for the Ziegler-Natta grade and ~ 5 nm in case of the metallocene-catalyzed grade were determined. As in both cases the long period was larger than twice the lamellar thickness ($d \approx 25$ nm (ZN) and 13 nm (metalloc.)), a potential interphase of 2 – 3 nm between the crystalline and amorphous domains seemed plausible. The early stages of crystallization were characterized by an increase in scattering intensity at low scattering vectors that were most probably caused by the formation of nuclei instead of long-range density fluctuations as will be discussed in chapter 8. Correlating the calculated SAXS invariants with the simultaneously measured reduced absolute complex viscosities during isothermal polymer crystallization led to noisy hardening curves compared to the results obtained by RheoNMR in chapter 6. Ultimately, the SAXS invariants were not found to provide a quantitative measure of crystallinity as the sample was probed locally and secondary crystallization decreased the absolute scattering intensity.

Flow-induced crystallization of isotactic polypropylene was studied using short-term steady shear profiles as in chapter 6. Because a stress-controlled rheometer was used, achieving the desired shear rates and steady-state conditions during the startup phase required 20 to 40 s depending on the chosen maximum shear rate. The lower degree of orientation for the experiment at a maximum applied shear rate of 5/s compared to an experiment at 3/s could be explained by the actually applied higher shear rates during the initial startup phase. For all pre-shear experiments, an overall increase in the speed of crystallization was detected by the rheological parameters and the appearance of anisotropic scattering patterns. The Ziegler-Natta grade showed characteristic dumbbell patterns soon after the cessation of flow that were likely caused by lamellae perpendicular to the applied flow direction. On the other hand, the metallocene-catalyzed, regio-defective material displayed cross-type patterns that might have originated from an average orientation of the fine cross-hatched microstructure. Herman's orientation function was employed to quantify the degree of orientation, independent of the absolute scattering intensity. The analysis revealed a certain degree of structural anisotropy at the early stages of polymer crystallization ($F_H \approx 0.3$), even for the experiment under quiescent conditions. A potential explanation is that convection upon cooling caused an alignment of

sheaf-like nuclei. When correlated with the simultaneously measured reduced absolute complex viscosity, a decrease in the average degree of orientation over the entire crystallization process was observed for the Ziegler-Natta grade, whereas for the metallocene-catalyzed grade it stayed almost constant. The obtained sample morphologies were further evaluated using *ex-situ* scanning electron microscopy, confirming a substantially higher nucleation density with small spherulites in the sheared samples (diameter: $\sim 10 - 20 \mu\text{m}$ for the highest shear rate). Row-nucleated structures were observed for the Ziegler-Natta grade that was subjected to the highest shear rate, which were $100 - 150 \mu\text{m}$ long and most certainly the origin of the measured strong anisotropic scattering. For the regio-defective grade, a highly cross-hatched morphology was found that explained the overall lower scattering intensities.

Hyphenated RheoSAXS provided correlated information on the effects of flow on the nano-scale morphology and related rheology of semi-crystalline polymers, which was not directly accessible before. By applying different flow conditions, we identified highly anisotropic structures as a potential cause for the observed strong increase in absolute viscosity at the early stages of the crystallization process, which supports the findings in the chapter on RheoNMR. The degree of orientation as quantified by Herman's orientation function F_H served as a sensitive measure for the relative number and dimensions of oriented lamellar structures. In future experiments, switching to applied stresses instead of shear rates would further enhance the comparability of the results as the used rheometer was a stress-controlled Thermo Haake MARS II. Furthermore, experiments using monodisperse polymers of different molecular weights would help to further clarify the mechanism between the imposed flow and the formed row-nucleated morphologies.

8 Relationship between Microstructure and Rheology in Polymer Crystallization: RheoMicroscopy

The following chapter contains results from simultaneous optical RheoMicroscopy investigations on the microstructure and rheology during quiescent and flow-induced polymer crystallization. All experiments were carried out in collaboration with Dr. Eric Stellamanns (German Electron Synchrotron (DESY), Hamburg, Germany). The effect of flow profiles on polymer crystallization with respect to the changes in the microstructure and rheology will be presented and compared against the results from RheoNMR (chapter 6) and RheoSAXS (chapter 7).

8.1 Introduction

Rheo-optical set-ups based on microscopy, scattering, or absorption of visible light in combination with flow cells and rheometers have been extensively used in the past to study soft matter. Reviews of different rheo-optical set-ups and their application can be found in texts by e.g., Fuller (1995), Wagner (1998), and Janeschitz-Kriegl (2012). As oftentimes micron-sized structural features determine the observed flow behavior of complex materials, simultaneous investigations of microstructure and rheology have been performed on suspensions (Champion *et al.* 1996; Paulin *et al.* 1997), emulsions (Montesi *et al.* 2004; Kawaguchi and Kubota 2004), or liquid crystals (Berghausen *et al.* 1997; Onogi and Asada 1980; Walker *et al.* 1997). Furthermore, experiments on amorphous polymeric material systems such as polymer solutions (Bossart and Oettinger 1995; Friedenbergl *et al.* 1996; Kume *et al.* 1997; Pathak and Hudson 2006), block copolymers (Chen and Kornfield 1998; Kannan and Kornfield 1994), and polymer melts (Dietz *et al.* 1978; Lee and Mackley 2001) have been carried out to investigate the effects of flow on the conformation of polymeric chains.

The structural buildup of semi-crystalline polymers under quiescent crystallization conditions has been studied to investigate the relationship between the microstructure and hardening behavior of crystallizing polymers by e.g., Pogodina *et al.* (1999, 2001), Elmoumni *et al.* (2003), and Pantani, Speranza and Titomanlio (2015). In experiments using small angle light scattering (SALS), Pogodina *et al.* (1999) could show that the observed long-range density fluctuations have a maximum at the gel point, which might be the origin for the nonlinear rheological behavior as pointed out in chapter 6 and will be further evaluated in this chapter. Flow-induced crystallization was studied by numerous groups using rheo-optical methods and some selected references are given in the following. Pioneering works were carried out by A. Keller

and M. Mackley at the University of Bristol (Mackley and Keller 1973; Mackley *et al.* 1975). They developed a multipass rheometer with *in-situ* microstructural characterization and could study crystallizing polymers under process-like conditions (Mackley *et al.* 1975, 2000; Hassell and Mackley 2008; Scelsi and Mackley 2008). The group of H. Winter at the University of Massachusetts (Amherst) investigated the molecular-weight dependence of flow-induced crystallization (Elmoumni *et al.* 2005; Elmoumni and Winter 2006). More recently, Pantani *et al.* studied the kinetics of crystallizing polymers under flow conditions using RheoMicroscopy (Pantani *et al.* 2010, 2014; De Santis *et al.* 2016). Further works were carried out by Koscher and Fulchiron (2002) and Housmans, Steenbakkens, Roozmond, Peters and Meijer (2009) who aimed at the validation of theoretical models for flow-induced crystallization.

8.2 Experimental

RheoMicroscopy set-up

The hyphenated RheoMicroscopy set-up shown in Figure 8.1 was developed by Dr. Eric Stelamanns from the German Electron Synchrotron (DESY) (see Appendix A for a photograph of the set-up). Similar to the RheoSAXS set-up presented in chapter 7, it was based on a stress-controlled Haake MARS II rheometer (Thermo Scientific, Karlsruhe, Germany) for which the motor was flipped by 180° to open up the top space for accessories. To be able to carry out *in-situ* microscopy, it was equipped with 35 mm parallel-plate geometries made from glass. The home-built optical microscopy unit consisted of a polarized white LED light source, an objective (achromatic triplet $f = 16$ mm), tubus lenses (achromatic doublets: $f = 10$ and 100 mm), and a 12-bit monochrome digital camera with a 1/1.2" CMOS sensor, 1936 × 1216 px (IDS Imaging Development Systems GmbH, Obersulm, Germany). The home-built oven was identical to that used for RheoSAXS and allowed to perform experiments over a temperature interval of 10 – 300 °C under a nitrogen atmosphere.

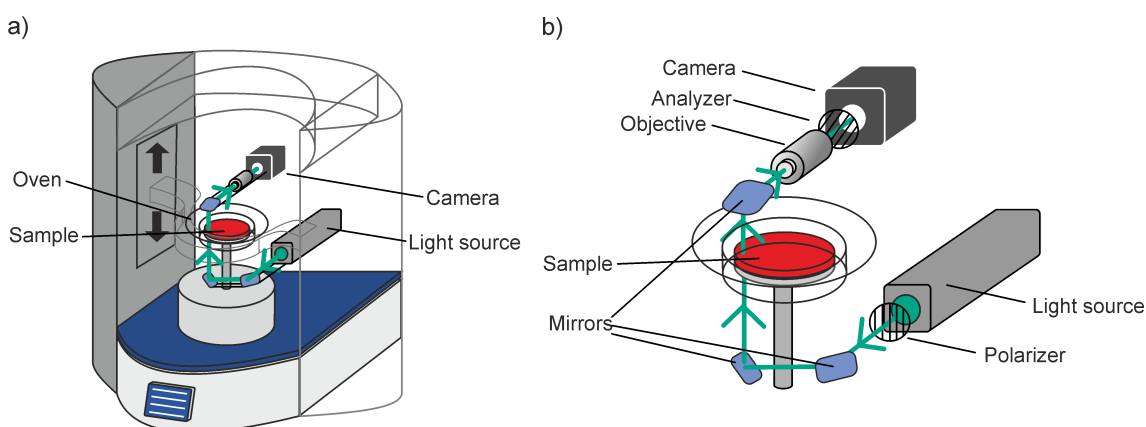


Figure 8.1: Rheo-Microscopy set-up based on a Thermo Haake MARS II rheometer equipped with 35 mm parallel-plate geometries made from glass and a home-built optical microscopy unit consisting of a polarized white LED light source, an objective, tubus lenses, and a 12-bit monochrome camera.

Procedures

All optical RheoMicroscopy experiments were conducted using the set-up described in the previous paragraph. Quiescent and flow-induced crystallization of isotactic polypropylene were studied under isothermal conditions at temperatures of 128 – 138 °C. Prior to all crystallization experiments, the 13 mm polypropylene samples were molten at 200 °C for 15 min to erase the thermal history. The sample thickness was adjusted to 200 – 250 μm to achieve a completely filled geometry. The observation window was at $r = 14$ mm as in the RheoSAXS experiments. All polymer crystallizations were monitored by rheological time sweeps with low strain amplitude $\gamma_0 = 0.5\%$ and angular frequency $\omega = 1$ rad/s to detect the change in flow behavior without disturbing crystal formation. For all flow-induced crystallizations, a steady shear step was included right after the desired crystallization temperature was reached (Figure 6.2). All micrographs were acquired in monochrome mode and under non-cross polarized conditions to be able to observe the flowing polymer melt prior to crystallization. Upon complete crystallization, the semi-crystalline morphologies were analyzed using *ex-situ* optical microscopy.

Materials

As in chapter 6 and chapter 7, the main material of investigation was a Ziegler-Natta polypropylene grade i-PP-1 (batch 1: $M_w = 246$ kg/mol, $D = 2.7$, 94% *mmmm*). Further information on the used material can be found in section 2.4, p. 19.

8.3 Quiescent crystallization experiments

The crystallization of isotactic polypropylene under quiescent conditions was studied using *in-situ* RheoMicroscopy (Figure 8.1). The evolution of the rheological moduli and simultaneously acquired micrographs for a crystallization of the Ziegler-Natta grade i-PP-1 at $T_{\text{crist}} = 138$ °C is shown in Figure 8.2. Soon after the temperature was reached small nuclei formed that grew into larger spherulites over time. At this stage, the rheological moduli didn't indicate any significant change, yet. The experiment was most likely dominated by heterogeneous nucleation from e.g., dust particles as there was no indication of a continuous nucleation process as it would be expected for homogeneous nucleation (see Figure 3.13 in subsection 3.3.6, p. 35). For $t \geq 30$ min, the moduli G' and G'' displayed an increasing behavior when considerably grown spherulites were present in the polymer melt. The crossover $G' = G''$ was reached shortly before 40 min and the micrographs showed a more and more dense microstructure with increasing time. As the sample gap of 250 μm was on the order of the growing spherulites, a distortion of the rheological parameters (especially G'') at later stages of the crystallization process was expected and observed. Furthermore, the final absolute values were lower compared to the experiments on the same polymer presented in chapter 6. This effect could have been a consequence of the large diameter (35 mm) in combination with the inherent compliance of the geometry as discussed in chapter 7.

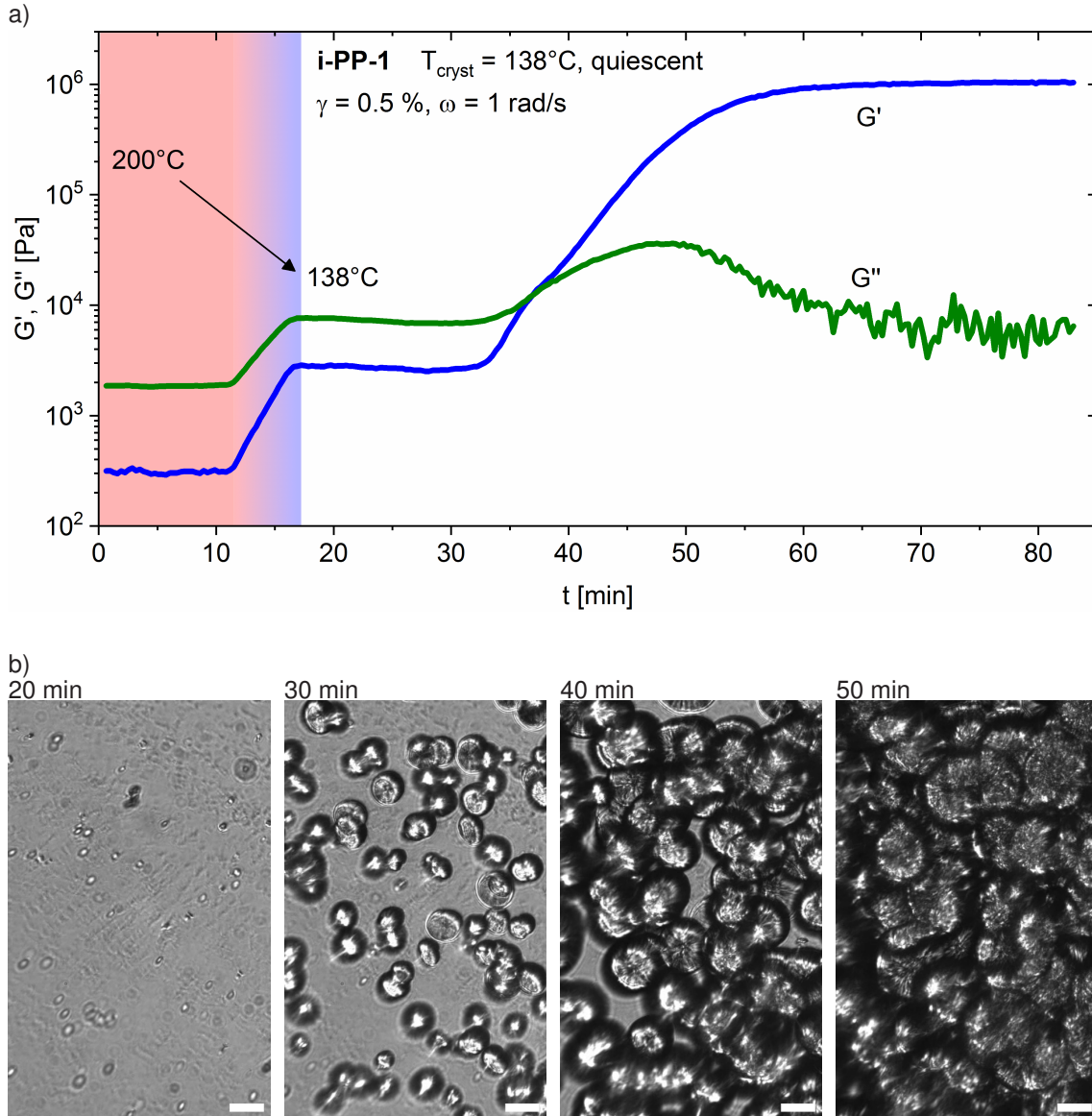


Figure 8.2: Moduli G' and G'' for a quiescent crystallization of i-PP-1 at 138°C (a) and simultaneously acquired micrographs (b) using hyphenated RheoMicroscopy. Scale bar: $50\ \mu\text{m}$.

8.3.1 Early stages of crystallization

As already pointed out in chapter 7, crystallizing polymer melts under quiescent conditions might still be subject to certain flows during heating and cooling. Here, these flows were observed by monitoring the position of dust particles during the nucleation phase as shown in Figure 8.3 (see Appendix A for additional micrographs recorded at $t = 0 - 20$ min). The intrinsic shear rates are several orders of magnitude smaller compared to the extra applied flow during steady-shear (e.g., $10^{-2}/\text{s}$ vs. $1/\text{s}$) and do not lead to row-nucleated morphologies. However, they are likely to have an effect on the orientation of the formed anisotropic nuclei at the early stages of crystallization. In Figure 8.3d, the ellipsoid nuclei were oriented along the flow direction. Likely, these nuclei were rotated under the influence of intrinsic flow as indicated in Figure 8.4. The combination of slightly anisotropic nuclei and their alignment

by intrinsic flow explains the net orientation at early stages of crystallization under quiescent conditions as determined by RheoSAXS in chapter 7. With increasing time these ellipsoid nuclei grow into spherulites and the net orientation is decreasing.

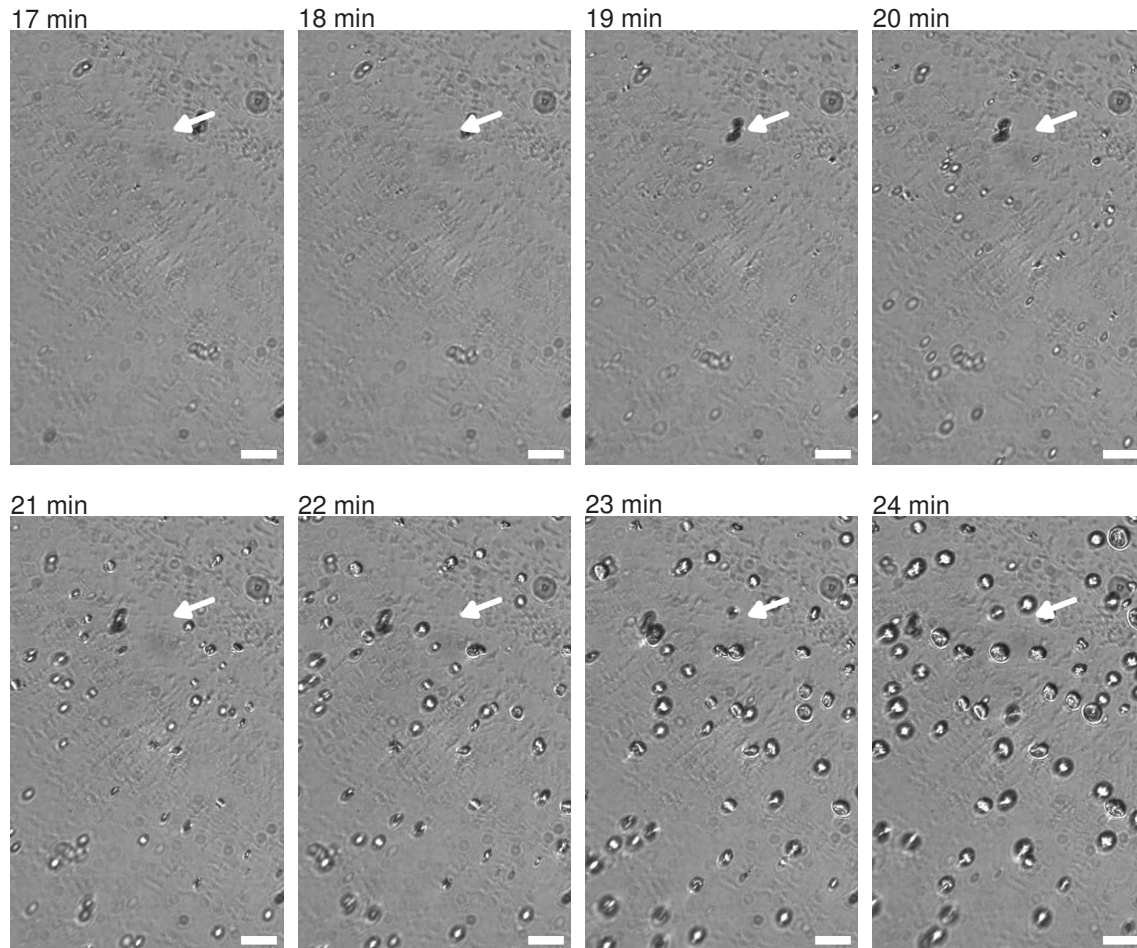


Figure 8.3: Micrographs of i-PP-1 crystallized at $T_{\text{cryst}} \approx 138$ °C under quiescent conditions acquired by RheoMicroscopy. Scale bar: 50 μm . White arrow indicates the direction of intrinsic flow.

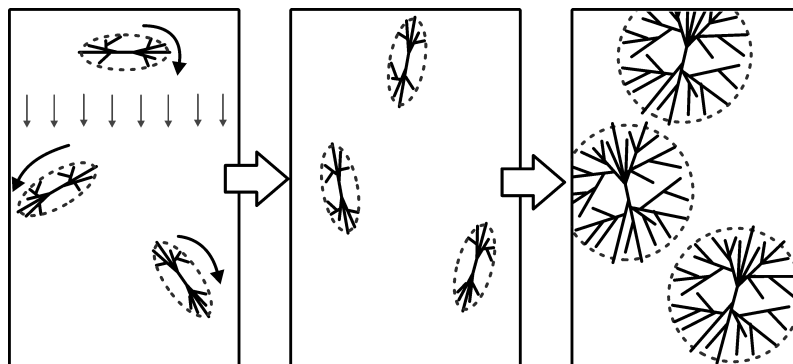


Figure 8.4: Schematic representation of the rotation of nuclei under the influence of intrinsic flow, which leads to a net orientation at early stages of the crystallization process. With increasing time, spherulitic growth leads to an again isotropic state of the material.

8.3.2 The microstructure at the point of gelation

Because the rheology data and the micrographs were acquired simultaneously, an analysis of the microstructure at the crossover of G' and G'' was possible. At low excitation frequencies the crossover is practically identical with the rheological gel point as shown in section 6.3, p. 98. Figure 8.5 shows the microstructure at the point of gelation for a quiescent crystallization of i-PP-1 at 138 °C. As the sample had a thickness of 250 μm , the micrograph represents a projection along the vertical sample direction.

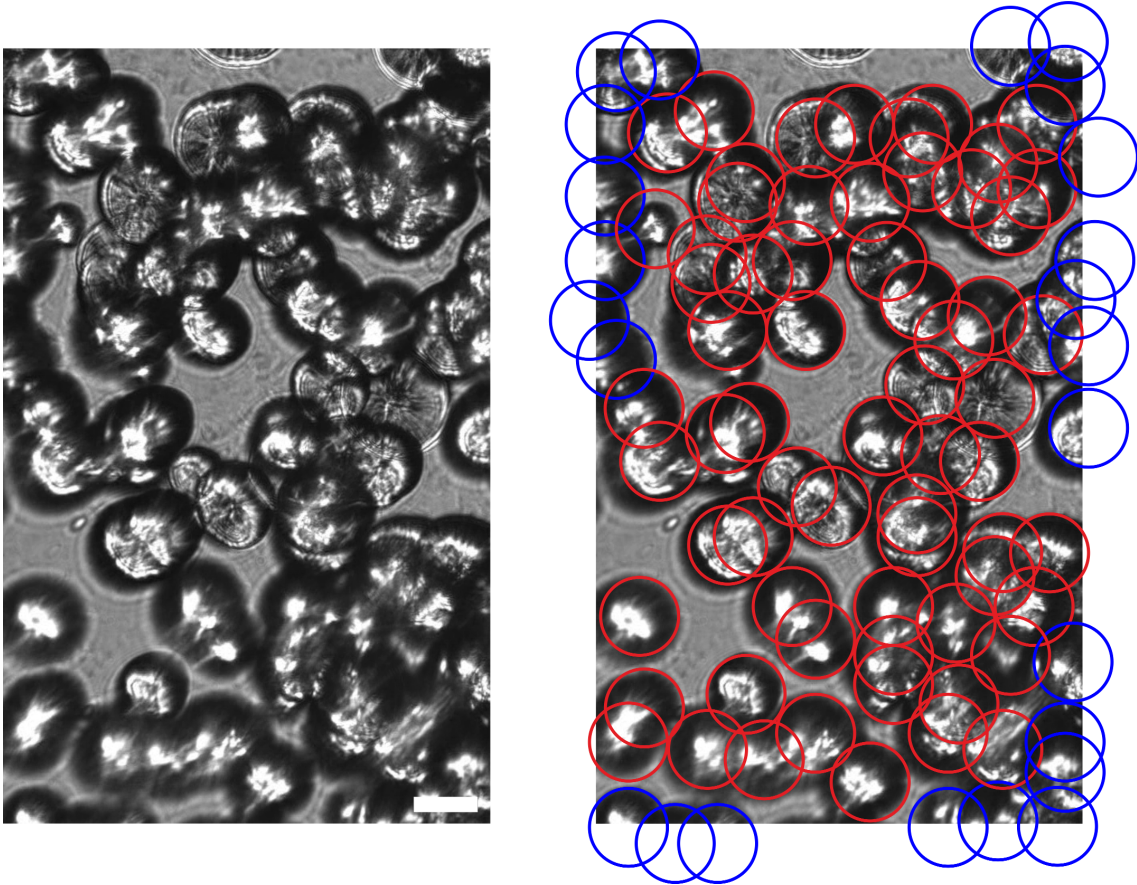


Figure 8.5: Micrograph recorded at the crossover of G' and G'' for a crystallization of i-PP-1 at 138 °C under quiescent conditions using RheoMicroscopy. By assuming monodisperse spheres of radius 30 $\mu\text{m} \pm 10\%$, the degree of space filling was calculated (circles in blue were counted half).

The degree of space filling ϕ was calculated by assuming a set of monodisperse spheres:

$$\begin{aligned} \text{Box dimensions : } a \times b \times c &: 600 \times 375 \times 250 \mu\text{m}^3 \\ 90 \text{ spheres with } r \approx 30 \mu\text{m}, 24 \text{ spheres at the edges counted half} &\Rightarrow 78 \text{ equiv. spheres} \\ \Rightarrow \text{degree of space filling : } \phi_{\text{crit}} &= \frac{78 \cdot 4/3\pi \cdot 30^3}{600 \cdot 375 \cdot 250} = \frac{8821592}{56250000} \approx 16\% \end{aligned}$$

The determined degree of space filling $\phi \approx 16\% \pm 5\%$ agreed well with the results obtained by RheoNMR for high crystallization temperatures (see chapter 6). Such low degrees of space filling point towards a percolation phenomenon of the growing and potentially inter-

acting spherulites. Theoretical site percolation threshold for the random close packing of hard spheres $p_{\text{crit}} \approx 0.3$ (Powell 1979; Ziff and Torquato 2017). Taking into account the geometrical filling factor of spheres ($f = 4/3\pi \cdot (r = 0.5)^3 = 0.524$), the critical volume fraction $\phi_{\text{crit}} = p_{\text{crit}} \cdot f \approx 16\%$ (Scher and Zallen 1970). This value agrees perfectly with the here observed degree of space filling $\phi_{\text{crit}} \approx 16\% \pm 5\%$ at the point of gelation. At lower crystallization temperatures, and consequently faster crystallizations, the values for ϕ_{crit} went down (e.g., 10% for $T_{\text{cryst}} \approx 132 \text{ }^\circ\text{C}$ as shown in Figure 6.9b, p. 104b). This behavior might be the consequence of a hydrodynamic effect due to the difference in density between the amorphous melt and the semi-crystalline spherulites. In Figure 8.6, potential hydrodynamic flows and the resulting boundary layer are illustrated. For faster crystallizations at lower temperatures, these stresses might lead to percolation at lower degrees of space filling. The boundary layer would be dependent on temperature, which explained the trends seen in chapter 6. Another reason for lower degrees of space filling at the point of gelation would be an anisotropy of the growing spherulites as observed for the regio-defective grade i-PP-2 (see section 6.5, p. 124), which indeed showed lower ϕ_{crit} values of $\sim 5 - 10\%$. As shown by (Akagawa and Odagaki 2007), particles with an aspect ratio of 5:1 (major : minor axis) exhibit half the critical volume fraction $\phi_{\text{crit}} \approx 8\%$ of round particles. For needles or fibers with even higher aspect ratios, ϕ_{crit} decreases to values below 5%.

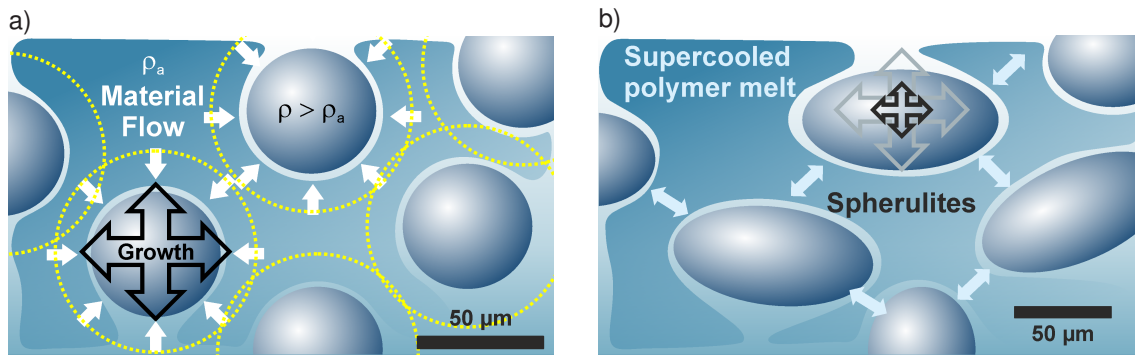


Figure 8.6: (a) Illustration of the potential temperature-dependent interaction of growing spherulites. The difference in density between the amorphous melt and the semi-crystalline spherulites might lead to stresses pointing towards the center of each spherulite. b) Anisotropic spherulites might percolate at lower degrees of space filling due to their higher aspect ratio.

8.4 Flow-induced crystallization experiments

The microstructure of semi-crystalline polymers gets drastically changed upon the application of flow (section 3.4, p. 38). The main two effects are an increase in nucleation density for relatively mild flow conditions and the formation of elongated row-nucleated structures for higher shear rates and longer shear durations. As in chapter 6 and chapter 7, the short-term shear protocol by Janeschitz-Kriegl (Figure 6.2) was employed to study the effects of flow independently from the chosen crystallization temperature. In Figure 8.8, acquired rheological moduli G' and G'' are plotted for different experimental conditions. Stresses of 12 – 24 kPa were applied for 60 s each, which led to an almost instantaneous application of shear rates

between $1 - 9/s$ and a linear increase of the total strain depending on the applied stress (Figure 8.8). As the Haake MARS II is a stress-controlled rheometer, this approach was found to provide better defined flow profiles compared to the *Controlled Rate (CR)* mode used in chapter 7. Up to 21 kPa, the rheological parameters indicated a speed-up of crystallization. For the highest applied stress of $\sigma = 24$ kPa, a slower overall crystallization was observed. In Figure 8.9), micrographs recorded at different points in time during the experiments of Figure 8.7 are shown. The microstructure of the experiment with 12 kPa was relatively similar to the quiescent case. However, at higher applied stresses, a significantly higher nucleation density was observed. For the experiment at 24 kPa the formation of row-nucleated structures was detected in the window of observation (see Appendix A for additional micrographs).

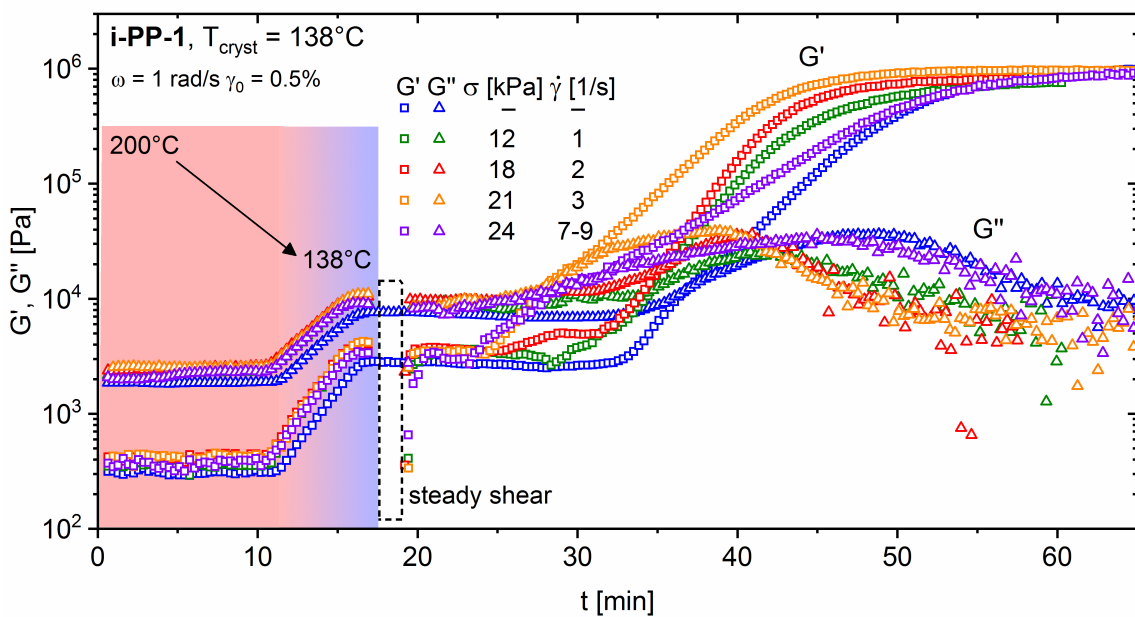


Figure 8.7: Moduli G' and G'' for the crystallization of i-PP-1 at 138 °C under different applied flow conditions acquired using hyphenated RheoMicroscopy.

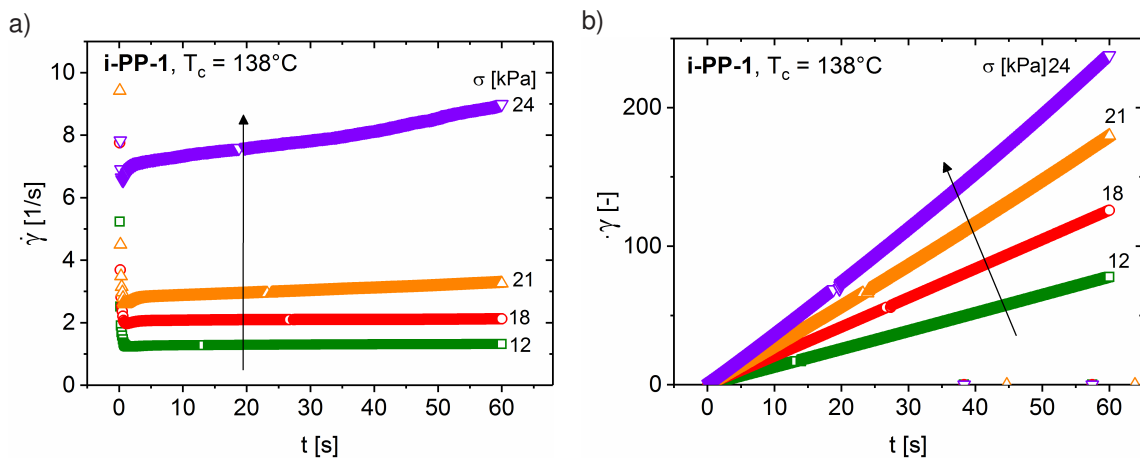


Figure 8.8: Applied shear rates (a) and total strains (b) during the short-term steady shear routine for the experiments in Figure 8.7.

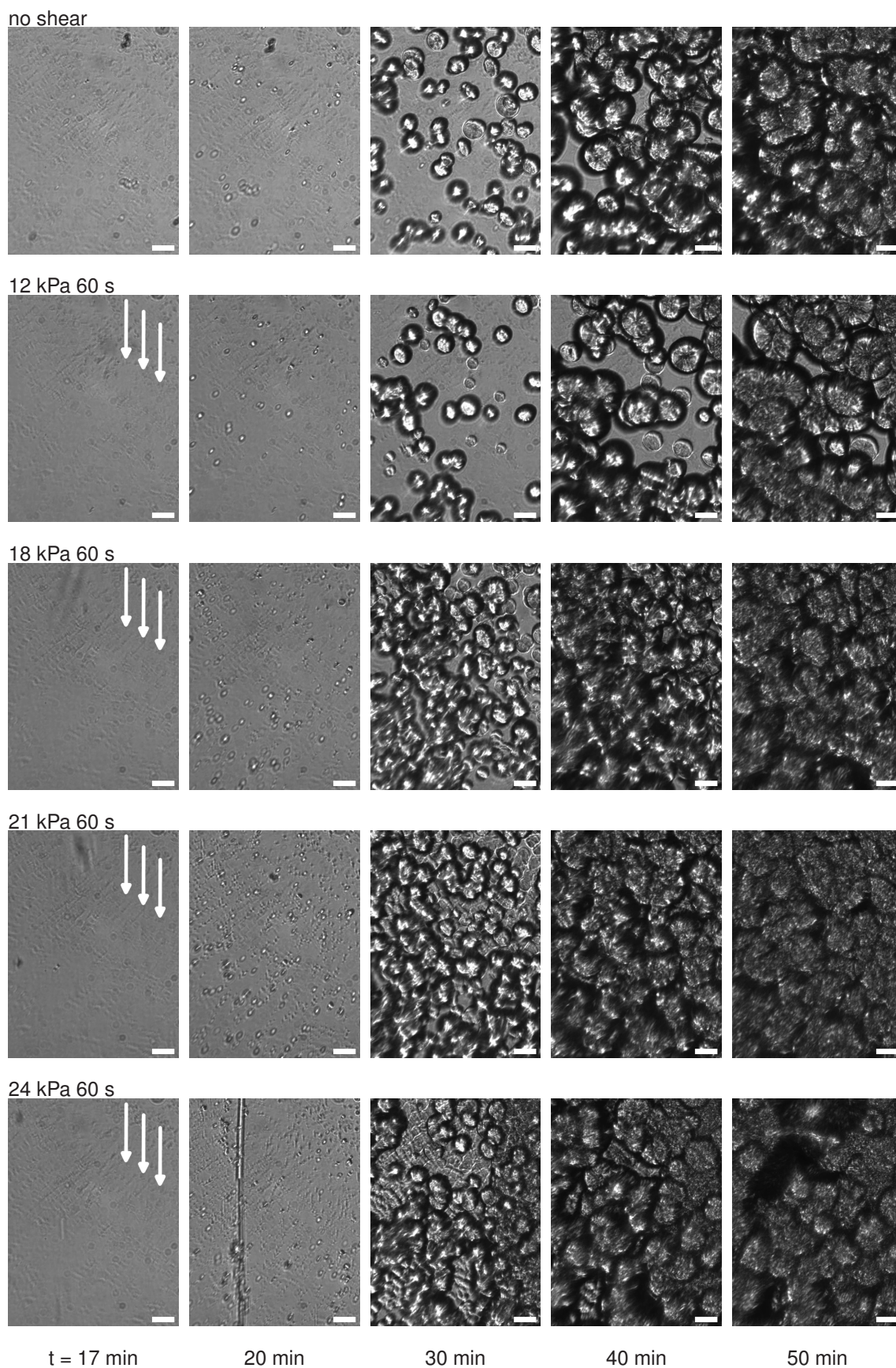


Figure 8.9: Micrographs of i-PP-1 crystallized at $T_{\text{cryst}} \approx 138^\circ\text{C}$ under different flow conditions simultaneously acquired to the rheological data shown in Figure 8.7 using hyphenated RheoMicroscopy. Scale bar: $50\ \mu\text{m}$.

8.4.1 The point of gelation under flow conditions

In Figure 8.10, micrographs of the microstructure at the crossover of G' and G'' are shown for each experiment. Again, as the sample had a thickness of 250 μm , the micrographs represented a projection along the vertical sample direction. For the experiment with $\sigma = 12$ kPa, a similar microstructure as for the experiment under quiescent conditions was observed. The experiments at higher applied stresses showed significantly increased nucleation and an overall higher degree of space filling at the point of gelation. Notably, many nuclei were formed close to the surface of the glass plates under stronger flow conditions. This effect might have been associated with a reduction in surface stresses of the growing nuclei as discussed in subsection 3.3.2, p. 25 in chapter 3. As the microstructure of strongly sheared samples becomes more and more heterogeneous, the micrographs shown in Figure 8.10 represented snapshots of the local microstructure at $r = 14$ mm. Thus, the degree of space filling was relatively high at the surfaces when the crossover of G' and G'' was detected.

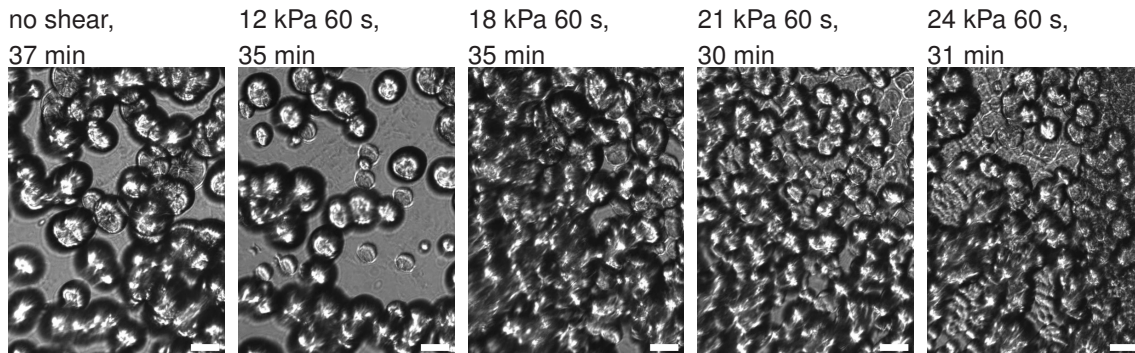


Figure 8.10: Micrographs recorded at the rheological crossover ($G' = G''$) for i-PP-1 crystallized at $T_{\text{crist}} \approx 138$ $^{\circ}\text{C}$ under different conditions using hyphenated RheoMicroscopy. Scale bar: 50 μm .

8.4.2 Ex-situ polarized light microscopy

To further investigate the microstructure upon complete crystallization, the specimens from the tests with applied stresses of 21 kPa and 24 kPa were analyzed using *ex-situ* polarized light microscopy (Zeiss Axiophot, Oberkochen, Germany). In Figure 8.11, obtained micrographs with magnifications of 25x and 200x are shown for both samples. In case of the sample from the 24 kPa experiment (a, b) voids and cracks were seen that pointed to a detachment from the glass surfaces during steady shear. Row-nucleated structures were confirmed for this sample close to the edges, which agreed with the findings in chapter 7. The micrograph for the experiment with an applied stress of 21 kPa displayed a more homogeneous microstructure with higher nucleation densities further away from the center of the specimen. However, no long extending row-nucleated structures (cylindrites) were visible, which was reasonable taking into account the relatively low shear rate of $\sim 3/\text{s}$ and agreed with the observations made in chapter 7.

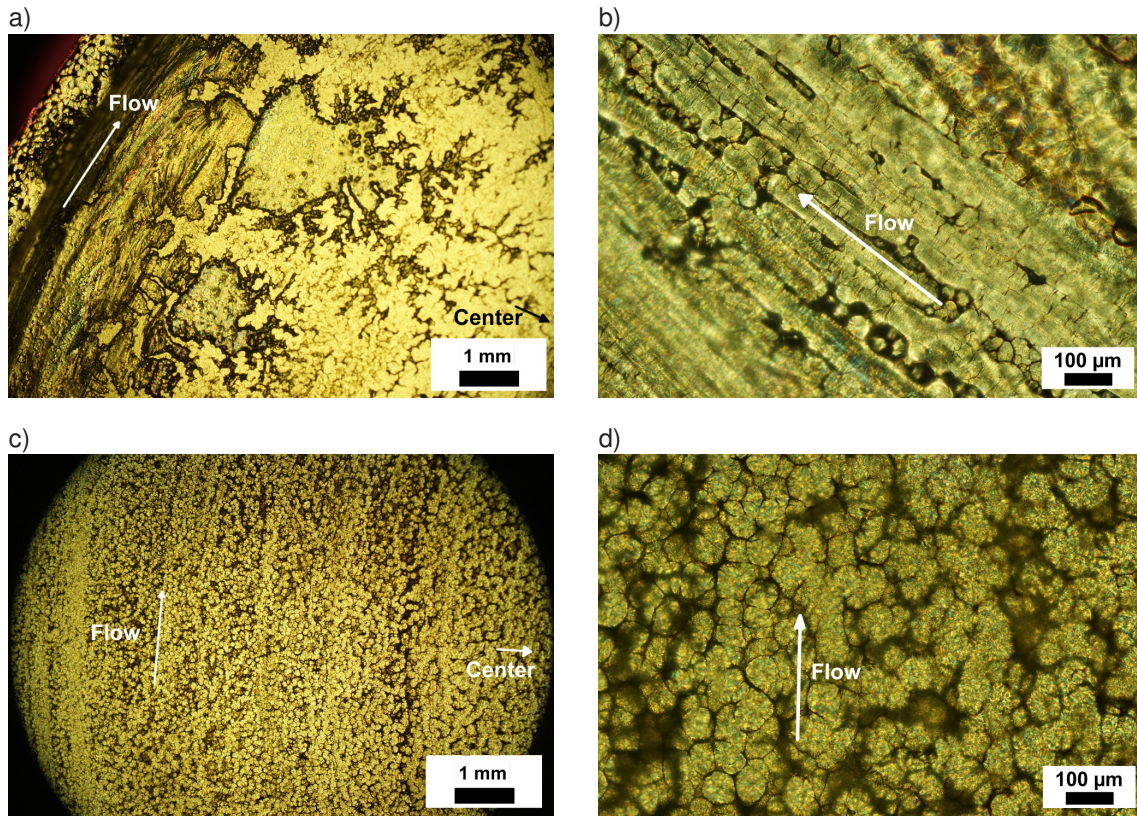


Figure 8.11: Micrographs of i-PP-1 crystallized at $T_{\text{cryst}} \approx 138$ °C with an applied stress of 24 kPa for 60 s (a, b) and 21 kPa for 60 s (c, d) recorded upon complete crystallization using a Zeiss Axiophot microscope.

8.5 Concluding remarks

In this chapter, the microstructure and rheology of isotactic polypropylene during crystallization under quiescent and flow conditions was investigated using optical RheoMicroscopy. This project was carried out in collaboration with Dr. Eric Stellamanns (DESY, Hamburg, Germany) using their hyphenated RheoMicroscopy set-up based on a stress-controlled Thermo Haake MARS II rheometer.

The tested Ziegler-Natta isotactic polypropylene grade showed an expected spherulitic crystallization behavior with final spherulite sizes on the order of 100 μm . During the nucleation period, ellipsoid nuclei were formed that grew into round spherulites over time. Interestingly, these nuclei were oriented in the direction of inherent intrinsic flows, which explained the observed anisotropic scattering patterns discussed in chapter 7. The occurrence of nuclei soon after reaching the desired crystallization temperature strongly suggested that the observed X-ray scattering at low scattering vectors was in fact caused by small nuclei and not long-range density fluctuations. Therefore, the mechanism was likely dominated by nucleation and growth under the tested experimental conditions. The microstructure at the point of gelation as characterized by the crossover of G' and G'' at low excitation frequencies showed a considerable degree of space filling $\phi_{\text{crit}} \approx 16\%$, which agreed with the results obtained by RheoNMR.

Taking into account the filling factor $f \approx 0.5$ of spherical objects, physical gelation was well explained by the percolation of randomly packed spherulites with a percolation threshold p_{crit} of ~ 0.3 . For lower crystallization temperatures, a hydrodynamic effect might lead to gelation at lower degrees of space filling due to the difference in densities between the amorphous melt and the semi-crystalline spherulites. Furthermore, anisotropically growing spherulites might generally percolate at lower loadings due to the higher aspect ratio as discussed in the context of rod-like particle suspensions.

Flow-induced crystallization of isotactic polypropylene was studied using short-term steady shear profiles as in chapter 6 and chapter 7. Here, selected stresses were applied that led to better defined steady shear conditions compared to the RheoSAXS experiments using the same stress-controlled rheometer in controlled rate mode. For all pre-shear experiments, an overall increase in the speed of crystallization was detected by the rheological parameters. The simultaneously recorded microstructure via polarized light microscopy revealed an increased nucleation density with increasing applied stresses. For the experiment under the highest applied stress of 24 kPa, row-nucleated structures (cylindrites) were confirmed. However, during this experiment parts of the sample detached from the smooth glass surfaces of the parallel-plate geometries, resulting in a heterogeneous microstructure that explains the overall slower crystallization behavior. Notably, a large number of nuclei that were created by the application of flow were formed close to the surfaces of the geometries, indicating the importance of surface stresses for the creation of stable nuclei.

Overall, hyphenated optical RheoMicroscopy provided correlated information on the effects of flow on the microstructure and related rheology of semi-crystalline polymers. This technique was found to be a useful complement to the investigations using RheoNMR chapter 6 and RheoSAXS (chapter 7) that focused on the *in-situ* characterization of molecular dynamics and nano-scale morphology, respectively. Generally, micrographs represent local microstructure, which limits the comparability if heterogeneities on larger length scales are present due to the application of flow, incorporated additives, or temperature gradients. Image analysis can become inherently difficult when the material turns turbid and the formed structures overlay each other. Additionally, uncertainties in the detection of rheological parameters increase when the formed semi-crystalline structures are on the order of the gap selected for *in-situ* optical microscopy. For a quantitative analysis of e.g., the degree of space filling at the rheological point of gelation, the presented RheoNMR method provides higher accuracy as it delivers global sample average values rather than position-dependent information.

9 Conclusion and Outlook

In this thesis, new hyphenated characterization techniques were employed to study the crystallization behavior of synthetic polymers under quiescent and flow conditions. A main focus was the study of the relationships between the molecular dynamics, morphology, and rheology of crystallizing polymers using custom-built RheoNMR, RheoSAXS, and RheoMicroscopy set-ups. Furthermore, a method to determine the crystallinity and crystallization kinetics of commercially relevant polymers via low-field ^1H -NMR was evaluated in detail and compared against established characterization techniques.

The molecular dynamics of semi-crystalline polymers were investigated using ^1H -NMR under the supervision of Prof. Gisela Guthausen (KIT-MVM, Pro 2 NMR) with support from Prof. Harald Horn (KIT-EBI). Low-field ^1H -NMR relaxometry was used to study the temperature-dependent NMR relaxation behavior over a wide temperature range and $T = T_g + 100$ K was identified as the minimum temperature with respect to the glass transition temperature T_g at which the mobility difference between the protons of crystalline and amorphous domains is sufficient for an unambiguous determination of polymer crystallinity. The obtained bulk crystallinities were compared to DSC and XRD data, and showed good agreement for all polymers within an estimated relative error of $\pm 10\%$ for the respective methods. Additionally, we focused on the determination of crystallization kinetics, i.e., monitoring of isothermal crystallization, where we found the combination of a mixed magic sandwich echo (MSE) followed by a Carr Purcell Meiboom Gill (CPMG) echo train to be the most suitable sequence for crystallization experiments. For all polymers, the relaxation behavior within the amorphous domains was rather invariant during crystallization, pointing towards a nucleation and growth mechanism for polymer crystallization. When compared to isothermal differential scanning calorimetry experiments, a quantitative analysis using the Avrami model showed good agreement for the crystallization rate, but deviations in the dimensionality parameter were seen. This behavior could have been caused by higher temperature gradients in the NMR experiments and therefore a growth rate distribution which lowered the apparent dimensionality value. Overall, low-field ^1H -NMR relaxometry was found to deliver valuable information on the molecular dynamics during polymer crystallization and was successfully employed to obtain information on the bulk crystallinity and crystallization kinetics of polymers.

The interplay between the molecular dynamics and macroscopic flow behavior during polymer crystallization was studied using a unique hyphenated low-field RheoNMR set-up. This novel characterization technique was based on a commercial strain-controlled shear rheometer with a portable ^1H NMR relaxometry unit, which allowed for the study of soft matter rheological

behavior while monitoring the molecular dynamics *in-situ* via ^1H NMR relaxometry. The crystallization of isotactic polypropylene under quiescent conditions and with a preceding steady shear protocol was investigated at varying the crystallization temperatures and applied flow conditions. The evolving crystallinities were determined *in-situ* using the previously evaluated multi-echo-based NMR sequence. As the sample was studied simultaneously by rheology and NMR relaxometry, hardening curves of e.g., the viscosity vs. the degree of space filling, were constructed and then evaluated using suspension and semi-empirical models. The analysis revealed that the relationship between viscosity and the degree of space filling is highly nonlinear with multiple regimes that are indicative of a physical gelation process. The best description of the hardening behavior of a neat Ziegler-Natta isotactic polypropylene grade was achieved using an extended Einstein model with exponents $C' \approx 4$ to 5 and dynamic ranges $D' \approx 30000$ to 60000 for the chosen crystallization temperatures of $T_{\text{cryst}} \approx 132$ to 136 °C. Different isotactic polypropylene grades were compared with respect to their crystallization kinetics and physical gelation behavior. A metallocene-catalyzed and regio-defective polypropylene grade showed a drastically inhibited crystallization speed and an unusually steeply increasing hardening curve at low degrees of space filling. The influence of fillers and nucleating agents on the crystallization behavior of isotactic polypropylene was studied in close collaboration with the groups of Prof. Alejandro Müller (Universidad del País Vasco, San Sebastián, Spain) and Prof. Hans-Werner Schmidt (University of Bayreuth, Germany). It was found that both fillers and nucleating agents sped up the crystallization of isotactic polypropylene by increasing the nucleation density when low amounts of well dispersed additives were embedded into the polymer matrix. It was found that the incorporated silica filler didn't change the hardening behavior significantly, whereas the 1,3,5-benzene tricarboxamide nucleating agent led to a faster rising hardening curve at the optimum concentration of 750 ppm. Flow-induced crystallization was studied using short-term steady shear protocols with either similar total strains or strain rates. An increase in the speed of crystallization was detected for the pre-shear experiments, with the samples that were subjected to the strongest flow conditions of 10/s for 20 s showing an almost immediate increase in the viscosity $|\eta^*|$ upon the cessation of flow. Scanning electron microscopy confirmed that a substantially higher nucleation density with small spherulites ($\sim 5 \mu\text{m}$) was present in the sheared samples. In addition, anisotropic row-nucleated structures (cylindrites) were observed that may be the origin of rigidification at very low crystallinities. The hyphenation of low-field NMR and rheometry into a RheoNMR set-up was a useful tool in studying polymer crystallization and could be further employed to study the crystallization of low molecular weight substances, gelation or curing reactions and to investigate how the application of shear can affect these processes.

To unravel the relationship between the evolving nano-scale morphology and rheology during polymer crystallization, experiments using hyphenated RheoSAXS were conducted at the German Electron Synchrotron (DESY) in collaboration with Dr. Eric Stellamanns and Dr. Michael Sprung (both DESY, Hamburg, Germany). The custom-built vertical set-up was based on a commercial stress-controlled shear rheometer that was integrated into a reflected X-ray beam path of the P10 beam line. Under quiescent crystallization conditions, the tested Ziegler-Natta

and metallocene-catalyzed polypropylene grades showed the formation of ring-type scattering patterns, indicating an isotropic orientation of the formed lamellae. The early stages of crystallization were characterized by an increase in scattering intensity at small scattering vectors that were most certainly caused by the formation of small nuclei rather than long-range density fluctuations. Ultimately, the SAXS invariants were not found to provide a quantitative measure of crystallinity as the sample was probed locally and secondary crystallization decreased the absolute scattering intensity. For all flow-induced crystallization experiments, an overall increase in the speed of crystallization was detected by the change in the rheological parameters and the appearance of anisotropic scattering patterns. The Ziegler-Natta grade showed characteristic dumbbell patterns soon after the cessation of flow that were likely caused by lamellae perpendicular to the applied flow direction. On the other hand, the metallocene-catalyzed, regio-defective material displayed cross-type patterns that might originate from an average orientation of the fine cross-hatched microstructure. The Herman's orientation function was employed to quantify the degree of orientation, independent of the absolute scattering intensity. The analysis revealed structural anisotropy at the early stages of polymer crystallization ($F_H \approx 0.3$), even for the experiment under quiescent conditions. Possibly, convection upon cooling caused local flow fields which directed the growth of sheaf-like nuclei. When correlated with the simultaneously measured viscosity, a decrease in the degree of orientation over the entire crystallization process was observed for the Ziegler-Natta grade, whereas for the metallocene-catalyzed grade, it stayed almost constant. The obtained sample morphologies were further evaluated using *ex-situ* scanning electron microscopy, confirming a substantially higher nucleation density with small spherulites in the sheared samples (diameter: $\sim 10 - 20 \mu\text{m}$ for the highest shear rate). Row-nucleated structures were observed for the Ziegler-Natta grade that was subjected to the highest shear rate, which were $100 - 150 \mu\text{m}$ long and most certainly the origin of the measured strong anisotropic scattering. The occurrence of this morphology was well explained by the necessity of a higher applied shear rate compared to the inverse of the longest relaxation time (Weissenberg criterion). Hyphenated RheoSAXS provided correlated information on the effects of flow on the nano-scale morphology and related rheology of semi-crystalline polymers, which was not directly accessible before. By applying different flow conditions, we identified highly anisotropic structures as a potential cause for the observed hardening behavior at the early stages of the crystallization process.

The microstructure and rheological behavior during polymer crystallization under quiescent and flow conditions was investigated using hyphenated optical RheoMicroscopy. All experiments were carried out in collaboration with Dr. Eric Stellamanns (DESY, Hamburg, Germany) on a custom-built set-up based on a commercial stress-controlled rheometer. The tested Ziegler-Natta polypropylene grade showed the expected spherulitic crystallization behavior with final spherulite sizes on the order of $100 \mu\text{m}$. During the nucleation period, ellipsoidal nuclei were formed that grew into round spherulites over time. Interestingly, these nuclei were oriented in the direction of inherent convectional flows, which explained the previously observed anisotropic SAXS patterns at small scattering vectors and ruled out the occurrence of spinodal decomposition. The microstructure at the point of gelation showed a considerable

degree of space filling (16%), which agreed with the results obtained by RheoNMR. The observed physical gelation process was well explained by the percolation of randomly packed spherulites with a percolation threshold of ~ 0.3 , taking into account the filling factor of spherical objects (~ 0.5). For lower crystallization temperatures, a hydrodynamic effect might have led to gelation at lower degrees of space filling due to the difference in densities between the amorphous melt and the semi-crystalline spherulites. Furthermore, anisotropically growing spherulites might generally percolate at lower loadings due to the higher aspect ratio. Flow-induced crystallization of isotactic polypropylene was studied using short-term steady shear profiles. For all pre-shear experiments, an overall increase in the speed of crystallization was detected by the rheological parameters. The simultaneously recorded microstructure via polarized light microscopy revealed an increased nucleation density with increasing applied stress. For the experiment under the highest applied stress, row-nucleated structures were confirmed. Notably, a large number of nuclei that were created by the application of flow were formed close to the surfaces, indicating the importance of surface stress for the creation of stable nuclei. Overall, hyphenated optical RheoMicroscopy was found to be a useful complement to the presented RheoNMR and RheoSAXS techniques and helped to span the gap between microscopic structural features and the observed rheological phenomena.

In conclusion, new characterization methods, especially when combined into hyphenated set-ups, helped to clarify the crystallization mechanism, the formation of row-nucleated structures, and the hardening behavior during quiescent and flow-induced crystallization. They allowed for a reliable correlation of experimental data as the average crystallization temperature and the temperature distribution were identical for both sets of data. They permitted the application of flow profiles and the study of the resulting molecular dynamics, morphology, and rheology during polymer crystallization, respectively. The obtained results point towards a nucleation mechanism for the early stages of polymer crystallization rather than spinodal decomposition because of the dependence on temperature, additives, and flow conditions. Furthermore, the observed intensity at small scattering vectors during nucleation is most certainly a consequence of scattering from small nuclei rather than of spontaneous demixing. The growth of lamellae might be accompanied by a mesomorphic phase transition at the growth front instead of a stem-wise addition, which however has to be a local phenomenon due to the invariance of the molecular dynamics of amorphous material during polymer crystallization. The hardening behavior of crystallizing polymer melts was almost certainly associated with the percolation of growing and interacting superstructures and was successfully modeled using semi-empirical suspension models. In future works, experiments on monodisperse polymers of different molecular weights would help to further understand the relationship between imposed flow and the formation of row-nucleated morphologies. Hyphenated set-ups using capillary rheometers would furthermore allow for the application of higher shear rates that mimic process conditions. Finally, experiments using hyphenated techniques based on strain-controlled shear rheometers and wide angle X-ray scattering, infrared or dielectric spectroscopy, could lead to an even better understanding of polymer crystallization on macroscopic and microscopic length and time scales.

Acknowledgements (Danksagung)

During my PhD I received strong support from all of my colleagues, collaborators, and many others. I especially would like to thank...

- Prof. Manfred Wilhelm and Prof. Gisela Guthausen for their excellent supervision, support, and motivation during this fascinating, diverse, and challenging project;
- Prof. Alejandro Müller and Dr. Jordana Palacios (University of the Basque Country, Spain) for a great collaboration and fruitful discussions;
- Prof. Hans-Werner Schmidt, Dr. Klaus Kreger, and Daniel Kremer (University of Bayreuth) for a productive and insightful collaboration;
- Prof. John Reynolds, Dr. Robert Braga, Dr. Cameron Tyson, and Dr. Jeff Hernandez (Georgia Institute of Technology, USA) for their support during my stay at Georgia Tech;
- Dr. Eric Stellamanns and Dr. Michael Sprung (DESY), and Dr. Karl-Friedrich Ratzsch for supporting me in the use of their hyphenated rheology techniques;
- Prof. Harald Horn, Dr. Xiaoi Guo, Dr. Pia Herrling, Dr. Felicitas Arndt, Eva Förster, Sebastian Schuhmann, and Nicolas Schork for their support and discussions;
- Dr. Martin Sack and Paul Dietrich for their dedicated work on the Q-switch;
- Dr. Jennifer Kübel, Jonas Keller, Mürüvvet Begüm Özen, Matthias Heck, Dr. Johannes Höpfner, and Dr. Karl-Friedrich Ratzsch for proofreading; Manuel Haas and Jochen Klein for their help; Dr. Christopher Klein and Dr. Kamran Riazi for introducing me to optical microscopy; Dr. Sandra Kauffmann-Weiss and Dr. Gülperi Cavusoglu for XRD measurements; Volker Zibat for electron microscopy; Helena Hörig for DSC measurements; the ITCP workshop team for realizing my ideas; Sabine Weiland for administrative support; and all other colleagues for great fun during coffee breaks, polyfilms, and parties;
- Dr. Timo Beskers (PSS) for GPC measurements, Dr. Matt Parkinson (Borealis, ExxonMobil) for ^{13}C NMR experiments, and Dr. Iakovos Vittorias (LyondellBasell) for providing polymer samples and GPC measurements;
- the Deutsche Forschungsgemeinschaft (DFG, Pro²NMR, SPP1369-B10) and Bundesministerium für Bildung und Forschung (BMBF, FUNgraphen) for funding our work;
- and most of all my family, friends, and Adriana for constantly supporting and motivating me over the past few years!

Thank you so much – Vielen Dank für die Unterstützung!

Volker Rätzsch

A Appendix

A.1 Additional experimental data

A.1.1 Solid-state $^1\text{H-NMR}$ (400 MHz)

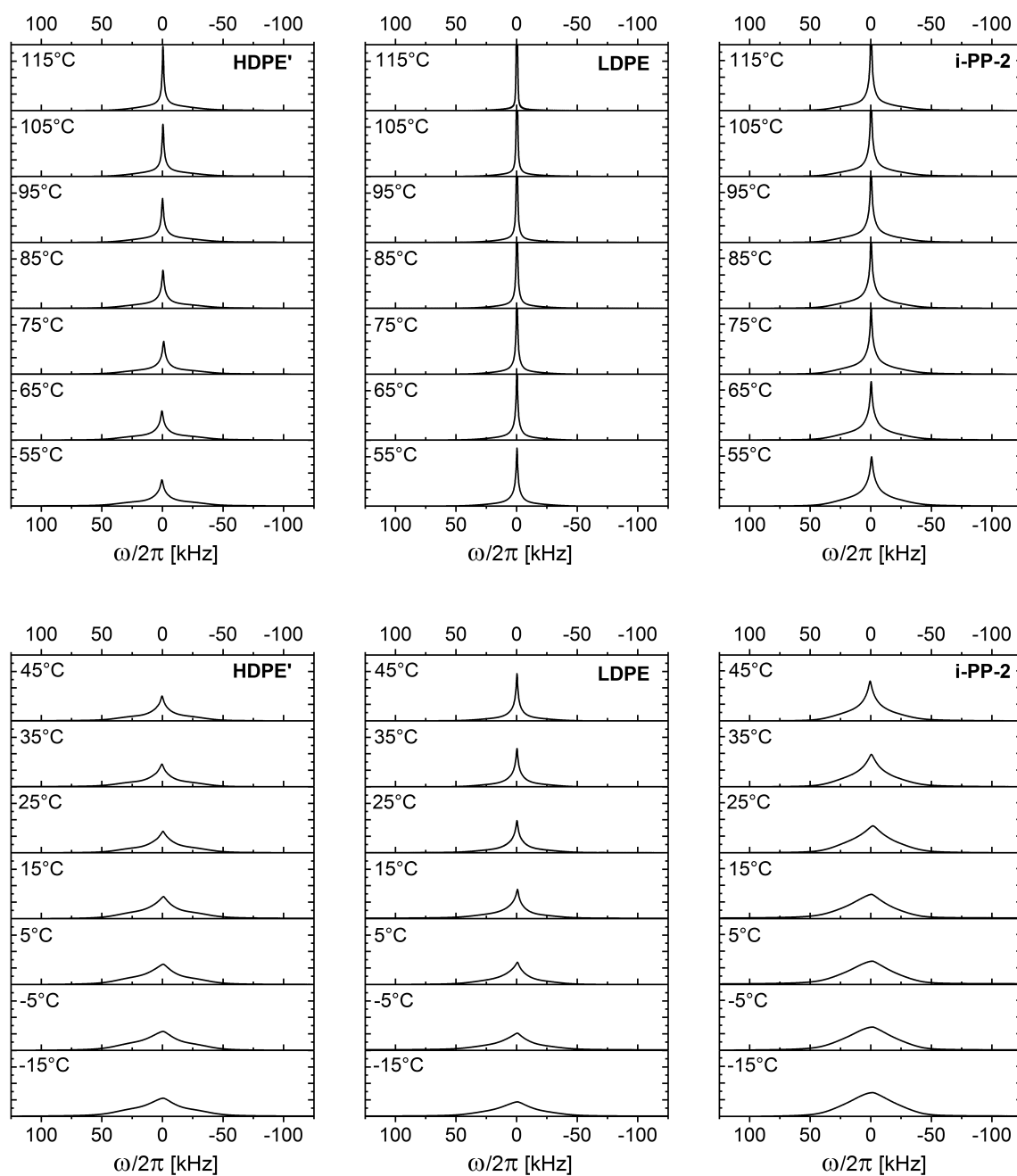


Figure A.1: $^1\text{H-NMR}$ spectra (400 MHz) of HDPE', LDPE, and i-PP-2 recorded at different temperatures.

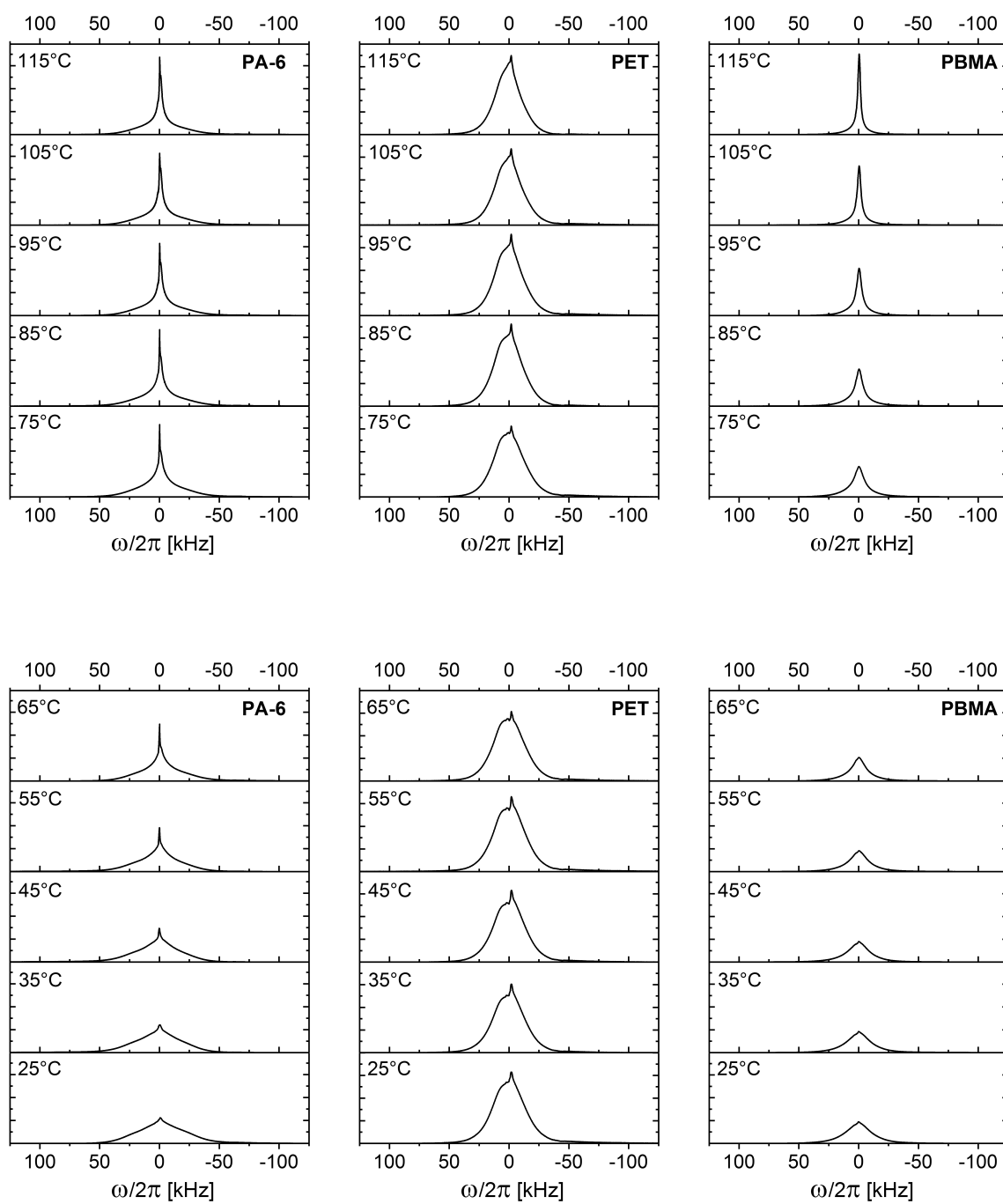


Figure A.2: ^1H -NMR spectra (400 MHz) of PA-6, PET, and PBMA recorded at different temperatures.

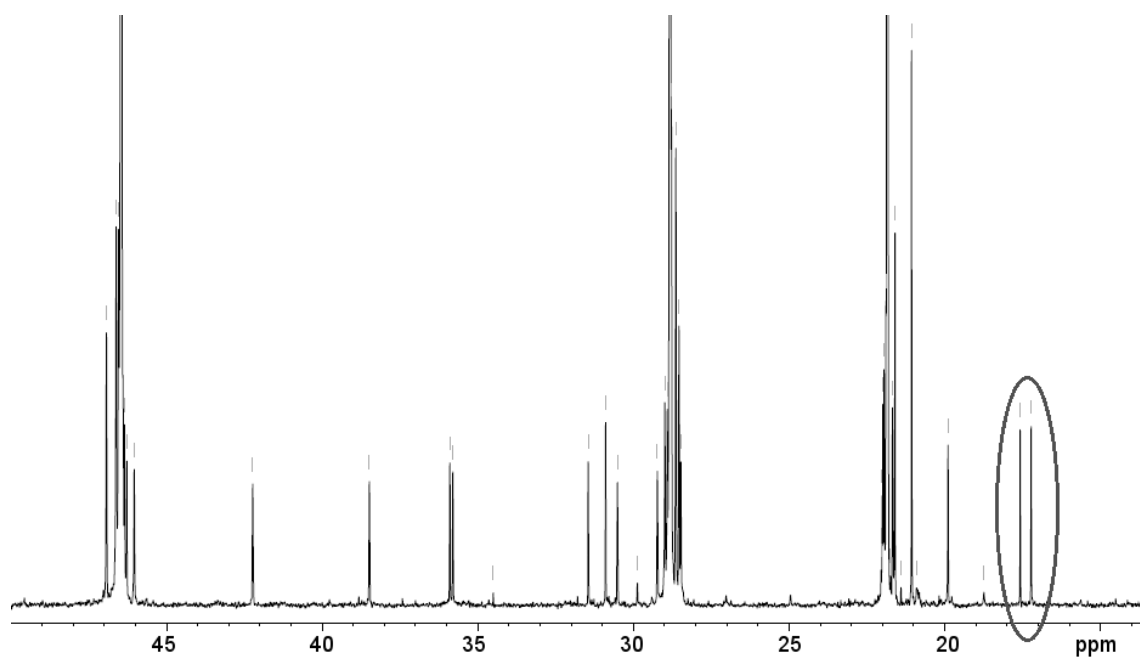
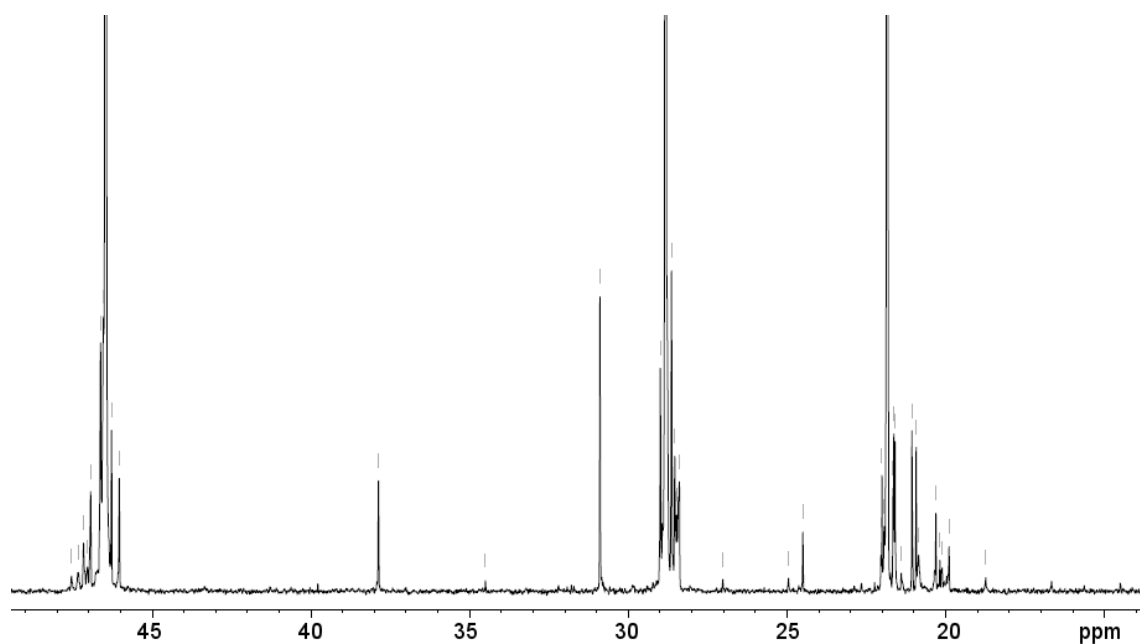
A.1.2 Liquid-state ^{13}C -NMR (400 MHz)

Figure A.3: Decoupled ^{13}C -NMR spectra of i-PP-1 (top) and i-PP-2 (bottom) dissolved in trichloroethylene (TCE) at 125 °C, which revealed a pentad isotacticity $mmmm = 94\%$ for both samples (peak at $\delta = 21.8$ ppm over all pentad-related peaks at 20 – 22 ppm) and 1 mol% of 2,1-erythro regio defects for the metallocene catalyzed i-PP-2 grade (peaks at ~ 18 ppm, Busico and Cipullo (2001)).

A.1.3 Differential scanning calorimetry (DSC)

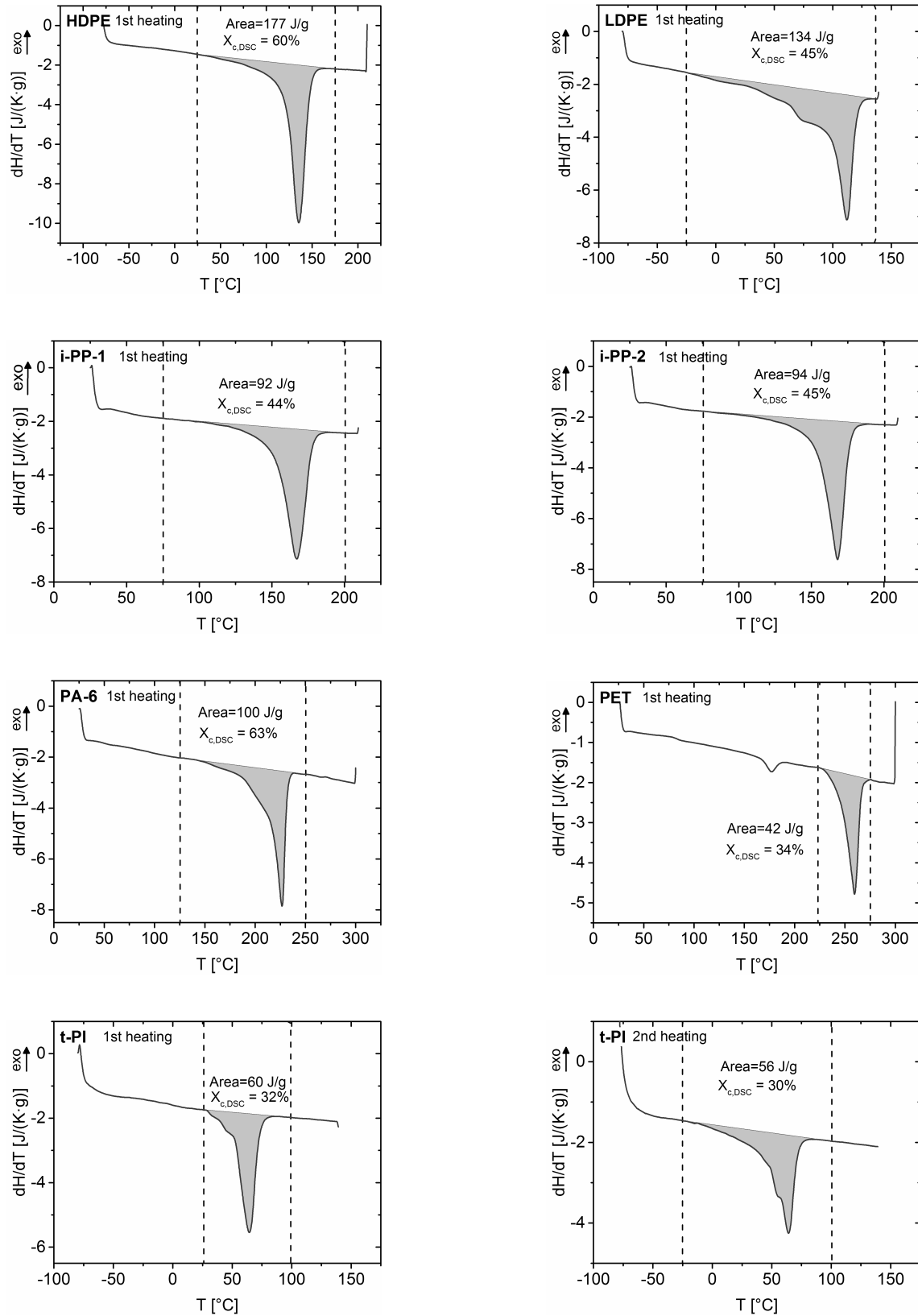


Figure A.4: DSC heating traces and obtained crystallinities for different polymers (heating rate: 10 K/min).

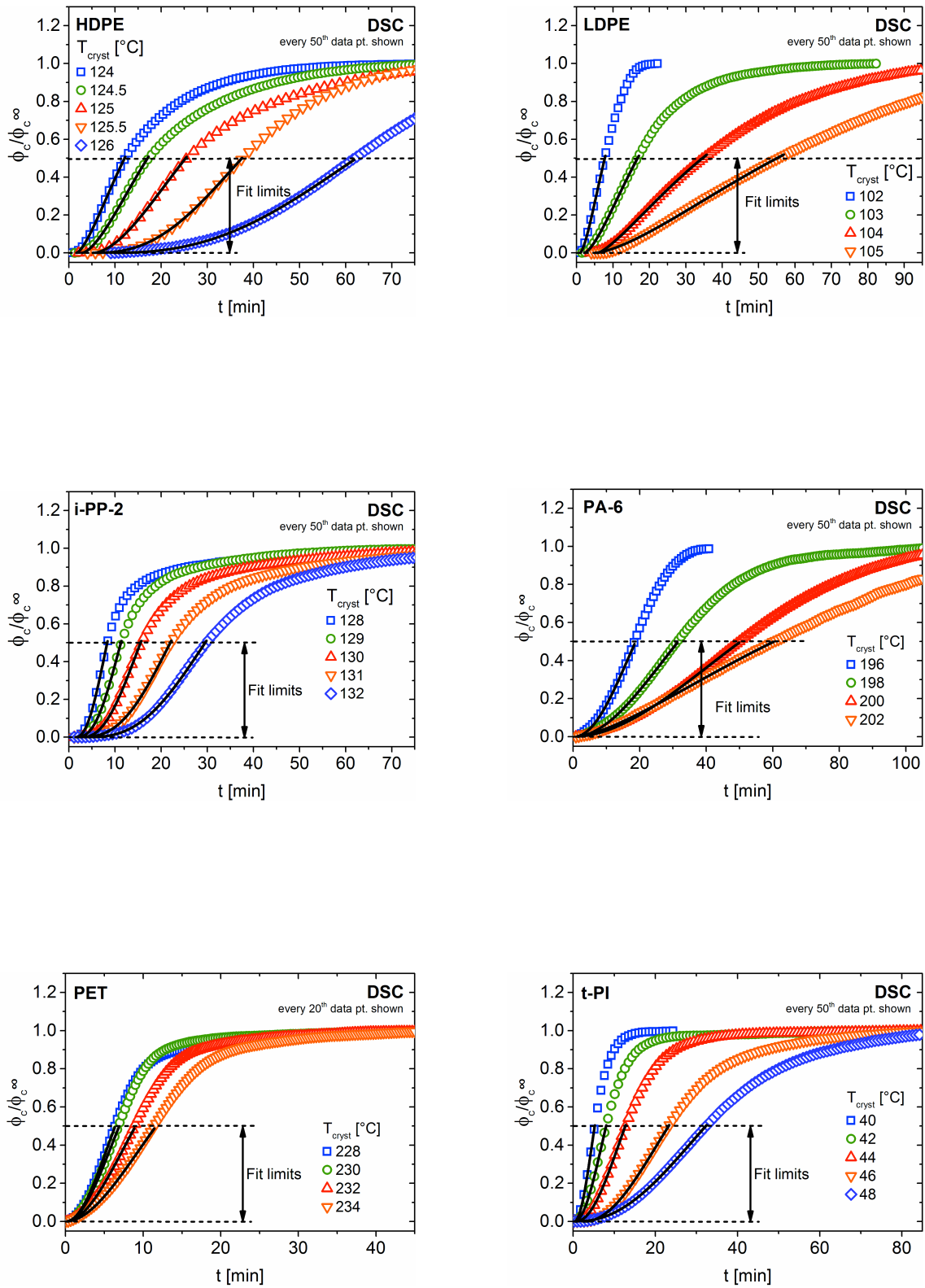


Figure A.5: Buildup of the relative crystallinity during isothermal crystallization as determined by DSC.

A.1.4 X-ray diffraction (XRD)

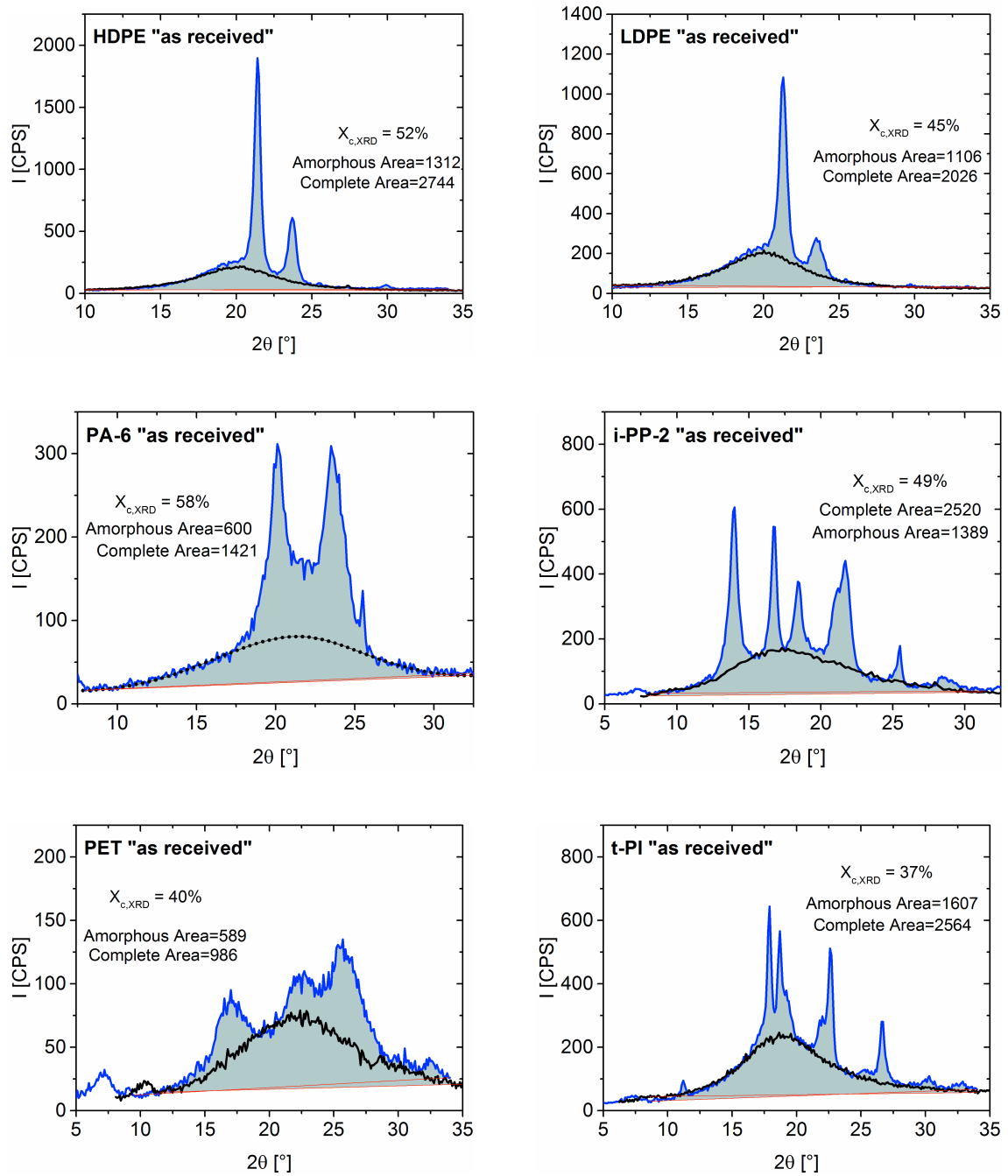


Figure A.6: X-ray diffractograms recorded at 30 °C (blue) for different neat polymer samples and shifted amorphous halos (black) from experiments on molten samples.

A.1.5 RheoNMR

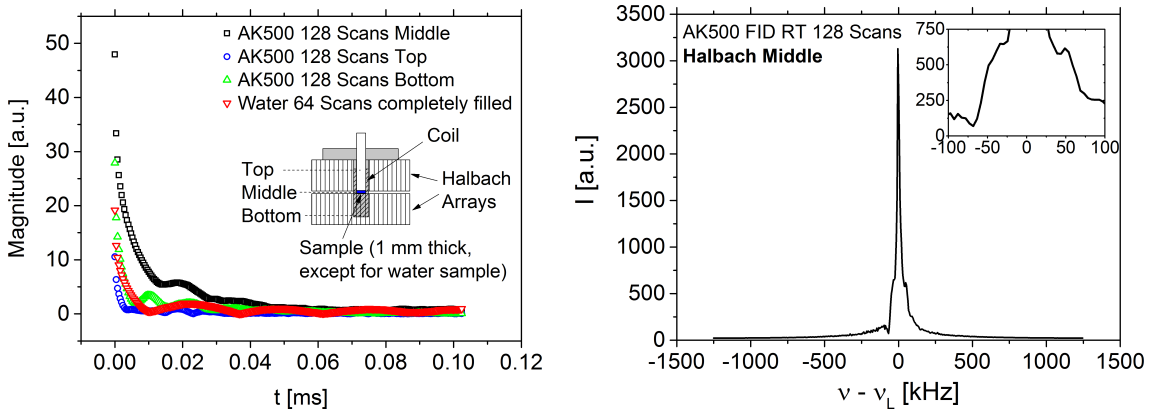


Figure A.7: Left: free induction decays of Wacker AK500 silicone oil (500 mPas, 1 mm sample height) and distilled water (completely filled NMR tube) for different positions in the Halbach magnet. Right: corresponding spectrum for the middle position ($\Delta\omega/2\pi \approx 50$ kHz).

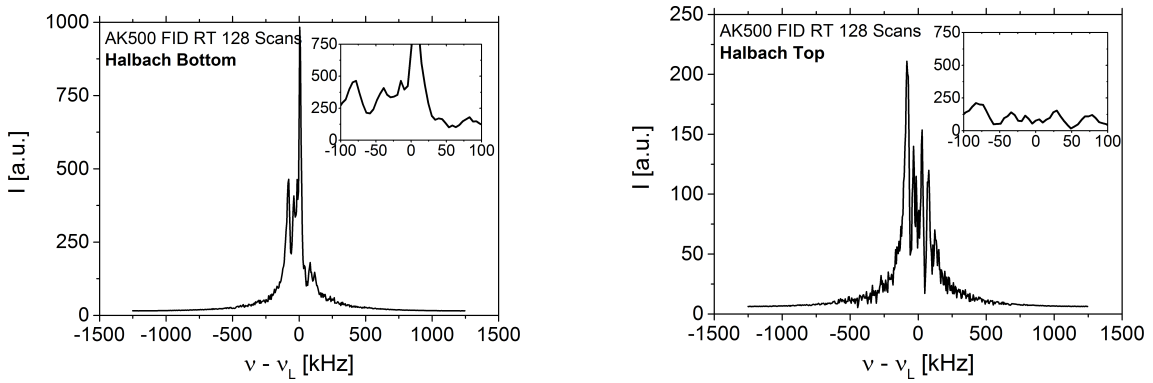


Figure A.8: ^1H -NMR spectra of Wacker AK500 silicone oil (500 mPas, 1 mm sample height) for different positions within the RheoNMR magnet.

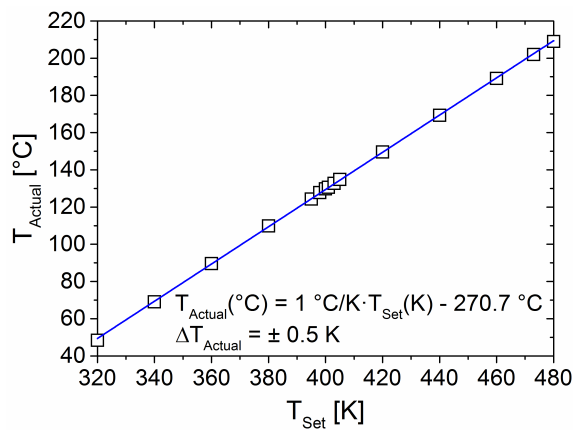


Figure A.9: RheoNMR temperature calibration using a digital thermometer and a type K thermocouple.

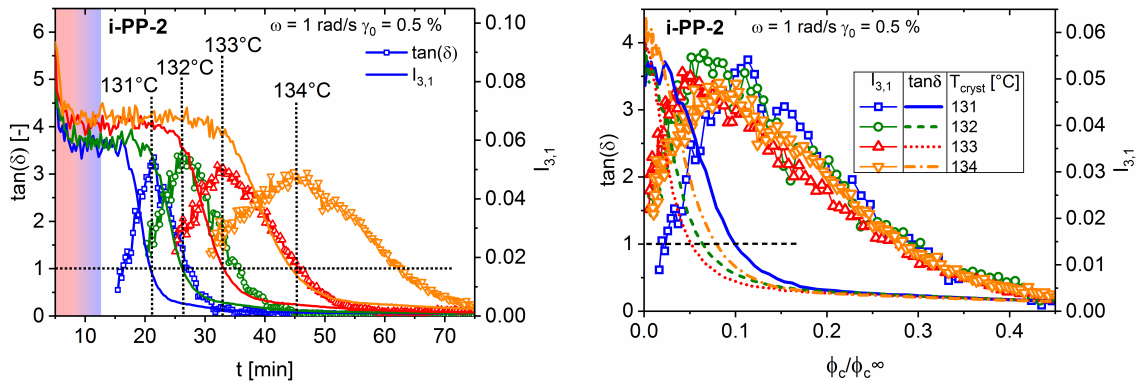


Figure A.10: Left: Loss tangent $\tan(\delta)$ and relative third harmonic $I_{3,1}$ vs. time for different isothermal crystallizations of i-PP-2. Right: corresponding correlation plot against the degree of space filling ϕ_c/ϕ_c^∞ (nonlinearity at lower and higher times not shown for clarity).

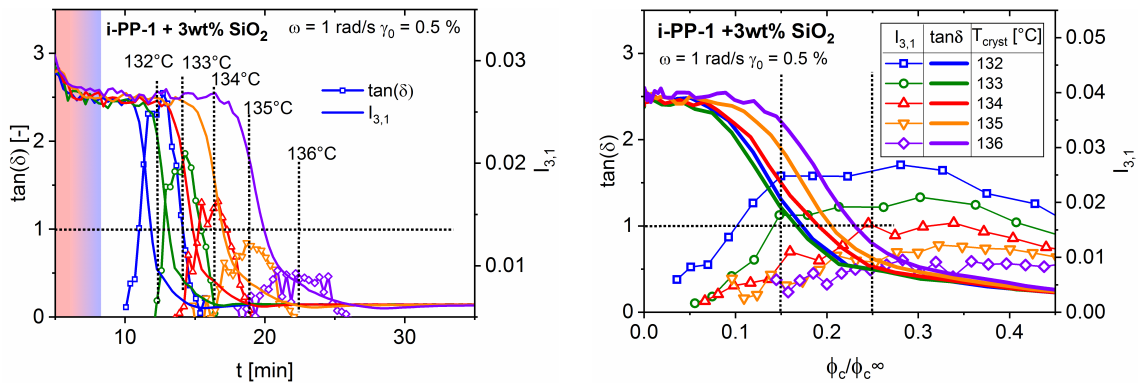


Figure A.11: Left: Loss tangent $\tan(\delta)$ and relative third harmonic $I_{3,1}$ vs. time for different isothermal crystallizations of i-PP-1 + 3wt% silica. Right: corresponding correlation plot against the degree of space filling ϕ_c/ϕ_c^∞ (nonlinearity at lower and higher times not shown for clarity).

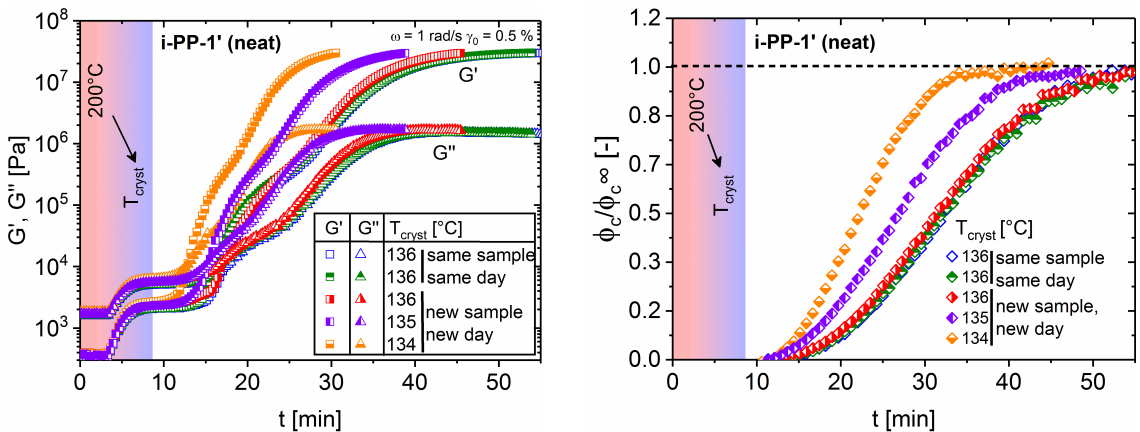


Figure A.12: Simultaneously acquired RheoNMR data for the crystallization of a neat isotactic polypropylene i-PP-1' at $T_{\text{cryst}} = 136^\circ\text{C}$. The repeatability is fairly high as the set-up was not disassembled between consecutive runs. However, an earlier crossover ($G' = G''$) was observed compared to older experiments, which was potentially due to an inhomogeneous temperature distribution.

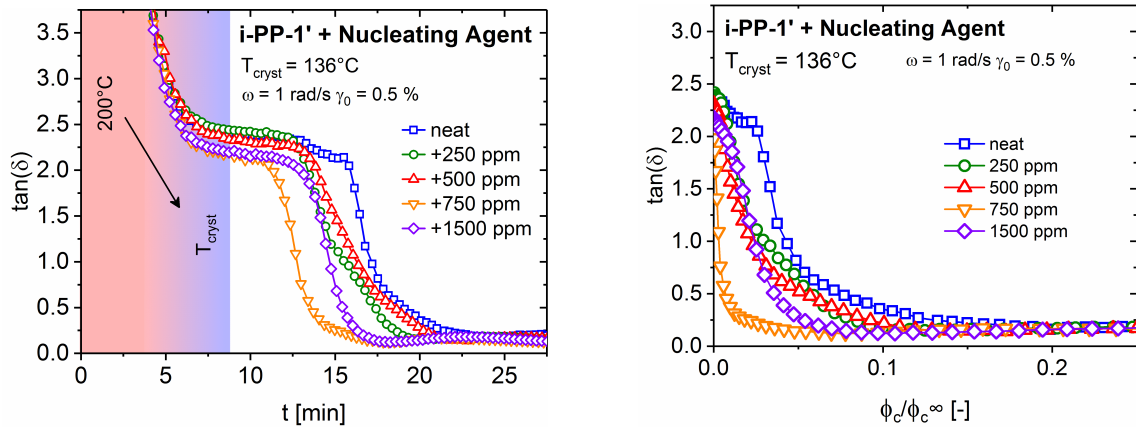


Figure A.13: Loss tangent $\tan(\delta)$ vs. time (left) and degree of space filling ϕ_c/ϕ_c^∞ (right) for isothermal crystallizations of i-PP-1' + different amounts of nucleating agent.

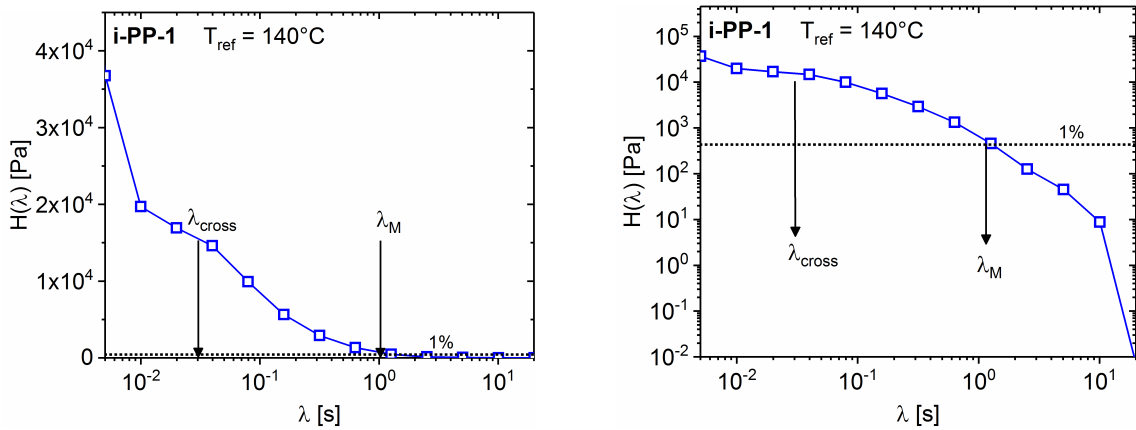


Figure A.14: Relaxation spectrum $H(\lambda)$ extracted from the mastercurve shown in Figure 6.27a.

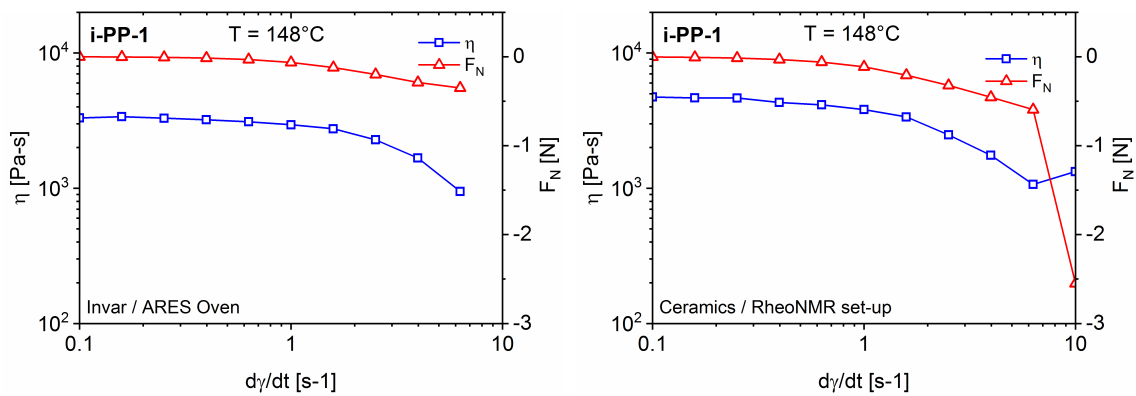


Figure A.15: Shear rate-dependent viscosity and normal force of i-PP-1 at 148 °C using the ARES oven + stainless steel geometry (left) and the RheoNMR set-up + ceramic geometries (right).

A.1.6 RheoSAXS

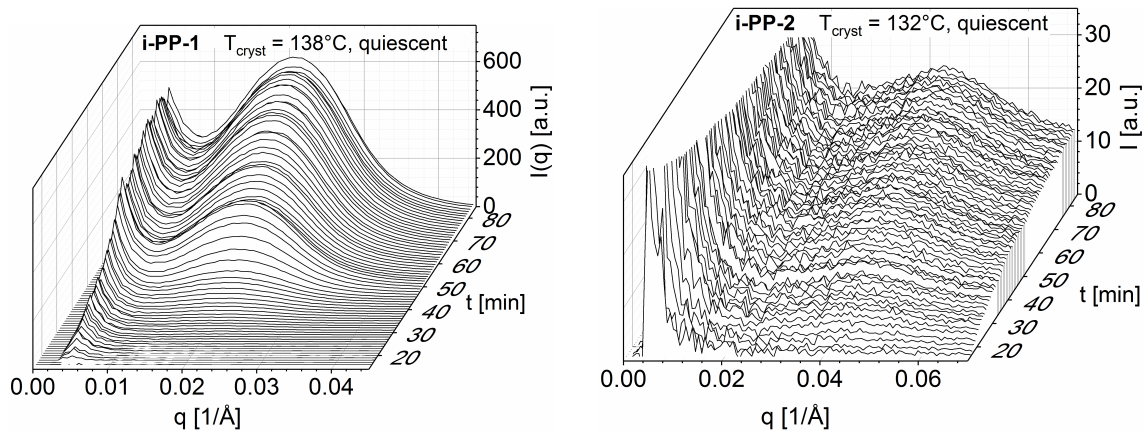


Figure A.16: Waterfall plots of radially averaged 2D-SAXS intensities for the quiescent crystallization of i-PP-1 at 138°C (top) and i-PP-2 at 132°C (bottom).

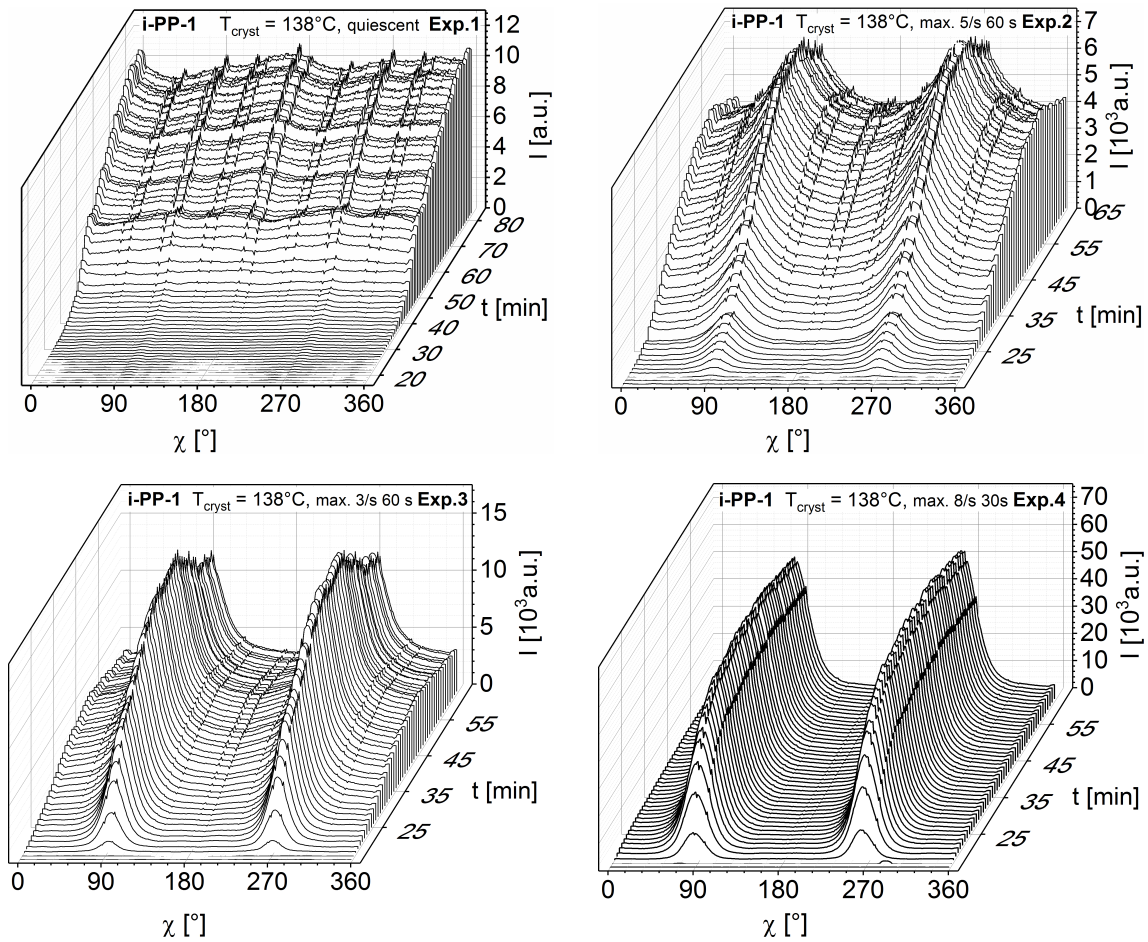


Figure A.17: Waterfall plots of azimuthally integrated 2D-SAXS intensity profiles for crystallizations of i-PP-1 at 138°C under different crystallization conditions.

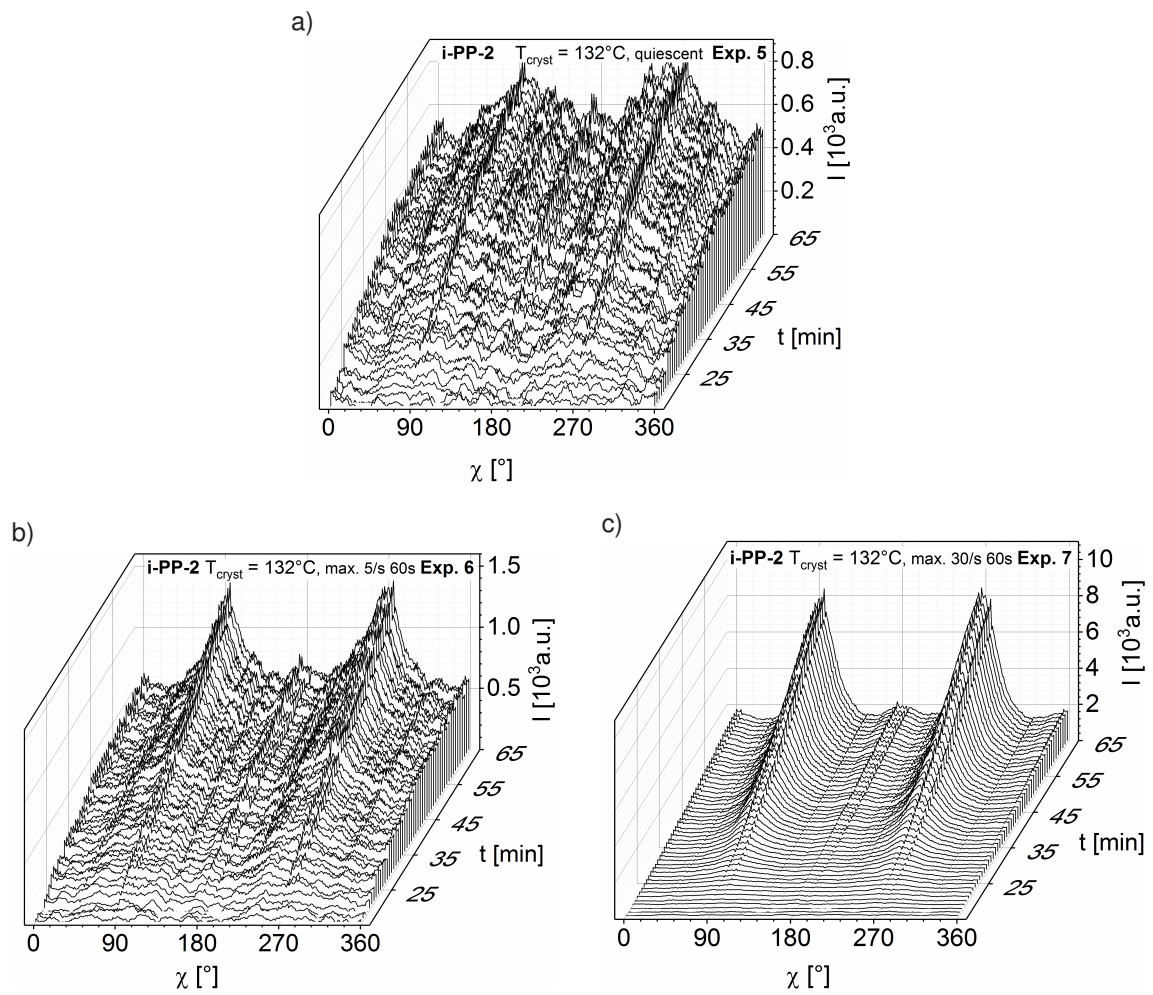


Figure A.18: Waterfall plots of azimuthally integrated 2D-SAXS intensity profiles for crystallizations of i-PP-2 at 132 °C under different crystallization conditions.

A.1.7 RheoMicroscopy

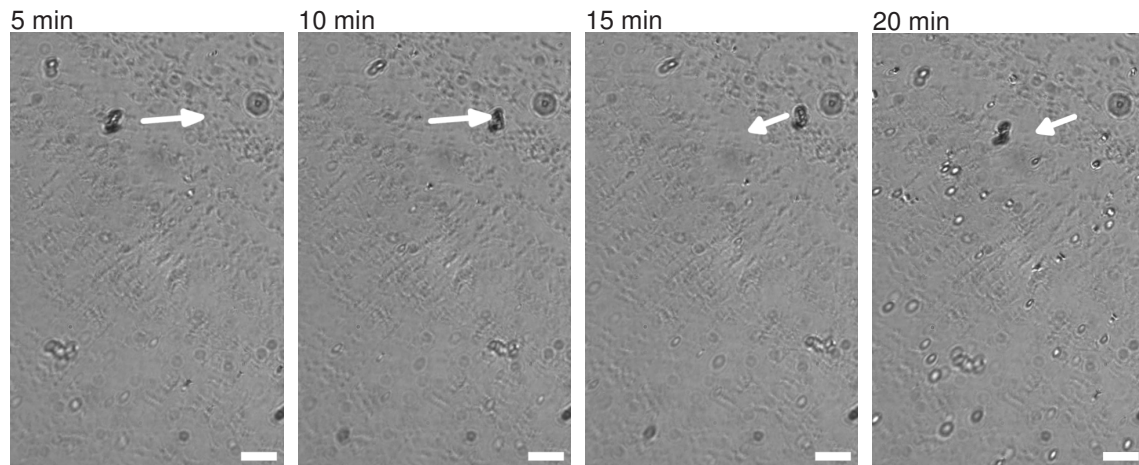


Figure A.19: Micrographs of i-PP-1 cooled from $T \approx 200$ °C to at $T_{\text{cryst}} \approx 138$ °C acquired using hyphenated RheoMicroscopy. Scale bar: 50 μm . The white arrow indicates the direction of intrinsic flow.

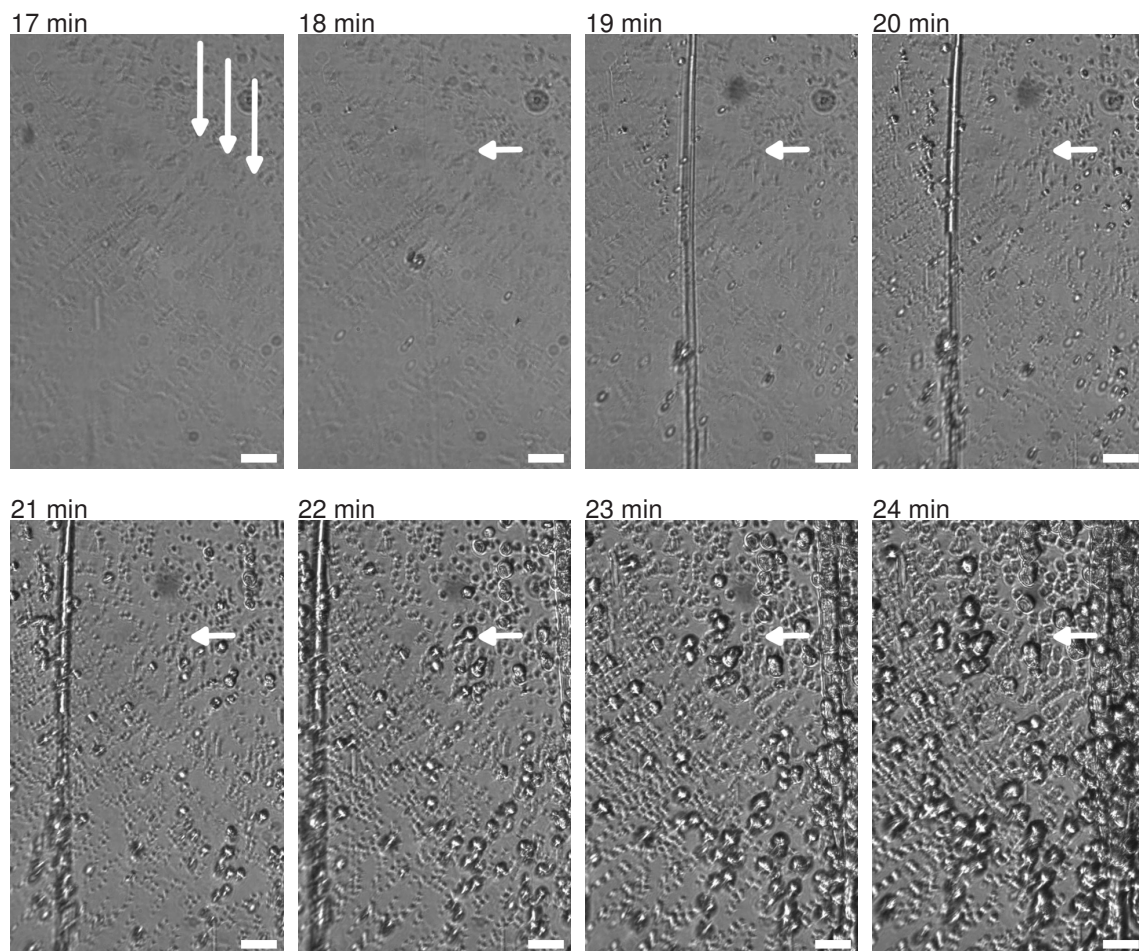


Figure A.20: Micrographs of i-PP-1 crystallized at $T_{\text{cryst}} \approx 138$ °C with a preceding steady-shear step of 24 kPa for 60 s acquired using hyphenated RheoMicroscopy. Scale bar: 50 μm . The white arrow indicates the direction of intrinsic flow.

A.1.8 Scanning electron microscopy (SEM)

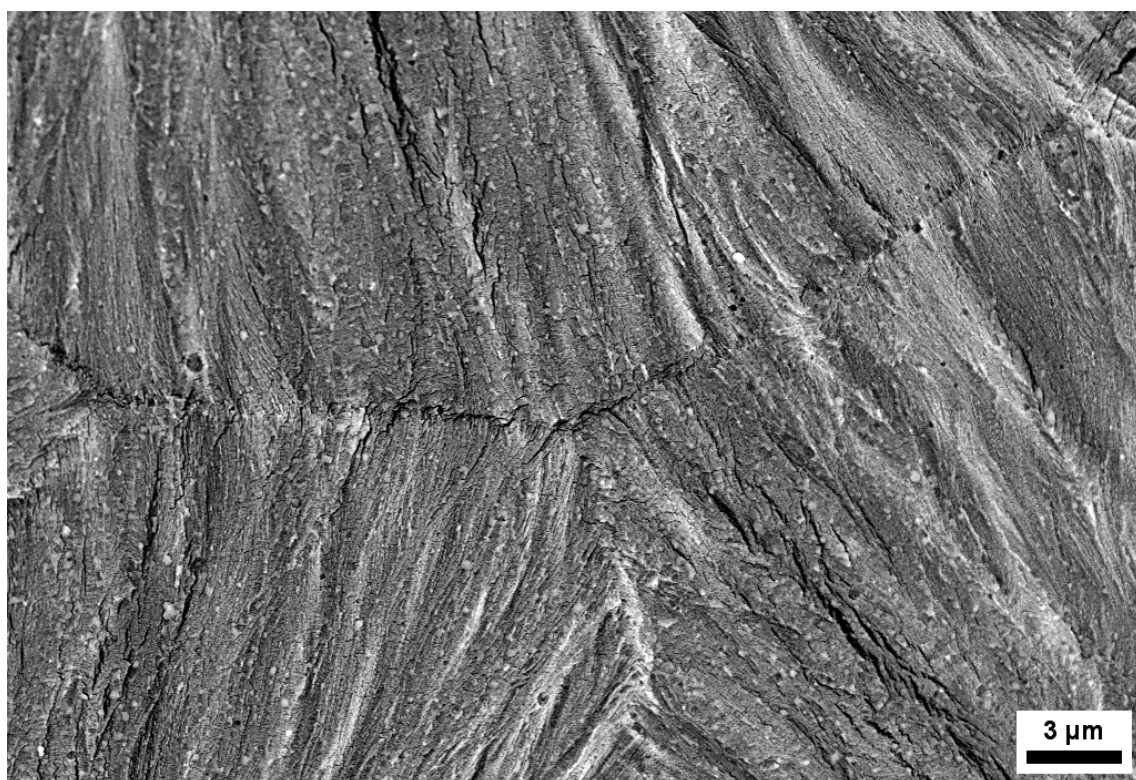
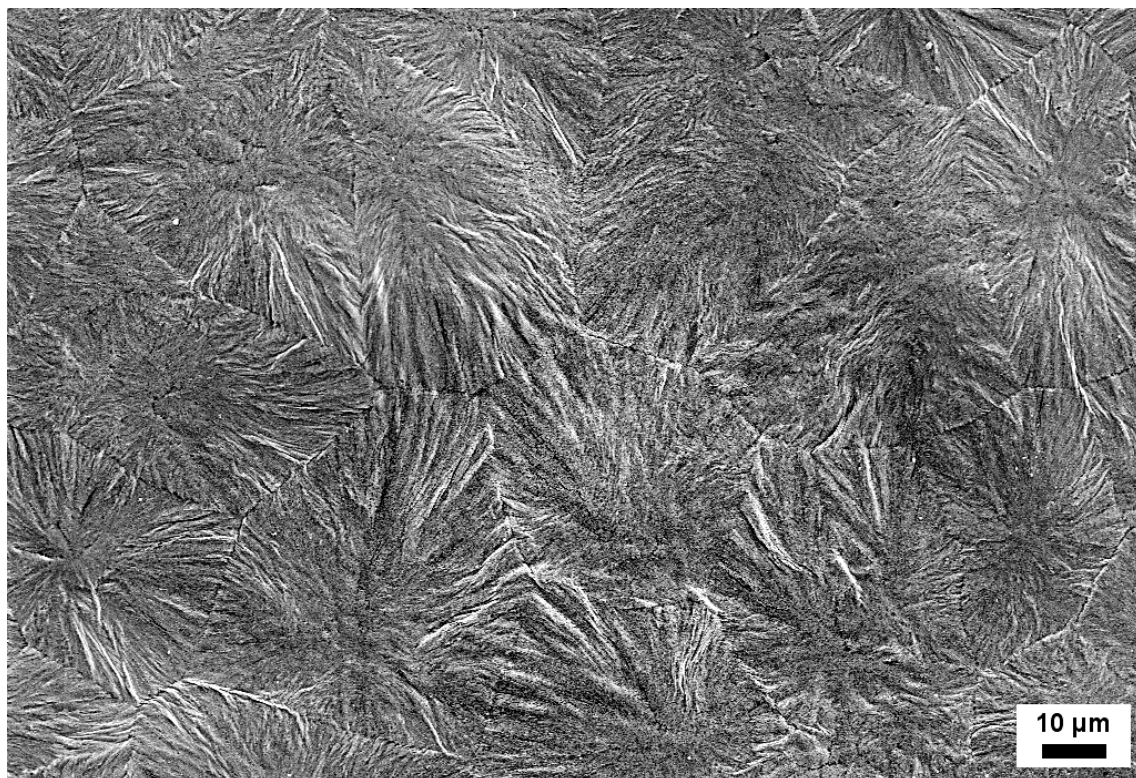


Figure A.21: SEM images of etched isothermally crystallized i-PP-1 at 131 °C under quiescent conditions with different magnifications.

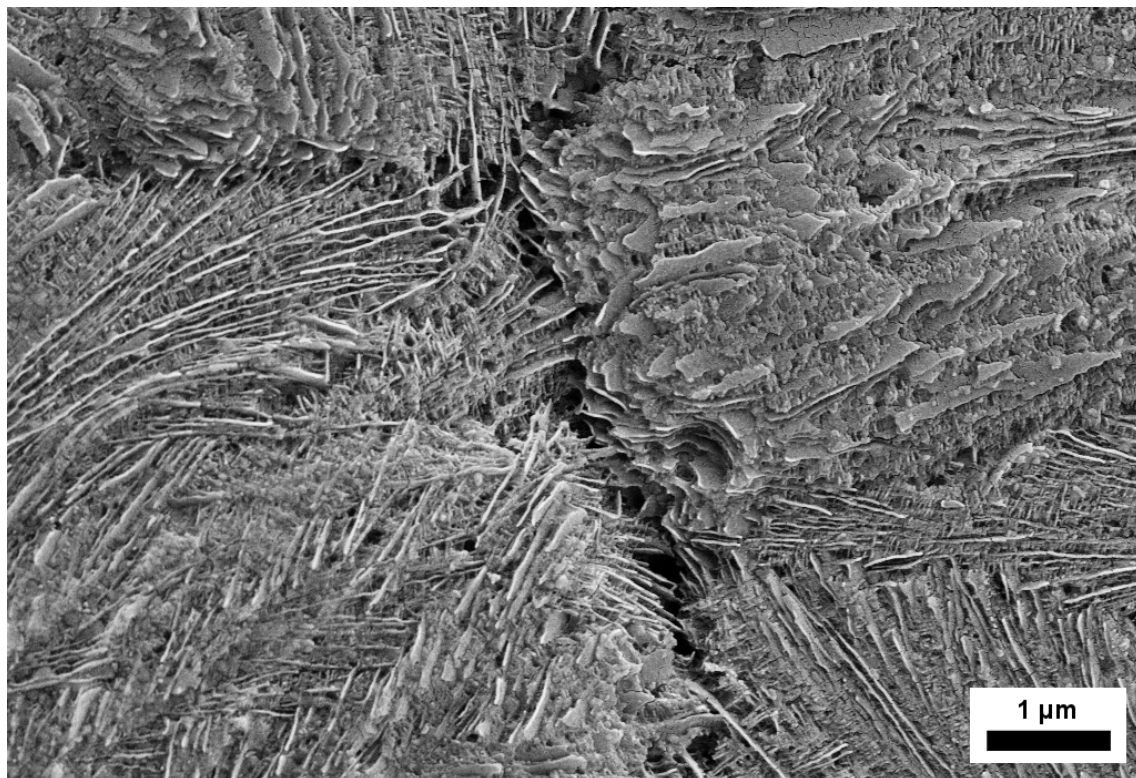
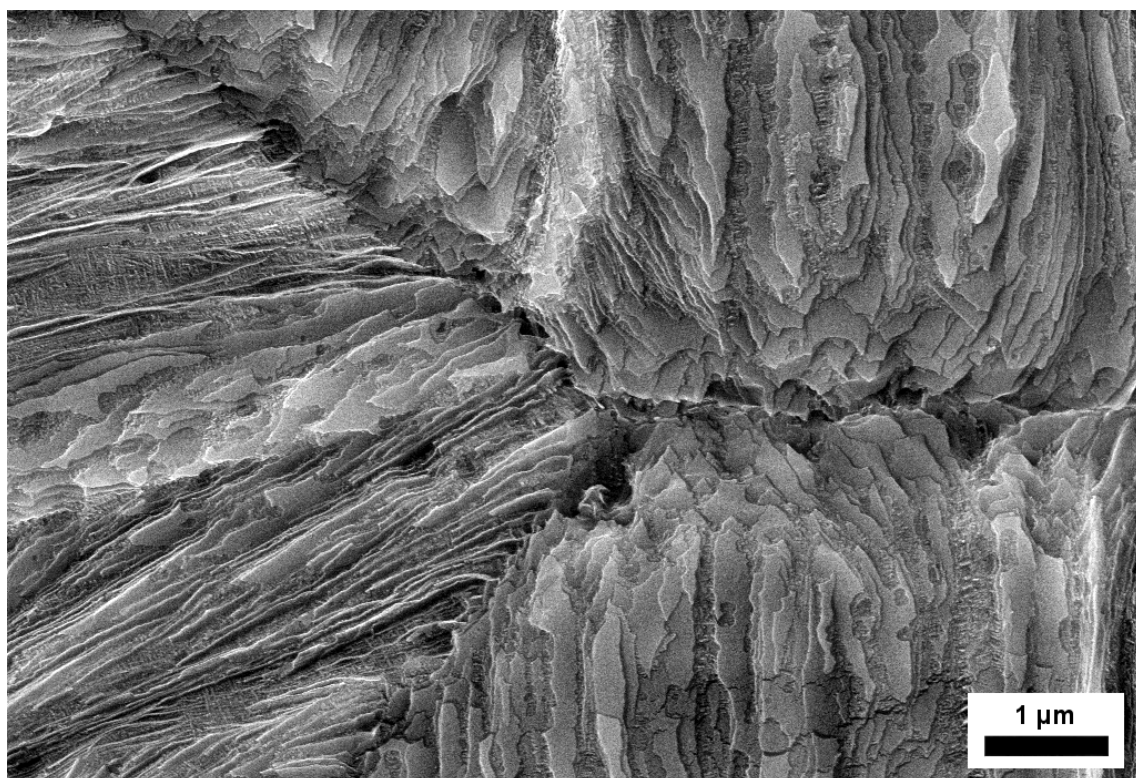


Figure A.22: SEM images of etched isothermally crystallized i-PP-1 at 136 °C under quiescent conditions recorded at different positions.

A.2 Photographs

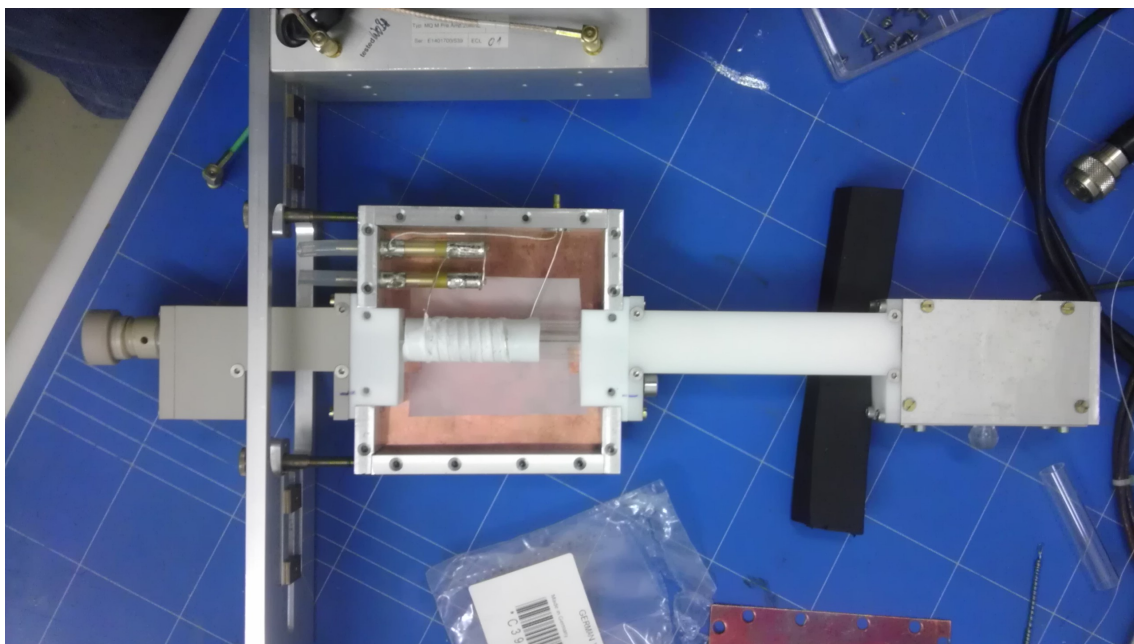


Figure A.23: High-temperature low-field NMR probe (20 MHz) with $Q \approx 150$, improved thermal insulation, and simplified match- and tunability.

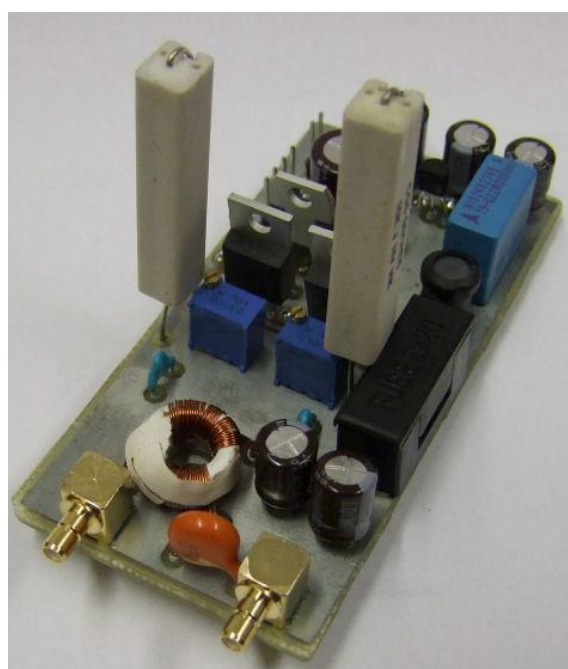


Figure A.24: Q-switch circuit.

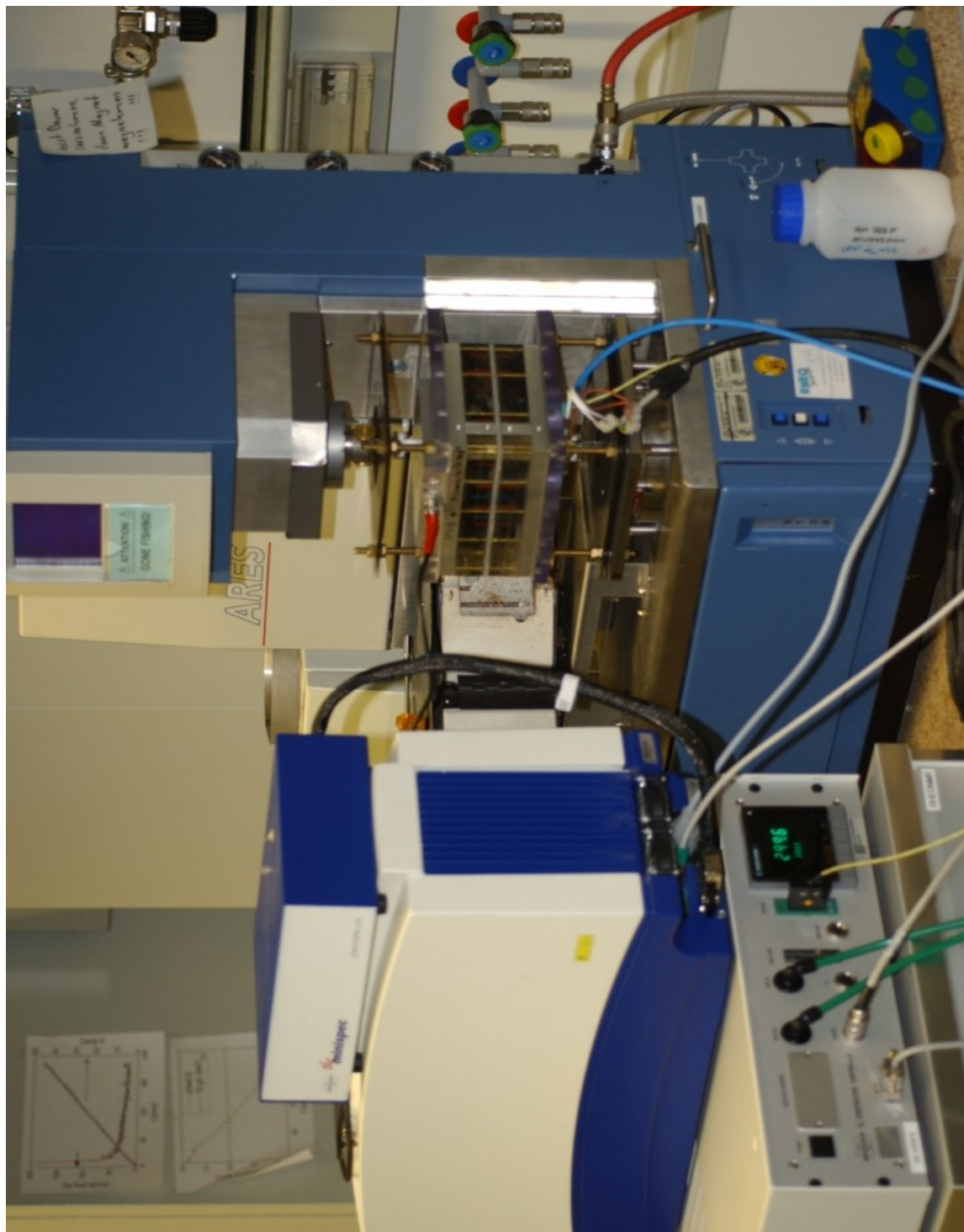


Figure A.25: Low-Field RheoNMR set-up used in chapter 6.

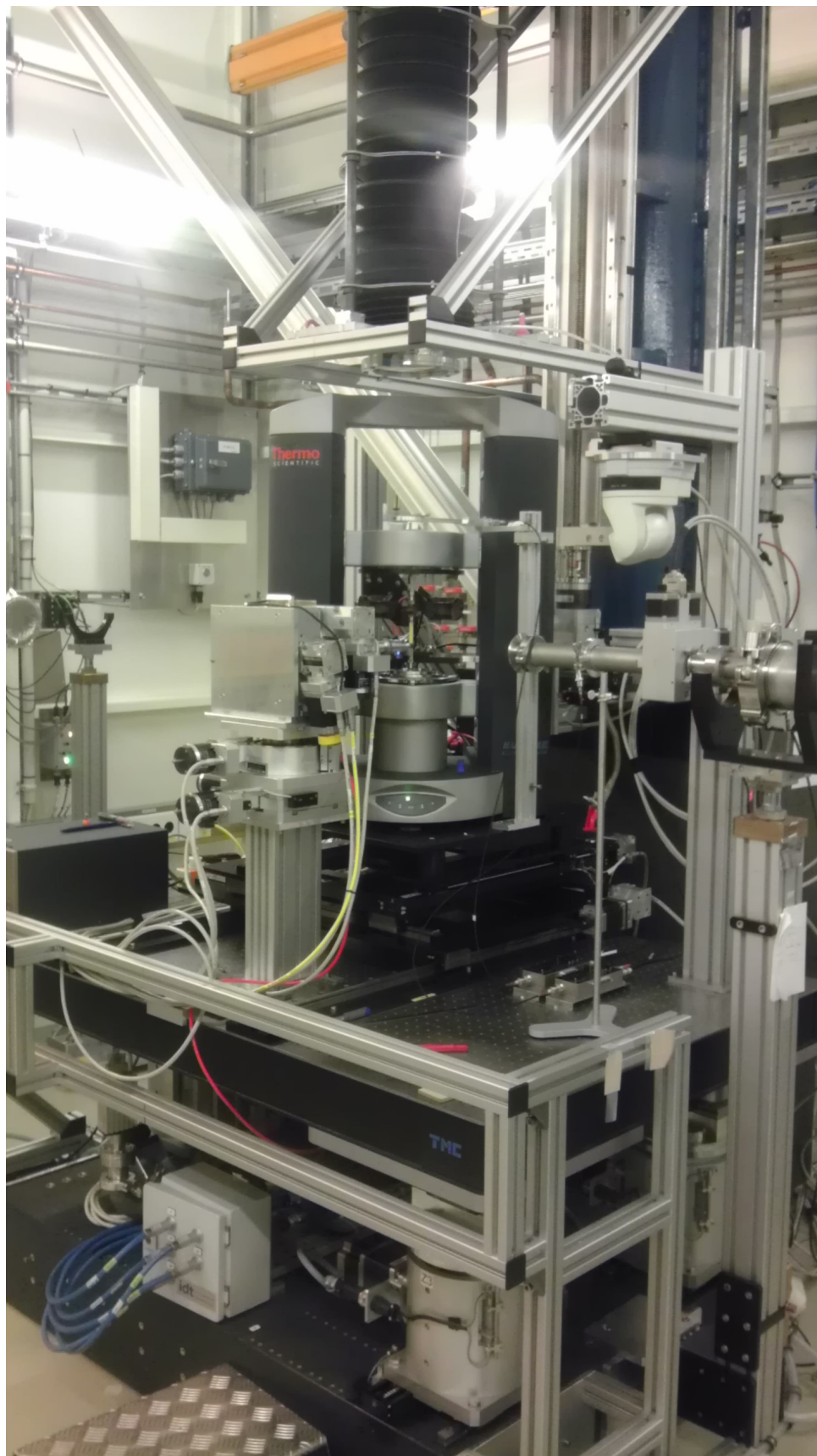


Figure A.26: RheoSAXS set-up at DESY (beamline P10) used in chapter 7.

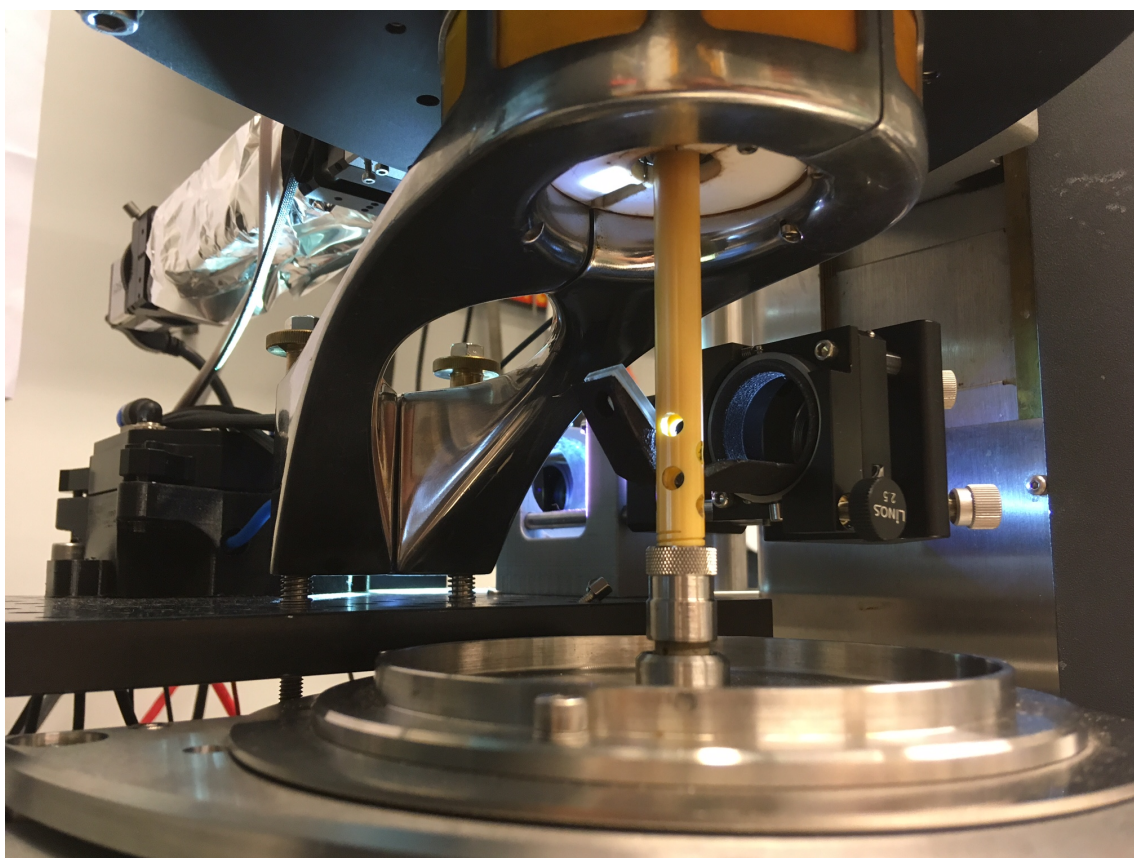
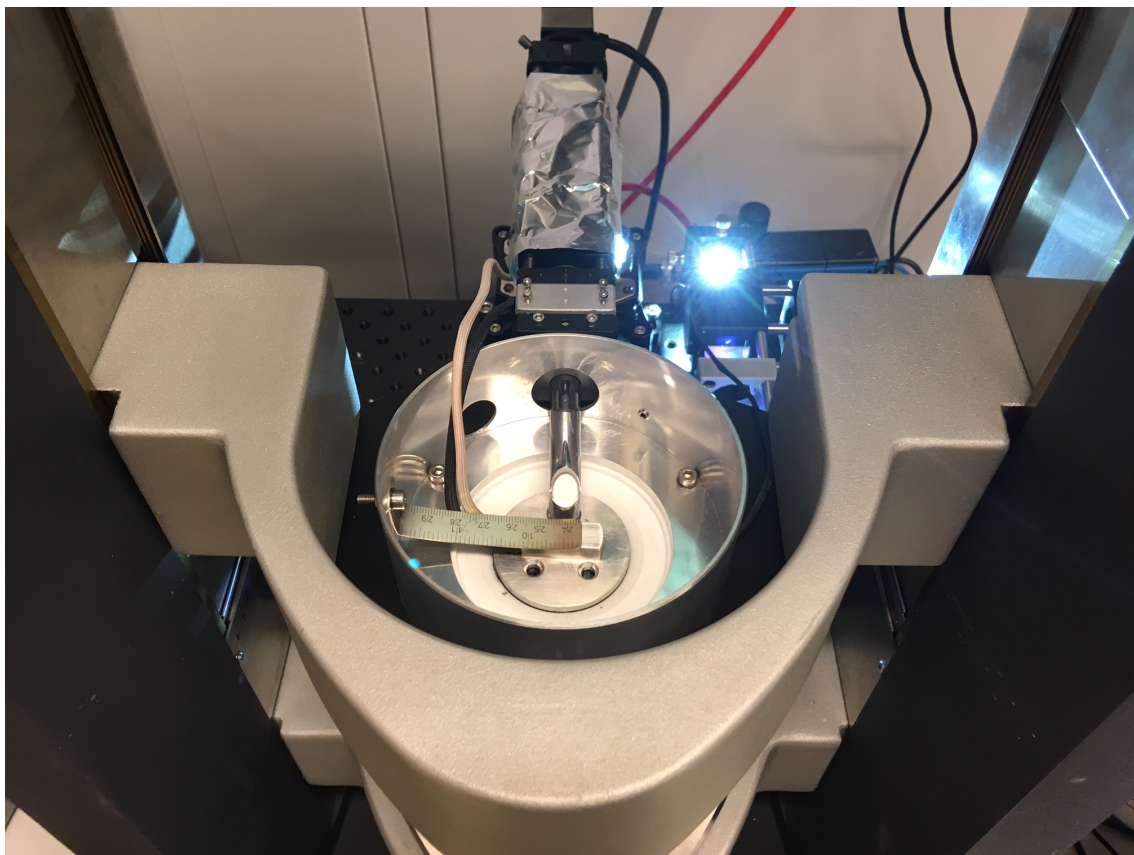


Figure A.27: RheoMicroscopy set-up at DESY used in chapter 8.

Nomenclature

Acronyms

CPMG	Carr-Purcell-Meiboom-Gill sequence
DSC	Differential scanning calorimetry
FID	Free induction decay
FT	Fourier transform
GPC	Gel permeation chromatography
HDPE	High-density polyethylene
HL theory	Hoffman-Lauritzen theory
i-PP	Isotactic polypropylene
LAOS	Large amplitude oscillatory shear
LDPE	Low-density polyethylene
LLDPE	Linear low-density polyethylene
MAOS	Medium amplitude oscillatory shear
MAS	Magic angle spinning
MSE	Magic sandwich echo
NMR	Nuclear magnetic resonance
PA-6	Polyamide 6
PBMA	Poly(butyl methacrylate)
PE	Polyethylene
PET	Polyethylene terephthalate
PLOM / PLM	Polarized light optical microscopy
PS	Polystyrene
SAOS	Small amplitude oscillatory shear
SAXS	Small-angle X-ray scattering
SE	Solid echo
SEM	Scanning electron microscopy
t-PI	Trans-1,4 polyisoprene
WAXS	Wide-angle X-ray scattering
WLF model	Williams-Landel-Ferry model
XRD	X-ray diffraction

Greek Symbols

χ	Azimuthal scattering angle
δ	Phase angle
η	Viscosity

η^*	Complex viscosity
γ	Magnetogyric ratio
γ	Strain
$\dot{\gamma}$	Strain rate
λ	Relaxation time
$\hat{\mu}$	Magnetic moment
ν	Frequency
ω	Angular frequency
ω_L	Larmor angular frequency
ϕ	Pulse phase
ϕ_c	Volume crystallinity
$\psi(t)$	Wave function
ρ	Density
σ	Stress
τ	Time
θ	Scattering angle

Roman Symbols

A	Amplitude
A	Area
a_T	Shift factor
\vec{B}	Magnetic field
d	Long period
De	Deborah number
E	Energy
f	Frequency
\vec{F}	Force
G	Gibbs free energy
G	Shear modulus
g	Lateral spreading rate
G	Radial growth rate
G'	Storage modulus
G''	Loss modulus
$G(\tau)$	Autocorrelation / memory function
G^*	Complex shear modulus
H	Free enthalpy
h	Height
h	Planck constant ($\sim 6.6 \cdot 10^{-34}$ J s)
\hat{H}	Hamiltonian
\hbar	Reduced Planck constant ($\sim 1 \cdot 10^{-34}$ J s)
$H(\lambda)$	Relaxation time distribution
I	Intensity

I	Nucleation rate
i	Secondary nucleation rate
\hat{I}	Spin angular moment
I_{31}	Third harmonic normalized to the fundamental
$J(\omega)$	Spectral density
K	Avrami rate
k	Boltzmann constant ($\sim 1.4 \cdot 10^{-23}$ J/K)
K_g	Secondary nucleation constant
L	Length
m	Magnetic quantum number
m	Mass
\vec{M}	Magnetization
N	Number
n	Avrami dimensionality
n	Number
P	Probability
Q	NMR probe quality factor
\vec{q}	Scattering vector
r	Radius
S	Entropy
T	Temperature
t	Time
T_1	Longitudinal / spin-lattice relaxation time
T_2	Transverse / spin-spin relaxation time
$T_{1\rho}$	Spin-lattice relaxation time in the rotating frame
V	Volume
\vec{p}	Momentum
Wi	Weissenberg number
x	Length
X_c	Mass crystallinity

References

- Abbasi, S., Carreau, P. J., Derdouri, A. and Moan, M. (2009), *Rheol. Acta* 48:943–959.
- Abragam, A. (1989), *Principles of Nuclear Magnetic Resonance*, Vol. 32 of *International Series of Monographs on Physics*, Oxford Science Publications.
- Acierno, S., Coppola, S., Grizzuti, N. and Maffettone, P. L. (2002), *Macromol. Symp.* 185:233–241.
- Agarwal, P. K., Somani, R. H., Weng, W., Mehta, A., Yang, L., Ran, S., Liu, L. and Hsiao, B. S. (2003), *Macromolecules* 36:5226–5235.
- Aissani, S., Guendouz, L. and Canet, D. (2014), *Concepts Magn. Reson.* 44:12–17.
- Akagawa, S. and Odagaki, T. (2007), *Phys. Rev. E* 76:051402(1–5).
- Andrady, A. L. (2011), *Mar. Pollut. Bull.* 62:1596–1605.
- Andrew, E. and Jurga, K. (1987), *J. Magn. Reson.* 73:268–276.
- Anklin, C., Rindlisbacher, M., Otting, G. and Laukien, F. (1995), *J. Magn. Reson.* 106:199–201.
- AOCS-Cd 16-81 (2009), *American Oil Chemists Society* pp. 1–5.
- AOCS-Cd 16b-93 (1997), *American Oil Chemists Society* pp. 1–13.
- Arlman, E. (1964), *J. Catal.* 3:89–98.
- Arlman, E. and Cossee, P. (1964), *J. Catal.* 3:99–104.
- Armitstead, K., Goldbeck-Wood, G. and Keller, A. (1992), *Macromolecules: synthesis, order and advanced properties* pp. 219–312.
- Auriemma, M., Piscitelli, A., Pasquino, R., Cerruti, P., Malinconico, M. and Grizzuti, N. (2015), *Eur. Polym. J.* 63:123–131.
- Avrami, M. (1939), *J. Chem. Phys.* 7:1103–1112.
- Avrami, M. (1940), *J. Chem. Phys.* 8:212–224.
- Avrami, M. (1941), *J. Chem. Phys.* 9:177–184.
- Baert, J. and Van Puyvelde, P. (2008), *Macromol. Mater. Eng.* 293:255–273.
- Baltá-Calleja, F. J. and Vonk, C. G. (1989), *X-ray scattering of synthetic polymers*, Vol. 8, Elsevier.
- Balzano, L., Kukalyekar, N., Rastogi, S., Peters, G. W. and Chadwick, J. C. (2008), *Phys. Rev. Lett.* 100:048302(1–4).
- Balzano, L., Ma, Z., Cavallo, D., van Erp, T. B., Fernandez-Ballester, L. and Peters, G. W. (2016), *Macromolecules* 49:3799–3809.
- Balzano, L., Rastogi, S. and Peters, G. W. (2009), *Macromolecules* 42:2088–2092.
- Barham, P., Chivers, R., Keller, A., Martinez-Salazar, J. and Organ, S. (1985), *J. Mater. Sci.* 20:1625–1630.
- Baugh, L. S. and Canich, J. A. M. (2007), *Stereoselective polymerization with single-site catalysts*, CRC Press.

- Baumgaertel, M., De Rosa, M., Machado, J., Masse, M. and Winter, H. (1992), *Rheol. Acta* 31:75–82.
- Becker, R. and Döring, W. (1935), *Ann. Physik* 416:719–752.
- Berghausen, J., Fuchs, J. and Richtering, W. (1997), *Macromolecules* 30:7574–7581.
- Berghausen, J., Zipfel, J., Diat, O., Narayanan, T. and Richtering, W. (2000), *Phys. Chem. Chem. Phys.* 2:3623–3626.
- Bergmann, K. (1978), *J. Polym. Sci.* 16:1611–1634.
- Bergmann, K. (1981), *Polym. Bull.* 5:355–360.
- Bergmann, K. and Nawotki, K. (1967), *Colloid Polym. Sci.* 219:132–144.
- Bernland, K., Goossens, J., Smith, P. and Tervoort, T. A. (2016), *J. Polym. Sci.* pp. 865–874.
- Bernland, K. M. (2010), *Nucleating and Clarifying Polymers*, Swiss Federal Institute of Technology (ETHZ), Zurich, Switzerland.
- Bernland, K., Tervoort, T. and Smith, P. (2009), *Polymer* 50:2460–2464.
- Binder, K. and Fratzl, P. (2005), *Spinodal Decomposition*, Wiley-VCH, pp. 409–480.
- Bloch, F. (1946), *Phys. Rev.* 70:460–474.
- Bloch, F., Hansen, W. W. and Packard, M. (1946), *Phys. Rev.* 70:474–485.
- Block, C., Van Mele, B., Van Puyvelde, P. and Van Assche, G. (2013), *React. Funct. Polym.* 73:332–339.
- Bloembergen, N., Purcell, E. M. and Pound, R. V. (1948), *Phys. Rev.* 73:679–712.
- Blomenhofer, M., Ganzleben, S., Hanft, D., Schmidt, H.-W., Kristiansen, M., Smith, P., Stoll, K., Mäder, D. and Hoffmann, K. (2005), *Macromolecules* 38:3688–3695.
- Bossart, J. and Oettinger, H. C. (1995), *Macromolecules* 28:5852–5860.
- Boulet-Audet, M., Vollrath, F. and Holland, C. (2011), *Phys. Chem. Chem. Phys.* 13:3979–3984.
- Boyd, R. H. (1985a), *Polymer* 26:323–347.
- Boyd, R. H. (1985b), *Polymer* 26:1123–1133.
- Bärenwald, R., Champouret, Y., Saalwächter, K. and Schäler, K. (2012), *J. Phys. Chem. B* 116:13089–13097.
- Bärenwald, R., Goerlitz, S., Godehardt, R., Osichow, A., Tong, Q., Krumova, M., Mecking, S. and Saalwächter, K. (2014), *Macromolecules* 47:7677–7678.
- Brintzinger, H. H., Fischer, D., Mülhaupt, R., Rieger, B. and Waymouth, R. M. (1995), *Angew. Chem. Int. Ed.* 34:1143–1170.
- Bruker, I. (1986), *Rheol. Acta* 25:501–506.
- Bruker, I. and Lodge, A. S. (1985), *J. Rheol.* 29:557–577.
- Busico, V. and Cipullo, R. (2001), *Prog. Polym. Sci.* 26:443–533.
- Byelov, D., Panine, P., Remerie, K., Biemond, E., Alfonso, G. C. and de Jeu, W. H. (2008), *Polymer* 49:3076–3083.
- Cahn, J. W. (1961), *Acta Metall.* 9:795–801.
- Cahn, J. W. and Hilliard, J. E. (1959), *J. Chem. Phys.* 31:688–699.

- Callaghan, P. T. (1999), *Rep. Prog. Phys.* 62:599–670.
- Callaghan, P. T. (2006), *Curr. Opin. Colloid Interface Sci.* 11:13–18.
- Callaghan, P. T. (2008), *Rheol. Acta* 47:243–255.
- Callaghan, P. T. and Gil, A. M. (2000), *Macromolecules* 33:4116–4124.
- Callaghan, P. T. and Komlosh, M. E. (2002), *Magn. Reson. Chem.* 40:S15–S19.
- Capaccioli, S., Prevosto, D., Best, A., Hanewald, A. and Pakula, T. (2007), *J. Non-Cryst. Solids* 353:4267–4272.
- Carr, H. Y. and Purcell, E. M. (1954), *Phys. Rev.* 94:630–638.
- Castelletto, V., Hamley, I., Holmqvist, P., Rekasas, C., Booth, C. and Grossmann, J. (2001), *Colloid Polym. Sci.* 279:621–628.
- Castelletto, V., Hamley, I., Yuan, X.-F., Kelarakis, A. and Booth, C. (2005), *Soft Matter* 1:138–145.
- Chai, C., Dixon, N., Gerrard, D. and Reed, W. (1995), *Polymer* 36:661–663.
- Champion, J., Gate, L., Meeten, G. and Wood, P. (1996), *Colloids Surf., A* 111:223–229.
- Chanda, M. and Roy, S. K. (2006), *Plastics technology handbook*, CRC press.
- Chen, Z.-R. and Kornfield, J. A. (1998), *Polymer* 39:4679–4699.
- Chevrel, M.-C., Hoppe, S., Falk, L., Nadège, B., Chapron, D., Bourson, P. and Durand, A. (2012), *Ind. Eng. Chem. Res.* 51:16151–16156.
- Chu, B. and Hsiao, B. S. (2001), *Chem. Rev.* 101:1727–1762.
- Conradi, M. S. (1977), *Rev. Sci. Instrum.* 48:359–361.
- Coppola, S., Balzano, L., Gioffredi, E., Maffettone, P. L. and Grizzuti, N. (2004), *Polymer* 45:3249–3256.
- Coppola, S., Grizzuti, N. and Maffettone, P. L. (2001), *Macromolecules* 34:5030–5036.
- Corver, J., Guthausen, G. and Kamlowski, A. (2005), *Pharm. Eng.* 25:18–30.
- Cossee, P. (1964), *J. Catal.* 3:80–88.
- Crawford, R. J. (1998), *Plastics engineering*, Butterworth-Heinemann.
- Cser, F. (2001), *J. Appl. Polym. Sci.* 80:2300–2308.
- Custódio, F. J., Steenbakkens, R. J., Anderson, P. D., Peters, G. W. and Meijer, H. E. (2009), *Macromol. Theory Simul.* 18:469–494.
- Cziep, M. A., Abbasi, M., Heck, M., Arens, L. and Wilhelm, M. (2016), *Macromolecules* 49:3566–3579.
- Dadayli, D., Harris, R. K., Kenwright, A. M., Say, B. J. and Sünnetçioğlu, M. M. (1994), *Polymer* 35:4083–4087.
- Davis, G. and Eby, R. (1973), *J. Appl. Phys.* 44:4274–4281.
- De Rosa, C., Auriemma, F., Paolillo, M., Resconi, L. and Camurati, I. (2005), *Macromolecules* 38:9143–9154.
- De Santis, F., Pantani, R. and Titomanlio, G. (2016), *Polymer* 90:102–110.
- Dealy, J. M. and Larson, R. G. (2006), *Structure and rheology of molten polymers*, Hanser.
- Dealy, J. M. and Wang, J. (2013), *Melt rheology and its applications in the plastics industry*, Springer.

- Demco, D. E., Fechete, R. and Blümich, B. (2003), *Chem. Phys. Lett.* 375:406–412.
- Derbyshire, W., Van den Bosch, M., Van Dusschoten, D., MacNaughtan, W., Farhat, I., Hemminga, M. and Mitchell, J. (2004), *J. Magn. Reson.* 168:278–283.
- Dietz, W., White, J. L. and Clark, E. S. (1978), *Polym. Eng. Sci.* 18:273–281.
- Dötsch, T., Pollard, M. and Wilhelm, M. (2003), *J. Phys.: Condens. Matter* 15:S923–S931.
- Duplay, C., Monasse, B., Haudin, J.-M. and Costa, J.-L. (2000), *J. Mater. Sci.* 35:6093–6103.
- Eberle, A. P. and Porcar, L. (2012), *Curr. Opin. Colloid Interface Sci.* 17:33–43.
- Eckman, R., Henrichs, P. and Peacock, A. (1997), *Macromolecules* 30:2474–2481.
- Eder, G. and Janeschitz-Kriegl, H. (1988), *Colloid Polym. Sci.* 266:1087–1094.
- Eder, G., Janeschitz-Kriegl, H. and Liedauer, S. (1990), *Prog. Polym. Sci.* 15:629–714.
- Eder, G., Janeschitz-Kriegl, H. and Liedauer, S. (1992), *Influence of flow on the crystallization kinetics of polymers*, Springer, pp. 129–131.
- Egres, R. G., Nettesheim, F. and Wagner, N. J. (2006), *J. Rheol.* 50:685–709.
- Elmoumni, A., Gonzalez-Ruiz, R. A., Coughlin, E. B. and Winter, H. H. (2005), *Macromol. Chem. Phys.* 206:125–134.
- Elmoumni, A. and Winter, H. H. (2006), *Rheol. Acta* 45:793–801.
- Elmoumni, A., Winter, H. H., Waddon, A. J. and Fruitwala, H. (2003), *Macromolecules* 36:6453–6461.
- Elsner, P., Eyerer, P. and Hirth, T., eds (2012), *Kunststoffe: Eigenschaften und Anwendungen*, Springer.
- Ewoldt, R. H., Hosoi, A. and McKinley, G. H. (2008), *J. Rheol.* 52:1427–1458.
- Ezquerro, T., Lopez-Cabarcos, E., Hsiao, B. and Balta-Calleja, F. (1996), *Phys. Rev. E* 54:989–992.
- Feio, G., Buntinx, G. and Cohen-Addad, J. (1989), *J. Polym. Sci.* 27:1–24.
- Feio, G. and Cohen-Addad, J. (1988), *J. Polym. Sci.* 26:389–412.
- Fermi, E. (1950), *Nuclear physics: a course given by Enrico Fermi at the University of Chicago*, University of Chicago Press.
- Frank, F. (1974), *J. Cryst. Growth* 22:233–236.
- Frenkel, J. (1946), *Kinetic Theory of Liquids*, Clarendon Press.
- Friedenberg, M. C., Fuller, G. G., Frank, C. W. and Robertson, C. R. (1996), *Macromolecules* 29:705–712.
- Fritzsche, K. J., Mao, K. and Schmidt-Rohr, K. (2017), *Macromolecules* 50:1521–1540.
- Fujimoto, K., Nishi, T. and Kado, R. (1972), *Polym. J.* 3:448–462.
- Fukuyama, Y., Kawai, T., Kuroda, S.-i., Toyonaga, M., Taniike, T. and Terano, M. (2013), *J. Therm. Anal. Calorim.* 113:1511–1519.
- Fuller, G. G. (1995), *Optical rheometry of complex fluids*, Oxford University Press.
- Galvosas, P. and Callaghan, P. T. (2006), *J. Magn. Reson.* 181:119–125.
- Gaur, U. and Wunderlich, B. (1980), *Macromolecules* 13:445–446.
- Gedde, U. (1999), *Polymer physics*, Springer.

- Glatter, O. and Kratky, O. (1982), *Small angle X-ray scattering*, Academic press.
- Grabowski, D. A. and Schmidt, C. (1994), *Macromolecules* 27:2632–2634.
- Graham, R. S. (2014), *Chem. Commun.* 50:3531–3545.
- Guinier, A. and Fournet, G. (1955), *Small Angle Scattering of X-Rays*, Vol. 14, John Wiley & Sons.
- Gullion, T., Baker, D. B. and Conradi, M. S. (1990), *J. Magn. Reson.* 89:479–484.
- Guthausen, G. and Kamlowski, A. (2009), in M. Guojonsdottir, P. Belton and G. A. Webb, eds, 'Magnetic Resonance in Food Science: Challenges in a Changing World', Vol. 293, RSC Publisher, pp. 46–56.
- Guthausen, G., Röntzsch, V., Biquet, C., Schlabach, S. and Wilhelm, M. (2014), *Macromol. Chem. Phys.* 215:851–858.
- Hafner, S., Demco, D. E. and Kimmich, R. (1996), *Solid State Nucl. Magn. Reson.* 6:275–293.
- Hahn, E. L. (1950), *Phys. Rev.* 80:580–594.
- Hamley, I., Pople, J., Booth, C., Derici, L., Impéror-Clerc, M. and Davidson, P. (1998), *Phys. Rev. E* 58:7620–7628.
- Hansen, E. W., Kristiansen, P. E. and Pedersen, B. (1998), *J. Phys. Chem. B* 102:5444–5450.
- Hassell, D. G. and Mackley, M. R. (2008), *Rheol. Acta* 47:435–446.
- Heeley, E., Maidens, A., Olmsted, P., Bras, W., Dolbnya, I., Fairclough, J., Terrill, N. and Ryan, A. (2003), *Macromolecules* 36:3656–3665.
- Helal, A., Divoux, T. and McKinley, G. H. (2016), *Phys. Rev. Appl* 6:064004(1–25).
- Hermans, P. H. (1946), *Contribution to the physics of cellulose fibres*, Elsevier.
- Hertlein, C., Saalwächter, K. and Strobl, G. (2006), *Polymer* 47:7216–7221.
- Höfl, S., Kremer, F., Spiess, H. W., Wilhelm, M. and Kahle, S. (2006), *Polymer* 47:7282–7288.
- Hikosaka, M. (1987), *Polymer* 28:1257–1264.
- Hikosaka, M. (1990), *Polymer* 31:458–468.
- Hikosaka, M., Watanabe, K., Okada, K. and Yamazaki, S. (2005), *Interphases and Mesophases in Polymer Crystallization III* pp. 137–186.
- Hikosaka, M., Yamazaki, S., Wataoka, I., Ch. Das, N., Okada, K., Toda, A. and Inoue, K. (2003), *J. Macromol. Sci. B* 42:847–865.
- Hilliou, L., Wilhelm, M., Yamanoi, M. and Gonçalves, M. P. (2009), *Food Hydrocoll.* 23:2322–2330.
- Hoffman, J. D., Davis, G. T. and Lauritzen Jr, J. I. (1976), *The rate of crystallization of linear polymers with chain folding*, Springer, pp. 497–614.
- Hoffman, J. D. and Lauritzen, J. I. (1961), *J. Res. Nat. Bur. Stand.* 65A:297–336.
- Hoffman, J. D. and Miller, R. L. (1988), *Macromolecules* 21:3038–3051.
- Hoffman, J. D. and Weeks, J. J. (1962), *J. Chem. Phys.* 37:1723–1741.
- Hoffman, J., Lauritzen, J., Passaglia, E., Ross, G., Frolen, L. and Weeks, J. (1969), *Colloid Polym. Sci.* 231:564–592.
- Hollingsworth, K. G., Sederman, A. J., Buckley, C., Gladden, L. F. and Johns, M. L. (2004), *J. Colloid Interface Sci.* 274:244–250.

- Hongladarom, K., Ugaz, V., Cinader, D., Burghardt, W., Quintana, J., Hsiao, B., Dadmun, M., Hamilton, W. and Butler, P. (1996), *Macromolecules* 29:5346–5355.
- Hoult, D. (1979), *Rev. Sci. Instrum.* 50:193–200.
- Housmans, J.-W., Gahleitner, M., Peters, G. W. and Meijer, H. E. (2009), *Polymer* 50:2304–2319.
- Housmans, J.-W., Peters, G. W. and Meijer, H. E. (2009), *J. Therm. Anal. Calorim.* 98:693–705.
- Housmans, J.-W., Steenbakkens, R. J., Roozmond, P. C., Peters, G. W. and Meijer, H. E. (2009), *Macromolecules* 42:5728–5740.
- Hürlimann, M. and Griffin, D. (2000), *J. Magn. Reson.* 143:120–135.
- Hu, W.-G., Boeffel, C. and Schmidt-Rohr, K. (1999), *Macromolecules* 32:1611–1619.
- Hugel, T., Strobl, G. and Thomann, R. (1999), *Acta Polym.* 50:214–217.
- Huo, H., Jiang, S., An, L. and Feng, J. (2004), *Macromolecules* 37:2478–2483.
- Huston, E., Cahn, J. W. and Hilliard, J. (1966), *Acta Metall.* 14:1053–1062.
- Hyun, K. and Wilhelm, M. (2008), *Macromolecules* 42:411–422.
- Hyun, K., Wilhelm, M., Klein, C. O., Cho, K. S., Nam, J. G., Ahn, K. H., Lee, S. J., Ewoldt, R. H. and McKinley, G. H. (2011), *Prog. Polym. Sci.* 36:1697–1753.
- Imai, M., Kaji, K. and Kanaya, T. (1994), *Macromolecules* 27:7103–7108.
- Imai, M., Kaji, K., Kanaya, T. and Sakai, Y. (1995), *Phys. Rev. B* 52:12696–12704.
- Imai, M., Mori, K., Mizukami, T., Kaji, K. and Kanaya, T. (1992), *Polymer* 33:4451–4456.
- Jain, S., Goossens, H., van Duin, M. and Lemstra, P. (2005), *Polymer* 46:8805–8818.
- Janeschitz-Kriegl, H. (1992), *Polymer solidification by crystallization under heat transfer and flow conditions*, Springer, pp. 116–128.
- Janeschitz-Kriegl, H. (2012), *Polymer melt rheology and flow birefringence*, Vol. 6, Springer.
- Janssens, V., Block, C., Van Assche, G., Van Mele, B. and Van Puyvelde, P. (2009), *J. Therm. Anal. Calorim.* 98:675–681.
- Janssens, V., Block, C., Van Assche, G., Van Mele, B. and Van Puyvelde, P. (2010), *Int. Polym. Process.* 25:304–310.
- Jay, F., Haudin, J.-M. and Monasse, B. (1999), *J. Mater. Sci.* 34:2089–2102.
- Kahle, S., Nussbaum, W., Hehn, M., Raich, H. P., Wilhelm, M. and Blümmler, P. (2008), *Kautsch. Gummi Kunstst.* 61:92–94.
- Kaji, K., Nishida, K., Kanaya, T., Matsuba, G., Konishi, T. and Imai, M. (2005), *Interphases and Mesophases in Polymer Crystallization III* pp. 187–240.
- Kaminsky, W., ed. (2013a), *Polyolefins: 50 years after Ziegler and Natta I: Polyethylene and Polypropylene*, Vol. 257 of *Advances in Polymer Science*, Springer.
- Kaminsky, W., ed. (2013b), *Polyolefins: 50 years after Ziegler and Natta II: Polyolefins by Metallocenes and Other Single-Site Catalysts*, Vol. 258 of *Advances in Polymer Science*, Springer.
- Kaminsky, W., Külper, K., Brintzinger, H. H. and Wild, F. R. (1985), *Angew. Chem.* 97:507–508.
- Kannan, R. M. and Kornfield, J. A. (1994), *Macromolecules* 27:1177–1186.

- Karger-Kocsis, J. (1994), *Polypropylene Structure, blends and composites: Volume 1 Structure and Morphology*, Vol. 1, Springer.
- Karger-Kocsis, J. (2012), *Polypropylene: an A–Z reference*, Vol. 2, Springer.
- Kawaguchi, M. and Kubota, K. (2004), *Langmuir* 20:1126–1129.
- Keeler, J. (2011), *Understanding NMR spectroscopy*, John Wiley & Sons.
- Keith, H. and Padden Jr, F. (1963), *J. Appl. Phys.* 34:2409–2421.
- Keller, A. (1957), *Philos. Mag.* 2:1171–1175.
- Keller, A., Hikosaka, M., Rastogi, S., Toda, A., Barham, P and Goldbeck-Wood, G. (1994), *J. Mater. Sci.* 29:2579–2604.
- Keller, A. K. and Mackley, M. R. (1974), *Pure Appl. Chem.* 39:195–224.
- Khastgir, D. and Adachi, K. (2000), *Polymer* 41:6403–6413.
- Kiewiet, S., Janssens, V., Miltner, H., Van Assche, G., Van Puyvelde, P and Van Mele, B. (2008), *Rev. Sci. Instrum.* 79:023905(1–7).
- Kilfoil, M. L. and Callaghan, P T. (2000), *Macromolecules* 33:6828–6833.
- Kim, J., Merger, D., Wilhelm, M. and Helgeson, M. E. (2014), *J. Rheol.* 58:1359–1390.
- Kim, S., Hyun, K., Kim, Y. S., Struth, B., Clasen, C. and Ahn, K. H. (2013), *Langmuir* 29:10059–10065.
- Kimata, S., Sakurai, T., Nozue, Y., Kasahara, T., Yamaguchi, N., Karino, T., Shibayama, M. and Kornfield, J. A. (2007), *Science* 316:1014–1017.
- Kimmich, R. (1997), *NMR - Tomography Diffusometry Relaxometry*, Springer.
- Kimmich, R. (2012), *Principles of Soft-Matter Dynamics: Basic Theories, Non-invasive Methods, Mesoscopic Aspects*, Springer.
- Kitamaru, R. and Horii, F. (1978), *NMR approach to the phase structure of linear polyethylene*, Springer, pp. 137–178.
- Kolb, R., Seifert, S., Stribeck, N. and Zachmann, H. (2000), *Polymer* 41:1497–1505.
- Koscher, E. and Fulchiron, R. (2002), *Polymer* 43:6931–6942.
- Kotek, J., Raab, M., Baldrian, J. and Grellmann, W. (2002), *J. Appl. Polym. Sci.* 85:1174–1184.
- Kotula, A. P., Meyer, M. W., De Vito, F., Plog, J., Hight Walker, A. R. and Migler, K. B. (2016), *Rev. Sci. Instrum.* 87:105105(1–8).
- Kotula, A. P. and Migler, K. B. (2018), *J. Rheol.* 62:343–356.
- Kristiansen, M., Smith, P., Chanzy, H., Baerlocher, C., Gramlich, V., McCusker, L., Weber, T., Pattison, P., Blumenhofer, M. and Schmidt, H.-W. (2009), *Cryst. Growth Des.* 9:2556–2558.
- Kristiansen, M., Tervoort, T., Smith, P. and Goossens, H. (2005), *Macromolecules* 38:10461–10465.
- Kristiansen, M., Werner, M., Tervoort, T., Smith, P., Blumenhofer, M. and Schmidt, H.-W. (2003), *Macromolecules* 36:5150–5156.
- Kristiansen, P., Hansen, E. and Pedersen, B. (1999), *J. Phys. Chem. B* 103:3552–3558.
- Kristiansen, P., Hansen, E. and Pedersen, B. (2000), *Polymer* 41:311–321.
- Kristiansen, P., Hansen, E. and Pedersen, B. (2001), *Polymer* 42:1969–1980.

- Kumaraswamy, G. (2005), *J. Macromol. Sci. C* 45:375–397.
- Kumaraswamy, G., Issaian, A. M. and Kornfield, J. A. (1999), *Macromolecules* 32:7537–7547.
- Kumaraswamy, G., Kornfield, J. A., Yeh, F. and Hsiao, B. S. (2002), *Macromolecules* 35:1762–1769.
- Kumaraswamy, G., Verma, R., Issaian, A., Wang, P., Kornfield, J., Yeh, F., Hsiao, B. and Olley, R. (2000), *Polymer* 41:8931–8940.
- Kumaraswamy, G., Verma, R. K., Kornfield, J. A., Yeh, F. and Hsiao, B. S. (2004), *Macromolecules* 37:9005–9017.
- Kume, T., Hashimoto, T., Takahashi, T. and Fuller, G. G. (1997), *Macromolecules* 30:7232–7236.
- Lagasse, R. and Maxwell, B. (1976), *Polym. Eng. Sci.* 16:189–199.
- Lalia, B. S., Kochkodan, V., Hashaikeh, R. and Hilal, N. (2013), *Desalination* 326:77–95.
- Lamberti, G. (2012), *Rheol. Acta* 51:259–265.
- Lamberti, G. (2014), *Chem. Soc. Rev.* 43:2240–2252.
- Lamberti, G., Peters, G. and Titomanlio, G. (2007), *Int. Polym. Process.* 22:303–310.
- Langela, M., Wiesner, U., Spiess, H. W. and Wilhelm, M. (2002), *Macromolecules* 35:3198–3204.
- Larson, R. G. (1999), *The Structure and Rheology of Complex Fluids*, Topics in Chemical Engineering, Oxford University Press.
- Larson, R., Sridhar, T., Leal, L., McKinley, G., Likhtman, A. and McLeish, T. (2003), *J. Rheol.* 47:809–818.
- Lauritzen, J. I. and Hoffman, J. D. (1960), *J. Res. Natl. Bur. Stand. A* 64:73–102.
- Lee, K. and Mackley, M. (2001), *Chem. Eng. Sci.* 56:5653–5661.
- Lellinger, D., Floudas, G. and Alig, I. (2003), *Polymer* 44:5759–5769.
- Lettinga, M., Holmqvist, P., Ballesta, P., Rogers, S., Kleshchanok, D. and Struth, B. (2012), *Phys. Rev. Lett.* 109:246001(1–5).
- Liberatore, M. W., Nettesheim, F., Wagner, N. J. and Porcar, L. (2006), *Phys. Rev. E* 73:020504(1–4).
- Liedauer, S., Eder, G. and Janeschitz-Kriegl, H. (1995), *Int. Polym. Process.* 10:243–250.
- Liedauer, S., Eder, G., Janeschitz-Kriegl, H., Jerschow, P., Geymayer, W. and Ingolic, E. (1993), *Int. Polym. Process.* 8:236–244.
- Litvinov, V. M. and Penning, J. P. (2004), *Macromol. Chem. Phys.* 205:1721–1734.
- Litvinov, V. M. and van Duin, M. (2002), *Kautsch. Gummi Kunstst.* 55:460–463.
- Liu, Y., Zhou, W., Cui, K., Tian, N., Wang, X., Liu, L., Li, L. and Zhou, Y. (2011), *Rev. Sci. Instr.* 82:045104(1–6).
- Lopez-Gonzalez, M. R., Holmes, W. M. and Callaghan, P. T. (2006), *Soft Matter* 2:855–869.
- Lorenzo, A. T., Arnal, M. L., Albuerne, J. and Müller, A. J. (2007), *Polym. Test.* 26:222–231.
- Lukaschek, M., Grabowski, D. A. and Schmidt, C. (1995), *Langmuir* 11:3590–3594.
- Luo, C. and Sommer, J.-U. (2011), *Macromolecules* 44:1523–1529.
- Ma, Z., Balzano, L. and Peters, G. W. (2012), *Macromolecules* 45:4216–4224.

- Ma, Z., Balzano, L., Portale, G. and Peters, G. W. (2014), *Polymer* 55:6140–6151.
- Mackley, M. R., Frank, F. C. and Keller, A. (1975), *J. Mater. Sci.* 10:1501–1509.
- Mackley, M. R. and Keller, A. (1973), *Polymer* 14:16–20.
- Mackley, M. R., Moggridge, G. D. and Saquet, O. (2000), *J. Mater. Sci.* 35:5247–5253.
- Macosko, C. W. (1994), *Rheology: principles, measurements, and applications*, Wiley-VCH.
- Madivala, B., Fransaer, J. and Vermant, J. (2009), *Langmuir* 25:2718–2728.
- Magonov, S. and Godovsky, Y. (1999), *Am. Lab.* 31:52–58.
- Malek, A., Dingenouts, N., Beskers, T., Fehrenbacher, U., Barner, L. and Wilhelm, M. (2013), *Eur. Polym. J.* 49:2704–2720.
- Mandelkern, L. (1964), *Crystallization of polymers*, Vol. 38, McGraw-Hill.
- Mandelkern, L. (2002), *Crystallization of Polymers: Volume 1, Equilibrium Concepts*, Cambridge University Press.
- Mandelkern, L. (2004), *Crystallization of Polymers: Volume 2, Kinetics and Mechanisms*, Cambridge University Press.
- Mandelkern, L., Quinn Jr, F. A. and Flory, P. J. (1954), *J. Appl. Phys.* 25:830–839.
- Maranzano, B. J. and Wagner, N. J. (2002), *J. Chem. Phys.* 117:10291–10302.
- Mark, J. E. (2007), *Physical properties of polymers handbook*, Vol. 1076, Springer.
- Mascia, L., Russo, P., Verdolotti, L., Clarke, J., Lavorgna, M. and Acierno, D. (2015), *Rubber Chem. Technol.* 88:560–573.
- Maus, A., Hertlein, C. and Saalwächter, K. (2006), *Macromol. Chem. Phys.* 207:1150–1158.
- Medronho, B., Schmidt, C., Olsson, U. and Miguel, M. G. (2010), *Langmuir* 26:1477–1481.
- Meer, D., Varga, J. and Vancso, G. (2015), *eXPRESS Polym. Lett.* 9:233–254.
- Mehring, M. (1983), *Principles of High Resolution NMR in Solids*, Springer.
- Meiboom, S. and Gill, D. (1958), *Rev. Sci. Instrum.* 29:688–691.
- Meille, S. V. and Brückner, S. (1989), *Nature* 340:455–457.
- Meille, S. V., Ferro, D. R., Bruckner, S., Lovinger, A. J. and Padden, F. J. (1994), *Macromolecules* 27:2615–2622.
- Meins, T., Dingenouts, N., Kübel, J. and Wilhelm, M. (2012), *Macromolecules* 45:7206–7219.
- Meins, T., Hyun, K., Ratzsch, K.-F., Friedrich, C., Struth, B. and Wilhelm, M. (2011), *Ann. Trans. Nordic Rheology Society* 19:1–6.
- Mewis, J. and Wagner, N. J. (2012), *Colloidal suspension rheology*, Cambridge University Press.
- Milner, S. T. (2011), *Soft Matter* 7:2909–2917.
- Montesi, A., Peña, A. A. and Pasquali, M. (2004), *Phys. Rev. Lett.* 92:058303(1–4).
- Morrison, F. A. (2001), *Understanding rheology*, Oxford University Press.
- Mueller, S., Llewellyn, E. and Mader, H. (2009), in ‘Proceedings of the Royal Society of London A: Mathematical, Physical and Engineering Sciences’, Vol. 466, The Royal Society, pp. 1201–1228.

- Muthukumar, M. (2003), *Philos. Trans. A Math. Phys. Eng. Sci.* 361:539–556.
- Muthukumar, M. (2004), *Adv. Chem. Phys.* 128:1–64.
- Mykhaylyk, O. O., Chambon, P., Graham, R. S., Fairclough, J. P. A., Olmsted, P. D. and Ryan, A. J. (2008), *Macromolecules* 41:1901–1904.
- Mykhaylyk, O. O., Chambon, P., Impradice, C., Fairclough, J. P. A., Terrill, N. J. and Ryan, A. J. (2010), *Macromolecules* 43:2389–2405.
- Natta, G., Pino, P., Corradini, P., Danusso, F., Mantica, E., Mazzanti, G. and Moraglio, G. (1955), *J. Am. Chem. Soc.* 77:1708–1710.
- Nitta, K.-h., Asuka, K., Liu, B. and Terano, M. (2006), *Polymer* 47:6457–6463.
- Nogales, A., Ezquerra, T. A., Batallan, F., Frick, B., Lopez-Cabarcos, E. and Balta-Calleja, F. J. (1999), *Macromolecules* 32:2301–2308.
- Nogales, A., Hsiao, B. S., Somani, R. H., Srinivas, S., Tsou, A. H., Balta-Calleja, F. J. and Ezquerra, T. A. (2001), *Polymer* 42:5247–5256.
- Odian, G. (2004), *Principles of polymerization*, 4. edn, John Wiley & Sons.
- O'Halloran, A., O'malley, F. and McHugh, P. (2008), *J. Appl. Phys.* 104:1–10.
- Ohgo, K., Bagusat, F., Asakura, T. and Scheler, U. (2008), *J. Am. Chem. Soc.* 130:4182–4186.
- Olmsted, P. D., Poon, W. C., McLeish, T., Terrill, N. and Ryan, A. (1998), *Phys. Rev. Lett.* 81:373–376.
- Onogi, S. and Asada, T. (1980), *Rheology and rheo-optics of polymer liquid crystals*, Springer, pp. 127–147.
- Ostroff, E. D. and Waugh, J. S. (1966), *Phys. Rev. Lett.* 16:1097–1099.
- Pabby, A., Rizvi, S. and Requena, A. (2008), *Handbook of Membrane Separations: Chemical, Pharmaceutical, Food, and Biotechnological Applications*, Taylor & Francis.
- Packer, K., Pope, J., Yeung, R. and Cudby, M. (1984), *J. Polym. Sci.* 22:589–616.
- Pake, G. E. (1948), *J. Chem. Phys.* 16:327–336.
- Palza, H., Vergara, R. and Zapata, P. (2011), *Compos. Sci. Technol.* 71:535–540.
- Panine, P., Di Cola, E., Sztucki, M. and Narayanan, T. (2008), *Polymer* 49:676–680.
- Panine, P., Gradzielski, M. and Narayanan, T. (2003), *Rev. Sci. Instrum.* 74:2451–2455.
- Pantani, R., Coccorullo, I., Volpe, V. and Titomanlio, G. (2010), *Macromolecules* 43:9030–9038.
- Pantani, R., De Meo, A., Speranza, V. and Titomanlio, G. (2015), *Aip Conf. Proc.* 1695:020065(1–8).
- Pantani, R., Nappo, V., De Santis, F. and Titomanlio, G. (2014), *Macromol. Mater. Eng.* 229:1465–1473.
- Pantani, R., Speranza, V. and Titomanlio, G. (2015), *J. Rheol.* 59:377–390.
- Papageorgiou, G. Z., Achilias, D. S., Bikiaris, D. N. and Karayannidis, G. P. (2005), *Thermochim. Acta* 427:117–128.
- Papon, A., Saalwächter, K., Schaler, K., Guy, L., Lequeux, F. and Montes, H. (2011), *Macromolecules* 44:913–922.
- Pathak, J. A. and Hudson, S. D. (2006), *Macromolecules* 39:8782–8792.
- Paulin, S., Ackerson, B. J. and Wolfe, M. (1997), *Phys. Rev. E* 55:5812–5819.

- Peshkovsky, A., Forguez, J., Cerioni, L. and Pusiol, D. (2005), *J. Magn. Reson.* 177:67–73.
- Pfleiderer, P., Baik, S. J., Zhang, Z., Vleminckx, G., Lettinga, M. P., Grelet, E., Vermant, J. and Clasen, C. (2014), *Rev. Sci. Instr.* 85:065108(1–8).
- Pines, A., Rhim, W.-K. and Waugh, J. (1972), *J. Magn. Reson.* 6:457–465.
- Piorkowska, E. and Rutledge, G. C. (2013), *Handbook of polymer crystallization*, John Wiley & Sons.
- Plastics Europe Report (2016), published online, www.plasticseurope.org (accessed 09/2017).
- Pogodina, N., Siddiquee, S., Van Egmond, J. and Winter, H. (1999), *Macromolecules* 32:1167–1174.
- Pogodina, N. V., Lavrenko, V. P., Srinivas, S. and Winter, H. H. (2001), *Polymer* 42:9031–9043.
- Pogodina, N. V. and Winter, H. H. (1998), *Macromolecules* 31:8164–8172.
- Point, J. and Dosiere, M. (1989), *Polymer* 30:2292–2296.
- Point, J.-J. (1979), *Faraday Discuss. Chem. Soc.* 68:167–176.
- Polushkin, E., Bondzic, S., de Wit, J., Alberda van Ekenstein, G., Dolbnya, I., Bras, W., Ikkala, O. and Ten Brinke, G. (2005), *Macromolecules* 38:1804–1813.
- Polushkin, E., van Ekenstein, G. A., Ikkala, O. and ten Brinke, G. (2004), *Rheol. Acta* 43:364–372.
- Portale, G., Cavallo, D., Alfonso, G. C., Hermida-Merino, D., Drongelen, M. v., Balzano, L., Peters, G., Goossens, J. and Bras, W. (2013), *J. Appl. Crystallogr.* 46:1681–1689.
- Pötschke, P., Fornes, T. and Paul, D. (2002), *Polymer* 43:3247–3255.
- Powell, M. (1979), *Phys. Rev. B* 20:4194–4198.
- Powles, J. and Strange, J. (1963), *Proc. Phys. Soc.* 82:6–15.
- Pulamagatta, B., Ostas, E., Herbst, F., Struth, B. and Binder, W. H. (2012), *Eur. Polym. J.* 48:1127–1134.
- Ran, S., Zong, X., Fang, D., Hsiao, B. S., Chu, B. and Ross, R. (2000), *J. Appl. Crystallogr.* 33:1031–1036.
- Ratzsch, K.-F., Friedrich, C. and Wilhelm, M. (2017), *J. Rheol.* 61:905–917.
- Ratzsch, K., Kádár, R., Naue, I. and Wilhelm, M. (2013), *Macromol. Mater. Eng.* 298:1124–1132.
- Redfield, A. G. (1957), *IBM J. Res. Dev.* 1:19–31.
- Reinheimer, K., Grosso, M. and Wilhelm, M. (2011), *J. Colloid Interface Sci.* 360:818–825.
- Reiter, G. and Strobl, G. R. (2007), *Progress in Understanding of Polymer Crystallization*, Vol. 714 of *Lecture Notes in Physics*, Springer.
- Resconi, L., Cavallo, L., Fait, A. and Piemontesi, F. (2000), *Chem. Rev.* 100:1253–1346.
- Rhim, W., Pines, A. and Waugh, J. (1971), *Phys. Rev. B* 3:684–696.
- Räntzsch, V., Haas, M., Özen, M. B., Ratzsch, K.-F., Riazzi, K., Kauffmann-Weiss, S., Palacios, J. K., Müller, A. J., Vittorias, I., Guthausen, G. and Wilhelm, M. (2018), *Polymer* 145:162–173.
- Räntzsch, V., Ratzsch, K.-F., Guthausen, G., Schlabach, S. and Wilhelm, M. (2014), *Soft Mater.* 12:S4–S13.
- Räntzsch, V., Wilhelm, M. and Guthausen, G. (2016), *Magn. Reson. Chem.* 54:494–501.
- Räntzsch, V., Özen, M. B., Ratzsch, K.-F., Guthausen, G. and Wilhelm, M. (2017a), *Aip Conf. Proc.* 1914:110001(1–5).

- Räntzsch, V., Özen, M. B., Rätzsch, K.-F., Guthausen, G. and Wilhelm, M. (2017b), *Aip Conf. Proc.* 1843:040001(1–7).
- Roozemon, P. C., Janssens, V., Van Puyvelde, P. and Peters, G. W. (2012), *Rheol. Acta* 51:97–109.
- Roozemon, P. C., Ma, Z., Cui, K., Li, L. and Peters, G. W. (2014), *Macromolecules* 47:5152–5162.
- Saalwächter, K., Herrero, B. and Lopez-Manchado, M. A. (2005), *Macromolecules* 38:9650–9660.
- Sadler, D. and Gilmer, G. (1984), *Polymer* 25:1446–1452.
- Sadler, D. M. (1987), *Nature* 326:174–177.
- Samon, J. M., Schultz, J. M., Wu, J., Hsiao, B., Yeh, F. and Kolb, R. (1999), *J. Polym. Sci.* 37:1277–1287.
- Sanchez, I. C. and DiMarzio, E. A. (1971), *J. Chem. Phys.* 55:893–908.
- Sawyer, L., Grubb, D. and Meyers, G. F. (2008), *Polymer microscopy*, Springer.
- Scelsi, L. and Mackley, M. R. (2008), *Rheol. Acta* 47:895–908.
- Scher, H. and Zallen, R. (1970), *J. Chem. Phys.* 53:3759–3761.
- Schmidt, C. (2006), *Rheo-NMR Spectroscopy*, Springer, Berlin, pp. 1495–1501.
- Schmidt-Rohr, K. and Spiess, H.-W. (1994), *Multidimensional Solid-State NMR and Polymers*, Academic Press.
- Schrauwen, B., Breemen, L. v., Spoelstra, A., Govaert, L., Peters, G. and Meijer, H. (2004), *Macromolecules* 37:8618–8633.
- Schultz, J., Hsiao, B. S. and Samon, J. (2000), *Polymer* 41:8887–8895.
- Sergeev, N., Ryabushkin, D. and Moskvich, Y. N. (1985), *Phys. Lett. A* 109:338–340.
- Shaw, M. T. (2012), *Introduction to polymer rheology*, John Wiley & Sons.
- Sirota, E. B. (2007), *Macromolecules* 40:1043–1048.
- Skotheim, T. A. and Reynolds, J. (2006), *Conjugated polymers: theory, synthesis, properties, and characterization*, CRC press.
- Slichter, C. P. (1996), *Principles of Magnetic Resonance*, Springer Series in Solid-State Sciences, Springer.
- Somani, R. H., Hsiao, B. S., Nogales, A., Fruitwala, H., Srinivas, S. and Tsou, A. H. (2001), *Macromolecules* 34:5902–5909.
- Somani, R. H., Hsiao, B. S., Nogales, A., Srinivas, S., Tsou, A. H., Sics, I., Balta-Calleja, F. J. and Ezquerro, T. A. (2000), *Macromolecules* 33:9385–9394.
- Somani, R. H., Yang, L., Hsiao, B. S., Agarwal, P. K., Fruitwala, H. A. and Tsou, A. H. (2002), *Macromolecules* 35:9096–9104.
- Somani, R. H., Yang, L., Hsiao, B. S. and Fruitwala, H. (2003), *J. Macromol. Sci. B* 42:515–531.
- Somani, R. H., Yang, L., Hsiao, B. S., Sun, T., Pogodina, N. V. and Lustiger, A. (2005), *Macromolecules* 38:1244–1255.
- Somani, R. H., Yang, L., Zhu, L. and Hsiao, B. S. (2005), *Polymer* 46:8587–8623.
- Sommer, J. and Luo, C. (2010), *J. Polym. Sci.* 48:2222–2232.
- Spaleck, W., Kueber, F., Winter, A., Rohrmann, J., Bachmann, B., Antberg, M., Dolle, V. and Paulus, E. F. (1994), *Organometallics* 13:954–963.

- Sperling, L. H. (2005), *Introduction to physical polymer science*, John Wiley & Sons.
- Spiess, H. W. (1983), *Colloid Polym. Sci.* 261:193–209.
- Steenbakkers, R. (2005), Modeling flow-induced crystallization of polymers, Eindhoven University of Technology, Eindhoven, Netherlands.
- Stehling, F. C. and Mandelkern, L. (1970), *Macromolecules* 3:242–252.
- Stellamanns, E., Meissner, D., Lohmann, M. and Struth, B. (2013), *J. Phys. Conf. Ser.* 425:1–3.
- Strickland-Constable, R. F. (1968), *Kinetics and Mechanism of Crystallization from the Fluid Phase and of the Condensation and Evaporation of Liquids*, Academic Press.
- Strobl, G. (2000), *Eur. Phys. J. E* 3:165–183.
- Strobl, G. (2006), *Prog. Polym. Sci.* 31:398–442.
- Strobl, G. (2009), *Rev. Mod. Phys.* 81:1287–1300.
- Strobl, G. and Cho, T. (2007), *Eur. Phys. J. E* 23:55–65.
- Strobl, G. and Schneider, M. (1980), *J. Polym. Sci.* 18:1343–1359.
- Struth, B., Hyun, K., Kats, E., Meins, T., Walther, M., Wilhelm, M. and Grübel, G. (2011), *Langmuir* 27:2880–2887.
- Swan, P. R. (1960), *J. Polym. Sci.* 42:525–534.
- Szkudlarek, E., Piorkowska, E., Boyer, S. A., Haudin, J.-M. and Gadzinowska, K. (2013), *Eur. Polym. J.* 49:2109–2119.
- Takegoshi, K. and McDowell, C. A. (1985), *Chem. Phys. Lett.* 116:100–104.
- Tanaka, H. and Nishi, T. (1986a), *J. Appl. Phys.* 59:1488–1492.
- Tanaka, H. and Nishi, T. (1986b), *J. Chem. Phys.* 85:6197–6209.
- Thimm, W., Friedrich, C., Marth, M. and Honerkamp, J. (1999), *J. Rheol.* 43:1663–1672.
- Thomann, R., Wang, C., Kressler, J. and Mülhaupt, R. (1996), *Macromolecules* 29:8425–8434.
- Todt, H., Guthausen, G., Burk, W., Schmalbein, D. and Kamlowski, A. (2006a), *Time-Domain NMR in Quality Control: Standard Application in Food*, Vol. 3, Springer, pp. 1717–1721.
- Todt, H., Guthausen, G., Burk, W., Schmalbein, D. and Kamlowski, A. (2006b), *Food Chem.* 96:436–440.
- Turnbull, D. and Fisher, J. C. (1949), *J. Chem. Phys.* 17:71–73.
- van Drongelen, M., Cavallo, D., Balzano, L., Portale, G., Vittorias, I., Bras, W., Alfonso, G. C. and Peters, G. W. (2014), *Macromol. Mater. Eng.* 299:1494–1512.
- Van Krevelen, D. W. and Te Nijenhuis, K. (2009), *Properties of polymers: their correlation with chemical structure; their numerical estimation and prediction from additive group contributions*, Elsevier.
- van Meerveld, J., Peters, G. W. and Hütter, M. (2004), *Rheol. Acta* 44:119–134.
- Varga, J. (1983), *Macromol. Mater. Eng.* 112:191–203.
- Varga, J. (1992), *J. Mater. Sci.* 27:2557–2579.
- Varga, J. (2002), *J. Macromol. Sci. B* 41:1121–1171.
- Varga, J. and Karger-Kocsis, J. (1996), *J. Polym. Sci.* 34:657–670.

- Vleeshouwers, S. and Meijer, H. E. (1996), *Rheol. Acta* 35:391–399.
- Volmer, M. and Weber, A. (1926), *Z. Phys. Chem.* 119:277–301.
- Vonk, C. (1978), *J. Appl. Crystallogr.* 11:541–546.
- Vonk, C. and Kortleve, G. (1967), *Colloid Polym. Sci.* 220:19–24.
- Wagner, N. J. (1998), *Curr. Opin. Colloid Interface Sci.* 3:391–400.
- Walker, L. M., Kernick, W. A. and Wagner, N. J. (1997), *Macromolecules* 30:508–514.
- Wang, Z.-G., Hsiao, B. S., Sirota, E. B., Agarwal, P. and Srinivas, S. (2000), *Macromolecules* 33:978–989.
- Ward, I. M. and Sweeney, J. (2012), *Mechanical properties of solid polymers*, John Wiley & Sons.
- Watanabe, H., Sato, T., Hirose, M., Osaki, K. and Yao, M.-L. (1998), *Rheol. Acta* 37:519–527.
- Watanabe, H., Sato, T., Matsumiya, Y., Inoue, T. and Osaki, K. (1999), *Nihon Reoroji Gakk.* 27:121–125.
- Westermeier, F., Pennicard, D., Hirsemann, H., Wagner, U. H., Rau, C., Graafsma, H., Schall, P., Lettinga, M. P. and Struth, B. (2016), *Soft Matter* 12:171–180.
- White, J. L. and Spruiell, J. E. (1983), *Polym. Eng. Sci.* 23:247–256.
- Wilchinsky, Z. W. (1968), *J. Polym. Sci.* 6:281–288.
- Wilhelm, M. (2002), *Macromol. Mater. Eng.* 287:83–105.
- Wilhelm, M., Reinheimer, P. and Ortseifer, M. (1998), *Rheol. Acta* 38:349–356.
- Williams, M. L., Landel, R. F. and Ferry, J. D. (1955), *J. Am. Chem. Soc.* 77:3701–3707.
- Wingstrand, S. L., Shen, B., Kornfield, J. A., Mortensen, K., Parisi, D., Vlassopoulos, D. and Hassager, O. (2017), *ACS Macro Lett.* 6:1268–1273.
- Winter, H. H. and Mours, M. (1997), *Rheology of polymers near liquid-solid transitions*, Springer, pp. 165–234.
- Wunderlich, B. (1976), *Macromolecular Physics*, Vol. 2, Academic Press.
- Wunderlich, B. (2005), *Thermal analysis of polymeric materials*, Vol. 1, Springer Science & Business Media.
- Xiao, Z. and Akpalu, Y. A. (2007), *Polymer* 48:5388–5397.
- Xu, J., Heck, B., Ye, H.-M., Jiang, J., Tang, Y.-R., Liu, J., Guo, B.-H., Reiter, R., Zhou, D.-S. and Reiter, G. (2016), *Macromolecules* 49:2206–2215.
- Yan, T., Zhao, B., Cong, Y., Fang, Y., Cheng, S., Li, L., Pan, G., Wang, Z., Li, X. and Bian, F. (2009), *Macromolecules* 43:602–605.
- Yemelyanov, D. N. (1990), in 'Third European Rheology Conference and Golden Jubilee Meeting of the British Society of Rheology', Springer, pp. 513–515.
- Yi, P., Locker, C. R. and Rutledge, G. C. (2013), *Macromolecules* 46:4723–4733.
- Ziegler, K., Holzkamp, E., Breil, H. and Martin, H. (1955), *Angew. Chem.* 67:541–547.
- Ziff, R. M. and Torquato, S. (2017), *J. Phys. A: Math. Theor.* 50:1–12.
- Zimmer, G., Helmle, M., Mehring, M. and Rachdi, F. (1994), *Europhys. Lett.* 27:543–548.
- Zimmer, G., Mehring, M., Goze, C. and Rachdi, F. (1995), *Phys. Rev. B* 52:13300–13305.
- Zuidema, H., Peters, G. W. and Meijer, H. E. (2001), *Macromol. Theory Simul.* 10:447–460.
- Zuppari, F., Chiacchio, F. R., Sammarco, R., Malinconico, M., d'Ayala, G. G. and Cerruti, P. (2017), *Polymer* 112:169–179.